Vibrational Spectroscopic Studies of Degradation and Diffusion Processes in Poly(ethylene terephthalate)

By

Christopher Sammon

A thesis submitted in part fulfilment of the requirements of Sheffield Hallam University for the degree of Doctor of Philosophy

December 1997

Declaration

The work described in this thesis was carried out by the author in the Materials Research Institute, Sheffield Hallam University, between September 1994 and October 1997. The author declares that this work has not been submitted for any other degree. The work is original except where acknowledged by reference.

Author:

(Christopher Sammon)

Supervisor:

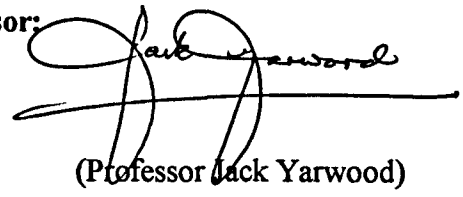

(Professor Jack Yarwood)

Acknowledgements

I'd like thank the people whose support during this project was greatly appreciated:

Especially Jack Yarwood and Neil Everall for their scientific input, useful (and not so useful !) comments, good (and not so good !) ideas and unflagging enthusiasm, which has been a major driving force since September 1994.

Mark Hodgson and Julian Robinson at ICI (or should that be Dupont) films for helping make and characterise the thin PET films for the RAIRS work.

My family; Mum, Dad, Nan, Paul and Clare who haven't got a clue what I've been doing or why I've been doing it, but who have given me a great deal of (financial) support throughout, I guess it's my round !

To all the Vib Spec group:
The Old School; The Fella, J.B., Cleggy, Beat-the, Tommy Castle-Eden, Evangy The Big Fella, The Big Dutch Centre-Forward, Tommy Cockles, Nigels' German Bird and while I'm at it Byron and Russ (*no mas*).
The New School; Peda da Pusieda, Frag, The Italian Mare, Carine the German, The Giant JPG, The Dwarf Sandra and Chris C. for being so easy to wind-up.

And finally, to someone who has been generous beyond the call of duty, kind, considerate, helpful and most importantly there when needed, Helen, thanks a million.

Contents

Abstract

The interaction of polyethylene terephthalate (PET) with water at both ambient and elevated temperatures has been studied. The diffusion of water, at ambient temperatures, into PET films, of the order of 10 μm thick, has been followed using Fourier transform infrared attenuated total reflectance, FT-IR ATR, spectroscopy. Films of differing degrees of crystallinity were prepared using two different methods. One method involved the annealing of the cast films at 85-90° C for different lengths of time, to obtain a range of crystallinities. The other method involved the incorporation of different amounts of an *iso*phthalate group, to obtain a range of crystallinities. The rate of water diffusion with time was then measured as a function of crystallinity. The diffusion was shown to be classically Fickian in nature and the diffusion coefficients decreased with increased polymer crystallinity for both sets of films. The perturbation of the ν(OH) band of the water in the polymer matrix was studied as both a function of time (i.e. concentration) and crystallinity. The water band was shown to be decoupled at low concentrations within the polymer matrix, indicating a breaking up of the water hydrogen bonding network. At higher concentrations, longer times, the ν(OH) band gained more 'pure water' like character, but remained at higher frequency than pure water even at equilibrium water content, suggesting clustering of the water molecules, but an overall weakening of the hydrogen bonding network relative to the pure water spectrum.

The study of the interactions of water at elevated temperatures including the degradative hydrolysis of PET at 90° C was undertaken using reflection absorption infrared spectroscopy (RAIRS). Films of < 150 nm were immersed in pure water at 52, 62, 70, 80 and 90° C and the effect on the polymeric structure was examined. At temperatures below 90° C the effects noted, on the time scales studied, were annealing effects, resulting in an increase in crystallinity. Estimations of the apparent activation energy of the *gauche* to *trans* isomerisation, for different degrees of crystallinity, were calculated and were found to be lower than those reported in the literature in air. This difference was thought to be a result of the plasticisation effects of water. At 90° C, during several days of immersion, the polymer was found to undergo hydrolysis. Complex changes in the RAIRS spectrum were related to changes in the polymeric structure, resulting from degradation. The autocatalytic nature of the degradation was highlighted, as was the loss of (small) mobile species from the polymer matrix. A mechanism involving the preferred site of hydrolysis being a terminal ester group was proposed. Comparisons with hot alkaline hydrolysis were made. This occurred much faster and with more random chain scission.

The diffusion of two organic liquids, methanol and ethylene glycol, into PET was studied. The diffusion was shown to be non-Fickian in nature due to the swelling and crystallisation that accompanied the diffusion. For the amorphous PET films, diffusion was accompanied by swelling and crystallisation for both molecules and was fitted to a dual sorption model. There was spectroscopic evidence for both a 'bound' alcohol - PET moiety and a 'free' alcohol species within the polymer matrix. For methanol in PET, the proportion of the sorbed alcohol which was 'bound' was found to increase with crystallinity, but for ethylene glycol the reverse was true. For methanol diffusion, increasing the crystallinity was shown to have a drastic effect on both the rate of diffusion and degree of swelling. For ethylene glycol diffusion, the degree of crystallinity appeared to affect the rate of swelling and the initial rate of sorption of penetrant, but the rate of the subsequent diffusion seemed to be unaffected by morphology.

The interface between two layers of 20 and 30 μm co-extruded PET laminates of PET and PET with an *iso*phthalate comonomer, were examined using confocal Raman microscopy. The methods of confocal depth profiling through the polymer laminate and scanning, step-wise, along a cut edge were compared. The interface was examined using the carbonyl band width of PET as an indicator of crystallinity. The interface was shown to be 2 - 3 μm thick, independent of film thickness and contain a gradient of ν(C=O) band width, indicating either interdiffusion or a *trans*-esterification reaction between the two polymer layers during co-extrusion.

Chapter 1

The structure and infrared spectrum of Poly(ethylene terephthalate)

1.1. Introduction

Poly(ethylene terephthalate) or PET is a semicrystalline polymer that is widely used in a whole range of commercial products. It is used in the audio and video tapes industry as the substrate to which magnetic materials are bound. It is widely used in the photography industry as the substrate for camera film. It can be used in the food packaging industry as one of the laminate layers in sandwich wrappers or blown to form carbonated beverage containers. It can be used in laminates for overhead projection sheets or as a 'shrink-wrap' type packaging material. It is also used as an insulating material in the electronics industry. With a world wide production of ~ 1.75 M tons [1.1] it is hardly surprising the amount of work that has been undertaken to characterise the properties of PET. But most of that work has been on the 'finished' PET film which has often been drawn, annealed and treated to give certain properties. During the manufacture of PET many treatments are carried out on the film. In order to allow coatings to bind to the surface of PET one side is generally treated with an aqueous latex containing a cocktail of acrylics with a catalyst. Another process in film manufacture involves the coextrusion of different types of PET to form a laminate.

This project will try to address the effects that the aqueous part of the latex has on the surface of PET and also investigate the interactions of the two very similar polymers in the PET laminate.

1.2. PET manufacture.

The manufacture of PET generally involves the direct esterification of terephthalic acid and ethylene glycol to form the monomer, (bis-(2-hydroxyethyl) terephthalate or BHET and water. When BHET is heated at 300°C at near vacuum pressure in the presence of a catalyst, polycondensation occurs and the monomers join in a head to toe arrangement. At this stage of the process additives such as fillers and stabilisers may be added. Typical PET contains around 100 repeating units. The raw polymer is extruded and made into small chips for film manufacture. The direct esterification and polycondensation processes are shown in figure 1.1.

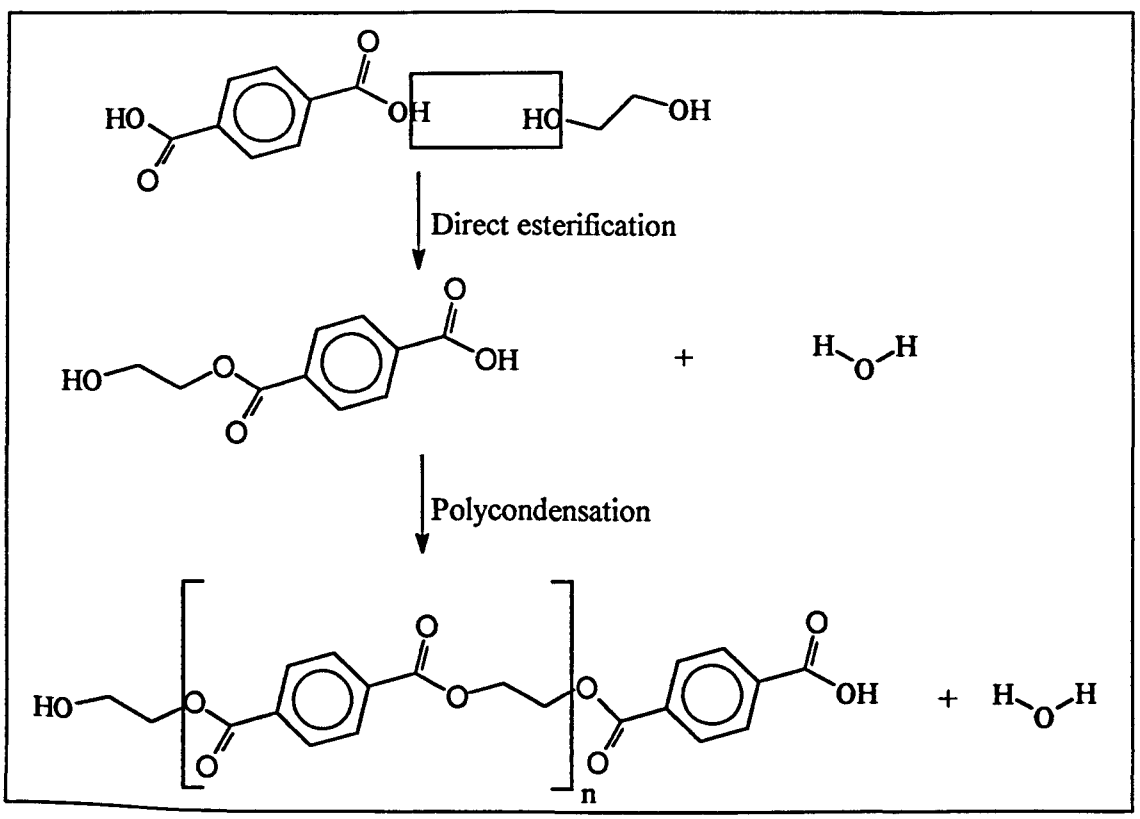

Figure 1.1. The formation of poly(ethylene terephthalate).

1.2.1. PET film manufacture.

The film manufacture process involves five basic stages; polymer preparation, casting, drawing, crystallisation and roll formation. Polymer preparation generally involves the blending of virgin polymer chips with recycled PET (known as reclaim) and subsequent drying of the mixture. The ratio of virgin chip to reclaim is important. Inorder to retain high film quality, low amounts of reclaim should be used, but environmental and economic pressures dictate that reclaim should be incorporated into the film manufacture process.

The dried PET is then placed in a heated vessel where it is melted under pressure and forced through filters to remove contamination. The molten PET then makes its way to the casting vessel known as the die, where under controlled conditions it is extruded onto a cooled rotating drum. At this stage of the process the film is totally amorphous. To improve the mechanical properties of the film, orientation is put into it by drawing, firstly in the forward direction at 90°C and secondly at 100°C in the transverse direction which is perpendicular to the forward direction. The second stage of this process is carried out in the stenter and the product is known as biaxially oriented film.

The tensile properties of PET film are enhanced by thermal crystallisation of the biaxially oriented film in the stenter at 200°C for several minutes. After the desired crystallisation time, the film is then cooled and the edges trimmed for reclaim. This is important as the film edges have not undergone the same drawing processes due to being gripped in the stenter and therefore have different mechanical properties. The cooled film is then simply cut and rolled to the required length.

The surface of PET has poor adhesive properties and as such during the film manufacture surface modification may be necessary depending on the final usage. There are two main methodologies for this; coextrusion and on line surface treatment.

The coextrusion process simply involves the modification of the casting die, so that two or more layers of different polymer are extruded onto the cooling drum. The rest of the manufacture is as before. The in-line treatment is carried out before the film is biaxially stretched and simply involves the spraying on of an aqueous latex, containing reactants. Part of this project deals with these two processes. How does the aqueous phase of the latex affect the film performance ? Is degradation of the surface likely under film manufacture conditions ? How much interpenetration occurs between phases during the coextrusion process ?

1.3. PET structure.

PET is a semicrystalline polymer, which means it is neither fully amorphous nor fully crystalline but a mixture of the two. From X-ray diffraction data it is possible to conclude that PET has an almost planar configuration in the crystalline state **[1.2]** The crystalline regions have been shown to contain an all *trans* conformation about the 'ethylene glycol' moiety **[1.2-1.5]**, whilst the amorphous regions contain both *trans* and *gauche* 'ethylene glycol' units **[1.6-1.10]**. These statements will be justified later in this chapter in the review of the conformational studies other workers have undertaken. Figure 1.1. shows PET in an all *trans* 'crystalline' conformation and figure 1.2. shows

PET in a mixed *trans* and *gauche* 'amorphous' conformation with the 'ethylene glycol' moiety highlighted.

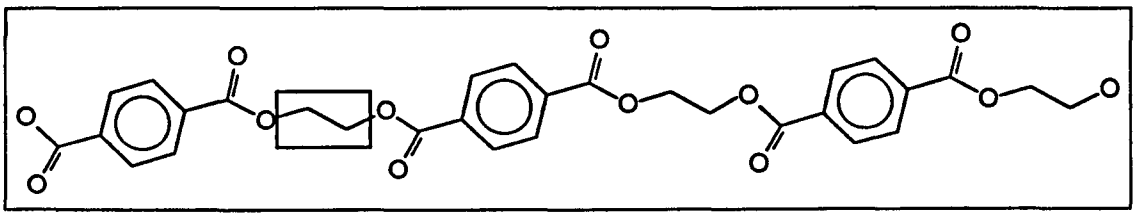

Figure 1.1. PET in the all trans 'crystalline' conformation.

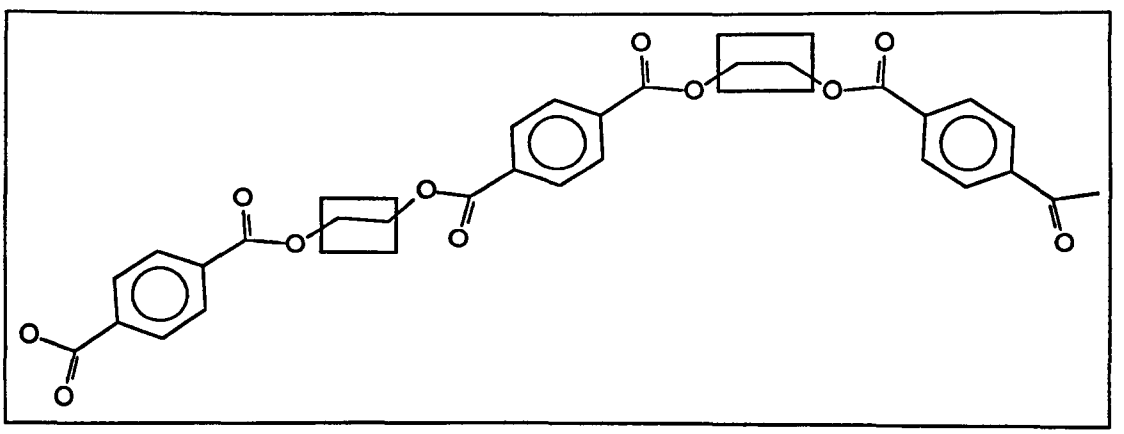

Figure 1.2. PET in a mixed trans and gauche 'amorphous' conformation.

Figures 1.1. and 1.2. clearly show that in the crystalline form PET should be more dense as the almost planar structure allows much closer packing than the random 'kinking' amorphous structure.

Sometimes it is desirable to retain a more amorphous structure even after treatment. This may be due to amorphous PET having a lower glass transition temperature **[1.11]**

or different optical properties. This can be achieved by the introduction of isophthalic acid as a comonomer. This introduces a 'kink' into the polymer chains reducing the tendency for chains to pack closely. This is clearly shown in figure 1.3. where even in an all *trans* conformation the introduction of an isophthalate group stops chain packing by introducing a 'kink' to the chain. The isophthalate group is highlighted.

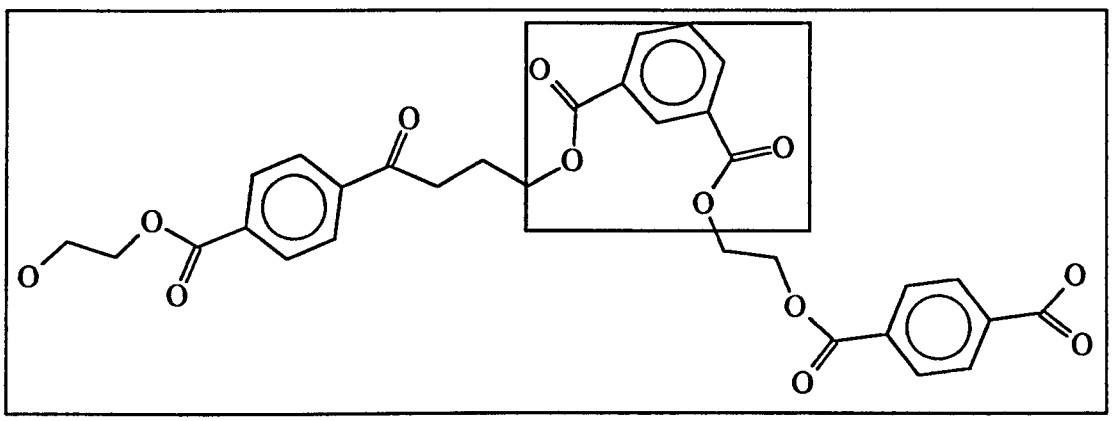

Figure 1.3. The structure of PET containing an isophthalate comonomer.

As PET is a widely used polymer and vibrational spectroscopy is a popular tool for the characterisation of polymers, it follows that there is a great deal of published literature on the vibrational spectroscopic studies of PET. The papers published include theoretical band assignments, band changes during stress, band changes on annealing and end group characterisation. It is intended to present a brief summary of the relevant findings of other workers in this vast field.

1.4. The infrared spectrum of PET.

In 1974, Bahl et al published the results of a complete vibrational analysis of a planar model of PET [**1.12**]. The work used a single set of force constants obtained from a valence force field calculation, on chemically related aromatic esters, to calculate the vibrational frequencies. The fact that a planar model was used limited the output to crystalline bands, as the amorphous structure is non-planar.

The characterisation of PET using infrared spectroscopy has predominantly been undertaken using a transmission technique to look at weak bands [**1.2-1.6, 1.8-1.10, 1.13-1.22**]. The infrared transmission spectrum of PET contains numerous strongly absorbing bands which present saturation problems in films of thickness > 2 μm. The solution to this problem is to use a different technique such as ATR [**1.23-1.26**], front surface reflection / specular reflection infrared spectroscopy [**1.7, 1.27, 1.28**] or photo acoustic spectroscopy (PAS) [**1.29, 1.30**] all of which limit the sampling depth (but to different degrees). It is also possible to use very thin films supported on a reflective substrate and use a RAIRS technique [**1.11, 1.31**].

Perhaps the most important feature of the structure of PET is the existence of both *trans* and *gauche* rotational conformers (rotamers) of the ethylene glycol section of the polymer chain. This is evident in the differences between the vibrational spectra of PET samples that contain more of one type of rotamer. As stated earlier both rotamers are present in the amorphous state, but the crystalline state contains only the *trans* conformer. Vibrational spectroscopy is very sensitive to conformational changes and is therefore an ideal tool for the characterisation of PET.

The transition from amorphous to crystalline PET involves several stages **[1.11, 1.14]**. Firstly there is a conversion from *gauche* to *trans* conformation. This is followed by an ordering of the polymer chain and subsequent three-dimensional lattice formation with chain folding. Conformational changes involving the benzene ring **[1.22-1.24]** and carbonyl groups **[1.7]** have also been noted. The effects that these conformational changes have on the vibrational spectrum are that bands associated with *trans* conformers increase with ordering. Conversely bands associated with *gauche* conformers decrease.

Workers have therefore used known procedures to induce order into isotropic PET films and followed the conformationally sensitive bands using vibrational spectroscopy. From these results coupled with force field calculations and characterisation on model compounds such as dimethyl terephthalate and ethylene glycol dibenzoate **[1.32]** a more complete assignment of the bands in the vibrational spectrum of PET is possible.

1.5. The effects of annealing on the vibrational spectrum of PET.

The effect of heating an isotropic PET film above its glass transition temperature (73 - 80° C) is to change some of the *gauche* conformers into *trans* conformers. What proportion of the conformers change is more dependent on the temperature used than the length of time that they are heated **[1.11]**. Higher temperatures lead to a greater *trans* content.

The group lead by Koenig [**1.6, 1.9, 1.10, 1.13**], Štokr et al [**1.8**] and Cole and co workers [**1.7**] have used spectral subtraction techniques to obtain 'pure' *trans* and 'pure' *gauche* spectra. It is somewhat surprising that little work has been focused on the C-H stretching region (3100 - 2800 cm^{-1}) as this region is conformationally sensitive. Most authors prefer to concentrate on the 1800 - 600 cm^{-1} region.

It is seen that after annealing there is a shift of the 1453 cm^{-1} CH_2 bending mode to 1470 cm^{-1}, the 1370 cm^{-1} CH_2 wagging mode to 1337 cm^{-1}, the 1043 cm^{-1} C-O stretching mode to 973 cm^{-1} and the 899 cm^{-1} CH_2 rocking mode to 845 cm^{-1}. All these changes are explained by a conversion of the ethylene glycol moiety from *gauche* to *trans* conformation. The shifts will, in a semi crystalline polymer, essentially result in the increase in one of the bands and a decrease in the other. The *trans* band at 1337 cm^{-1} is also present in amorphous PET but at slightly higher frequency. This difference in frequency has been attributed to slight perturbations caused by interactions in the crystal lattice [**1.6**].

The changes that occur in the bands associated with the benzene ring modes are not so obvious. The C-C stretching peak at 1580 cm^{-1} and the in plane C-H bending mode at 1174 cm^{-1} lose intensity upon annealing. It is suggested that in the crystalline phase the carbonyl groups lie in the same plane as the benzene ring and these modes become non IR active due to the resulting centrosymmetric structure [**1.22-1.24**]. As crystallinity increases a band at 1385 cm^{-1}, which has been attributed to an in-plane bending mode of the benzene ring ,appears. Slight shifts to higher frequency of the other in plane C-H peaks at 1505, 1410 and 1018 cm^{-1} have been reported [**1.7**] and the out-of-plane mode at 873 cm^{-1} undergoes a slight blue shift.

Because of saturation problems little work has been carried out on the strongly absorbing carbonyl band at 1725 cm^{-1}. This also applies to the complex conformationally sensitive bands centred around 1280 cm^{-1} and 1100 cm^{-1}. Both these bands are multicomponent bands and are mainly due to the C-O ester stretching mode. But using front surface reflection infrared spectroscopy the saturation problems are overcome. Cole and co-workers used this technique to characterise annealed PET samples [**1.7**]. They compared their results with those obtained in transmission but also attempted to characterise the strongly absorbing bands mentioned earlier. The publication by Cole et al stated that amorphous PET had a carbonyl maximum at 1725 cm^{-1} and a full width at half height (FWHH) of 23 cm^{-1}, whilst the more crystalline annealed films had a maximum at 1718 cm^{-1} and a FWHH of 18 cm^{-1}. Štokr et al also gave the same frequencies for their assignments of the bands in PET [**1.8**]. These findings are similar to those of Melveger who looked at the carbonyl bandwidth of PET as a function of crystallinity using Raman spectroscopy [**1.33**]. It was shown that crystallinity could be directly correlated to carbonyl bandwidth. It is also important to note that in the Raman spectrum there is no reported bandshift, but the band does go from being asymmetric to symmetric upon inceasing in crystallinity.

Spectral subtraction suggest that the infrared carbonyl band has two components at 1734 cm^{-1} and 1720 cm^{-1} in amorphous PET and 1722 cm^{-1} and 1714 cm^{-1} in the crystalline state [**1.7**]. These findings agree with the Fourier deconvolution work carried out in this work.

The complex band at 1280 cm^{-1} has three components in the amorphous phase, 1287, 1265 and 1248 cm^{-1} but loses the band at 1287 cm^{-1} on annealing. One explanation is that the band becomes IR inactive upon annealing due to symmetry effects **[1.8]**. Štokr et al **[1.8]** have adapted the findings of Bahl et al **[1.12, 1.32]** in an attempt to identify these bands.

The complex band at 1100 cm^{-1} also undergoes drastic changes upon annealing. Cole et al **[1.7]** suggest three bands in the amorphous state at 1138, 1119 and 1100 cm^{-1} but make no attempt to characterise the crystalline phase due to its increased complexity. Štokr et al **[1.8]** again suggest three bands in the amorphous state at 1139, 1122 and 1101 cm^{-1} and three bands also in the crystalline state at 1126, 1112 and 1102 cm^{-1}. Again they have used the calculations of Bahl et al **[[1.12, 1.32]** to make assignments. Table 1.1. shows an assignment of the infrared bands of PET.

Band position / cm^{-1}	Morphology	Assignment	Reference
3081	A/C	ν_{ring} (CH)	1.12
3067	A/C	ν_{ring} (CH)	1.12
2962	A/C	ν_a (CH_2)	1.12
2912	A/C	ν_s (CH_2)	1.12
1734	A	ν (C=O)	1.7
1722	C	ν (C=O)	1.7
1720	A	ν (C=O)	1.7
1714	C	ν (C=O)	1.7
1685	A/C	$\nu_{end\ group}$ (C=O)	1.35
1615	C	ring ν (C-C)	1.5, 1.12
1580	A	ring ν (C-C)	1.39
1507	A/C	in plane δ (C-H)	1.12
1470	C	δ (CH_2)	1.5
1453	A	δ (CH_2)	1.5
1410	A/C	in plane δ (C-H)	1.5, 1.12
1385	C	in plane δ (C-H)	1.37
1370	A	w (CH_2)	1.5
1339	C	w (CH_2)	1.5, 1.12
1287	A	-	1.7
1265	A/C	-	1.7
1248	C	-	1.7
1178	A	in plane δ (C-H)	1.39
1138	A	-	1.7
1126	C	-	1.7
1110	C	-	1.7
1102	A/C	ν_A (C-O)	1.5
1043	A	ν_B (C-O)	1.5
1023	C	in plane δ (C-H)	1.6, 1.12
1020	A	in plane δ (C-H)	1.6, 1.22
1019	A	in plane δ (C-H)	1.6, 1.22
972	C	ν (O-CH_2)	1.5, 1.12
896	A	γ_r (CH_2)	1.5
875	A/C	out-of-plane δ (C-H)	1.13
850	C	γ_r (CH_2)	1.5, 1.12
793	A/C	out-of-plane δ (C=O)	1.12
734	A	out-of-plane δ (C-H) & out-of-plane δ (C=O)	1.39
724	C	out-of-plane δ (C-H) & out-of-plane δ (C=O)	1.12

Table 1.1. The infrared band assignments of PET.

Belali and Vigoureux [1.38] have suggested a model for the calculation of the percentage crystallinity in PET using the 'amorphous' and 'crystallinity' bands associated with the *trans* and *gauche* conformers of the CH_2 wagging modes. The model is based on the assumption that at each point in a spectrum the absorbance can be treated as the crystalline and amorphous parts superimposed. It is concluded that the percentage crystallinity is given by the equation

$$\chi_c = \frac{a_i - a_j(A_i / A_j)}{(c_j - a_j)A_i / A_j - (c_i - a_i)} \qquad \text{(eq. 1.1)}$$

Where a and c refer to the molar absorption coefficients of the amorphous and crystalline parts at ν_i and ν_j.
A is the absorption at ν_i and ν_j.

For spectra obtained using ATR a correction factor must be included in the equation to account for the increase in sample penetration at lower wavenumbers. Equation 1.1 now becomes

$$\chi_c = \frac{a_i - a_j(A_i / A_j)(\upsilon_i / \upsilon_j)}{(c_j - a_j)(A_i / A_j)(\upsilon_i / \upsilon_j) - (c_i - a_i)} \qquad \text{(eq. 1.2)}$$

The main problem with the equations shown is that the coefficients a and c have to be calculated by calibration with samples of known crystallinity. The results obtained in this work were calculated using the a and c values of Zajcek [1.39].

Other groups, notably the group led by Ward [1.15-1.19], have examined in great detail the conformational and mechanical changes that occur in PET films upon drawing. Drawing is shown to introduce conformational order into disordered PET films by converting the *gauche* ethylene glycol conformers into *trans* conformers. This is not

necessarily a crystallisation effect. Drawing at temperatures between 80 and 95° C, the 'order' introduced will be a crystalline oriented matrix, with orientation in the drawing direction. At higher temperatures, relaxation of the amorphous phase results in oriented amorphous material. Different draw ratios have also been shown to induce different levels of *gauche* to *trans* conversion **[1.17-1.19, 1.26]**. The higher the draw ratio (i.e. the greater the stress applied to the film) the higher the level of *gauche* to *trans* conversion.

Walls et al **[1.23, 1.24]** have shown that the amount of *gauche* to *trans* conversion is different at the surface compared to the bulk. It was shown using ATR that the *trans* content of the surface was greater than the bulk after uniaxially drawing the films at 60°C. Two different ATR materials were used, KRS5 and Ge, which gave penetration depths of 1 μm and 0.5 μm respectively. Marked difference in the *trans* content at the surface was noted between the two penetration depths, indicating a surface effect. Differences in amount of crystallinity induced at the surface compared to the bulk has also been noted during annealing by Beamson et al **[1.31]**. These two studies although on different systems, under different experimental conditions, do seem to imply that the surface of PET has different characteristics to the bulk material. This is an important point for the work carried out using RAIRS to try and mimic the near surface of a PET film.

1.6. The Infrared spectrum of PET.

Figures 1.4. - 1.14. show example spectra of PET obtained using a variety of different sampling techniques and of varying morphologies. A brief discussion of the key differences will follow. Table 1.2 gives a summary of the samples presented and how they were obtained.

Sample name	Polymer type	Thickness	Treatment	Sampling method
CSR137	E47	0.3 μm	Dipped from TCE	RAIRS
CSR331	E47	0.1 μm	Spin cast from OCP	RAIRS
CST78	E47	<2 μm	Dipped from TCE	Transmission
CST132	E99	8.2 μm	Cast from TCE	Transmission
CST134	E99	8.4 μm	Cast from TCE	Transmission
CST136	E99	8.2 μm	Sample CST134, annealed at 85-90°C for 3 hours	Transmission
CST155	E47	9.6 μm	Cast from OCP	Transmission

Table 1.2. Characteristics of the films used for the demonstration of spectral features.

The C-H stretching region of PET obtained using a RAIRS technique (figure 1.4) shows a series of very weak bands which can be attributed to the antisymmetric and symmetric C-H stretching. Although some of the bands are conformationally sensitive it is difficult to draw any firm conclusions about the differences due to the weak nature of the bands. The aromatic C-H stretching of PET (~ 3070 cm^{-1}) are very weak in the infrared spectrum and with these thin films it is unsurprising that they are barely noticeable.

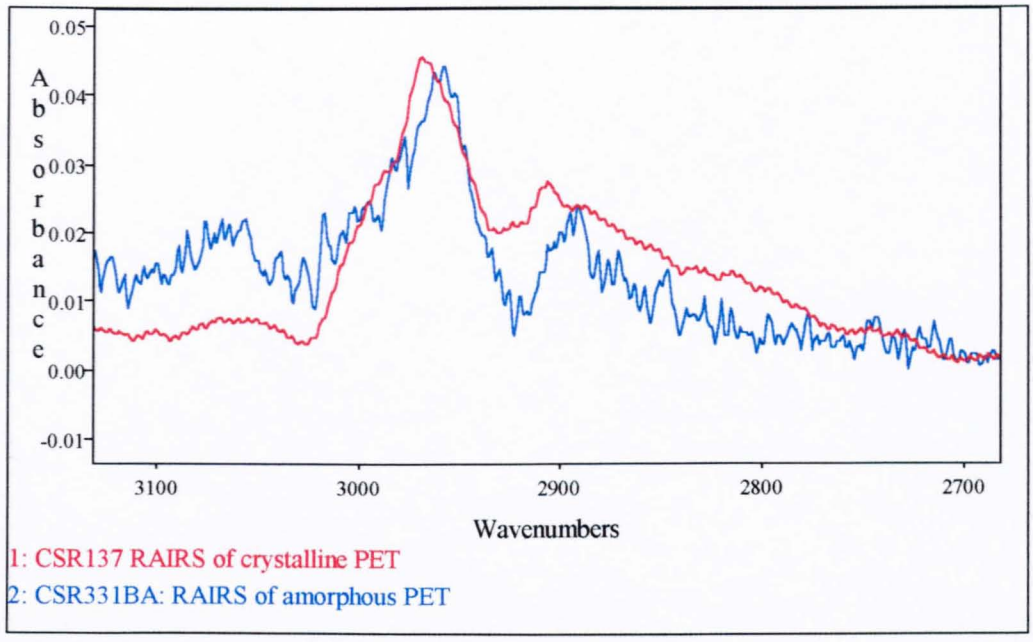

Figure 1.4. The C-H stretching region of E47 PET obtained using RAIRS.

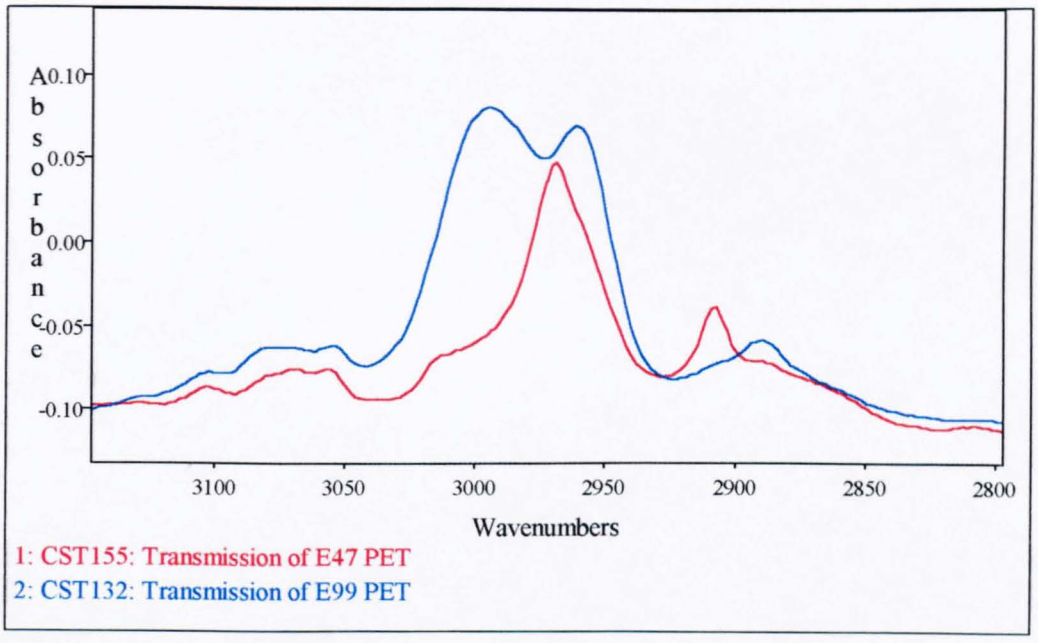

Figure 1.5. The C-H stretching region of E47 and E99 PET obtained in transmission.

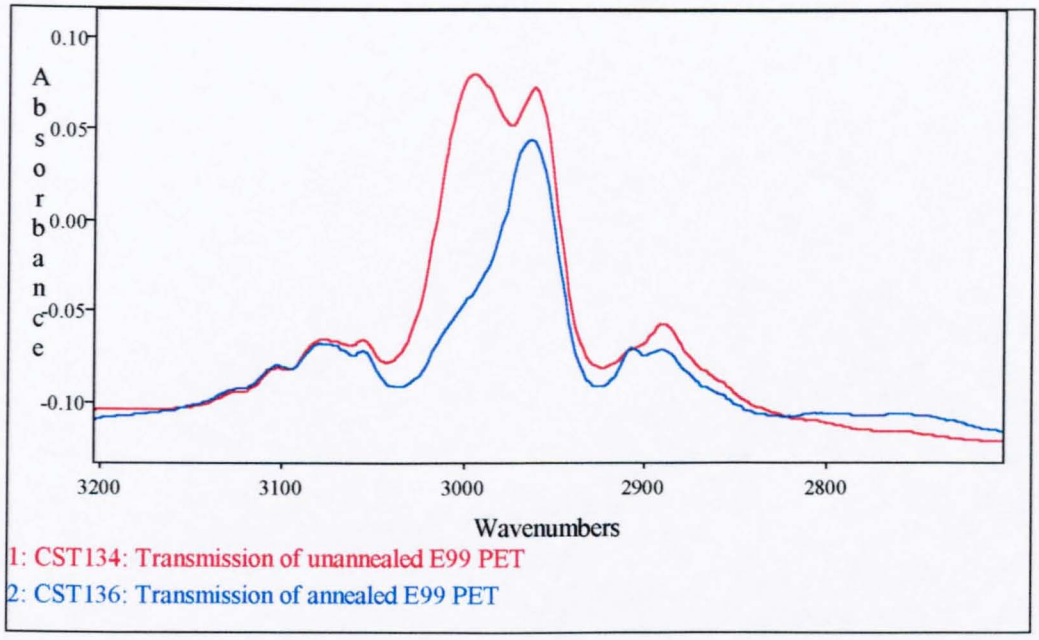

Figure 1.6. The C-H stretching region of E99 PET obtained in transmission.

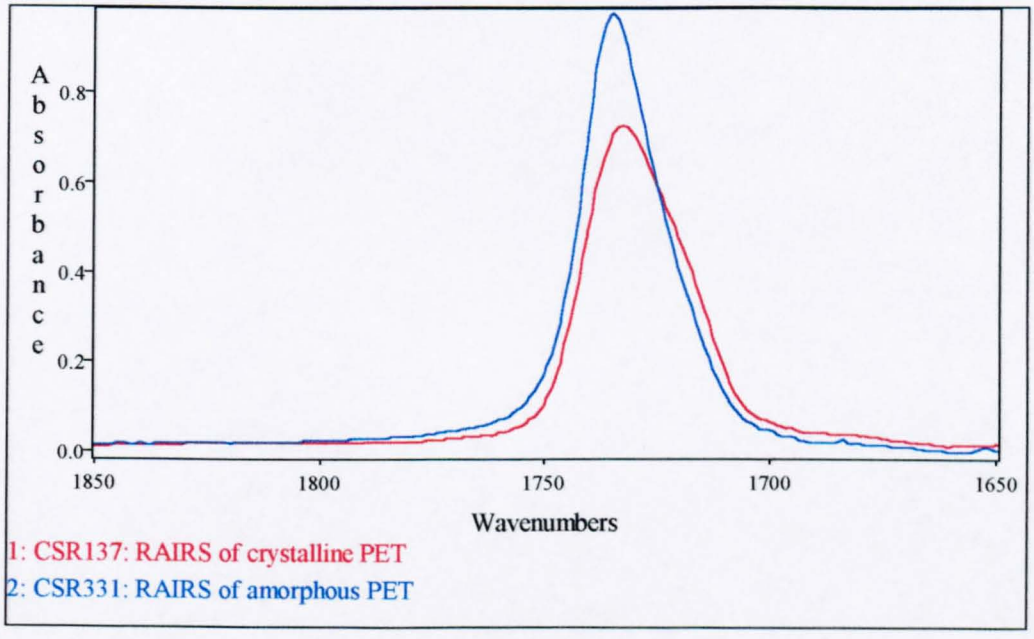

Figure 1.7. The carbonyl band of PET obtained using RAIRS.

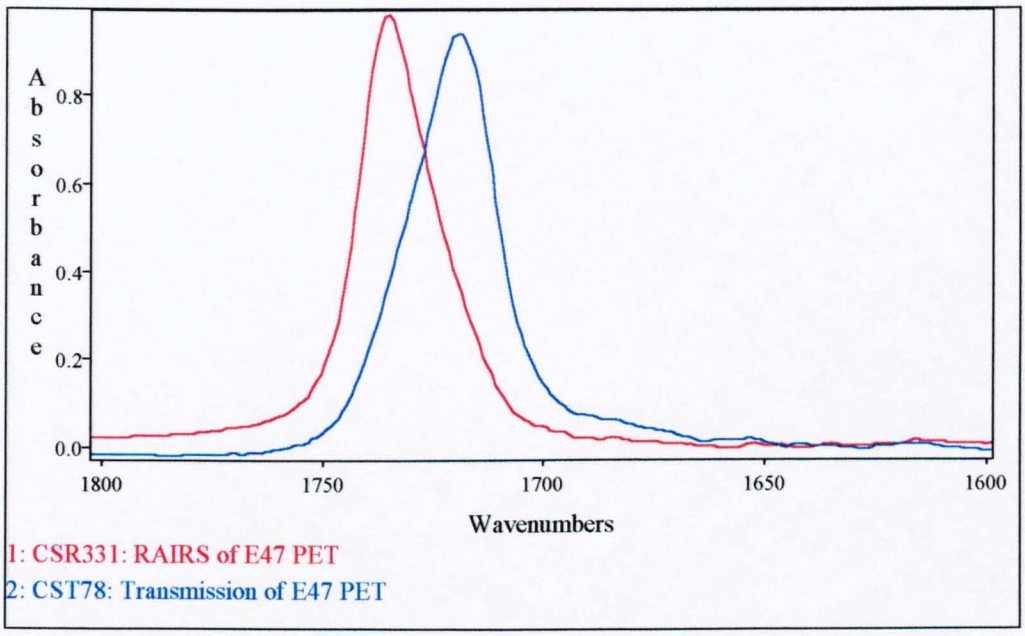

Figure 1.8. Comparison of the carbonyl band of PET obtained using RAIRS and transmission.

Figure 1.7. shows the ν(C=O) of PET obtained using RAIRS. The shift to lower frequency in the sample with higher crystallinity is clearly shown. There is also a noticeable intensity drop in the more crystalline sample (the spectra had been normalised using the 1410 cm^{-1} band the intensity of which is independent of morphology) [**1.23, 1.24**].

Figure 1.8. shows the difference in the carbonyl region between samples of a similar thickness obtained in RAIRS and transmission. There is a shift of around 20 cm^{-1} of the peak centre in the RAIRS spectrum. This shift cannot be accounted for by a difference in crystallinity, but is most likely to be a dichroic effect, as in the RAIRS experiment we are only observing the electric dipole moments with a component normal to the substrate. As the annealed E99 samples were quite thick (> 4 μm) the absorbances are

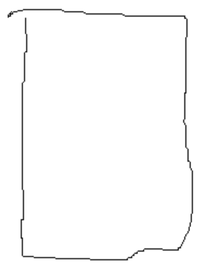

PAGES ARE MISSING IN ORIGINAL

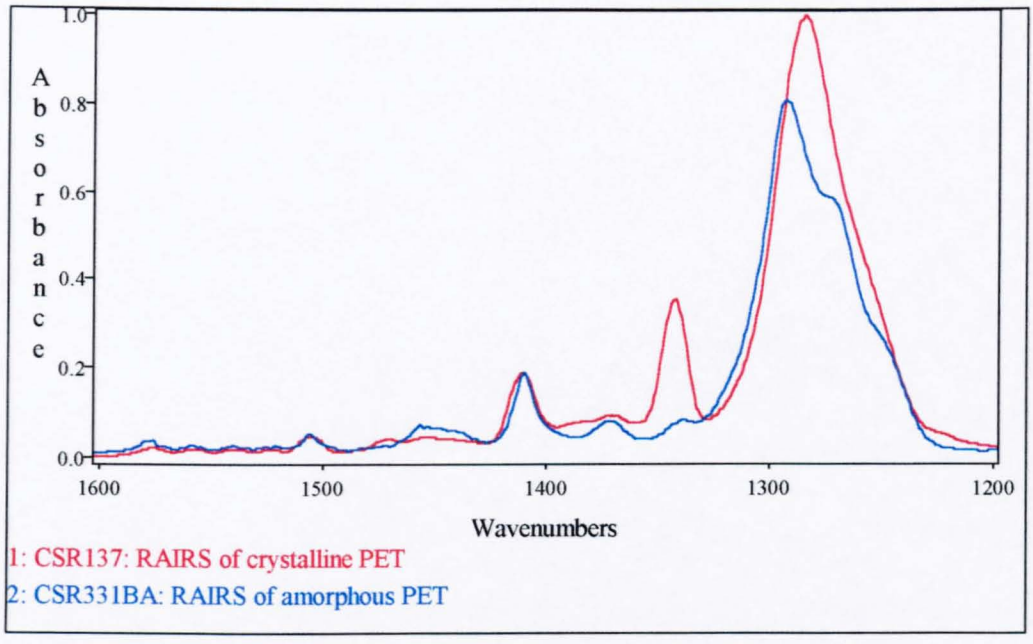

Figure 1.9. The 1600 to 1200 cm^{-1} region of PET obtained using RAIRS.

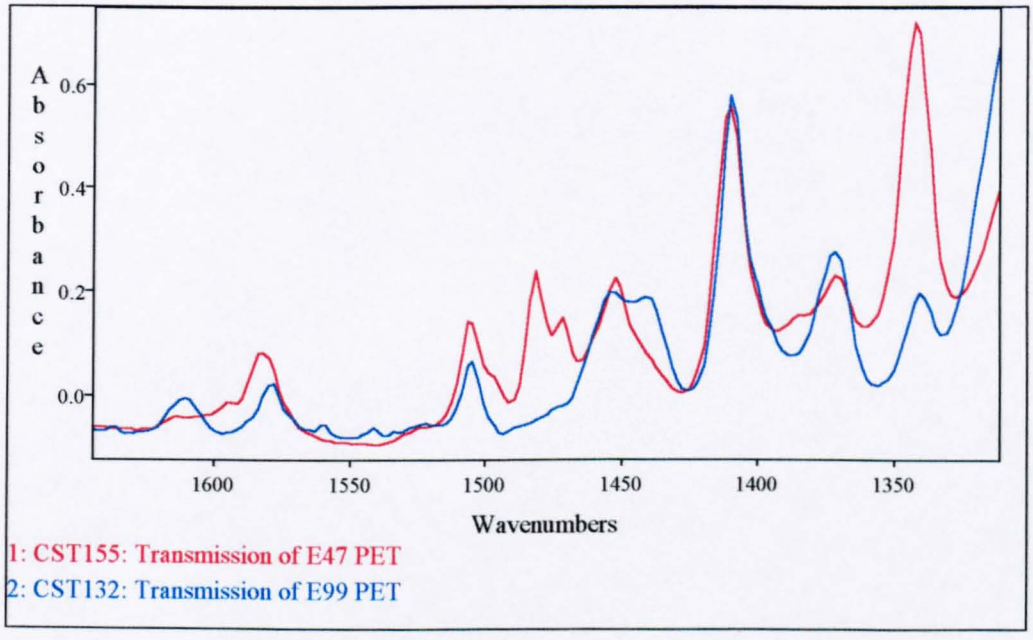

Figure 1.10. The 1650 to 1200 cm^{-1} region of E47 and E99 PET obtained using transmission.

Because of the thicknesses involved it is not possible to show the effects of morphology on the more strongly absorbing bands in transmission. Figure 1.10. shows the ring modes and CH_2 wagging modes of E99 and E47 PET. It is clearly shown that the

inclusion of the isophthalate group reduced the numbers of *trans* conformers in the film. Figure 1.11. shows the effect of annealing on an E99 PET film. The CH_2 wagging modes are indicative of an increase in *trans* conformer.

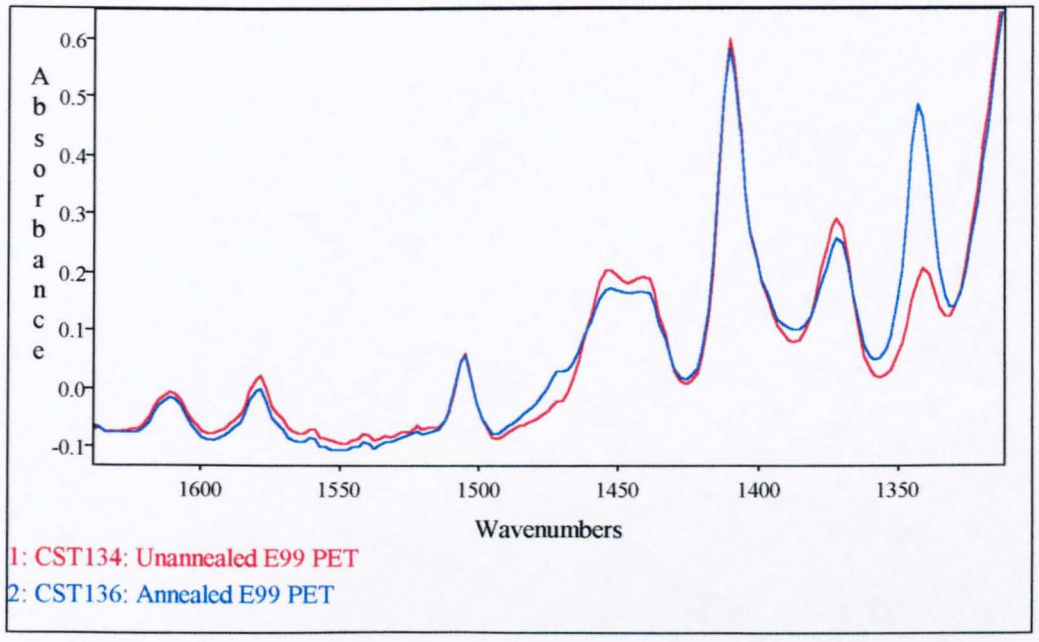

Figure 1.11. The 1650 to 1200 cm^{-1} region of annealed and unannealed E99 PET obtained using transmission.

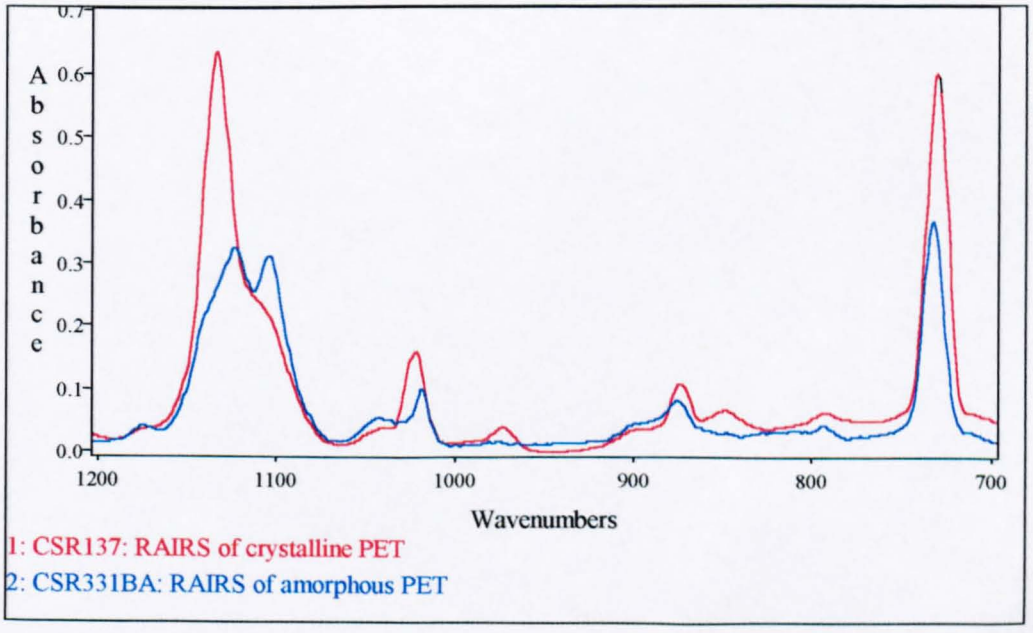

Figure 1.12. The 'fingerprint' region of PET obtained using RAIRS.

Figure 1.12. shows clearly the effects of conformation on the ester band at 1100 cm^{-1}. This is another band that has not fully been interpreted. Cole et al [**1.7**] suggest that this band may also have up to 5 components, whilst Štokr et al suggest 4 components [**1.8**]. The component at 1130 cm^{-1} is clearly a 'crystalline' band, whilst the band at 1100 cm^{-1} is clearly an 'amorphous' band. These bands have both been assigned by Beorio and Bahl [**1.6**] as containing C-O stretching and ring bending mode components. Figure 1.13. shows similar changes due to conformation, again the strongly absorbing (1100 cm^{-1}) band is left out due to saturation problems. In this instance the spectral changes can be accounted for by the isophthalate group reducing the number of *trans* conformers. Figure 1.14 shows that upon annealing the number of *trans* conformers has increased.

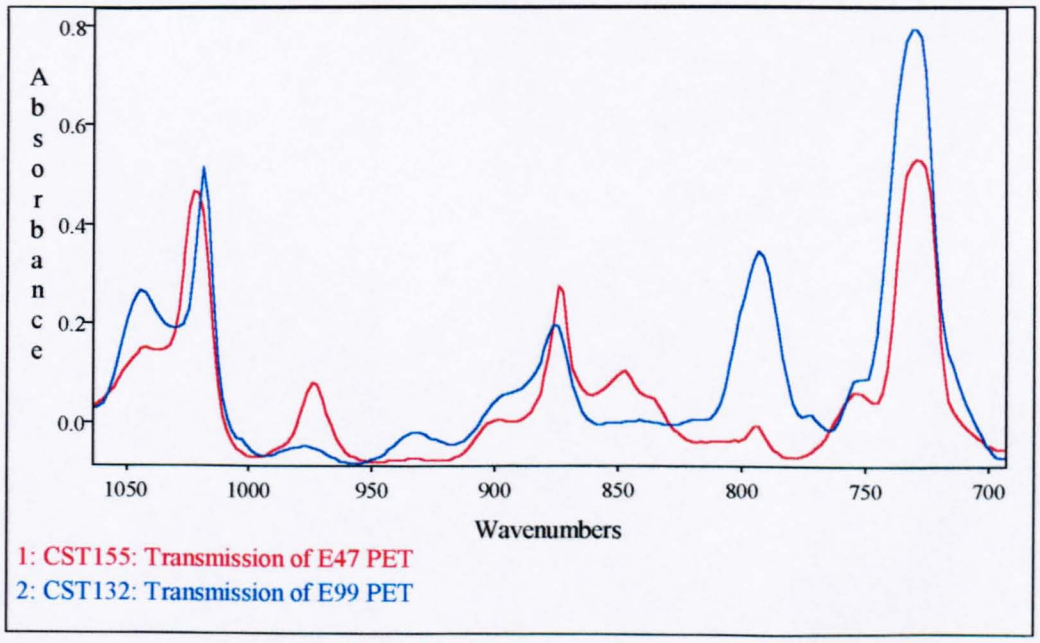

Figure 1.13. The 'fingerprint' region of E99 and E47 PET obtained using transmission.

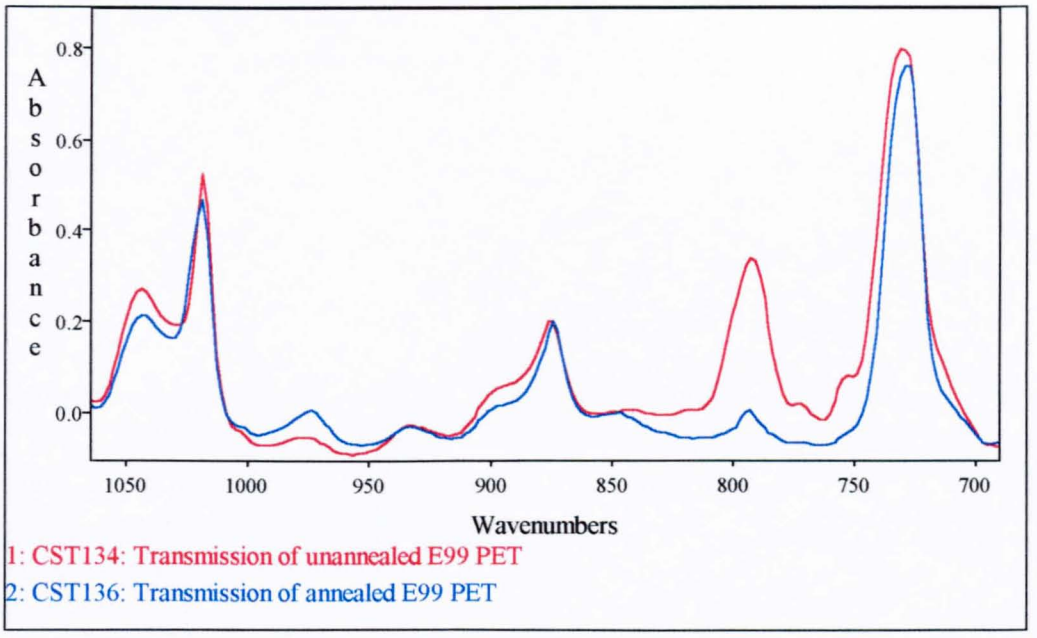

Figure 1.14. The 'fingerprint' region of E99 and E47 PET obtained using transmission.

1.7. The microstructure of PET films.

The co-existence of both diffuse and sharp features in x-ray data show that many polymers are partially crystalline. Polymer single crystals can be formed in solution **[1.40]**. Polymer single crystals are in general thin flat platelets known as lamellae. The size and shape of the lamellae depends on factors that govern growth conditions such as solvent, temperature and growth rate **[1.41]**. The thickness of the lamellae will depend on the crystallisation temperature and any subsequent annealing conditions. In general lamellar thickness increases with annealing time and temperature. The growth of crystals from solution can lead to more complex crystal structures such as spherulites. These structures are generally similar to those found in polymers crystallised from the melt. Historically a model based on smaller crystalline regions in an amorphous matrix known as the fringed micelle model was often used to explain the structure of semi-crystalline polymers. As the polymer chain lengths are much greater than the crystalline domain sizes, it was envisaged that polymer chains contributed to both the crystalline and amorphous regions. This model over simplified the detail of the microstructure and did not account for spherulitic formation.

Spherulites are made up of chain folded lamellae. It is also important to recognise the existence of defects within the polymer structure. Defects include, point defects, dislocations, 2-D imperfections, chain disorder defects and amorphous effects. Point defects can be the chain ends or other foreign material (e.g. a comonomer) and both 2-D imperfections and chain disorder defects may account for chain folding structures. The net result of these observations is a better correlation between the theoretical predictions and observed experimental data of polymer structure on a microscopic scale.

Perhaps the most prominent organisation an a macro-scale in polymers is the spherulite. It is not fully understood whether the formation of spherulites is a result of the reorganisation of existing crystallites or the product of primary crystallisation. The nucleus of the spherulite may be a foreign body (heterogeneous nucleation) or simply formation within the melt (homogenous nucleation). There is evidence from the electron microscopic examination of fracture surfaces that spherulites have a lamellar structure.

Amorphous PET is comprised of both *gauche* and *trans* conformers of the ethylene glycol moiety. Annealing amorphous PET above the T_g has been shown to increase the number of *trans* ethylene glycol conformers. This crystallisation process has been shown to occur in two stages. The initial increase in *trans* conformer, at the expense of *gauche* conformers, results in new crystalline domains of small size and low degrees of perfection. At lower temperatures (<160° C) this initial crystallisation process dominates. Prolonged annealing results in further isomerisation by a similar mechanism and the small crystallites develop into larger crystalline blocks. Because of limited segmental mobility at lower temperatures, the crystallites are generally small paracrystalline forms with irregular folds. At temperatures above 160° C a secondary crystallisation process occurs which results in thicker lamellae and larger crystallites. PET crystallised from dilute solution has been shown to be composed of aggregates of lamella-like structures radiating from a central nucleus (fibrils) **[1.10]**. Solution crystallised films generally are characterised by their high degree of perfection and absence of interlamellar material.

1.8. References

1.1. 'Modern Plastics Encyclopedia - 94', (Ed. A.K. Mitchell), McGraw-Hill, U.K., (1993)

1.2. R.P. Daubney, C.W. Bunn and C.J. Brown, *Proc. R. Soc.* (London), **A226**, 531, (1954)

1.3. I.M. Ward, *Chem. and Ind.*, (London) 1102, (1957)

1.4. W.W. Daniels and R.E. Kitson, *J. Polym. Sci.*, **33**, 161, (1958)

1.5. A. Miyake, *J. Polym. Sci.*, **38**, 479, (1958)

1.6. L. D'Esposito and J.L. Koenig, *J. Polym. Sci. Polym. Phys. Ed.*, **14**, 1731, (1976)

1.7. K.C. Cole, J. Guèvremont, A. Ajji and M.M. Dumoulin, *Appl. Spec.*, **48**, 12, 1513, (1994)

1.8. J. Štokr, B. Schneider, D. Doskoilová, J. Lövy and P. Sedlácek, *Polymer*, **23**, 714, (1982)

1.9. S-B. Lin and J.L. Koenig, *J. Polym. Sci. Polym. Phys. Ed.*, **20**, 2277, (1982)

1.10. L.J. Fina and J.L. Koenig, *Macromolecules*, **17**, 2572, (1984)

1.11. P.D. Richards, E. Weitz, A.J. Ouderkirk and D.S. Dunn, *Macromolecules*, **26**, 1254, (1993)

1.12. S.K. Bahl, D.D. Cornell, F.J. Boerio and G.E. McGraw, *J. Polym. Sci. Polym. Lett.*, **12**, 13, (1974)

1.13. S-B. Lin and J.L. Koenig, *J. Polym. Sci. Polym. Phys. Ed.*, **21**, 2067, (1983)

1.14. S-B. Lin and J.L. Koenig, *J. Polym. Sci. Polym. Phys. Ed.*, **21**, 2365, (1983)

1.15. P. Spiby, M.A. O'Neill, R.A. Duckett and I.M. Ward, *Polymer*, **33**, 21, 4479, (1992)

1.16. J.B. Faisant de Champchesnel, D.I. Bower, I.M. Ward, J.F. Tassin and G. Lorentz, *Polymer*, **34**, 18, 3763, (1993)

1.17. P. Lapersonne, D.I. Bower and I.M. Ward, *Polymer*, **33**, 6, 1266, (1992)

1.18. I.J. Hitchinson, I.M. Ward, H.A. Willis and V. Zichy, *Polymer*, **21**, 55, (1980)

1.19. P. Lapersonne, D.I. Bower and I.M. Ward, *Polymer*, **33**, 6, 1277, (1992)

1.20. R.M. Gohil, *J. Appl. Polym. Sci*, **52**, 925, (1994)

1.21. A. Garton, D.J. Carlsson, L.L. Holmes and D.M. Wiles, *J. Appl. Polym. Sci*, **25**, 1505, (1980)

1.22. X. Yang, F. Long, D. Shen and R. Quian, *Polym. Comm.*, **32**, 4, 125, (1991)

1.23. D.J. Walls, *Appl. Spec.*, **45**, 7, 1193, (1991)

1.24. D.J. Walls and J.C. Coburn, *J. Polym. Sci. Part B: Polym. Phys.*, **30**, 887, (1992)

1.25. J.P. Hobbs, C.S.P. Sung, K.Krishnan and S. Hill, *Macromolecules*, **16**, 193, (1983)

1.26. K.H. Lee and C.S.P. Sung, *Macromolecules*, **26**, 3289, (1993)

1.27. J.A.J. Jansen, J.H. Van der Maas and A. Posthuma de Boer, *Macromolecules*, **24**, 4278, (1991)

1.28. N.J. Everall, J.M. Chalmers, A. Local and S. Allen, *Vib. Spec.*, **10**, 253, (1996)

1.29. K.Krishnan, S. Hill, J.P. Hobbs and C.S.P. Sung, Appl. Spec., **36**, 3, 257, (1982)

1.30. L. Quintanilla, J.C. Rodriguez-cabello, T. Jawhari and J.M. Pastor, *Polymer*, **34**, 18, 3787, (1993)

1.31. N.W. Hayes, G. Beamson, D.T. Clark, D.S-L. Law and R. Raval, *Surface and Interface Analysis*, **24**, 19, 723, (1996)

1.32. F.J. Boerio, S.K. Bahl and G.E. McGraw, *J. Polym. Sci. Polym. Phys. Ed.*, **14**, 1029, (1976)

1.33. A.J. Melveger, *J. Polym. Sci. Part A-2*, **10**, 317, (1972)

1.34. P. de Donato, J.M. Cases, B. Humbert, P. Lutgen and G. Feyder, *J. Polym. Sci.: Part B: Polym. Phys.*, **30**, 1305, (1992)

1.35. D. Grine and I.M. Ward, *Trans. Farad. Soc.*, **54**, 959, (1958)

1.36. S. Krimm, *Adv. Polym. Sci.*, **2**, 51, (1960)

1.37. A. Cunningham, I.M. Ward, H.A. Willis and V. Zichy, *Polymer*, **15**, 749, (1974)

1.38. R. Belali and J.M. Vigoureux, *Appl. Spec.*, **48**, 4, 465, (1994)

1.39. T. Zajicek, Thèse, 3ème Cycle, Besaçon, (1987).

1.40. W. Schlesinger and H.M. Leeper, *J. Polym. Sci.*, **11**, 203, (1953)

1.41. 'Textbook of Polymer Science' 3rd edition, (Ed. F.W. Billmeyer Jr.), John Wiley & Sons, U.K., (1984)

Chapter 2

Infrared Spectroscopy

2.1. Frequencies and time scales of infrared radiation.

Infrared (IR) radiation is electromagnetic radiation that encompasses all the wavelengths between the visible and microwave regions of the electromagnetic spectrum. The IR region can also be subdivided into three smaller regions known as near-IR, mid-IR and far-IR, the ranges of which are neatly summed up in table 2.1.

Region	Wavenumber Range	Vibrational / Rotational Information
near IR	14000 - 4000	Changes in vibrational and rotational levels, overtone region and some low energy electron transitions
mid-IR	4000 - 400	Changes in fundamental vibrational levels of most molecules
far-IR	400 - 20	Rotational energy level changes

Table 2.1 ***A summary of infrared ranges and the information gained.***

The observation time for an infrared transition is between 10^{-13} and 10^{-15} seconds which is important as this time governs the processes that can be studied using infrared spectroscopy. For example if one was to compare the H^1 NMR and FT-IR spectra of phenol and acetonitrile in tetrachloroethane, then one would gain different information from each technique. The H^1 NMR would indicate that there was only one (averaged) type of phenolic hydrogen present in the system. Conversely FT-IR would suggest that there were in fact two phenolic protons within the system, one as a 'free' phenol, the other hydrogen bonding to the nitrile forming a complex. This apparent discrepancy is easily explained when one considers the observation time for each technique compared

to the timescale of proton exchange which is occurring. With H^1 NMR the observation time is longer than the exchange rate between the two sites. Hence only an average of the two states of the proton is seen, whereas with FT-IR the opposite is true, the observation time being shorter than the proton exchange rate between the two sites. Hence both phenolic environments are observed. This rapid observation time has important implications for the kinetic work carried out during this work.

2.2. Molecular vibrations.

In order to discuss molecular vibrations it is first necessary to consider some simplistic models.

2.2.1. The energy of a diatomic molecule.

A stable molecule consisting of two atoms can be thought to exist in a state of equilibrium between attractive and repulsive forces. If one attempts to squeeze the atoms together then the repulsive forces keep the atoms apart. Likewise the attractive forces operate if one tries to pull the atoms apart. This system can be likened to a spring and in an idealised system follows Hooke's law.

$$f = -k(r - r_{eq}) \qquad \text{(eq. 2.1)}$$

Where f is the restoring force

k is the force constant

r is the internuclear distance

The system is known as the simple harmonic oscillator (SHO) and the potential energy curve of this model is parabolic. In a SHO the potential energy can be given by the following equation

$$E = -\frac{1}{2}k\left(r - r_{eq}\right)^2 \qquad \text{(eq. 2.2)}$$

Where k is the force constant of the bond

r_e is the internuclear distance at equilibrium or bond length

Vibrational energies are quantized and the allowed vibrational energies can be calculated from the Schrödinger equation. For the SHO these are

$$E_v = \left(v + \frac{1}{2}\right)h\omega_{osc} \qquad (v = 0, 1, 2, 3, ...) \qquad \text{(eq. 2.3)}$$

Where v is the vibrational quantum number

h is Plancks constant

ω_{osc} is the oscillating frequency

Further use of the Schrödinger equation leads to the simple selection rule for the SHO undergoing vibrational energy changes

$$\Delta v = \pm 1 \qquad \text{(eq. 2.4)}$$

2.2.2. The effects of anharmonicity.

Unfortunately real molecules do not harmonically oscillate so real bonds do not obey Hooke's law. At low amplitudes of vibration then the SHO gives a good approximation, but at longer extensions the bonds in a molecule break leading to dissociation of the atoms. This is shown in figure 2.1 using the Morse (empirical) approximation for the potential energy of a diatomic molecule

$$E = D\left[1-\exp\left\{a\left(r_{eq}-r\right)\right\}\right]^2 \qquad \text{(eq. 2.5)}$$

Where D is the depth of the potential minimum

a is a constant.

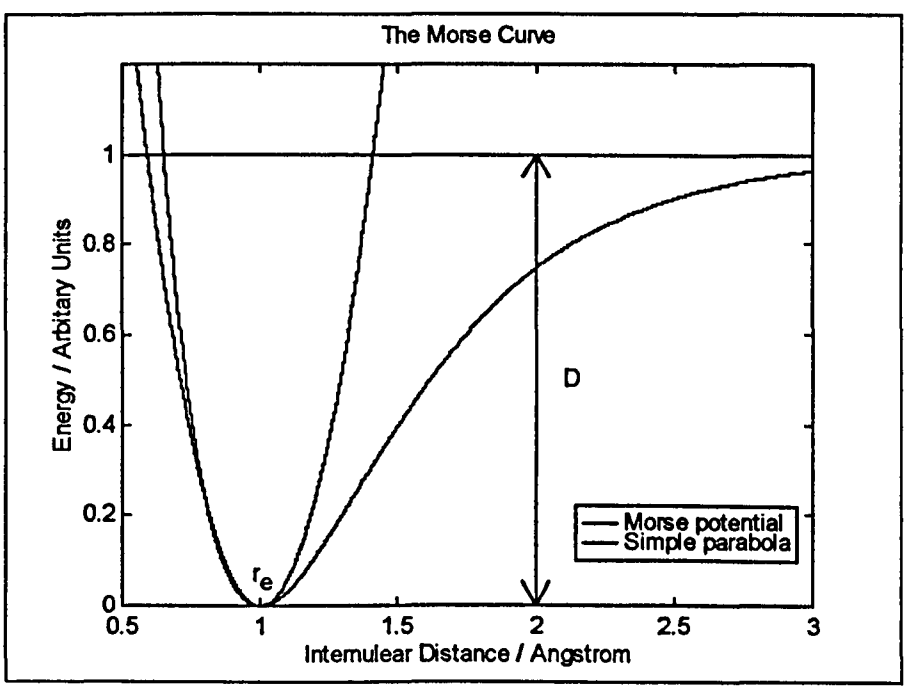

Figure 2.1. The energy of a diatomic molecule undergoing anharmonic extensions and compressions.

The Schrödinger equation can also be used to calculate energy levels from the Morse function and these are found to be

$$\varepsilon_v = \left(v+\frac{1}{2}\right)\varpi_e - \left(v+\frac{1}{2}\right)^2 \varpi_e x_e \qquad (v = 0, 1, 2, ...)(\text{eq. } 2.6)$$

Where x_e is the anharmonicity constant.

This can be rearranged to give a general expression for the energy levels which can be used to find the dissociation energy of the molecule from experimental data

$$\varepsilon_v = \varpi_e\left\{1 - x_e\left(v+\frac{1}{2}\right)\right\}\left(v+\frac{1}{2}\right) \qquad (\text{eq. } 2.7)$$

Diagram 2.2 shows typical vibrational energy levels for a diatomic molecule.

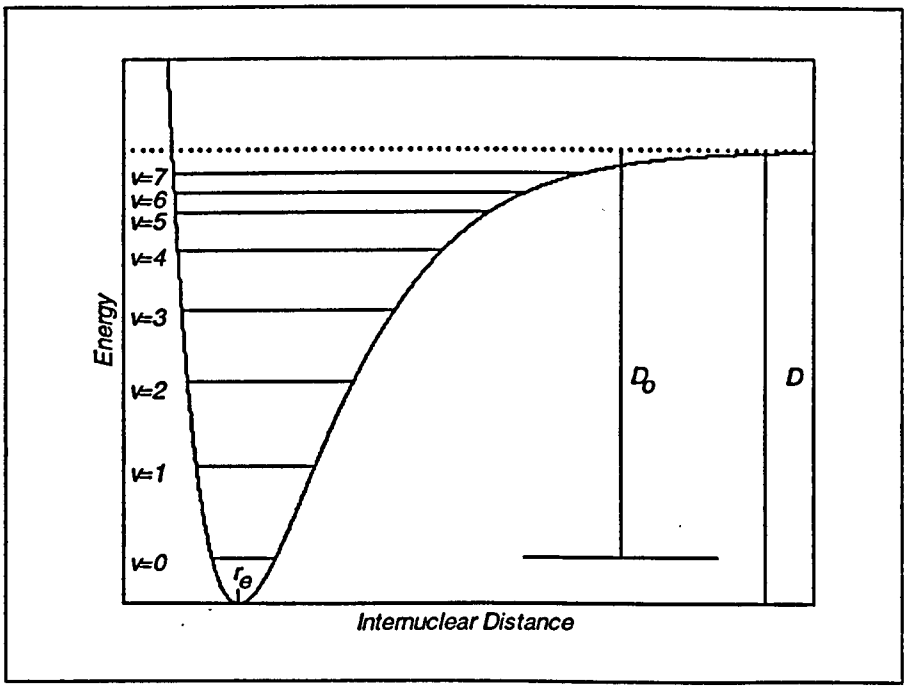

Figure 2.2. ***The allowed vibrational energy levels for a diatomic molecule undergoing anharmonic oscillations.***

The relevant transitions that are generally observed are;

$v = 1 \leftarrow 0$	Fundamental
$v = 2 \leftarrow 0$	1st overtone
$v = 3 \leftarrow 0$	2nd overtone

It is also important to note that the energy corresponding to $v = 0$ is not zero, but is termed the zero-point enery, which can be calculated from equation 2.7.

2.3. Normal modes and intensities.

The discussion so far has only been based on diatomic molecules. Most molecules are polyatomic, hence their motion is far more complex, but despite this only slight modifications to the theory are required to help understand their spectra. The number of normal modes of motion can be shown to be;

$3N-6$	For polyatomic molecules
$3N-5$	For linear molecules

2.3.1. Intensities of bands in infrared spectroscopy.

There are several factors that affect the intensity of the bands seen in an infrared spectrum; the selection rules (i.e. symmetry), vibrational level population and amount of sample in the beam.

2.3.1.1. Selection rules.

Selection rules indicate whether a transition is 'allowed' or 'forbidden' and are derived from the transition probability. For a vibrational transition

$$\rho^{v'v''} \propto \left[\int \varphi_{v'} \hbar \varphi_{v''} dQ \right]^2 \qquad \text{(eq. 2.8)}$$

Where $\hbar$ is the corresponding operator, in this case the molecular dipole moment (μ_k)

Q is the displacement 'normal co-ordinate', dependent on the internuclear distances for each bond displacement.

This can be expanded to give

$$\mu_k = \mu_0 + \left(\frac{\partial \mu}{\partial Q}\right) Q + \frac{1}{2}\left(\frac{\partial^2 \mu}{\partial Q^2}\right) Q^2 + \ldots \qquad \text{(eq. 2.9)}$$

Normal modes of vibration are only infrared active if they modulate the molecular dipole moment (μ_k). The intensity of the band seen is proportional to the square of the transition dipole moment ($\partial\mu / \partial Q$).

$$I \propto \left(\frac{\partial \mu}{\partial Q}\right)^2 \qquad \text{(eq. 2.9)}$$

Some infrared bands have zero intensity because they are forbidden by symmetry. Taking benzene for example, it should have 3N-6, (30) normal modes of motion. But, many of the vibrations are multiply degenerate. Hence there are only 4 fundamental bands in its infrared spectrum and 7 fundamental bands in its Raman spectrum.

2.3.1.2 Vibrational level population.

The intensity of a spectral line is dependent on the population of the initial vibrational state at thermal equilibrium. The Boltzmann distribution can be used to calculate the population, N_i, of a particular energy level, at a given temperature, T, where the difference in energy between levels is given by ΔE.

$$\frac{N_i}{N_0} = \frac{g_i}{g_0} \exp\left(-\frac{\Delta E}{kT}\right) \qquad \text{(eq. 2.10)}$$

Where g_i and g_0 are the degeneracies of the particular levels.

It is found that for most systems at room temperature, the ground state is the most heavily populated.

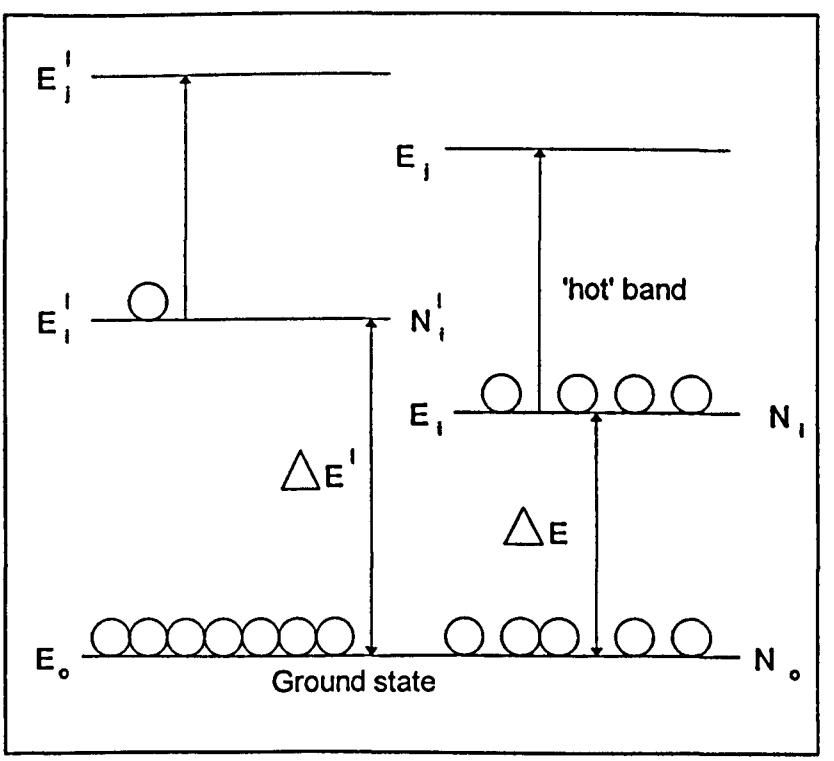

Figure 2.4. A schematic of the occurrence of 'hot' bands.

The numbers of molecules in each vibrational level are temperature dependent. In figure 2.4. it is clear that the population of state E_i is greater than that of E'_i ($N_i > N'_i$). Assuming equal probabilities for transitions, the intensity that is due to $E_f \leftarrow E_i$ will be greater than that due to $E'_f \leftarrow E'_i$. Transitions starting from excited vibrational states can be shown to be 'hot-bands' by increasing the temperature. An increase in band intensity should result. Since, at room temperature, most molecules will be in the ground state this explains the relatively weak intensities, in absorption, of transitions occurring from levels other than the ground state.

2.3.1.3 The number of molecules in the sample beam.

In all types of absorption spectroscopy the fundamental governor of intensity is the number of molecules sampled. A simple relationship between the intensity of the transmitted (I) and incident radiation (I_0) and the amount of sample in the beam (concentration or thickness) exists and is known as the Beer-Lambert law,

$$I = I_0 \exp(-\varepsilon c l) \qquad \text{(eq. 2.11)}$$

Or in the logarithmic form

$$\log\left(\frac{I_0}{I}\right) = \varepsilon c l \qquad \text{(eq. 2.12)}$$

Where in both cases c is the concentration, l is the cell thickness and ε is the frequency dependent extinction coefficient. The Beer-Lambert law is the foundation for all quantitative infrared spectroscopy.

2.4. Instrumentation.

Traditional (dispersive) infrared techniques experience difficulties due to the '1 wavenumber at a time' nature of data acquisition. This leads to either a poor signal to noise ratio in a spectrum or a very long time needed to obtain a high quality spectrum. Both these situations cause problems with kinetic work. The first gives inherent large errors, the second prohibits *in-situ* work. These problems can be overcome using Fourier transform infrared spectroscopy (FT-IR) which is based on the interferometer originally designed by Michelson and a mathematical procedure developed by Fourier which converts response from the time to the frequency domain.

2.4.1. Interferometry.

The Michelson interferometer is shown in figure 2.5 and the functions that each of the working parts, labelled A-F, serve is described. A parallel, polychromatic beam of radiation from a source (A) such as a mercury lamp or a silicon carbide (Globar) rod is directed to a beam splitter (B), made from an infrared transparent material, such as KBr. The beam splitter reflects approximately half of the light to a mirror, known as the fixed mirror (C), which in turn reflects the light back to the beam splitter. The rest of the light passes through to a mirror, moving continuously, at a known velocity, back and forth along the direction of the incoming light and this is known as the moving mirror (D). Upon reflection from the moving mirror, radiation is then directed back to the beam splitter. At the beam splitter some of the light that has been reflected from the fixed mirror combines with light reflected from the moving mirror and is directed towards the

sample. After passing through the sample (**E**) the radiation is focused onto the detector (**F**), which can be a liquid nitrogen cooled mercury cadmium telluride (MCT) or pyroelectric detector. The detectors are sufficiently fast to cope with time domain signal changes from the modulation in the interferometer.

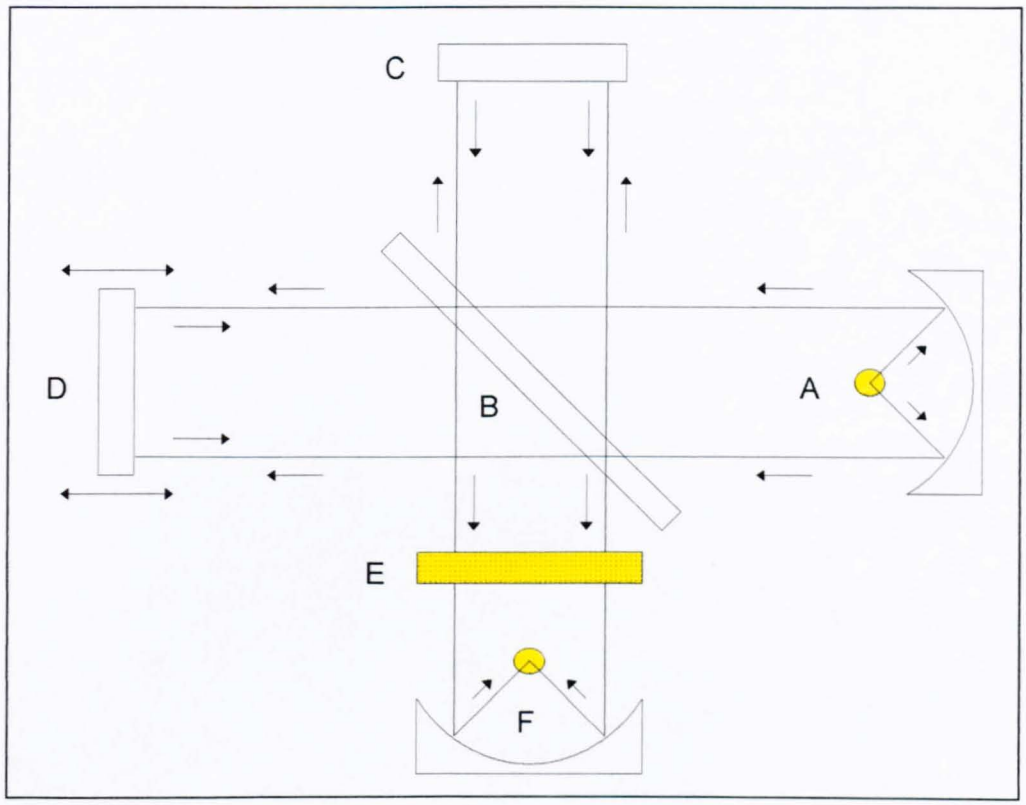

Figure 2.5. ***The Schematic of the Michelson interferometer which forms the basis of most FTIR instruments.***

There will be both destructive and constructive interference during recombination. This is due to the path distance that the light travels between the beam splitter and the fixed mirror (B → A) and the beam splitter and the moving mirror (B → C) changing.

Constructive interference will only occur when the radiation coming from both the fixed and moving mirrors is in phase,

$$(B-C)=(B-D)\pm n\lambda \qquad \text{(eq. 2.13.)}$$

Where n is an integer

λ is the wavelength of radiation

Destructive interference will occur when the path lengths differ by integer multiples of $\lambda/2$,

$$(B-C)=(B-D)\pm n\frac{\lambda}{2} \qquad \text{(eq. 2.14.)}$$

As the distance that the moving mirror changes from the beam splitter, different wavelengths of radiation are in-phase and out-of-phase at a frequency that is dependent both upon the rate at which the mirror moves and the frequency of radiation.

The complex pattern of overlaid sinusoidal waves of light (in the time domain) is known as an interferogram. The interferogram can be converted back to the original frequency distribution (spectrum) by means of a Fourier transform, which can be done very rapidly on a PC.

2.4.1.1. Fourier Transforms

As stated earlier the signal that the detector 'sees' is a series of sinusoidal waves in the 'time domain'. The response of the detector, i.e. the intensity of the radiation at a given time, at any point where the retardation (x) is an integer multiple of λ will be at a maximum and equal to the intensity of the source $I(\bar{\upsilon})$. The intensity of the beam at the detector at any value of x is given by

$$I'(x) = \frac{1}{2} I(\bar{\nu})[1 + \cos 2\pi\bar{\nu}x] \qquad \text{(eq. 2.15)}$$

The modulated component $\frac{1}{2} I(\bar{\nu})\cos 2\pi\bar{\nu}x$ is known as the interferogram and it is this that is recorded in infrared spectrometry. The interferogram obtained from an ideal interferometer using a monochromatic source can be described by

$$I(x) = \frac{1}{2} I(\bar{\nu})\cos 2\pi\bar{\nu}x \qquad \text{(eq. 2.16)}$$

Instrument factors such as beam splitter efficiency, detector response and amplifier characteristics will affect the amplitude of the interferogram but will remain constant for a particular instrument. Another factor that will affect the amplitude is the source intensity, which is frequency dependent. If one corrects for this using a single factor, $H(\bar{\upsilon})$, the interferogram for a sample at each frequency becomes

$$I(x) = \frac{1}{2} H(\bar{\nu}) I(\bar{\nu})\cos 2\pi\bar{\nu}x \qquad \text{(eq. 2.17)}$$

or

$$I(x) = S(\bar{\nu})\cos 2\pi\bar{\nu}x \qquad \text{(eq. 2.18)}$$

where $S(\bar{\upsilon}) = \frac{1}{2}H(\bar{\nu})I(\bar{\nu})$

For a polychromatic source the interferogram can be given as

$$I(x) = \int_{-\infty}^{+\infty} S(\bar{\nu})\cos 2\pi\bar{\nu}x.d\bar{\nu} \qquad \text{(eq. 2.19)}$$

Equation 2.19 is one half of a cosine Fourier transform pair, the other is

$$S(\bar{\nu}) = C' \int_{-\infty}^{+\infty} I(x)\cos 2\pi\bar{\nu}x.dx \qquad \text{(eq. 2.20)}$$

Since I(x) is an even function , equation 2.20 can be rewritten

$$S(\bar{\nu}) = 2\int_{0}^{+\infty} I(x)\cos 2\pi\bar{\nu}x.dx \qquad \text{(eq. 2.21)}$$

Most FT instruments are single beam instruments which means that they record single beam responses rather than a spectrum. Therefore in order to obtain a spectrum of a sample the user must first obtain a 'background'. This is simply the response of the instrument without a sample in the beam, or a 'source profile'. The Fourier transformed responses both with and without the sample in the beam are then ratioed to give a spectrum.

2.5. The advantages of FTIR spectroscopy.

The traditional (dispersive) approach of infrared spectroscopy was to 'record' the spectrum of a sample at discrete frequencies, building up a spectrum as one went along. In a spectrum that has regions of interest over a wide range of wavelengths this proved to be a time consuming process. In an instrument reliant on many moving parts, the accuracy of these 'discrete' frequencies is always in some doubt. The following sections will discuss the advantages of Fourier transform infrared spectroscopy over the dispersive technique.

2.5.1. The throughput (Jaquinot) advantage.

This is realised because of the inherent simplicity of FT instruments, needing no slits which can attenuate the radiation. As a consequence, the power of the radiation that reaches the detector is greater than that in dispersive systems. Hence an increase in signal to noise ratio is observed.

The spectral optical conductance of a grating instrument can be expressed as

$$G_{\bar{\upsilon}}^{G} = \frac{hH}{f\bar{\nu}} R_0 \qquad \text{(eq. 2.22)}$$

Where $G_{\bar{\upsilon}}^{G}$ is the optical conductance per wavenumber of grating,

H is the height of the grating

h is the length of the entrance slit,

f is the focal length of the collimator,

and R_0 is the theoretical resolving power.

In order to compare this directly with the interferometer one must choose the beam area of the interferometer F_1 to be equal to the beam area at the grating H^2. Therefore in an interferometer the optical conductance can be expressed as

$$G_{\bar{\upsilon}}^{I} = \frac{2\pi H^2}{\bar{\nu}} \qquad \text{(eq. 2.23)}$$

The ratio of the two optical conductances is therefore

$$\frac{G_{\bar{\upsilon}}^{I}}{G_{\bar{\upsilon}}^{G}} \approx \frac{2\pi \mathrm{f}}{h} \qquad \text{(eq. 2.24)}$$

This equates to around 100 times more throughput in an interferometer.

2.5.2. The multiplex (Fellgett) advantage.

This is achieved because all the frequency elements of the source reach the detector simultaneously. This allows an entire spectrum to be obtained in a very short period of time. If one considers a spectrum to be made up of M individual measurements at equal frequency intervals, resolution elements, then the amount of spectral detail will obviously increase with M. In a dispersive system increasing the number of spectral

elements (M) will increase the length of time (τ) required to do a particular experiment. This advantage also has signal to noise(S/N) implications. In a dispersive system the signal to noise ratio is shown to be

$$S/N_D \propto \frac{\tau^{\frac{1}{2}}}{M^{\frac{1}{2}}} \qquad \text{(eq. 2.25)}$$

For a FT system the signal to noise is given by

$$S/N_{FT} \propto \tau^{\frac{1}{2}} \qquad \text{(eq. 2.26)}$$

Since all spectral elements are recorded at once in an FT system, one can average the response and for the same time length experiment, one can expect an increase in S/N of the order of $\sqrt{M}$.

2.5.3. The Connes advantage.

This advantage is derived from the method of sampling used in FTIR spectroscopy and gives the analyst absolute control of the spectral wavelength. In an FT system the spectral wavelength is known very accurately. This is achieved by 'sampling' at accurately known time intervals utilising the highly monochromatic nature of the laser output; usually fixed at a wavelength of 632.8 nm (15798.002 cm^{-1}). The time domain spectrum is then converted to a frequency domain spectrum, and since it is easy to

measure time accurately, the conversion to frequency is also highly accurate.. This absolute spectral control allows manipulative techniques such as spectral subtraction to be applied successfully and means that spectral calibration is not necessary. From a practical point of view the Connes advantage means that many spectra can be collected and averaged to further improve S/N; S/N α $\sqrt{M}$.

2.5.4. Disadvantages of FTIR.

The advantages of FTIR over dispersive systems far outweigh the disadvantages. The first disadvantage is the cost, which is becoming less and less important as low end FTIR systems are now as cheap as most single frequency dispersive infrared systems. The other disadvantage is the fact that an FTIR machine does not produce a spectrum but an interferogram. Most people cannot deduce much information from an interferogram and require the use of some computational power to perform a Fourier transform and obtain the frequency domain spectrum. This used to present a problem, but with cheap, fast CPUs, the Fourier transforms can now be carried out on the bench top instrument and the spectrum (or single beam spectrum) can be produced in fractions of a second.

Another disadvantage (the Fellget disadvantage) is that if the light from the source is 'noisy' then the detector will detect noise at all frequencies, even if the noise only occurs within a certain frequency range. Finally perhaps the most relevant problem from a practical point of view is the presence of bands associated with CO_2 and water vapour in the spectrum. These can be eliminated in dispersive instruments by the use of

a dual beam system but in FT-IR spectosopy the user has to eliminate unwanted CO_2 peaks or water vapour bands by purging the sample compartment, with a dry infrared inactive gas such as nitrogen, during measurement or by using interactive subtraction using commercially available software.

FT-IR is important for this project as it allows the rapid acquisition of spectral data, allowing the *in-situ* calculation of diffusion coefficients and structural data for small molecules diffusing into PET films. The absolute control of the frequency of the output means that wavenumber shifts can be accurately measured and allows the application of data manipulation techniques such as Fourier deconvolution and spectral subtraction.

2.6. Sampling techniques.

In most instrument based scientific techniques, the method of sampling is vitally important when trying to interpret the output data. Infrared spectroscopy is no exception. Obviously, regardless of the sampling technique, one will be looking at the vibrations of the molecule / compound. By careful selection of the sampling technique, the versatility of infrared spectroscopy can maximised. For example, one would not use the same infrared sampling technique to look at an inorganic powder, a polymer laminate or a very thin film of charge transfer material on a metal substrate. But all three are successfully studied using different sampling techniques. In this sub-section most of the infrared sampling techniques will be mentioned but only those relevant to this project will be discussed in any detail.

2.6.1. Transmission.

This is the most simple and basic of the infrared spectroscopic techniques. Essentially infrared radiation is passed through a sample and the transmitted radiation is measured. The spectra obtained will be representative of the whole of the sampled area and 'localised' (e.g. surface) properties can quite easily be lost in the 'bulk' properties depending on the size and nature of the sample. It is only useful for thin (<10 μm) samples or when looking at weak bands, such as overtones, in thicker samples. Often sample preparation such as the manufacture of KBr discs or Nujol mull preparation is necessary which can be time consuming and difficult to reproduce.

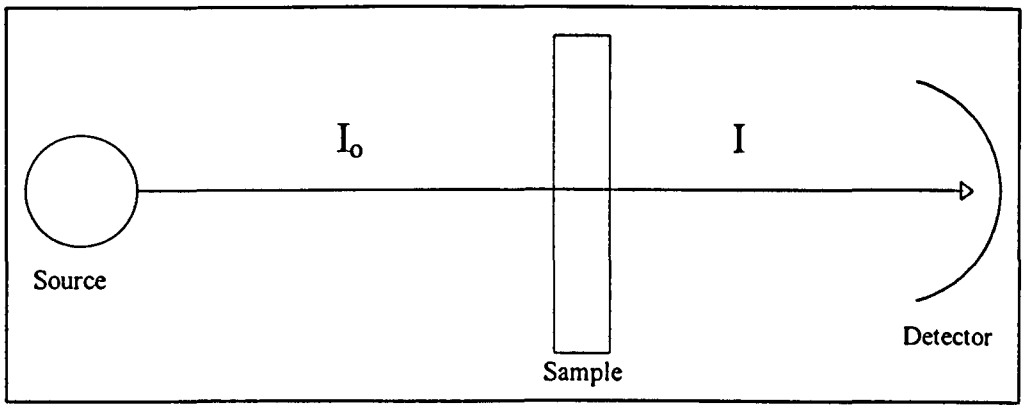

Figure 2.3. The transmission experiment.

In the transmission experiment the transmitted radiation or transmittance (T) is given by

$$T = \frac{I}{I_0} = \exp(-\alpha \ell) \qquad \text{(eq. 2.27)}$$

where I is the transmitted intensity

I_0 is the incident intensity

α is the absorption coefficient

ℓ is the sample thickness .

2.6.2. Attenuated total reflectance infrared spectroscopy (ATR-FTIR).

Attenuated total reflectance (ATR) is also known as internal reflectance spectroscopy (IRS) and is a popular sampling technique for a wide variety of 'difficult' samples. Thick solids, strongly absorbing solids / liquids, fibres, pastes and polymer laminates are all difficult to sample using the transmission technique, but are readily sampled using ATR The detailed theory of ATR is given elsewhere and the reader is referred to

texts by Harrick [**2.1**] and Mirabella [**2.2**] for a more detailed explanation. Here only the main points will be discussed.

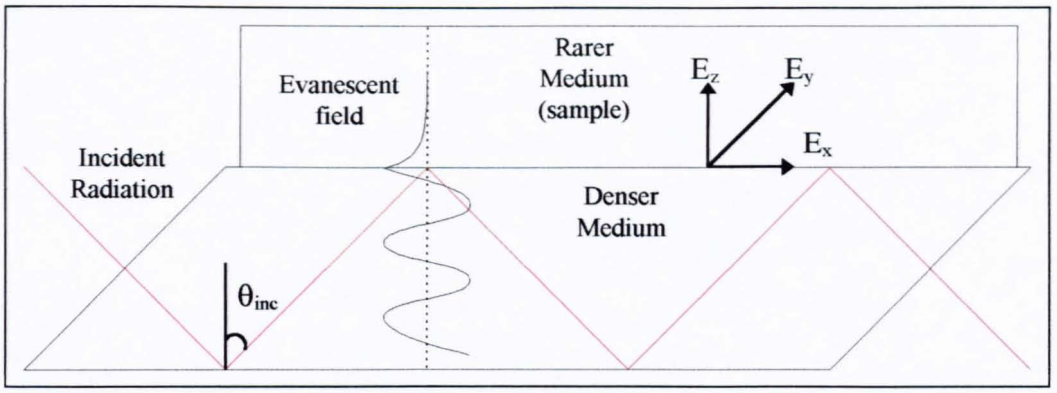

Figure 2.4. Schematic of the ATR experiment.

The most important feature of ATR theory is associated with the properties of the evanescent field at the surface of the ATR crystal. Light (in this case infrared radiation) propagating through a medium with a high refractive index (ATR crystal), at an angle greater than the critical angle (θ_c) undergoes total internal reflection at the interface with a medium of lower refractive index (i.e. the sample). Under these conditions the incident light is totally internally reflected at each ATR crystal - sample interface. The infrared radiation propagates through the ATR crystal but an electric field penetrates slightly into the sample and the magnitude of this electric field decays exponentially with distance from the interface. This non-transverse wave, which has components in all spatial directions, is known as the evanescent field. The rate of decay of the evanescent field is dependent on the wavelength and angle of incidence of the light and the refractive indices of both the rarer and denser media. In a situation where the rarer medium is non absorbing , the reflected rays will be of the same intensity as the incident rays. However

rays. However in most instances the rarer medium is absorbing and the reflection is said to be attenuated.

At incident angles greater than the critical angle, total internal reflection occurs. In an ideal system radiation is not lost during the reflection unless it is absorbed by the propagating medium. Therefore experimentally the ATR material should be both of high refractive index and be infrared transparent. Such materials do exist and some common ATR prism materials are shown in table 2.2

Material	Refractive index	IR window
ZnSe	2.4	450 - 20000 cm^{-1}
KRS5	2.4	250 - 20000 cm^{-1}
Ge	4.0	600 - 5500 cm^{-1}
Si	3.4	1100 - 8300 cm^{-1}

Table 2.2. Common ATR prism materials and some properties.

The evanescent field (E.F.) has been briefly touched upon but it is important to mention some of its properties.

I. E.F. is confined to the surface of the rarer medium and decreases in intensity with distance normal to the interface, i.e. along the z axis.

II. E.F. is non transverse and has components in all directions, which can interact with transition dipoles ($\partial\mu/\partial Q$) in the rarer medium with all orientations.

III. There is no loss of energy at the interface between the rarer and denser media and total internal reflection occurs.

IV. There is a non-zero energy flow, parallel to the surface, i.e. along the x axis, which results in a displacement of the incident and reflected waves and is known as the Goos-Hänchen shift.

The decrease in intensity of the E.F. from the interface can be written

$$E = E_o \exp\left[\frac{-2\pi}{\lambda_1}\left(\sin^2\theta_{inc} - n_{21}^2\right)^{\frac{1}{2}} Z\right] \qquad \text{(eq. 2.28)}$$

Where E_o is electric field amplitude at the surface of rarer medium

E is the value the electric field at distance Z into rarer medium

θ_{inc} is angle of incidence

λ_1 is wavelength of radiation in denser medium ($\lambda_1 = \lambda / n_1$)

Equation 2. 28. can be rewritten by replacing the exponential constant with the electric field amplitude decay coefficient, γ.

$$E = E_o \exp[-\gamma Z] \qquad \text{(eq. 2.29)}$$

$$\gamma = \frac{2\pi\left(\sin^2\theta_{inc} - n_{21}^2\right)^{\frac{1}{2}}}{\lambda_1} \qquad \text{(eq. 2.30)}$$

The depth of penetration (d_p) of the E.F. into the rarer medium is given by equation 2.31 and is defined as the depth (Z) at which E has a value of E_o exp[-1].

$$Z = d_p = \frac{1}{\gamma} \qquad \text{(eq. 2.31)}$$

Although d_p is sometimes known as the 'sampling depth', the real sampling depth (d_e) is approximately three times d_p. The effective thickness (d_e) is the thickness of the rarer medium that will give the same absorbance as that obtained in transmission at normal

incidence. The absorbing rarer medium can be considered in terms of intensity loss per reflection. In this case the reflectivity, R, is given by

$$R = \frac{I_R}{I_0} = \exp(-\alpha d_e) \approx (1 - a) \qquad \text{(eq. 2.32)}$$

$$a = \alpha d_e \qquad \text{(eq. 2.33)}$$

Where α is the same as the absorption coefficient for transmission

a is the absorption parameter for one reflection

The effective thickness parameter is useful for weak absorbers as it allows both the comparison of ATR with transmission spectroscopy and the calculation of an upper limit for absorbance. In order to calculate d_e the electric field components (E_x, E_y and E_z) must be evaluated.

There are two polarisations of the electromagnetic wave, transverse electric (TE), which is perpendicular to the plane of incidence and transverse magnetic (TM), which is parallel to the plane of incidence. The TE wave has components in the y plane only i.e. consists of just E_y. The TM wave has components in both the x and z planes i.e. consists of E_x and E_z. For this discussion the plane of the interface between the rarer and denser media is perpendicular to the plane of the incident radiation.

$$TE = E_{\text{perpendicular}} = E_y \qquad \text{(eq. 2.34)}$$

$$TM = E_{\text{parallel}} = \sqrt{|E_x|^2 + |E_z|^2} \qquad \text{(eq. 2.35)}$$

The thickness of the rarer medium can be placed into two distinct categories, namely the semi-infinite case and the thin film case. In the semi-infinite case the electric field amplitude falls to a very low value entirely within the thickness of the film (t);

i.e. $t >> \frac{1}{\gamma}$ or $t >> d_p$

In the thin film case the electric field amplitude remains essentially constant over the thickness of the film;

i.e. $t << \frac{1}{\gamma}$ or $t << d_p$

It should be apparent that in the thin film case the properties of the rarer medium have little impact on the E.F. and that the controlling refractive index is that of the next medium (n_3).

1. Semi-infinite bulk case i.e. $t >> \frac{1}{\gamma}$

TE wave,

$$E_y = \frac{2\cos\theta}{\sqrt{\left(1-n_{21}^2\right)}} \qquad \text{(eq. 2.36)}$$

TM wave,

$$E_x = \frac{2\cos\theta\sqrt{\left(\sin^2\theta - n_{21}^2\right)}}{\sqrt{\left(1-n_{21}^2\right)}\sqrt{\left[\left(1+n_{21}^2\right)\sin^2\theta - n_{21}^2\right]}} \qquad \text{(eq. 2.37)}$$

$$E_z = \frac{2\cos\theta\sin\theta}{\sqrt{\left(1-n_{21}^2\right)}\sqrt{\left[\left(1+n_{21}^2\right)\sin^2\theta - n_{21}^2\right]}} \qquad \text{(eq. 2.38)}$$

Where $n_{21} = \frac{n_2}{n_1}$

2. The thin film case i.e. $t << \frac{1}{\gamma}$

TE wave,

$$E_y = \frac{2\cos\theta}{\sqrt{\left(1-n_{31}^2\right)}} \qquad \text{(eq. 2.39)}$$

TM wave,

$$E_x = \frac{2\cos\theta\sqrt{\left(\sin^2\theta - n_{31}^2\right)}}{\sqrt{\left(1-n_{31}^2\right)}\sqrt{\left[\left(1+n_{31}^2\right)\sin^2\theta - n_{31}^2\right]}} \qquad \text{(eq. 2.40)}$$

$$E_z = \frac{2\cos\theta\sin\theta n_{32}^2}{\sqrt{\left(1-n_{31}^2\right)}\sqrt{\left[\left(1+n_{31}^2\right)\sin^2\theta - n_{31}^2\right]}} \qquad \text{(eq. 2.41)}$$

Where $n_{31} = \frac{n_3}{n_1}$

$$n_{32} = \frac{n_3}{n_2}$$

Figure 2.5 shows a plot of the angle of incidence versus electric field amplitude for a typical system.

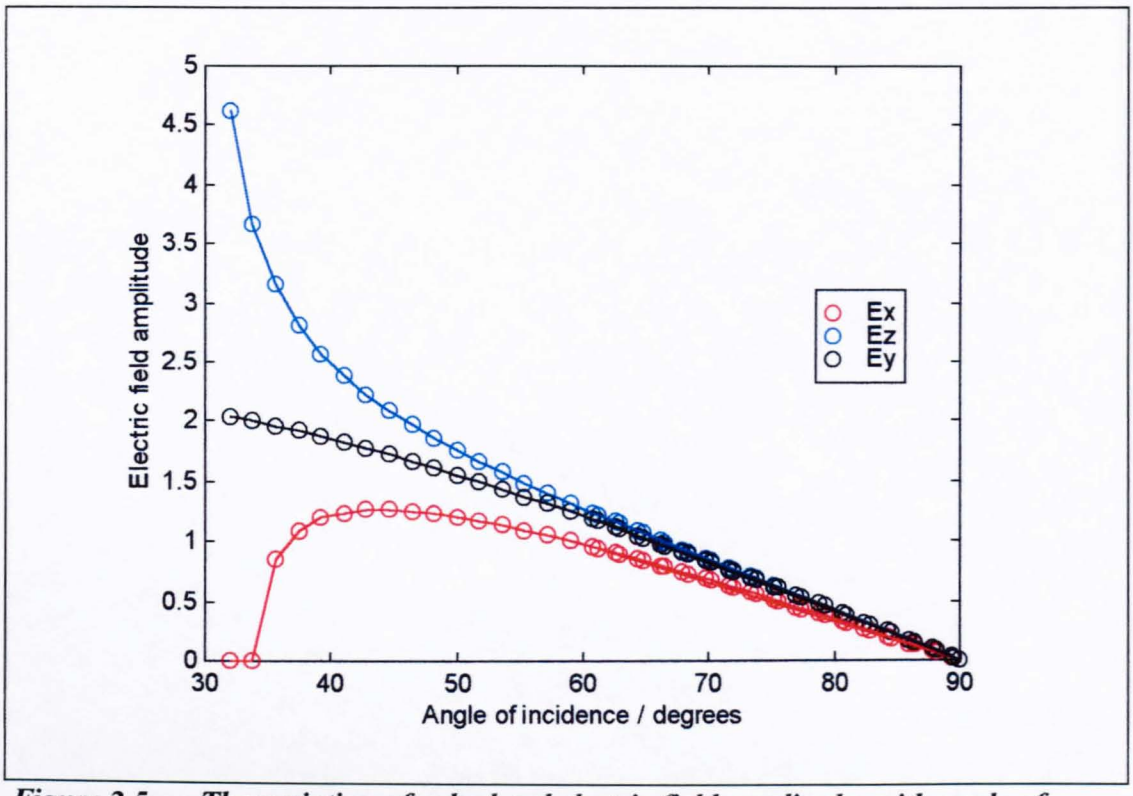

Figure 2.5 ***The variation of calculated electric field amplitudes with angle of incidence for polarised radiation***

From the plot it can be shown that whilst both E_y and E_z reach maxima at the critical angle, E_x is zero. This produces intense fields normal to the surface. It is also interesting to note that the electric field is zero in all directions at 90°.

The relation between the electric field, E, and the absorption parameter, a, for a weak absorber is

$$a = \frac{n_{21}\alpha}{\cos\theta}\int_0^t E^2 dz \qquad \text{(thin film case)} \qquad \text{(eq. 2.42)}$$

or

$$a = \frac{A}{N} = \frac{n_{21}\alpha C}{\cos\theta}\int_0^\infty E^2 dz \qquad \text{(semi-infinite bulk case)} \qquad \text{(eq. 2.43)}$$

$$a = \frac{A}{N} = \frac{n_{21}\alpha C}{\cos\theta}\int_0^\infty E^2 dz \qquad \text{(semi-infinite bulk case)} \qquad \text{(eq. 2.43)}$$

Where A is absorbance

N is the number of reflections

C is the concentration

α is the molar absorption coefficient

For the semi infinite bulk case this gives

$$a = \frac{n_{21}\alpha E_0^2}{2\gamma\cos\theta} \qquad \text{(eq. 2.44)}$$

And for the thin film case

$$a = \frac{n_{21}\alpha d E_0^2}{2\gamma\cos\theta} \qquad \text{(eq. 2.45)}$$

By the substitution of equation 2.45 into equation 2.34 one gets

$$d_e = \frac{2\gamma\cos\theta}{\alpha n_{21}\alpha d E_0^2} \qquad \text{(eq. 2.46)}$$

Hence for the semi infinite bulk case,

TE wave,

$$d_{e\,\text{perpendicular}} = \frac{n_{21}\lambda_1\cos 0}{\pi\left(1-n_{21}^2\right)\sqrt{\left(\sin^2 0 - n_{21}^2\right)}} \qquad \text{(eq. 2.47)}$$

TM wave,

$$d_{e\,\text{parallel}} = \frac{n_{21}\lambda_1\left(2\sin^2\theta - n_{21}^2\right)\cos\theta}{\pi\left(1-n_{21}^2\right)\left[\left(1+n_{21}^2\right)\sin^2\theta - n_{21}^2\right]\sqrt{\left(\sin^2\theta - n_{21}^2\right)}} \qquad \text{(eq. 2.48)}$$

And for the thin film case,

TE wave,

$$d_{e\,\text{perpendicular}} = \frac{4n_{21}d\cos\theta}{\left(1-n_{21}^2\right)} \qquad \text{(eq. 2.49)}$$

TM wave,

$$d_{e\,\text{parallel}} = \frac{4n_{21}d\cos\theta\left[\left(1+n_{32}^4\right)\sin^2\theta - n_{31}^2\right]}{\left(1-n_{31}^2\right)\left[\left(1+n_{31}^2\right)\sin^2\theta - n_{31}^2\right]} \qquad \text{(eq. 2.50)}$$

The total effective sampling thickness is given by

$$d_e = \frac{d_{e\,\text{parallel}} + d_{e\,\text{perpendicular}}}{2} \qquad \text{(eq. 2.51)}$$

There are several parameters that govern d_e such as the electric field decay constant (γ) which itself is wavelength dependent, the electric field at the surface (E_0^2) which is dependent on θ_{inc}, the sampling area and the refractive index matching, n_{21}. (See figure 2.6.)

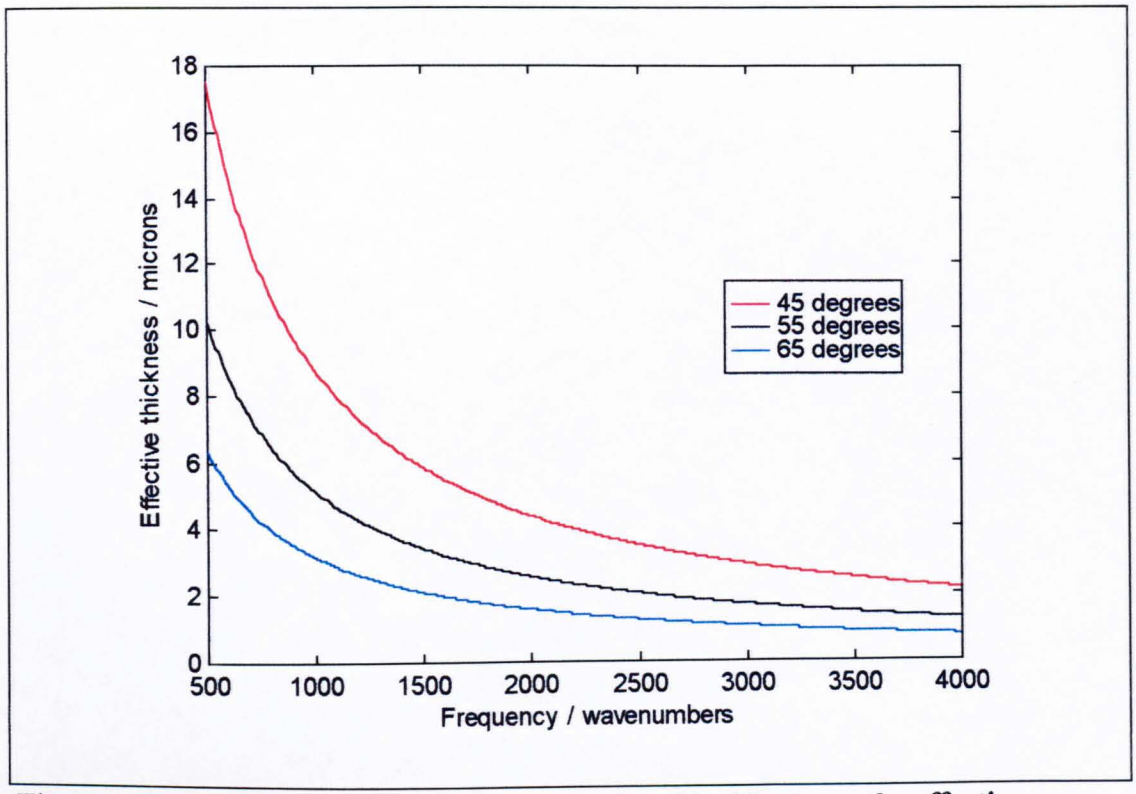

Figure 2.6. The effect of frequency and angle of incidence on the effective sampling depth on a typical (polymer) sample

ATR is an invaluable research tool allowing a broad range of different, so-called difficult, samples such as fibres [**2.3, 2.4**], strongly absorbing materials [**2.5-2.8**] and thick materials [**2.9-2.11**] to be studied using infrared. The ability to control the sampling depth has allowed depth profiling of polymer laminates [**2.12, 2.13**]. Perhaps the most useful aspect of the ATR methodology is its ability to lend itself to *in-situ* kinetic work. This has encompassed a whole range of areas such as polymer mineral interactions [**2.14**], clay solvent interactions [**2.15**], curing processes [**2.16**] and the diffusion of small molecules into polymers (see chapters 4,5 and 7).

2.6.3. Reflection absorption infrared spectroscopy (RAIRS).

Reflection absorption infrared spectroscopy (RAIRS) also known as external reflection spectroscopy (ERS) or grazing angle infrared spectroscopy is a technique that has long been used for the study of monolayers and thin organic and inorganic films on reflective (usually metal) surfaces. It makes use of the so-called 'surface selection rule' and is highly sensitive to the orientation of the electric dipoles associated with the sample. The theory of RAIRS is well documented [**2.17, 2.18**] so only a brief summary will be included in this chapter.

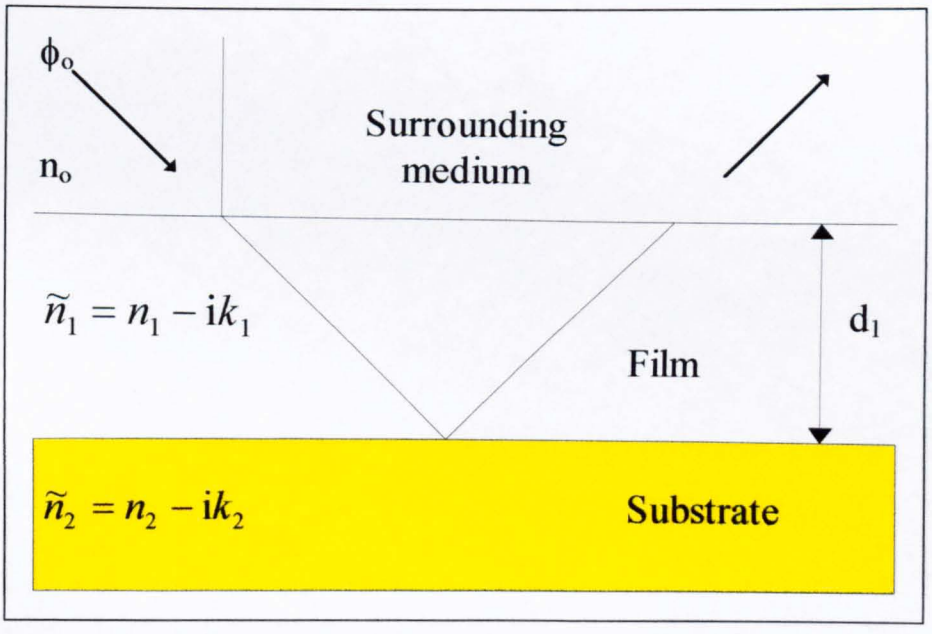

Figure 2.7. A model for the RAIRS experiment

Consider a metal substrate with the complex refractive index

$$\tilde{n}_2 = n_2 - ik_2 \qquad \text{(eq. 2.52.)}$$

The surrounding medium (generally air) has a refractive index n_o and a film deposited on this substrate has the complex refractive index

$$\tilde{n}_1 = n_1 - ik_1 \qquad \text{(eq. 2.53.)}$$

When parallel polarised radiation is reflected from the surrounding medium through the film and back to the surrounding medium (figure 2.7.), the total electric field amplitude reflected back is given by

$$r = \frac{r_1 + r_2 \exp(-2i\delta)}{1 + r_1 r_2 \exp(-2i\delta)} \qquad \text{(eq.2.54.)}$$

Where $$r_1 = \frac{n_0 \cos\phi_1 - \tilde{n}_1 \cos\phi_0}{n_0 \cos\phi_1 + \tilde{n}_1 \cos\phi_0} = \rho_1 \exp(i\beta_1) \qquad \text{(eq 2.55.)}$$

$$r_2 = \frac{\tilde{n}_1 \cos\phi_1 - \tilde{n}_2 \cos\phi_1}{\tilde{n}_1 \cos\phi_1 + \tilde{n}_2 \cos\phi_1} = \rho_2 \exp(i\beta_2) \qquad \text{(eq 2.56.)}$$

$$\delta = \frac{(2\pi\tilde{n}_1 d_1 \cos\phi_1)}{\lambda} \qquad \text{(eq. 2.57.)}$$

β_1 and β_2 are the phase shifts for radiation being reflected at the surrounding medium / film and film / metal interface. The phase thickness of the film (ϕ_1) can be calculated from n_o, ϕ_o, $\tilde{n}_1$ and $\tilde{n}_2$ using Snell's law i.e.

$$n_0 \sin\phi_0 = \tilde{n}_1 \sin\phi_1 \qquad \text{(eq. 2.58.)}$$

$$\tilde{n}_1 \sin\phi_1 = \tilde{n}_2 \sin\phi_2 \qquad \text{(eq. 2.59.)}$$

It follows that as $\tilde{n}_1$ and $\tilde{n}_2$ are complex then ϕ_1 and ϕ_2 are also complex and therefore do not represent angles of refraction but in fact are reflections. The intensity of the reflection, or reflectivity, is given by

$$R = rr^* \qquad \text{(eq. 2.60.)}$$

Where r* is the complex conjugate of r

The intensity of the absorption band is given by

$$A = \frac{(R - R_0)}{R_0} \qquad \text{(eq. 2.61.)}$$

Where R_o is the reflectivity for $k_1 = 0$

R is the reflectivity for $k_1 \neq 0$

When radiation is polarised perpendicular to the incidence plane the same analysis can be used but r_1 and r_2 now become

$$r_1 = \frac{n_0 \cos\phi_1 - \tilde{n}_1 \cos\phi_1}{n_0 \cos\phi_1 + \tilde{n}_1 \cos\phi_1} = \rho_1' \exp(i\beta_1') \qquad \text{(eq 2.62.)}$$

$$r_2 = \frac{\tilde{n}_1 \cos\phi_1 - \tilde{n}_2 \cos\phi_2}{\tilde{n}_1 \cos\phi_1 + \tilde{n}_2 \cos\phi_2} = \rho_2' \exp(i\beta_2') \qquad \text{(eq 2.63.)}$$

Placing equations 2.62. and 2.63. back into equation 2.54. and subsequently calculating A from equation 2.60., it is found that A is very small for all incident angles, hence one would expect to see no bands. Comparisons of theoretical A values for polarised light at constant wavelength with differing incident angles are shown in figure 2.8.

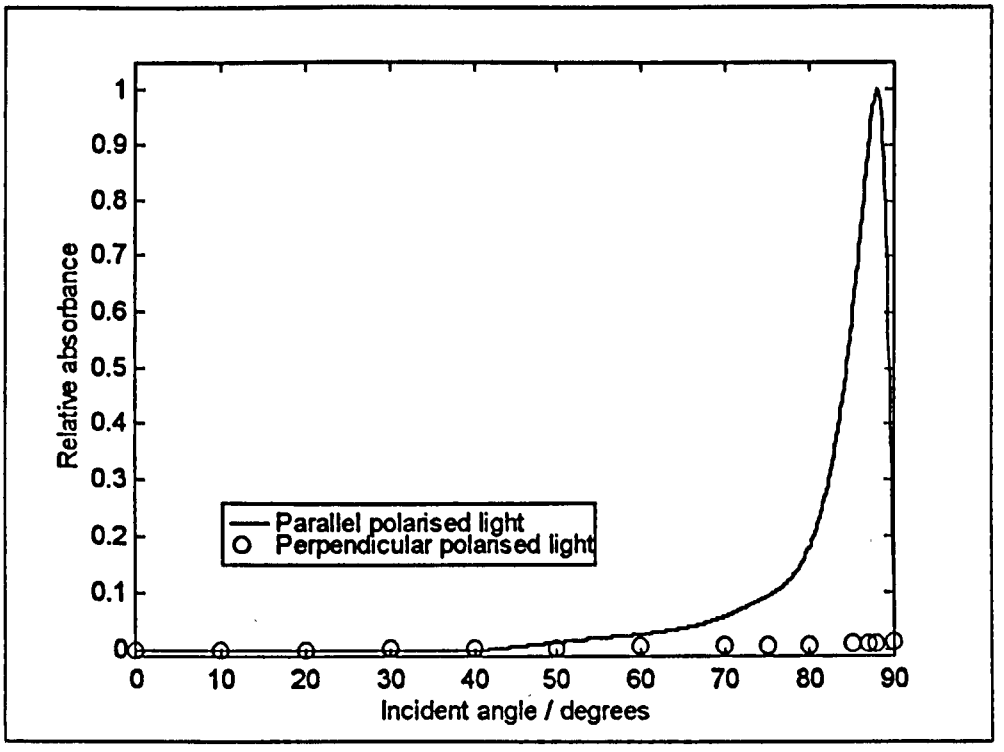

Figure 2.8. The effect of angle of incidence on the relative absorbance observed duringthe RAIRS experiment.

From figure 2.8. one can see that for all incident angles there is little or no contribution from the perpendicular polarised radiation. Conversely band intensities for the parallel polarised light above angles of 40° show a sharp increase with incident angle, in general reaching a maximum at around 88° and falling sharply towards 90°. The angle where the intensity is at a maximum is known as the Brewster angle and can readily be calculated from equation 2.64.

$$\sin\phi\tan\phi = \frac{\sqrt{2}}{1.05\times10^{-6}\sqrt{(\upsilon\varepsilon\rho)}} \qquad \text{(eq. 2.64.)}$$

Where ε is the dielectric constant for the ambient phase

υ is the frequency of the incident radiation

ρ is the resistivity of the metal.

From a practical point of view angles of 88° are difficult to obtain but good S/N can be obtained with angles of around 85°. The optical configuration of the RAIRS experiment is shown in figure 2.9. the most interesting feature of which is the inversion of the TE polarised light upon reflection which essentially causes a 'node' at the surface the consequence of which will now be discussed.

In RAIRS, absorption takes place when infrared radiation interacts with the electric transition dipoles of the sample on reflection. The fact that a 'node' exists at the surface with the TE polarisation means that no interaction can occur between TE polarised radiation and the sample, and hence no bands are observed. This is known as the 'surface selection rule' where only $(\partial\mu/\partial Q)^{\perp}$ components can be 'seen' in RAIRS. But the TE component will still contribute noise to the spectrum which is an important consideration in a detector noise limiting system.

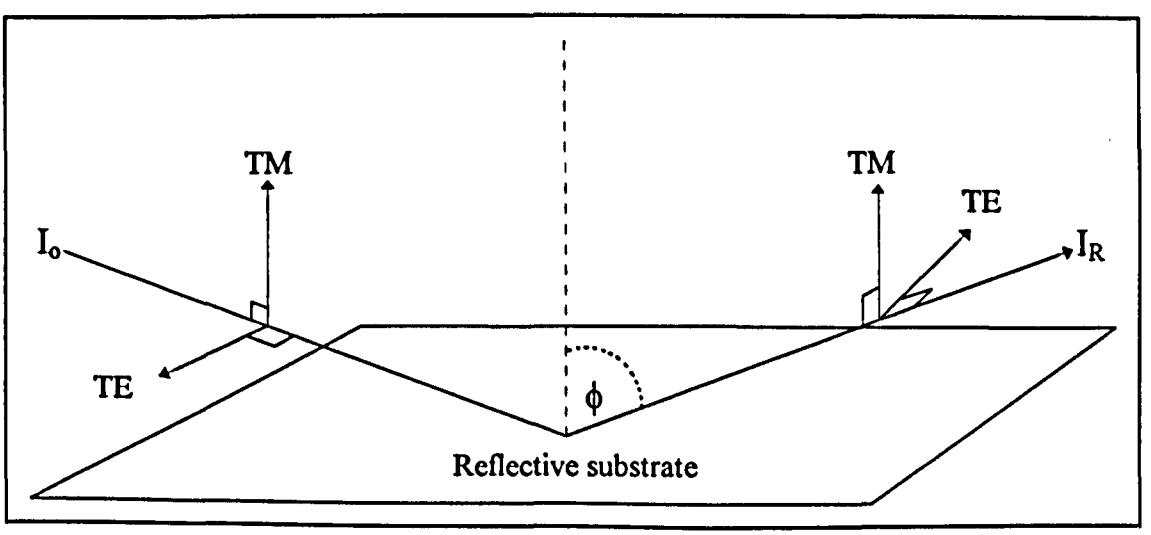

Figure 2.9. The optical configuration of the RAIRS experiment.

As shown in theory from equations 2.60 and 2.61 and qualitatively discussed in the previous paragraph there is no absorbance associated with TE polarised infrared radiation. From a S/N point of view it therefore makes sense to block out the TE component of the incoming beam which will contribute only noise to the spectrum. Practically it has also been shown by Song et al **[2.19]** that the use of TM polarised radiation not only reduces the noise but gives a two-fold signal enhancement. RAIRS is a very useful technique for the study of thin ($1 > \mu m$) inorganic and organic films **[2.20]**. It can be used to give detailed information on the orientation of monlayers on reflective substrates **[2.21]** and has also been used to interpret the interactions between multilayers **[2.22]**.

2.7. Fourier Self-Deconvolution and band fitting.

The interpretation of spectral data can often be made difficult by the fact that many vibrations occur at similar frequencies thus causing overlapping bands. Numerical techniques can be used to extract information from such spectra. Techniques that are commonly used include Fourier self-deconvolution [2.23,2.24], 2nd derivative analysis and band fitting [2.25-2.28]. Whilst all three techniques give information about the position and relative intensities of vibrations, it would be dangerous to be reliant on just one technique for quantitative results. Therefore using one or more technique in conjunction with another should lead to more reliable information. This section will discuss the theory behind some of the techniques used during this work.

2.7.1. Fourier self-deconvolution.

In order for Fourier self deconvolution (FSD) to be applied, one must consider that an experimentally observed spectrum is a convolution of the band positions, $E'(\bar{\nu})$, with a band shape function, $G(\bar{\nu})$. The bands are not Dirac delta functions due to inherent broadening effects such as the normal distribution of zero point energies. Instrumental effects such as the choice of apodisation function, dynamic range of digitisation and the distance the mirror has travelled may also cause band broadening.

$$E(\bar{\nu}) = E'(\bar{\nu}) * G(\bar{\nu}) \qquad \text{(eq. 2.65.)}$$

Where * indicates the convolution operation.

The relationship between a spectrum, $E(\bar{\nu})$, in the wavenumber domain and its interferogram, $I(x)$, is given by,

$$E(\bar{\nu}) = \int_{-\infty}^{\infty} I(x)\exp(i2\pi\bar{\nu}x)dx = F\{I(x)\} \qquad \text{(eq. 2.66.)}$$

And,

$$I(x) = \int_{-\infty}^{\infty} E(\bar{\nu})\exp(i2\pi\bar{\nu}x)d\bar{\nu} = F^{-1}\{E(\bar{\nu})\} \qquad \text{(eq. 2.67.)}$$

Where F is the Fourier transform (FT) and F^{-1} is the inverse Fourier transform

Any spectrum can be expressed as a convolution of a lineshape function, $G(\bar{\nu})$, and a spectrum

$$E(\bar{\nu}) = G(\bar{\nu}) * E'(\bar{\nu}) \qquad \text{(eq. 2.68.)}$$

Therefore in order to obtain the lineshape function, $G(\bar{\nu})$, it is necessary to take the inverse FT of equation 2.65. i.e.

$$I(x) = F^{-1}\{G(\bar{\nu})\}I'(x) \qquad \text{(eq. 2.69.)}$$

The interferogram corresponding to the deconvoluted spectrum is given by

$$I'(x) = \frac{I(x)}{F^{-1}\{G(\bar{\nu})\}} \qquad \text{(eq. 2.70.)}$$

If equation 2.70. is then multiplied by an appropriate apodisation function, $D(x)$, the deconvoluted spectrum, $E'(\bar{\nu})$, can be obtained by the inverse FT of $I'(x)$.

$$E'(\bar{\nu}) = F^{-1}[D(x)I'(x)] \qquad \text{(eq. 2.71.)}$$

In this general case the final lineshape of $E'(\bar{\nu})$ is highly dependent on the particular form of the apodisation function used.

The FSD process is easier to envisage pictorially. Figure 2.9 shows some Lorentzian line shapes and their Fourier transforms. It is noticeable that as the Lorentzian lineshape gains more width, the amplitude of the Fourier transform reaches a minimum more quickly. For a Dirac delta function the Fourier transform is a propagating broad sine wave.

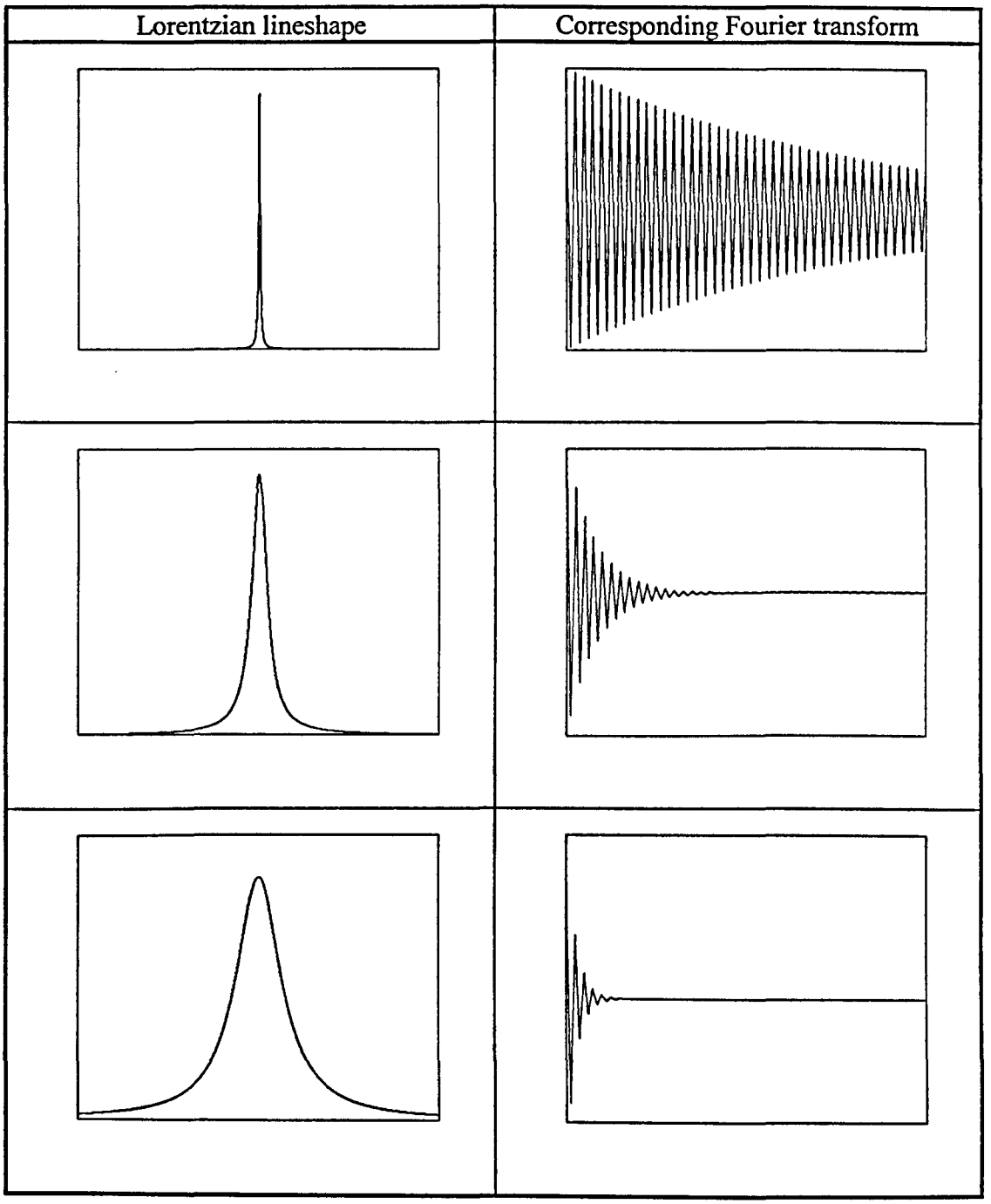

Figure 2.9 ***Some Lorentzian lineshapes and the corresponding Fourier transforms***

The aim of FSD is therefore to go from the bottom lineshape case, i.e. broad, to the top lineshape case, i.e. narrow. In practice this is limited by; the S/N of the spectrum, the instrumental resolution and the dynamic range of the digitisation and computational

processes. These result in a truncation of the useful range of the interferogram. For example if the instrumental resolution is $\Delta\bar{\nu}$, there is no information obtainable beyond $x = \frac{1}{\Delta\bar{\nu}}$. The factor by which we attempt to improve the spectral resolution is given the symbol κ. A rough estimation of the maximum practical value of κ is $\log_{10}(S/N)$. The major drawback of FSD is that some knowledge of the spectrum is required as an estimation of the band width of the components must be included in the initial data input. The final output is also highly dependent on the apodisation function used during the FSD procedure. The FSD process is shown pictorially in figure 2.10.

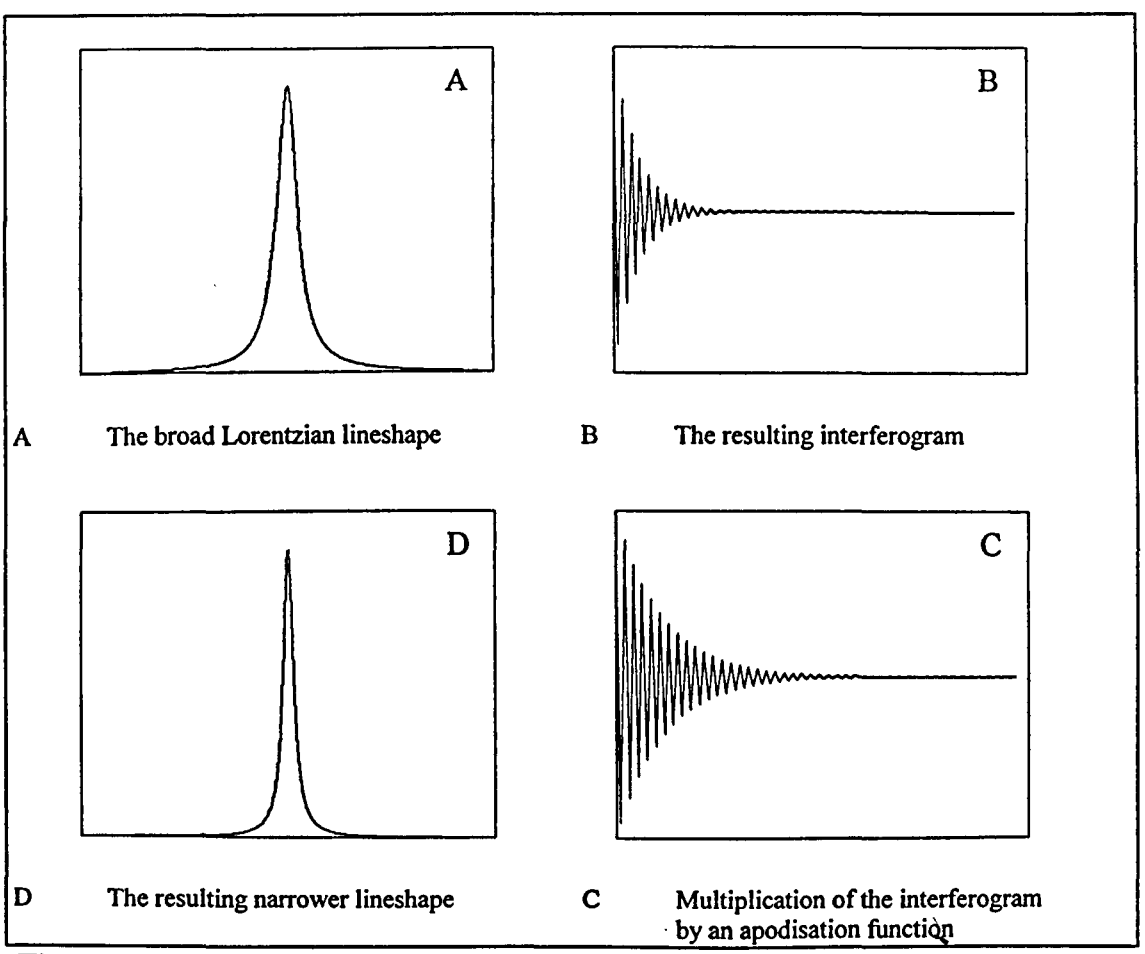

Figure 2.10. Schematic of the processes involved during Fourier self deconvolution.

2.7.2. Second derivative analysis.

Second derivative analysis (SDA) is the simplest band narrowing technique to apply as it requires no knowledge of the system and no assumptions of the numbers of bands or widths of bands within the spectrum. It is achieved simply by taking a second derivative of the spectrum and reduces the bandwidth by 20%.

The information obtained from a second derivative spectrum is the number of components, the band centres of the components and the relative intensities of components. The major draw back of SDA is that the output is often complicated by noise, as the mathematics treat 'noise' and 'real' features with the same importance.

How SDA reduces the linewidth is shown using an idealised Lorentzian function in figures 2.11a, b and c. It is important to note that the output 'peak' in SDA is actually a 'trough'.

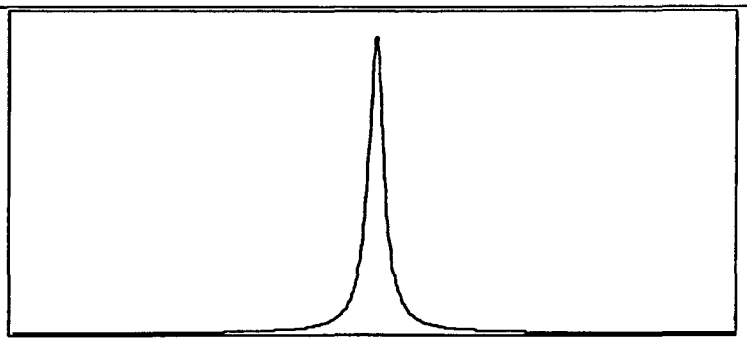

(A) Lorentzian lineshape

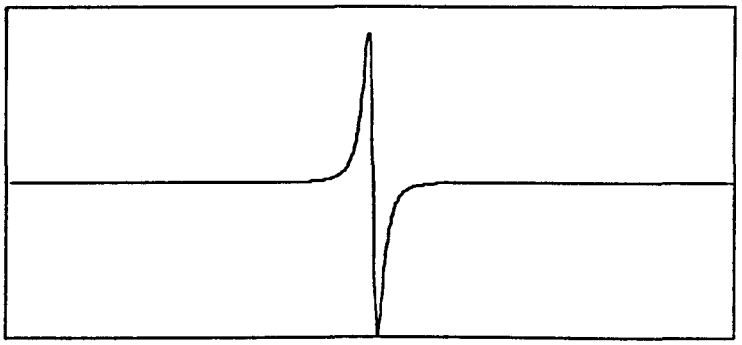

(B) First derivative of Lorentzian lineshape

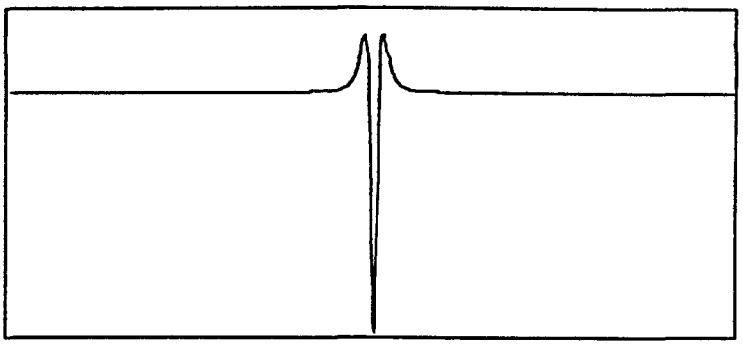

(C) Second derivative of Lorentzian lineshape

Figure 2.11 ***Schematic of the 'band narrowing' in the second derivative analysis process.***

2.7.3. Curve fitting routines.

Curve fitting or band fitting is the procedure of decomposing a spectrum into its constituent parts thus creating a synthetic spectrum that closely resembles the real

spectrum. The general procedure is to specify the number of bands, the lineshape of the bands, the position of the bands and the amplitude of the bands. Then one can use some kind of optimisation technique e.g. a least squares iterative approach or 'spectroscopists eye' to obtain the 'best fit'.

The decomposition can therefore be expressed as a function of a number of bands

$$S = \sum_{n=1}^{N} f_n(b_1, b_2 .... b_N) \qquad \text{(eq. 2.68)}$$

Where N is the number of overlapping bands

b contains the parameters for each band

And the 'fit' or cost function of a solution can be expressed as

$$E = \sum_{k=1}^{N_p} w_k \left(Ex_k - Ca_k\right)^2 \qquad \text{(eq. 2.69)}$$

Where N_p is the number of data points

Ex and Ca are the experimental and calculated values at point k

w_k is the statistical weight which is related to the standard deviation at point k

The usefulness of such a procedure is highly dependent on the accuracy of the initially assumed parameters such as the number of bands and their bandshapes, since there is generally no unique fit for a given spectrum. It is for this reason that band fitting is generally carried out in conjunction with SDA or FSD.

In infrared spectroscopy most bands should theoretically be Lorentzian in shape, but inorder to obtain a 'perfect fit' using Lorentzian bands, an infinite baseline would be required, which in practice is obviously impossible. Therefore it is safe to assume that the synthetic spectrum will never be a perfect fit to the real spectrum.

The fitting routines used for this work were carried out using a least squares iterative approach and full freedom of movement and amplitude change during optimisation was allowed.

The advantage of band fitting is the easy visualisation of the output. The main disadvantage is the reliance on estimated parameters such as lineshape function and number of bands. Hence it is only really useful quantitatively when used in conjunction with another technique.

2.8. References

2.1. 'Internal Reflection Spectroscopy', (Ed N.J. Harrick), Harrick Scientific Corporation, New York, (1987)

2.2. 'Internal Reflection Spectroscopy : Theory and Applications', Ed F.M. Mirabella, Marcel-Dekker, New York, (1993)

2.3. Y.Y. Sun, Z.Z. Shao, M.H. Ma, P. Hu, Y.S. Liu and T.Y Yu, *J. Appl. Polym. Sci.*, **65**, 5, 959, (1997)

2.4. J. Yang and H. Kim, *Polymer Composite*, **67**, 7, 486, (1997)

2.5. Y. Marachel and A. Chamel, *J. Phys. Chem.*, **100**, 8551, (1996)

2.6. Y. Marachel and A. Chamel, *Faraday discussions*, **103**, 349, (1996)

2.7. Y. Marachel, *J. Mol. Structure*, 322, **105**, (1994)

2.8. Y. Marachel, *J. Phys. Chem.*, **97**, 2846, (1993)

2.9. D.J. Walls, *Appl. Spec.*, **45**, 7, 1193, (1991)

2.10. D.J. Walls and J.C. Coburn, *J. Polym. Sci. Part B: Polym. Phys.*, **30**, 887, (1992)

2.11. R. Belali and J.M. Vigoureux, *Appl. Spec.*, **48**, 4, 465, (1994)

2.12. G. Boven, R.H.G. Brinkhuis, E.J. Vorenkamp, G. Challa and A.J. Schouten, *Polymer*, **33**, 6, 1150, (1992)

2.13. M.R. Pereira and J. Yarwood, *J. Polym. Sci. Part B: Polym. Phys.*, **32**, 1881, (1994)

2.14. N.I.E. Shewring, T.J.G. Jones, G. Maitland and J. Yarwood, *J. Colloid Int. Sci.*, **176**, 2, 308, (1995)

2.15. J. Billingham, C. Breen and J. Yarwood, *Vib. Spec.*, **14**, 1, 19, (1997)

2.16. Skourlis and R.L. McCullogh, *J. Appl. Polym. Sci.*, **52**, 9, 1241, (1994)

2.17. S.A. Francis and A.H. Ellison, *J. Opt. Soc. Am.*, **49**, 131, (1959)

2.18. R.G. Greenler, *J. Chem. Phys.*, **44**, 310, (1966)

2.19. Y.P. Song, M.C. Petty and J. Yarwood, *Vib. Spec.*, **1**, 305, (1991)

2.20. F.J. Boerio, J.P. Boerio and R.C. Bozian, *Appl. Surf. Sci.*, **31**, 42, (1988)

2.21. R.M. Crooks, C. Xu, L.Sun, S.L. Hill and A.J. Ricco, *Spectroscopy*, **8(7)**, 28, (1993)

2.22. D.L. Allara and J. Swalen, *J. Phys. Chem.*, **86**, 2700, (1982)

2.23. J.K. Kauppinen, D.J. Moffat, H.H. Mantsch and D.G. Cameron, *Appl. Spec.*, **35**, 3, (1981)

2.24. K. Rahmelow and W. Hübner, *Appl. Spec.*, **50**, 6, (1996)

2.25. A. Ferry and P. Jacobsson, *Appl. Spec.*, **49**, 3, (1995)

2.26. P. Spiby, M.A. O'Neill, R.A. Duckett and I.M. Ward, *Polymer*, **33**, 21, 4479, (1992)

2.27. I.J. Hitchinson, I.M. Ward, H.A. Willis and V. Zichy, *Polymer*, **21**, 55, (1980)

2.28. Yang, F. Long, D. Shen and R. Quian, *Polym. Comm.*, **32**, 4, 125, (1991)

Chapter 3

Raman Microscopy

3.1. Introduction to Raman spectroscopy

Although the Raman effect was predicted as early as 1923 by Smekal and experimentally observed 5 years later by Raman [3.1], it was only the development of cheap modern visible lasers 4 decades later, that Raman spectroscopy became really established as a viable research tool. It is still regarded primarily as a research tool, but as innovation and technology continue to improve sources, optics and detectors, the technique is becoming more common in industrial applications. The theory of Raman spectroscopy is covered in many texts [3.2-3.4] so only brief summary will be presented here.

3.2. The Raman effect.

The Raman effect is most simply described as the inelastic scattering of light by matter. When light is scattered by a molecule there can be one of three outcomes:

1. Elastic (Rayleigh) scattering where there is no net energy loss or gain to the incident light beam.
2. The light is scattered to lower energy and frequency (Stokes scattering).
3. The light is scattered to higher energy and frequency (anti-Stokes scattering).

The theory of Raman scattering can be described by using a mixture of quantum mechanical and classical theory

3.2.1. Classical theory.

The classical theory of the Raman effect introduces the concept of the polarisability of a molecule. When a molecule is placed in a static electric field (E), an electric dipole (μ') is induced. The size of the induced dipole is dependent on the magnitude of the field and the ease with which distortion can occur, or polarisability of the molecule (α).

$$\mu' = \alpha E \qquad \text{(eq. 3.1.)}$$

If the applied field is modulating then the induced dipole will vibrate at the same frequency. The electric field can be written as

$$E = E_0 \sin 2\pi t \nu_0 \qquad \text{(eq. 3.2.)}$$

And the induced dipole

$$\mu = \alpha E = \alpha E_0 \sin 2\pi t \nu_0 \qquad \text{(eq. 3.3.)}$$

Where E_0 is the field at equilibrium

ν_0 is the angular frequency of radiation

t is time

This oscillating dipole emits radiation at the same frequency, which accounts for the Rayleigh scattered light. If in addition there is also some internal motion, for example a

vibration of frequency ν_v, then the oscillating dipole will have superimposed on it a vibrational oscillation (q_v) which changes the polarisability.

$$q_v = q_0 \sin 2\pi\nu_v t \qquad \text{(eq. 3.4.)}$$

Hence

$$\alpha = \alpha_0 + \left(\frac{\partial\alpha}{\partial q_v}\right)_0 q_v \qquad \text{(eq. 3.5.)}$$

Substituting eq. 3.4. into 3.5. one obtains

$$\alpha = \alpha_0 + \left(\frac{\partial\alpha}{\partial q_v}\right)_0 q_0 \sin 2\pi\nu_v t \qquad \text{(eq. 3.6.)}$$

If the radiation of frequency ν_0 interacts with the molecule then the induced dipole is given as

$$\begin{aligned} \mu' &= \alpha_0 E_0 \sin 2\pi\nu_0 t + \left(\frac{\partial\alpha}{\partial q_v}\right)_0 E_0 q_0 \sin 2\pi\nu_v t \sin 2\pi\nu_0 t \\ \mu' &= \alpha_0 E_0 \sin 2\pi\nu_0 t + \left(\frac{\partial\alpha}{\partial q_v}\right)_0 \frac{E_0 q_0}{2}\left[\sin 2\pi(\nu_0 + \nu_v)t + \sin 2\pi(\nu_0 - \nu_v)t\right] \end{aligned} \qquad \text{(eq. 3.7.)}$$

This shows that for Raman scattering to occur the polarisability must change during the vibration i.e.

$$\left(\frac{\partial\alpha}{\partial q_v}\right)_0 \neq 0 \qquad \text{(eq. 3.8.)}$$

3.2.2. Quantum mechanical theory.

The quantum mechanical approach recognises that light energy is quantised. Photons of light of frequency ν can be scattered by molecules elastically or inelastically. Figure 3.1 shows the energy changes occurring during interactions with a monochromatic light source (v represents the vibrational energy quantum number).

From figure 3.1 it is clear that Stokes lines will be more intense than the anti-Stokes line because Stokes lines arise from a transition from the ground state to a higher energy level. Anti-Stokes lines, on the other hand arise from transitions from a higher vibrational level to a lower energy level. The ground state vibrational level is generally the most populated at ambient temperature. Hence there is a greater probability of Stokes lines occurring. When a beam of monochromatic radiation impinges on a sample around 99.9% of the scattered light will be Rayleigh and only 0.1% will be Raman light. The proportions of the Stokes and anti-Stokes scattering are dependent on the vibrational energy population distribution before irradiation (and therefore temperature).

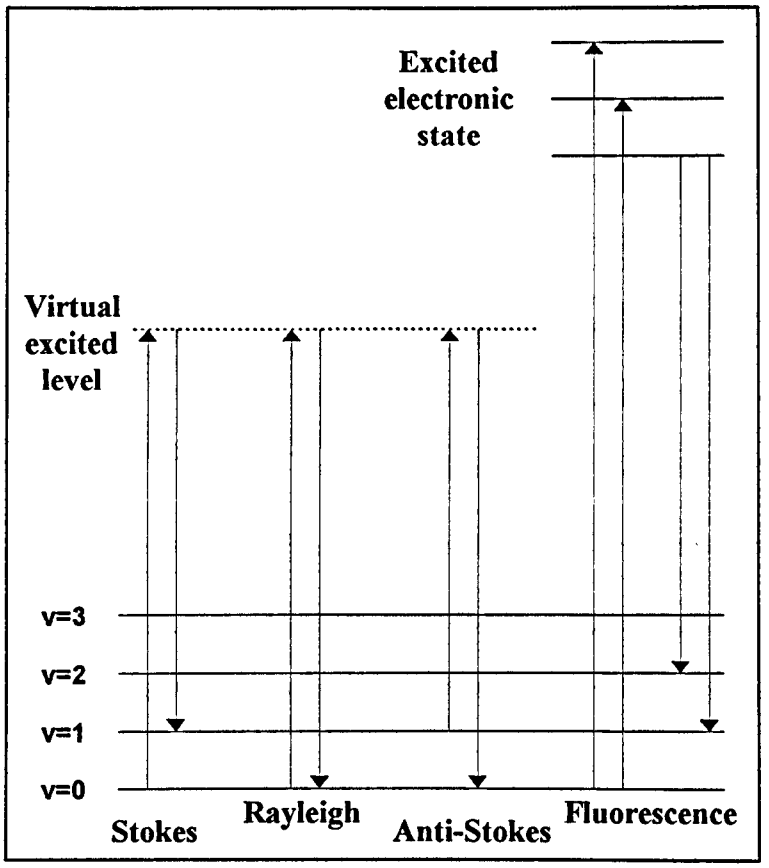

Figure 3.1. A schematic of Rayleigh and Raman scattering from a quantum mechanical approach.

Figure 3.2. shows the Stokes and anti-Stokes lines of a silicon wafer. Note that the majority of the Rayleigh scattered light is filtered out by the system.

It is clear that the Raman effect is relatively weak, so sensitive and carefully constructed apparatus is necessary for successful use practically.

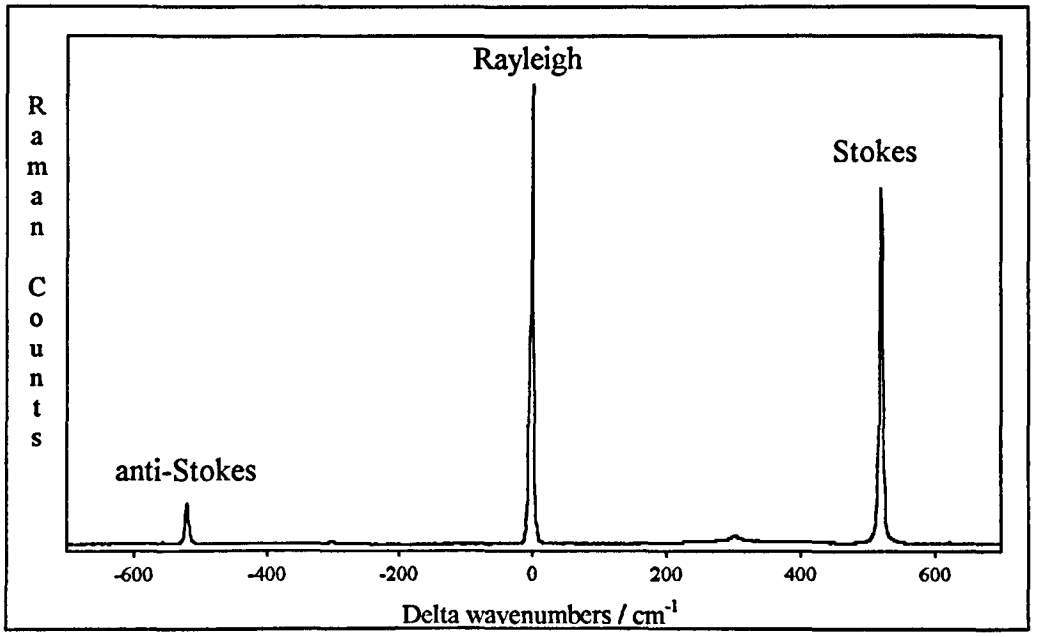

Figure 3.2 The Raman spectrum of silicon showing the relative intensities of the Stokes and anti-Stokes bands.

3.3. Raman Microscopy

There are numerous instrumental set-ups for the collection of Raman spectra such as dispersive spectrometers, FT spectrometers and microscopes. The work for this project was carried out using a Raman microscope in the confocal mode and it is for this reason that only the instrumentation for Raman microscopy will be discussed.

A simplified schematic of the Renishaw microprobe is shown in figure 3.3, the workings of each of the relevant components will be discussed elsewhere in this chapter. It is important to note that the purpose of the holographic notch filter is to remove the unwanted Rayleigh scattering which would otherwise dominate the spectrum.

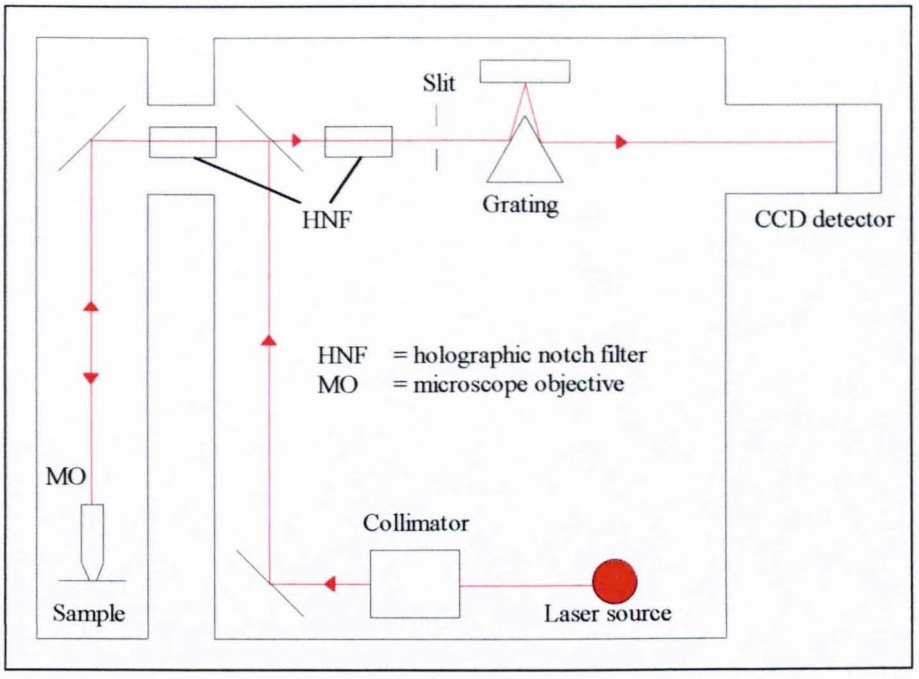

Figure 3.3. A simplified schematic of the Renishaw Microprobe.

Hirschfeld outlined the basic requirements for a successful micro Raman set-up [**3.5**] and his ideas were acted upon by other workers [**3.6-3.10**] who set about building the first Raman microprobe prototypes.

The basic optical system employs the so-called back scattering configuration, where the laser beam is focused on a particular spot using a microscope objective and the Raman scattered light is collected by the same objective. This is shown in figure 3.3.

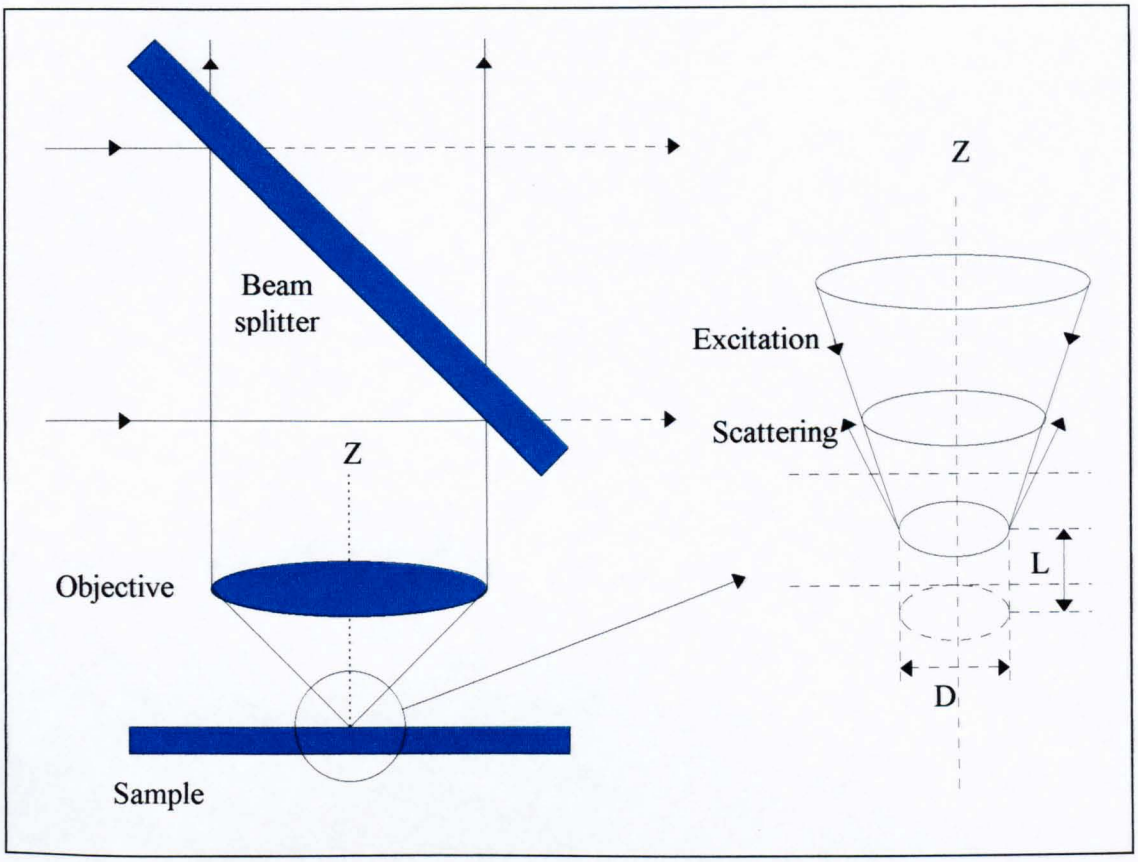

Figure 3.4 The backscattering geometry of a Raman microscope.

Figure 3.4. shows the exciting laser beam being focused on the sample by a lens. The laser light is concentrated in a 'focal cylinder' the diameter of which is, in theory, determined by the diffraction limit. This considerably increases the intensity of the Raman scattering but can also damage the sample (see section 3.5.3.). The volume of the focal cylinder is dependent on two parameters; L, the depth of focus within the medium (or waist) and D, the diameter of this waist. The wavelength of laser excitation will determine D, but the parameter L can be controlled by changing the numerical aperture. This is an important consideration when using the microscope in the confocal mode.

3.4. Confocal Raman microscopy

In the 1950's, as a post doctoral fellow, Minskey built a revolutionary light microscope that could view successively deeper layers in a transparent sample [**3.11**]. The design remained unmanufactured until the 80's where it was applied to different types of microscopy, including Raman microscopy. This approach is known as confocal microscopy.

The confocal set-up of a Raman microscope can serve two useful purposes. Firstly it can be used to depth profile, i.e. obtain Raman spectra of sections of a sample of the same depth. It can also be used to minimise stray light and background fluorescence coming from outside the focal volume. The technique does have some disadvantages which will be discussed in section 3.5.

3.4.1. Theory.

For many years Raman microscopy with a spatial resolution of the order of 1 μm in the x or y direction has been used to obtain vibrational information about small particles or small areas within bigger samples. In confocal microscopy it is also necessary to obtain 'tight' spatial resolution in the z direction or optical axis. The signal intensity that reaches the detector for a given Raman line at the wavelength, λ, is

$$signal \approx I_0 \sigma \lambda N \theta T_\lambda s_\lambda \qquad \text{(eq. 3.9.)}$$

Where I_0 is the laser irradience (watts / unit area)

σ_λ is differential cross-section for the analysed Raman line (cm^2 $sterad^{-1}$ $molecule^{-1}$)

N is the number of molecules in the probed volume

θ is the angle of collection of Raman light

T_λ is the throughput of the instrument at the given wavelength

s_λ is the sensitivity of the detector at the given wavelength

A direct consequence of the confocal approach is an inherently small volume (V) hence a small N. To compensate for this only the parameters I_0 and θ can be modified. Conveniently one can optimise both the laser irradience and angle of Raman collection by using microscope objectives and geometry. The numerical aperture (NA) of an objective will determine the distribution of the laser field around the focus and is given by

$$NA = n\sin\left(\frac{\theta}{2}\right) \qquad \text{(eq. 3.10.)}$$

Where θ is the angle of entrance.

n is the refractive index of the transmitting medium

Note NA can have maximum value of 1 in air. Microscope objectives with a high NA are therefore able to focus the laser beam into a small volume and collect the Raman scattered light from a wide angle. The focal length of the working objective will determine the waist. Figure 3.5. shows the distribution of laser light around the focus with both a high and low NA.

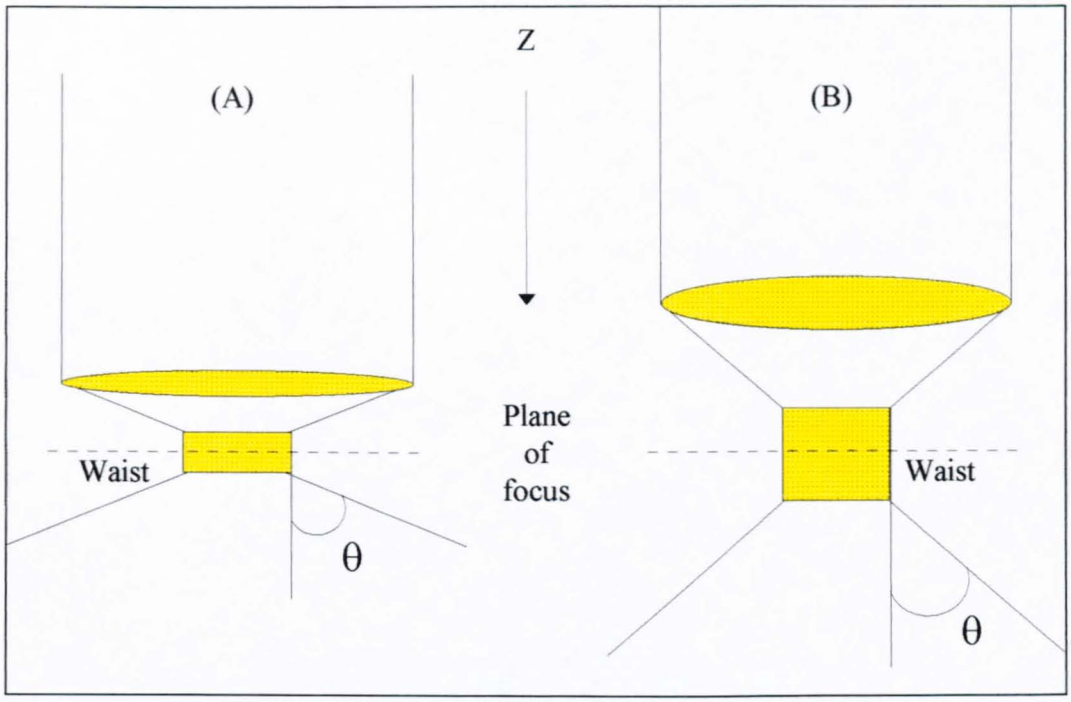

Figure 3.5. The distribution of laser light around the focus with (A) high NA and (B) low NA, note the high NA leads to smaller depth of focus.

As the work for this project has required the depth of resolution to be as good as possible only a high NA has been used. For comparative purposes table 3.1 shows the calculated relationship of NA with θ and L.

Objective	NA	θ / °	L / μm
100 X	0.95	71.8	0.1
50 X	0.80	53.13	0.4
10 X	0.30	17.46	6.4

Table 3.1 The relationship between NA, θ and L

The inclusion of a pinhole or slits in the back focal plane of a microscope greatly enhances the depth resolution. It works by blocking the light from planes higher or lower than the focal plane. This is clearly illustrated in figure 3.6.

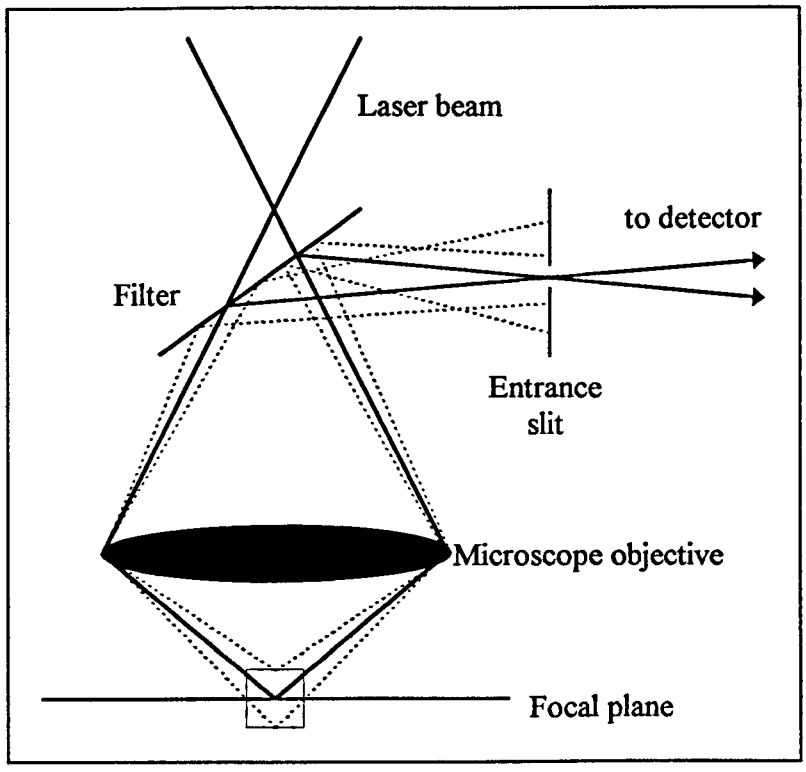

Figure 3.6. ***Schematic to show how confocal Raman microscopy works. The solid line shows the path of light in the focal plane. The dotted lines show paths of light outside the focal plane. The Renishaw Ramascope uses slits rather than a pinhole as this improves the ease of alignment.***

Numerous systems are reported **[3.12, 3.13]** where pinholes with dimensions of 100 and 300 μm are used to block unwanted light. The pinhole is aligned using micrometer adjustments both in and along the optical axis but the alignment is generally regarded as being painstakingly difficult. It was for this reason that Williams and co-workers **[3.14]** developed a CCD detector with a stigmatic Raman spectrograph. In this system a spectrometer slit of around 15 μm provides the primary aperture and controls the 'height' of the incoming light beam, whilst specifying which pixels to use on the CCD camera controls the 'width' of the incoming light effecting a 'pinhole'.

The role that the 'pinhole' plays can be explained geometrically if one assumes that the diffraction effects at the pinhole can be ignored. This assumption has been shown to be valid [3.15] for pinholes of over 100 μm, which is the case for this work. Other assumptions are that the influence of refraction, scattering and absorption at the sample surface are minimal. A schematic of the optical arrangement of a microscope coupled to a Raman spectrograph is shown in figure 3.7.

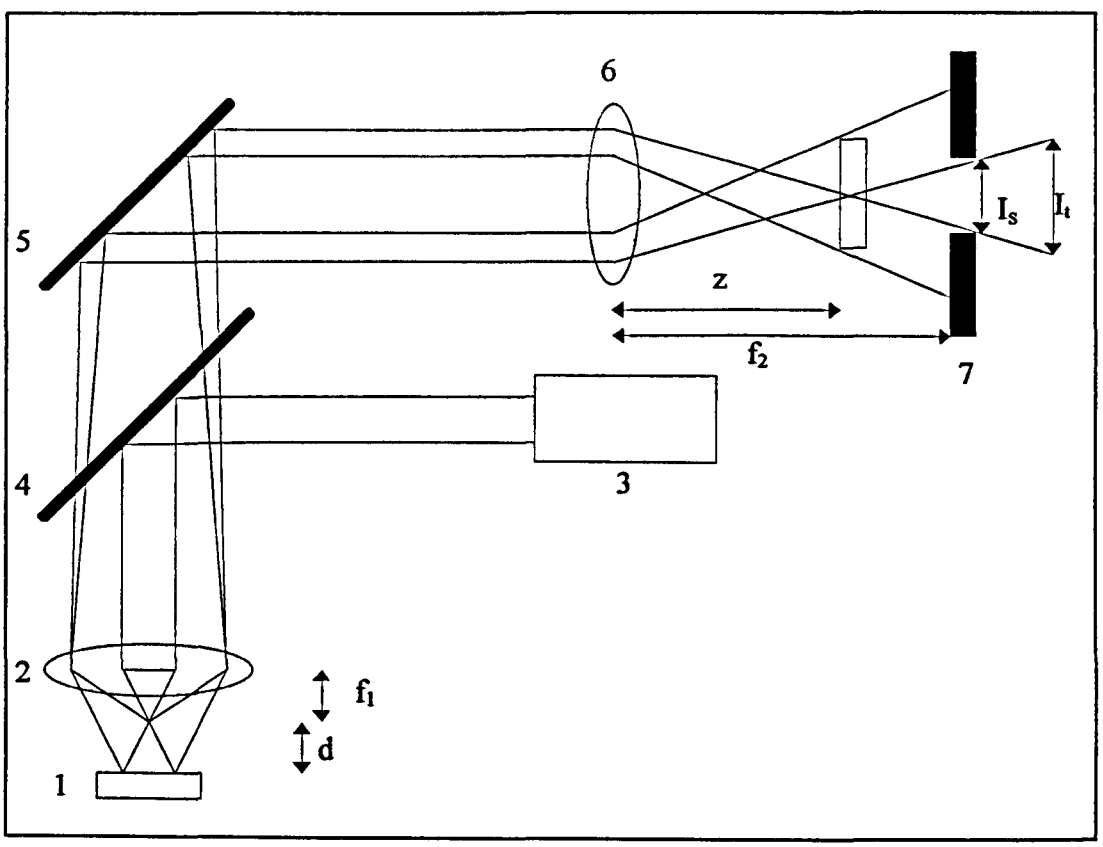

Figure 3.7. ***The schematic set-up of a Raman microscope in the confocal mode. (1) Sample plane, (2) objective lens, (3) laser source, (4) beam splitter, (5) mirror, (6) slit focusing lens, (7) pinhole.***

For this discussion the two lenses, the objective lens and the slit focusing lens, are called L_1 and L_2 respectively.

The laser beam has its smallest diameter in the focal plane of the objective lens and this diameter remains essentially constant within a certain distance from the focal plane **[3.16]**. This distance is known as the depth of focus or the waist and is given the symbol L. L can be calculated from **[3.17]**

$$L = 6.4\left(\frac{\lambda}{2\pi}\right)\left(\frac{1}{\tan\theta}\right)^2 \qquad \text{(eq. 3.12)}$$

or approximated from

$$L \approx \lambda\left(\frac{1}{\tan\theta}\right)^2 \qquad \text{(eq. 3.13)}$$

Where θ is the entrance half angle

λ is the wavelength of the exciting laser light

The size of the laser spot can be expressed by

$$s(f_1 \pm d) = s(f_1) \qquad \text{for} \quad d < \frac{L}{2} \qquad \text{(eq. 3.14)}$$

$$s(f_1 \pm d) = s(f_1) + 2\left(d - \frac{L}{2}\right)\tan\theta \qquad \text{for} \quad d > \frac{L}{2} \qquad \text{(eq. 3.15)}$$

Where f_1 is the focal length of the objective lens

d is the distance from the plane of focus

In a confocal arrangement a pinhole or slit is positioned at the back image of the microscope and an out of focused laser spot with size s(f_1±d) will be imaged outside the back focal plane at a distance Z_2 from the slit focusing lens. This is shown clearly in figure 3.6. Therefore one can write

$$Z_2 = \left[\frac{1}{f_2} - \frac{1}{f_2 - \left(\frac{1}{f_1} - \frac{1}{f_1 \pm d}\right)^{-1}}\right]^{-1} \qquad \text{(eq. 3.16)}$$

Where f_2 is the focal length of the slit focusing lens

This image which is bigger than the laser spot image is projected on the back plane of the microscope. The diameter of the out of plane projection, I_t, can be calculated from

$$I_t = \frac{f_2 M\{s(f_1 \pm d)\}}{Z_2} \qquad \text{(eq. 3.17)}$$

Where M is the magnification power of the objective.

As the out of focus projection is bigger than the in focus projection, it is possible to block out the light coming from the out of focus regions by placing a pin hole with a diameter less than I_t in front of the detector. The result of a high NA is that one produces a divergent beam outside the focal plane making it easier to discriminate unwanted light.

The intensity distribution as a function of distance away from the object focal plane can be compared in conventional and confocal Raman microscopy (figure 3.8). This has important implications for the work carried out in this project the consequences of which shall be discussed in section 3.6.

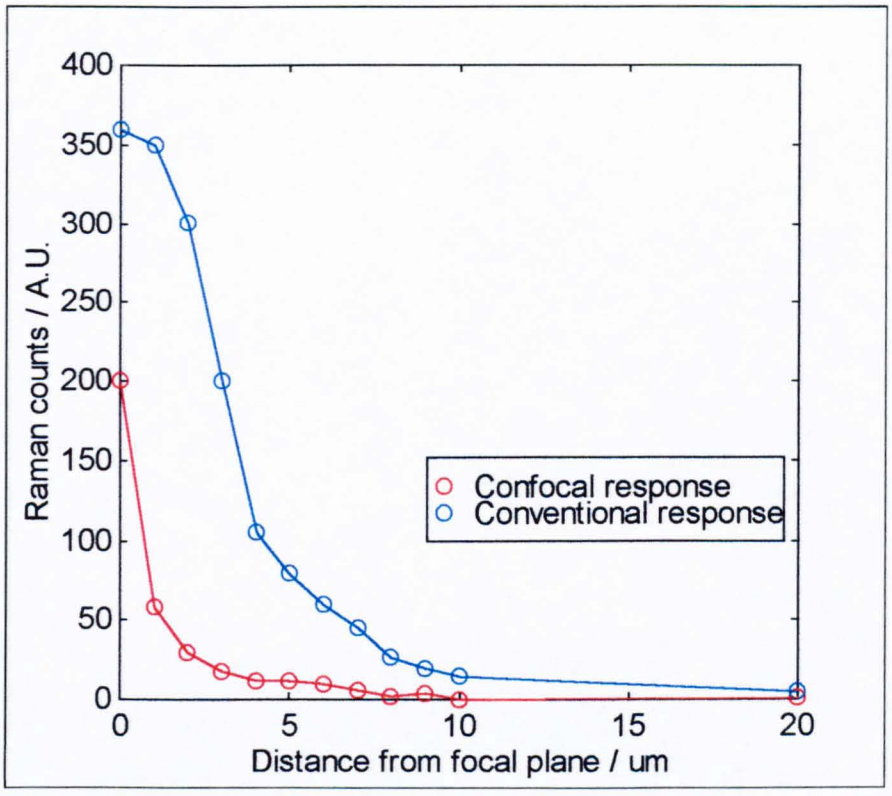

Figure 3.8. ***Comparison of confocal Raman and non-confocal Raman microscopy response as a function of distance from the focal plane.***

It is experimentally quite simple to show the effect that microscope objectives of differing magnification have on the confocal response. The test is to focus the laser spot on the surface of a silicon wafer. The objective is then moved at 1 μm intervals away from the wafer and a spectrum is taken at each interval. The Raman response is then plotted as a function of distance away from the wafer. This is known as the confocal response and by using the FWHH criterion, the depth resolution for each objective can be calculated.

The confocal response for different microscope objectives is shown in figure 3.9. As figure 3.9 clearly shows as the NA decreases (longer working objective) the depth resolution decreases. When looking at the interface between two polymers it is desirable

to have as good a depth resolution as possible, it is for this reason that the 100x objective has been used for all the work discussed in this thesis.

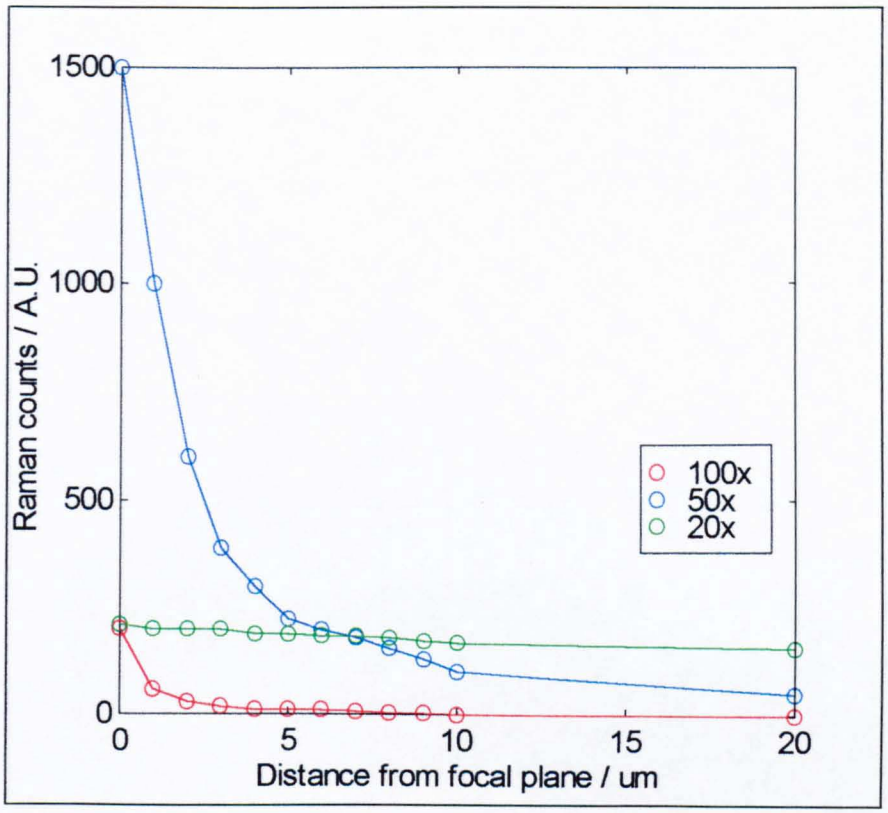

Figure 3.9. ***The effect of the microscope objective on the confocal response as a function of distance from the focal plane.***

3.5. Problems associated with Raman spectroscopy

3.5.1. Sensitivity

The Raman effect is intrinsically a weak effect, 99.9% of the scattered light being Rayleigh light. It follows that as we are looking at a low signals any noise that is introduced to the system will have a marked effect on the system performance. The Renishaw system uses holographic notch filters to remove the unwanted Rayleigh light, but these also remove some of the Raman scattered light. Each filter removes around 5% of the Raman scattered light and 99% of the Rayleigh scattered light. It is only the development of powerful sources and sensitive detection systems that allows Raman spectroscopy to be employed successfully.

3.5.2. Fluorescence

Sample fluorescence is arguably the Raman spectroscopists' biggest problem. Many samples have a Raman spectrum that is superimposed on a fluorescence background. The exact source of such a problem is not fully understood and trace amounts of 'luminescing' sample impurities has been suggested **[3.18]**. Figure 3.1 shows the energy transitions that are involved during fluorescence Note that the fluorescently scattered light also undergoes a Stokes shift.

There is no complete cure for this problem but there are several preventative measures that one can take to reduce the levels of fluorescence.

1. Apply Raman microscopy. This is thought to 'burn out' the impurities by the relatively high power density of the laser light. This itself leads to problems that will be discussed in 3.5.3.
2. Chose a different frequency of laser excitation. Workers have used different lasers such as UV lasers which are further away from the excitation frequencies of most fluorophores, but this causes problems with alignment (the beam is invisible to the naked eye) and sample burning **[3.19]**.
3. Use a phase sensitive detection technique **[3.20]**. This utilises the fact that Raman scattering is an instantaneous phenomenon and therefore occurs at a much faster rate than fluorescence which has a time scale of the order of nanoseconds for transitions to occur.
4. Use FT-Raman which uses lasers in the near-IR region. High power lasers (up to 50 W) can be used as the near-infrared radiation does not cause photodecomposition. The detectors used to detect near-IR radiation are not as sensitive as CCD detectors used in dispersive systems, but the Fellget advantage does apply.

3.5.3. Sample heating.

One of the advantages of Raman microscopy, i.e. the focusing of the laser light in a specific position also can create problems by damaging the sample. By focusing the beam to a very small area the laser power density in that area of the sample is relatively high. In polymers, high laser powers may cause heating to such an extent that this may change the morphology and structure of the polymeric chains in the sampling region. Damage to carbon fibres has been reported **[3.21-3.23]** but it is fair to note that carbon

fibres contain many absorbing species that will not dissipate the heat. The distribution of the generated heat will be greatly influenced by the thermal conductivity of the sample [3.24]. A non-uniform distribution of energy density or opaque inclusions within a sample may well cause localised absorption. This problem can be exacerbated using a laser at 514.5 nm where photochemical effects have degraded amino acid samples [3.19] in the presence of oxygen and a sensitiser.

3.6. Deconvolution of Raman profiles

The work undertaken during this project involving confocal Raman microscopy was to probe the interface of a coextruded polymer laminate. The rationale was to focus the laser beam on the top surface and in 1μm steps go down through the laminate taking Raman spectra at each interval. The interface of the two polymers could then be determined by looking at changes in the Raman spectra with depth. Figure 3.8 shows that although the majority of the Raman signal in the confocal set-up comes from a region of approximately 2 μm around the focal plane there is still a considerable contribution from the surrounding region. Therefore the depth profile that would be obtained in this experiment can be thought of as a convolution of the depth profile with the confocal profile. It is with this in mind that it was decided that, to obtain the 'real' depth profile, a deconvolution process was necessary. This was achieved using the following simplified scheme.

1. Obtain models for the shape of the confocal profile and the step profile.
2. Take the Fourier transform of the models obtained

3. Divide the Fourier transform of the depth profile with the Fourier transform of the confocal response.
4. Take the inverse Fourier transform of the result.

This is based on the fact that

$$FT(A * B) = FT(A) \times FT(B) \qquad \text{(eq. 3.18)}$$

Where FT is the Fourier transform procedure

* is the convolution process

$f(con)$ is the model of the confocal response

$f(depth)$ is the model of the depth profile

$FTD = FT\{f(depth)\}$

(Where FT is the Fourier transform operation)

$FTC = FT\{f(con)\}$

$$FTR = \frac{FTD}{FTC}$$

$f(result) = FT^{-1}\{FTR\}$

$f(result)$ is the deconvoluted depth profile.

3.7. The applications of Raman microscopy

Raman microscopy is now being widely used in many areas of science. It is now used extensively in the semiconductors industry [3.25-3.27], being versatile in its ability to characterise the microstructure of small devices.

Vibrational spectroscopy is extremely useful in giving information about orientation and as the diffraction limit of Raman microscopy is much lower than that of infrared microscopy it is no surprise that small inclusions in bulk materials are often studied by this technique [3.28-3.30].

Materials that are readily characterised using Raman microscopy include carbon composites [3.31], defects in glass [3.32], diamond like films [3.33, 3.34] and bubbles in fibres in the fibre optics industry [3.35].

Confocal Raman microscopy has also been used to depth profile a number of polymer systems including PVOH / PMMA laminates [3.36, 3.37] and PVC / silane systems [3.38], which gave complementary information to an ATR diffusion experiment on the same system.

3.8. References

3.1. D.J. Gardiner in, 'Practical Raman Spectroscopy', (Eds D.J. Gardiner and P.R. Graves), Springer-Verlag, Berlin, (1989)

3.2. 'Laser Raman spectroscopy', (Eds T.R. Gilson and P.J. Hendra), Wiley-Interscience, London, (1972)

3.3. 'The Raman Effect', (Ed G.W. Chantry), Marcel-Dekker, New York, (1971)

3.4. 'Raman Spectroscopy', (Ed D.A. Long), McGraw-Hill, U.K., (1977)

3.5. T.Hirschfeld, *J. Opt. Soc. Am.*, **63**, 476, (1973)

3.6. G.J. Rosasco, E.S. Etz and W.A. Cassatt, *IVth International Conference On Raman Spectroscopy*, Brunswick, Maine, (1974)

3.7. G.J. Rosasco, E.S. Etz and W.A. Cassatt, *Appl. Spec.*, **29**, 396, (1975)

3.8. M. Delhaye and P. Dhamelincourt, *IVth International Conference On Raman Spectroscopy*, Brunswick, Maine, (1974)

3.9. M. Delhaye and P. Dhamelincourt, *J. Raman Spec.*, **3**, 33, (1975)

3.10. G.J. Rosasco and E.S. Etz, *Res. Dev.*, **28**, 20, (1977)

3.11. J.W. Lichtman, *Scientific Am.*, **Aug.**, 30, (1994)

3.12. A. Garton, D.N. Batchelder and C.W. Cheng, *Appl. Spec.*, **47**, 922, (1993)

3.13. R. Tabaksblat, R.J. Meier and B.J. Kip, *Appl. Spec.*, **46**, 60, (1992)

3.14. K.P.J. Williams, G.D. Pitt, D.N. Batchelder and B.J. Kip, *Appl. Spec.*, **48**, 2, 232, (1994)

3.15. P. Dhamelincourt, J. Barbillat and M. Delhaye, *Spec. Eur.*, **5**, 16, (1993)

3.16. A. Boivin and E. Wolf, *Phys. Rev.*, **138**, 1561, (1965)

3.17. 'Principles Of Optics', (Eds M. Born and E. Wolf), Pergamon Press, Oxford, (1980)

3.18. J.P. Meier and B.J. Kip, *Microbeam Analysis*, **3**, 61, (1994)

3.19. C.S. Foote in, 'Free Radicals In Biology', (Ed W.A. Pryor), Academic Press, New York (1976)

3.20. A.Z. Genack, *Anal. Chem.*, **56**, 2957, (1984)

3.21. I.M. Robinson, M. Zakikhani, R.J. May and R.J. Young, *J. Mat.Sci.*, **6**, 1212, (1987)

3.22. H. Sakata, G. Dresselhaus, M.S. Dresselhaus and M. Endo, *J. Appl. Phys.*, **63**, 2769, (1988)

3.23. J.W. Ager, K.D. Veirs, J. Shamir and G.M. Rosenblatt, *J. Appl. Phys.*, **68**, 3598, (1990)

3.24. G.J. Rosasco in, 'Advances In Infrared And Raman Spectroscopy', (Eds R. Clark and R.E. Hester), Heyden and Son, London, (1980)

3.25. S. Nakashima, NATO ASI Ser., Ser. B, **273**, 291, (1991)

3.26. G. Abstrelter, *Appl. Surf. Sci.*, **50**, 73, (1991)

3.27. W.C. Tang and H.J. Rosen, *Microbeam Analysis*, **26**, 101, (1991)

3.28. H. Boyer and D.C. Smith, *Microbeam Analysis*, **26**, 33, (1984)

3.29. F.J. Purcell and W.B. White, *Microbeam Analysis*, **26**, 107, (1983)

3.30. T. Jawhari, J.C. Merino, J.C. Rodiguez-Cabello and M. Pastor, *Polymer*, **33**, 4199, (1992)

3.31. L.S. Grigoryan, H.D. Birt, S. Sathaiah, S.V. Sharma, H. Clara and A.K. Majumdar, *J. Raman. Spec.*, **23**, 127, (1992)

3.32. H. Boyer, *Microbeam Analysis*, 265, (1983)

3.33. D.N. Batchelder, C. Cheng and G.D. Pitt, *Adv. Mat.*, **3**, 566, (1991)

3.34. I.P. Hayward, K.J. Baldwin, D.M. Hunter, D.N. Batchelder and G.D. Pitt, *Diamond and Related Materials*, 4, 617, (1995)

3.35. M. Bowden, N.M. Dixon, D.J. Bardiner and S.F. Carter, *J. Mat. Sci. Mat. in Elect.*, 34, (1990)

3.36. S. Hajatdoost and J. Yarwood, *Appl. Spec.*, **50**, 5, 558, (1996)

3.37. S. Hajatdoost, M. Olsthoorn and J. Yarwood

3.38. P. Eaton, *Polymer Surfaces and Interfaces III*, Abst., Durham, (1997)

Chapter 4

The Diffusion of small molecules into polymeric membranes

4.1. Introduction.

Diffusion is the process by which matter is transported as a result of random motion from one part of a system to another. The direction of movement of a single molecule cannot be predicted, but it is possible to predict the mean-square distance travelled in a given time interval. Generally, molecules transfer from regions of higher to those of lower concentrations.

The diffusion of small molecules through polymeric membranes is an important phenomenon in many different areas of science. For example, the use of polymeric membranes as selective filters, may change the way we look at water purification in the future and will almost certainly play a major role within developing countries as a source of cheap, drinkable water. The diffusion rate of gases through food packaging has important implications with regards to the shelf-life of foodstuffs [**4.1**]. Diffusion rates of water and oxygen into plastics can drastically affect their working lifetime [**4.2, 4.3**].

Diffusion or molecular transport is a function of both the diffusant and the polymer. The chemical structure and the long range molecular order (morphology) of the polymer are important parameters. Other factors such as temperature, reactivity, solubility and orientation also play an important role in the transport process [**4.4, 4.5**].

4.2. Modes of diffusion.

Numerous authors, most notably Crank [4.4, 4.6] and Comyn [4.5] have discussed the modes of diffusion and the mathematical models one can use to characterise them in great detail. It is beyond the scope of this work to go into the background of diffusion too deeply. Therefore only a brief summary of the ideas and equations relevant to this work will be given.

Diffusion in isotropic substances is found to obey Ficks first law [4.7], which is an empirical relationship stating that the rate of transfer of a diffusing substance through a unit area is proportional to the concentration gradient measured normal to the unit area. Ficks first law states that the flux in the x-direction (F_x) is proportional to the concentration gradient ($\delta c/\delta x$). Therefore Ficks first law can be given as;

$$F_x = D\left(\frac{\partial C}{\partial x}\right) \qquad \text{(eq. 4.1.)}$$

Where D is the diffusion coefficient

Ficks first law can only be directly applied to diffusion in the steady state. For non-steady state conditions the rate of the change of penetrant concentration at any given point is given by Ficks second law, which, when diffusion occurs in the z-direction can be given as;

$$\frac{\partial C}{\partial t} = D\left(\frac{\partial^2 C}{\partial z^2}\right) \qquad \text{(eq. 4.2.)}$$

Where D is the diffusion coefficient

C is the concentration of the diffusing material

t is time

z is the space co-ordinate normal to the polymer surface

Equation 4.2. can be readily solved given the appropriate boundary conditions for a particular experiment.

In polymers, the mechanical relaxation time decreases with increasing temperature and the ease of polymer motion is enhanced. As molecules diffuse into a polymeric matrix a broad range of mechanical relaxations associated with structural changes may occur. The mass of molecules diffused at a time, t, in a plane sheet of thickness L, can be given by

$$\frac{M_t}{M_\infty} = \frac{4}{L}\left(\frac{Dt}{\pi}\right)^n \qquad \text{(eq. 4.3.)}$$

Where M_t is the sorbed mass at time t

M_∞ is the mass sorbed at equilibrium.

L is the film thickness.

Experimental diffusion in polymeric materials can be categorised as follows [4.8].

Case I - This occurs when the rate of diffusion is less than the mechanical relaxation time of the polymer. This type of diffusion is slow and constant and is also known as Fickian diffusion and is based on a 'random walk' without interactions. In this instance equation 4.3. would have n = 0.5 and a single parameter is sufficient to describe the diffusion.

Case II - In this case diffusion is very fast compared to the mechanical relaxation time of the polymer. This diffusion is often associated with a sharp penetrant front which propagates into the polymer at a constant velocity and is based on strong interactions and a moving interface. Again a single parameter is sufficient to describe the system and equation 4.3. would have n = 1.

Case III - This is non-Fickian diffusion that occurs when the relaxation process and diffusion rates are similar. Case III diffusion accounts for all diffusion which cannot be modelled by case I or case II. In this instance one or more parameters are needed to describe the behaviour and the n in equation 4.3 can be between 0.5 and 1 or change sigmoidally as a function of time between the two.

There are a number of different techniques used to follow diffusion processes including gravimetric methods **[4.9-4.11]**, following radioactive tracer labels **[4.12]**, mass labels utilising Rutherford backscattering (RBS) **[4.13]**, electrochemical impedance spectroscopy **[4.3, 4.11]**, chemical labelling **[4.14, 4.15]**, Raman microprobing sections of polymer **[4.16]**, following thickness changes using laser interferometry **[4.17]**, NMR **[4.17]**, UV absorption **[4.18]**, FTIR **[4.19-4.21]** and FTIR-ATR **[4.1, 4.22-4.39]**.

FTIR-ATR is an elegant tool for the *in-situ* measurement of small molecule diffusion into polymeric membranes as it allows both kinetic and structural data to be obtained simultaneously.

The evanescent field has been used to follow the classical Fickian penetration of decanol into a number of polybutadienes by Schlotter and Furlan **[4.32]** varying the branch

content to control the amorphous and crystalline ratio. A numerical method to obtain the diffusion coefficient of absorbing species has been proposed by Balik and Xu [4.33] using FTIR-ATR. It involves the measurement of the intensity of the infrared bands associated with the diffusants as a function of time.

Work has been carried out using FTIR-ATR to measure the amount of water '*in-situ*' at the coating / metal interface [4.36]. It was found that water bands increased and coating bands decreased at short exposure times but both levelled off as the exposure times increased.

Ion exchange into Langmuir-Blodgett films has also been studied using the ATR technique [4.37]. This work looks at the change in microstructure of the films after the addition of water and dilute solutions. The bulk and surface composition of foulants on polysulphone ultrafiltration membranes has been analysed [4.38] and the diffusion of glucose into a PVA membrane has been used to model the determination of carbohydrates in polymer matrices [4.39].

The use of sorption kinetics is one of the most common techniques used to study small molecule diffusion into polymers. If a film of thickness, 2L, is placed in a bath of infinite penetrant (i.e. constant concentration at the surface), with initial concentration of the penetrant in the film being zero, then the concentration of the penetrant, C, at any position, z, in the film is given by equation 4.4. [4.6]

$$\frac{C}{C_0} = 1 - \frac{4}{\pi}\sum_{n=0}^{x}\frac{(-1)^n}{2n+1}\exp.\left[\frac{-D(2n+1)^2\pi^2 t}{4L^2}\right]\cos\left[\frac{(2n+1)\pi z}{2L}\right] \qquad \text{(eq. 4.4.)}$$

In this instance the boundary conditions for a region of $-L < x < L$ are

$C = 0$ at $t < 0; 0 \leq z \leq L$

$C = C_0$ at $t \geq 0; z = L$

$\delta C / \delta z = 0$ at $t \geq 0; z = 0$

In sorption kinetics, the mass of penetrant is measured as a function of time. The integration of equation 4.4. over the whole of the film thickness gives the sorbed mass

$$\frac{M_t}{M_\infty} = 1 - \sum_{n=0}^{x}\frac{8}{(2n+1)^2\pi^2}\exp.\left[\frac{-D(2n+1)^2\pi^2 t}{4L^2}\right] \qquad \text{(eq. 4.5.)}$$

Where M_t is the mass sorbed at time t

M_∞ is the equilibrium concentration

Equation 4.5. is a general solution to the equation for the mass of penetrant as a function of time undergoing Fickian diffusion in a film. Many experimental techniques can make use of this equation by exchanging the mass (M_t) by some other parameter for example, β counts of a radio label etc. The technique used in this work cannot make use of this general solution because the boundary conditions are different in the ATR experiment. The theory of ATR is explained in chapter 2.7.2. but by the convolution of equation 4.5 with Harricks' equations [4.40] for the ATR experiment it is possible to generate a Fickian model for the expected output from an ATR diffusion experiment [4.34].

When total reflection of a light beam occurs at the interface between a medium with high refractive index (ATR crystal, n_2) and one with a lower refractive index (polymer sample, n_1), the penetration of the electromagnetic field causes the formation of an evanescent wave propagating in all directions, decaying exponentially with distance from the surface. The decay can be represented in the following form;

$$E = E_o \exp(-\gamma z) \qquad \text{(eq. 4.6.)}$$

Where E_0 is the electrical field strength at the surface,

$$\gamma = \frac{2n_2\pi\sqrt{\sin^2\theta - \left(\frac{n_1}{n_2}\right)^2}}{\lambda} \qquad \text{(eq. 4.7.)}$$

When the rarer medium absorbs radiation at a specific wavelength the reflected wave has a reduced intensity at this wavelength resulting in an absorption spectrum. If one assumes that only weak absorption occurs it is possible to combine the Beer-Lambert law with the evanescent field strength equation.

$$\frac{I}{I_o} = e^{-A} \approx (1 - A) \qquad \text{(eq. 4.8.)}$$

Or

$$dI = -I_0 dA \qquad \text{(eq. 4.9.)}$$

If equation 4.9. is substituted into the differential form of the Beer-Lambert law and integrated,

$$A = \int_0^L \frac{\varepsilon CI}{I_o} dz \qquad \text{(eq. 4.10.)}$$

And for multiple reflections,

$$A = \int_0^L N\varepsilon^* CE_0^2 \exp(-2\gamma z) dz \qquad \text{(eq. 4.11.)}$$

Where $\varepsilon^* = \frac{\varepsilon}{I_0}$

In the ATR experiment the penetrant only enters from one side of the film therefore one only integrates between 0 and L.

Substituting equation 4.5. into equation 4.11. and integrating, the absorbance for the Fickian model can be given by;

$$\frac{A_t}{A_\infty} = 1 - \frac{8\gamma}{\pi\left[1-\exp(2L\gamma)\right]} \sum_{n=0}^{\infty} \left[\frac{\exp\left(\frac{-D(2n+1)^2\pi^2 t}{4L^2}\right)\left[\frac{(2n+1)\pi}{2L}\exp(-\gamma 2L) + (-1)^n(2\gamma)\right]}{(2n+1)\left(4\gamma^2 + \left(\frac{(2n+1)\pi}{2L}\right)^2\right)} \right].$$

(eq. 4.12.)

Where A_t is the absorbance at time t

A_∞ is the absorption at equilibrium

Equation 4.12 describes Fickian diffusion in an ATR diffusion experiment. In this work this model is found to describe the diffusion of water into PET very well. But, the diffusion of organic liquids into PET were found to produce a different response to the ATR experiment: therefore a different model was required.

The dual-sorption model has been shown to be an appropriate model in systems that require more than one diffusion coefficient [4.41]. Generally the model has described a system with one species being totally mobile and able to diffuse rapidly and freely into the polymer matrix. The other species has been described as partially mobile. The diffusion coefficients for both these species are constant but different. The modified ATR diffusion model for the dual sorption mode can be derived as follows.

Diffusion across a membrane is described by Ficks second law (equation 4.2.). The modified model can be described as ;

$$\frac{\partial C_1}{\partial t} = D_1 \frac{\partial^2 C_1}{\partial z^2} \qquad \text{(eq. 4.13.)}$$

With the new boundary conditions

$$C_1(0) = x_1 C_0$$

and $$C_1(t = \infty) = x_1 C_\infty$$

Where x_1 refers to the proportion of partially mobile molecules

For the totally mobile species

$$\frac{\partial C_2}{\partial t} = D_2 \frac{\partial^2 C_2}{\partial z^2} \qquad \text{(eq. 4.14.)}$$

With the boundary conditions

$$C_2(0) = x_2 C_0$$

and $C_2(t=\infty) = x_2 C_\infty$

The values of x_1 and x_2 are related to the molar fraction of the partially and totally mobile molecules, and therefore, $x_1 + x_2 = 1$

If the boundary conditions are substituted into equation 4.12. we now get;

$$\frac{A_1 - x_1 A_0}{x_1(A_\infty - A_0)} = 1 - \frac{8\gamma}{\pi[1-\exp(2L\gamma)]} \sum_{n=0}^{\infty} \left[\frac{\exp\left(\frac{-D_1(2n+1)^2\pi^2 t}{4L^2}\right)\left[\frac{(2n+1)\pi}{2L}\exp(-\gamma 2L) + (-1)^n(2\gamma)\right]}{(2n+1)\left(4\gamma^2 + \left(\frac{(2n+1)\pi}{2L}\right)^2\right)} \right]$$

(eq. 4.15.)

For the first sorption mode, and similarly for the second mode;

$$\frac{A_2 - x_2 A_0}{x_2(A_\infty - A_0)} = 1 - \frac{8\gamma}{\pi[1-\exp(2L\gamma)]} \sum_{n=0}^{\infty} \left[\frac{\exp\left(\frac{-D_2(2n+1)^2\pi^2 t}{4L^2}\right)\left[\frac{(2n+1)\pi}{2L}\exp(-\gamma 2L) + (-1)^n(2\gamma)\right]}{(2n+1)\left(4\gamma^2 + \left(\frac{(2n+1)\pi}{2L}\right)^2\right)} \right]$$

(eq. 4.16.)

$$A_1 = (1 - \sum D_1) x_1 (A_\infty - A_0) + x_1 A_0 \qquad \text{(eq. 4.17.)}$$

$$A_2 = (1 - \sum D_2) x_2 (A_\infty - A_0) + x_2 A_0 \qquad \text{(eq. 4.18.)}$$

Where

$$\sum D_x = \frac{8\gamma}{\pi[1-\exp(2L\gamma)]}\sum_{n=0}^{\infty}\left[\frac{\exp\left(\frac{-D_x(2n+1)^2\pi^2 t}{4L^2}\right)\left[\frac{(2n+1)\pi}{2L}\exp(-\gamma 2L)+(-1)^n(2\gamma)\right]}{(2n+1)\left(4\gamma^2+\left(\frac{(2n+1)\pi}{2L}\right)^2\right)}\right].$$

And $x = 1$ or $x = 2$.

If equations 4.17. and 4.18. are added and x_2 is substituted by $(1-x_1)$ the total absorbance at time t is given by;

$$\frac{A_t - A_0}{A_\infty - A_0} = (1-\sum D_1)x_1 + (1-\sum D_2)(1-x_1) \qquad \text{(eq. 4.19.)}$$

Equation 4.19. is the model for dual sorption mode diffusion in the ATR experiment.

4.3. Calculation of diffusion coefficients from the models.

The calculation of the diffusion coefficients from the models has been carried out in numerous ways. Fieldson and Barbari **[4.34]** have used a simplified version of the ATR-Fickian model which ignores all terms in equation 4.12. beyond the first. This simplification is accurate for $A_t/A_\infty > 0.5$ i.e. the later stages of diffusion and yields.

$$\ln\left(\frac{A_t}{A_\infty}\right) = \ln\left(\frac{4}{\pi}\right) - \frac{D\pi^2}{4L^2}t \qquad \text{(eq. 4.20)}$$

Using this simplified equation the linear portion of the plot of the logarithm of the absorbance data verses time gives a diffusion coefficient. This requires the measurement

of A_∞ which can be unreliable using infrared spectroscopy due to saturation problems associated with strongly absorbing vibrators.

Another method used, developed by Brandt [4.22] and favoured by Schühler et al [4.1] calculated the diffusion coefficient by determining the intercept of the tangent through the inflection point of the absorbance verses time plot. This does not require the determination of the equilibrium absorbance value.

If one was to write suitable software, then equations 4.12. and 4.19. can be easily used calculate the diffusion coefficients from real data obtained from *in-situ* ATR experiments. This section will describe how the D values for the Fickian diffusion model were obtained for this work. The dual sorption D values were obtained using a program written in PASCAL, by Dr Marcia Pereira, which utilises the Levenberg-Marquart least squares fitting procedure. This fitting procedure allows the rapid fitting of two unknown parameters, minimised using a χ^2 merit function. The details of the program are given elsewhere [4.42]. The diffusion coefficients for the Fickian diffusion model were calculated from a program written in Matlab. The program uses a simple procedure to calculate the best D values. The theoretical normalised output for a given D is calculated and compared to the real data using a sum of the squares criterion. The D values are changed accordingly and when the lowest sum of the squares is reached then that is deemed to be the 'D of best fit'. The program is detailed as follows.

```
% Main program                                    (dcalc)
clc
global X
global D
global beta
global alpha
global bestd
global T
global A
global as
global dp
global sum1
global sum2
global sum3
global N
global file
lodat
done=0;
bestd=D*1e-8;
draw
fchi
in=chi;
bestd=bestd-1e-11;
draw
fchi
do=chi;
bestd=bestd+2e-11;
draw
fchi
upf=chi;
if upf > do up=0;
else up=1;
end
fit
bestd=oldd;
done=1;
draw
fchi
be=num2str(bestd);
be=['D = ' be ' cm^2/s'];
ch=num2str(chi);
ch=['Chi^2 = ' ch];
le=num2str(l);
le=[le ' um thick'];
legend('Experimental','Calculated',",le,be,ch)
xlabel('t^1/2 / s')
ylabel('Normalised integrated intensity / cm^-1')
end
```

'dcalc' is the main program that calls all the other procedures. It lists all the 'global' variables, which are those that can be used by more than one routine. Variables that are used in just one routine are called local variables. It calls **'lodat'** which loads and normalises the data and **'draw'** which calculates the theoretical data for specific D values. It calls **'fchi'** which calculates the χ^2 merit function and **'fit'** which changes the current D value until an optimum is reached. Finally, on screen, the raw data with the theoretical D of best fit overlaid and a legend of the relevant parameters are displayed.

```
% Read and Input data.                                    (lodat)
file=input('Give the filename of the raw data (excluding extension) ','s');
f=[file '.txt'];
eval(['load ' f]);
data=eval(file);
temp=size(data);
N=temp(1);
dp=input('Give the Dp value for the band investigated (in um) ');
l=input('Give the thickness of the film studied (again in um) ');
as=input('Give the integrated intensity at equilibrium ');
D=input('Give an estimate for the diffusion coefficient (cm2s-1) ');
D=D*1e8;
alpha=exp(-2*l/dp);
beta=8/(pi*dp*(1-alpha));
for i=1:N
A(i)=(data(i,2))/as;
T(i)=(((data(i,1)*60))^0.5);
end
end
```

'lodat' loads the raw data into the Matlab working window and normalises the data. Firstly the filename of the data is input, along with an estimate for dp (in μm), the film thickness (in μm), the absorbance at equilibrium (the largest absorbance value obtained during the experiment will work just as well) and an estimate for the diffusion coefficient. From the data the constants that are used in the summation procedure are calculated. The time is converted from minutes, to square root seconds.

```
% Draw diffusion curve                                    (draw)
D=bestd*1e8;
np=N;
for z=1:N;
 time=T(z);
 if time==0 time=1e-1;,end
 X=time;
 sumcal
 ycurve=1-sum1;
 if ycurve<0 ycurve=0;
  oycurve=1;
 else oycurve=sum1;
 end
f(z)=oycurve;
c(z)=ycurve;
C(z)=c(z)-c(1);
end
q=1/C(np);
for z=1:np
C(z)=C(z)*q;
end
if done ==1
plot(T,A,'rO')
hold on
plot(T,C,'r')
hold off
end
end
```

The **'draw'** procedure actually only draws the output once the optimum D has been reached. During the other loops it calculates the theoretical data at each time interval for the currently specified D. This procedure calls the **'sumcal'** procedure which calculates the summation part of equation 4.12.

```
% Procedure to calculate increments                    (sumcal)
sme=exp(-300);
j=-1;
sum1=0;, sum2=0;, sum3=0;
err1=1;,err2=1;,err3=1;
while err1 > sme | err2 > sme | err3 > sme;
osum1=sum1;, osum2=sum2;, osum3=sum3;
j=j+1;
factor=fix(j/2)-j/2;
if factor == 0 sign=1;
else sign=-1;
end
kj=pi*(2*j+1)/(2*l);
sign1=alpha*kj+sign*2/dp;
power1=-(kj)^2*D*X+log(abs(sign1))-log((kj^2)+4/(dp^2))-log(2*j+1);
sign1=sign1/abs(sign1);
power2=power1+2*log(kj)+log(X);
power3=power2+2*log(kj)+log(X);
if power1>=-300 term1=sign1*exp(power1);
else term1=0;
end
if power2>=-300 term2=-sign1*exp(power2);
else term2=0;
end
if power3>=-300 term3=sign1*exp(power3);
else term3=0;
end
sum1=sum1+term1;
sum2=sum2+term2;
sum3=sum3+term3;
err1=abs(sum1-osum1)*beta;
err2=abs(sum2-osum2)*beta;
err3=abs(sum3-osum3)*beta;
end
```

The '**sumcal**' procedure calculates the summation part of equation 4.12. It loops continuously until the increments to the summation become negligible.

```
% Chi^2 fit to data                                    (fchi)
chi=0;
for g=1:N
tmp=(C(g)-A(g))^2;
chi=chi+tmp;
end
end
```

The **'fchi'** procedure simply calculates a 'sum of the squares' χ^2 merit function for the calculated data verses the normalised real data for the current D value.

```
% engine Chi^2 fit to data                    (fit)
draw
 fchi
 ochi=chi;
while chi <= ochi
 oldd=bestd;
 ochi=chi;
 if up==0 bestd=bestd-1e-10;
  else bestd=bestd+1e-10;
  end
 draw
 fchi
 end
 maxd=1;
 end
 ochi=chi;
while chi <= ochi
 oldd=bestd;
 ochi=chi;
  if up==0 bestd=bestd+1e-11;
  else bestd=bestd-1e-11;
  end
 draw
 fchi
 end
 best_D = oldd
 best_chi = ochi
```

The **'fit'** procedure works by deciding whether the previous χ^2 was better or worse than the current χ^2. It then either increases or decreases the D value accordingly. Once the χ^2 is no longer decreasing, the procedure then retraces its' steps in smaller increments. Once the χ^2 ceases to decrease for a second time, then the optimum D value is deemed to have been reached.

4.4. Sample output from the Matlab Fickian diffusion program.

In a 'normal' sorption kinetics experiment, eg. a gravimetric technique, the diffusion coefficient, which has units cm^2s^{-1}, can be obtained from a simple equation

$$D = \frac{\pi}{16} L^2 G^2 \qquad \text{(eq. 4.20.)}$$

Where L is the thickness in cm,

G is the gradient of the linear region of the $\sqrt{t}$ versus response plot.

Unfortunately in the ATR diffusion experiment, this relationship no longer holds true, due to the convolution of the evanescant field with the diffusion profile. Comparative plots of the expected output from the ATR experiment and a weighing experiment is shown in figure 4.1.

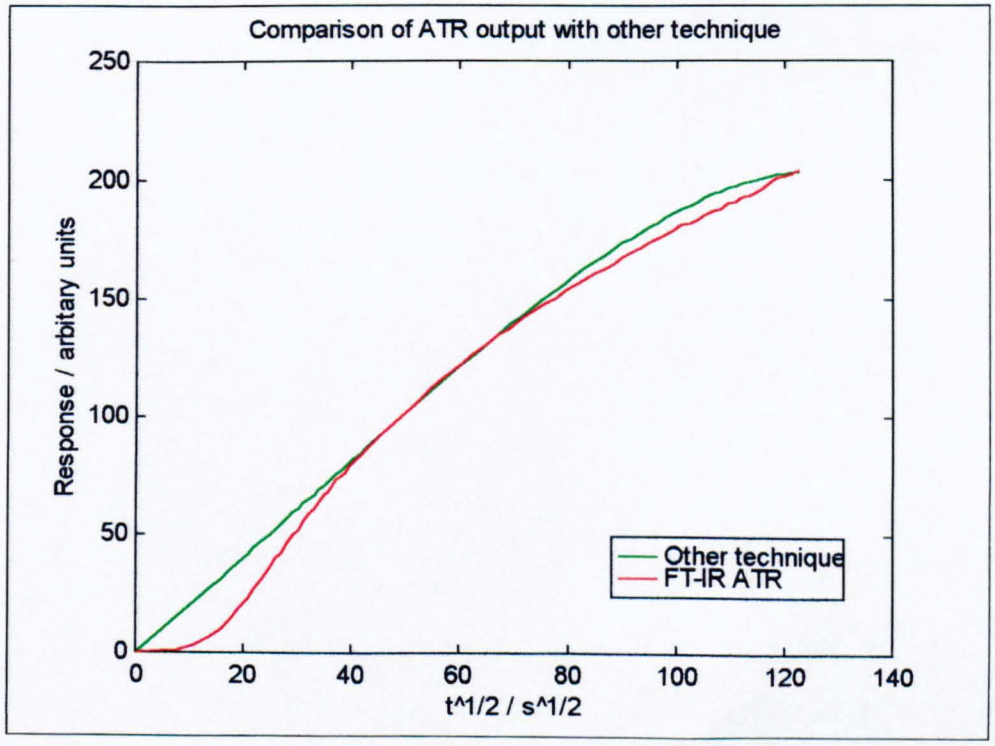

Figure 4.1. ***Comparison of the FT-IR ATR Fickian diffusion output, to that from another technique (e.g. gravimetric) for a 10 μm sample with a D value of 3 x 10^{-9} cm^2s^{-1}.***

The response of the ATR diffusion experiment is also dependent on the diffusion coefficient and the film thickness. This is perhaps easiest to show pictorially. From figure 4.3. it is clear that there will only be a response to the penetrant (i.e. penetrant seen in the spectrum) when the penetrant enters the Evanescent field. This will depend on the rate at which the diffusion occurs (the D value), the evanescent field and the thickness of the film. In a thick film the spectrum of the diffusant will be relatively weak at shorter times as there is less of it in the Evanescent field. This manifests itself as a 'tail' in the ATR diffusion profile and gives the profile its characteristic sigmoidal shape.

If all other parameters are identical, then if one decreases the D values then one will observe an increase in the 'tail' corresponding to short time responses. This is shown in figures 4.4. and 4.5.

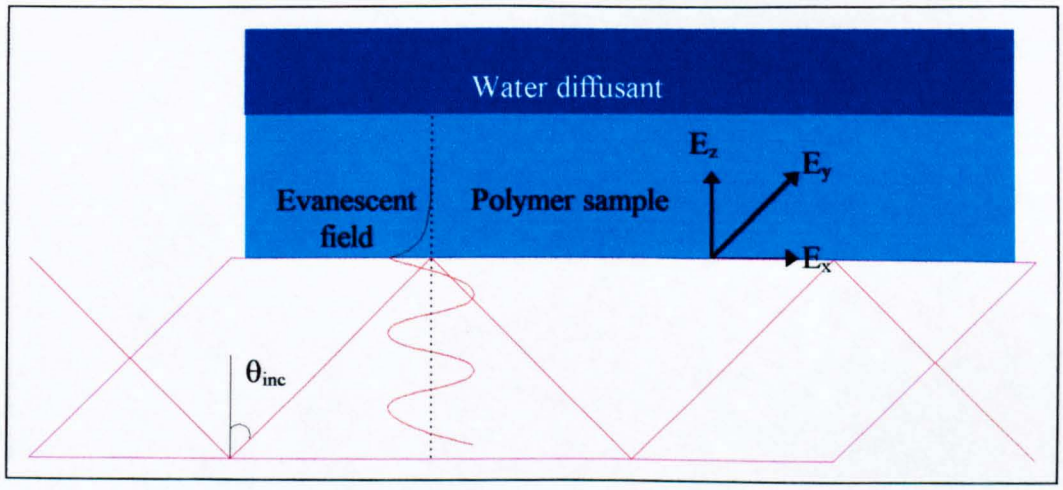

Figure 4.3. Schematic of the ATR diffusion experiment.

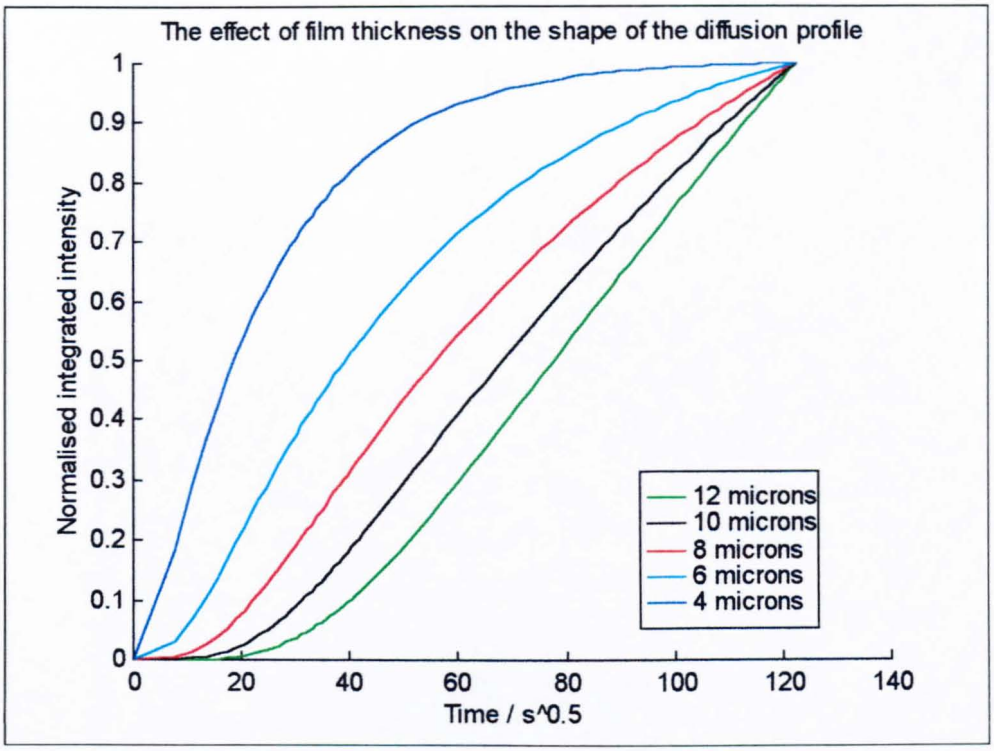

Figure 4.4. ***The output from the Fickian diffusion program for samples of differing thickness with a dp of 1.5μm and a D value of 3 x 10^{-9} $cm2s^{-1}$.***

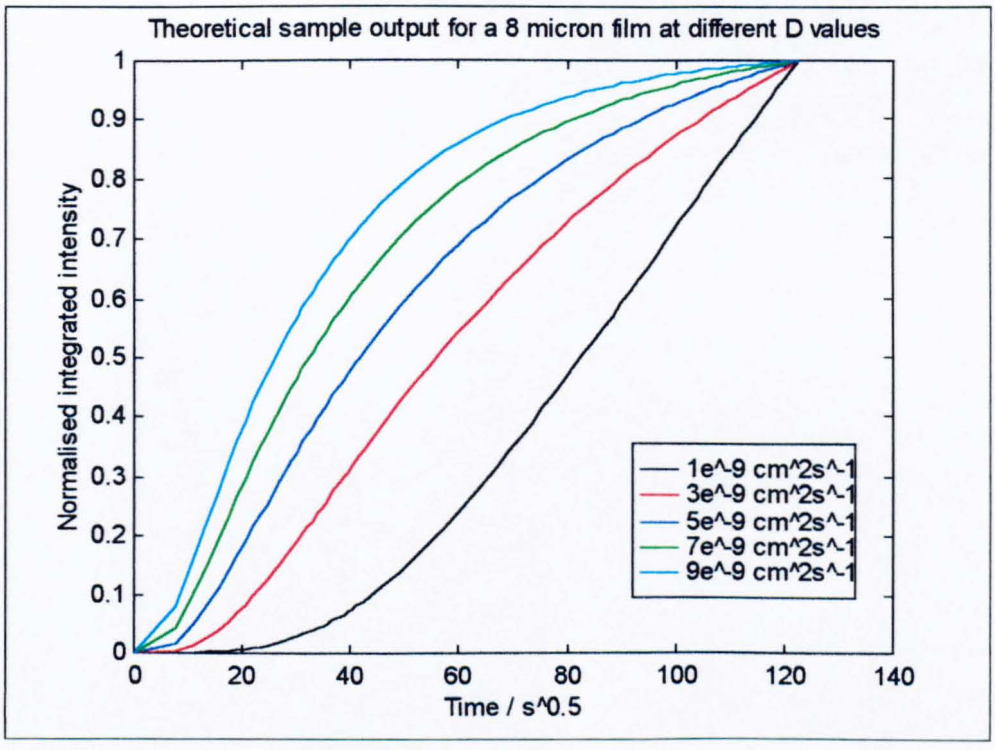

Figure 4.5. ***The output from the Fickian diffusion program for an 8μm sample with dp of 1.5μm.***

4.5. The effect of the experiment length on the calculation of D.

Although the experimental data was taken over a 5 1/2 hour period, it is clear from most of the diffusion profiles (see chapter 5) that equilibrium has not been reached i.e. the diffusion process is still continuing when the experiment has 'finished'. This meant that the value of A_∞ cannot be obtained, which is required for equation 4.12. and used in the Matlab diffusion program.

Figures 4.6 - 4.8. show the effects of the length of the experiment on the estimated D value. The data for figures 4.6 - 4.8. were taken from the same experiment which was allowed to reach equilibrium with spectra being taken every 8 hours or so after the initial 5 1/2 hours.

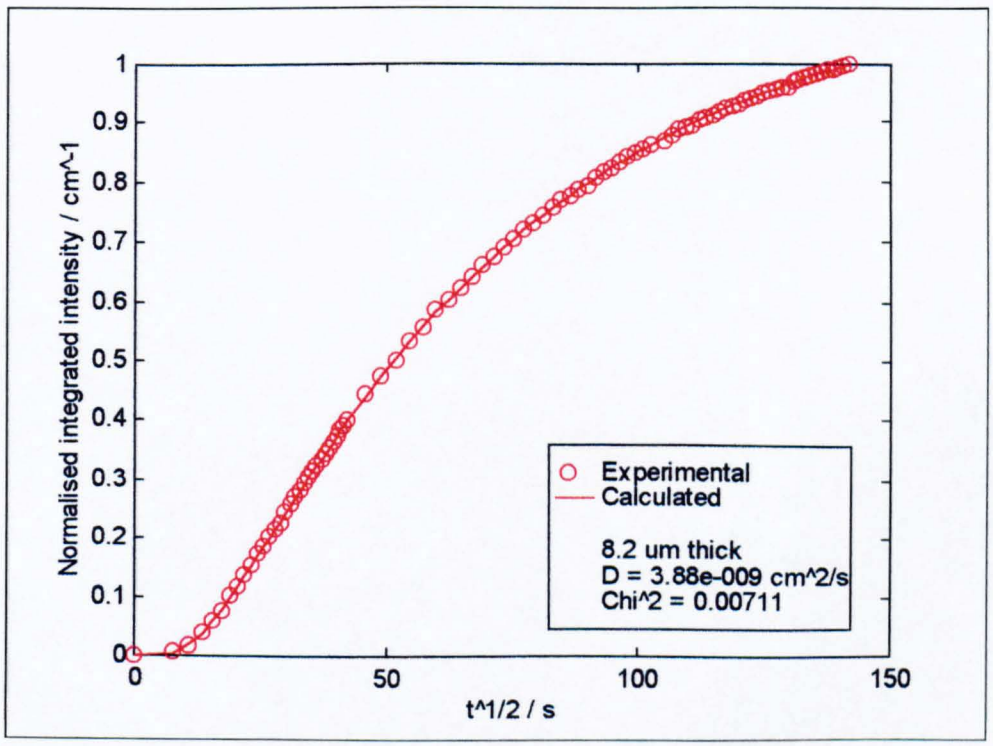

Figure 4.6. The output from a typical 5 1/2 hour experiment.

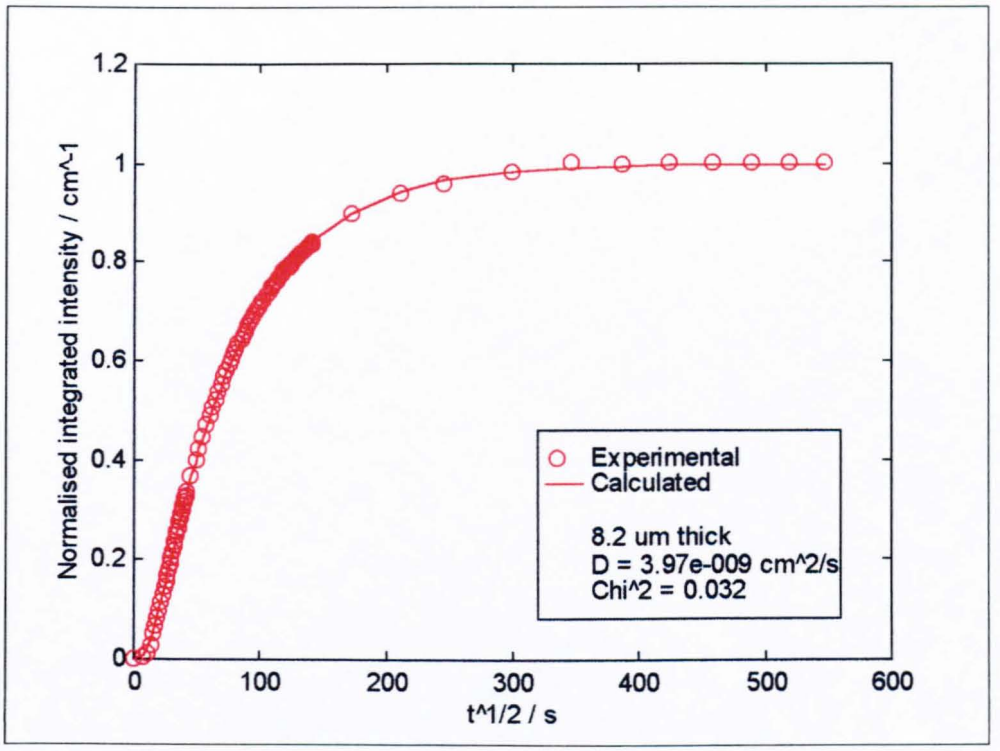

Figure 4.7. ***The output from a diffusion experiment allowed to reach equilibrium (~4 days).***

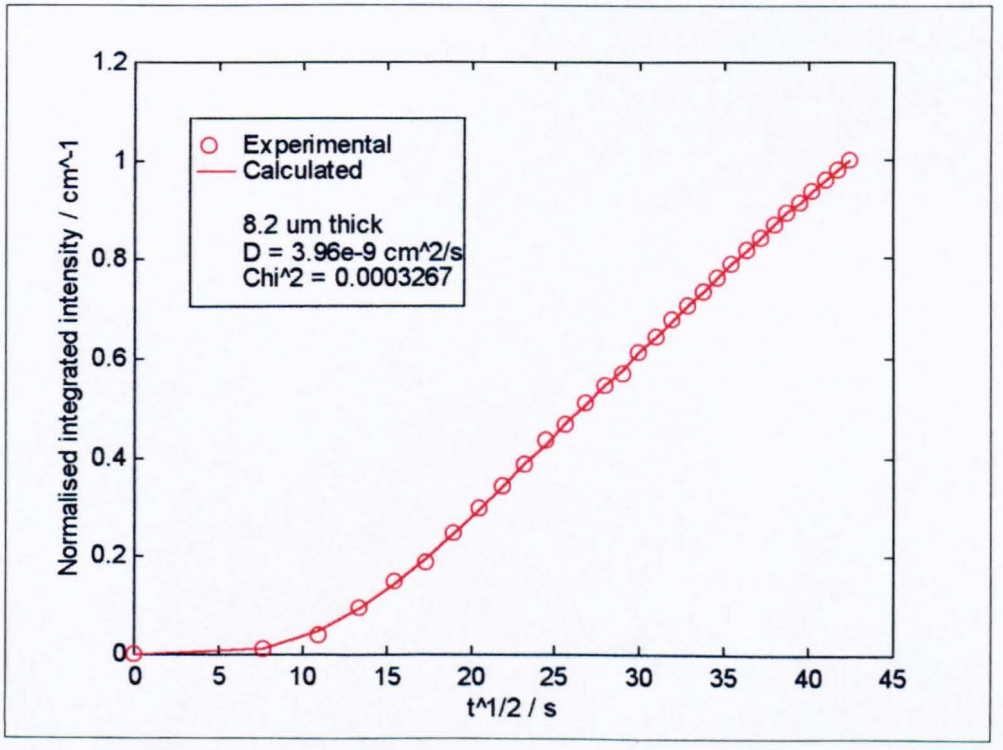

Figure 4.8. ***The output from the first 1/2 hour of the experiment.***

As is shown the length of the experiment was seen not to create large differences in the calculation of D values. The Matlab diffusion program normalises the experimental data by using the highest obtained integrated absorbance value or the equilibrium absorbance value (only if the equilibrium absorbance value is included in the experimental data set). During the calculation of theoretical data the program also normalises the calculated At/A_∞ against the At/A_∞ value at the longest time in the calculated data set. Because both the experimental and calculated data sets have been normalised in the same way the χ^2 merit function was valid and the estimated D values were meaningful.

This resulted in the equilibrium value having no real effect on the estimated D as long as the value given to the Matlab program was the highest integrated absorbance value, at the longest time interval within the experimental data set.

4.6. Obtaining the infrared diffusion data.

So far in this chapter much has been made about the diffusion models used for this work and the computer software used to obtain physical data from the experimental data. This section will deal with the setting up of the ATR diffusion experiment and obtaining the experimental data to use with the Matlab diffusion program.

Figure 4.9. shows the experimental layout of the liquid ATR cell used in the diffusion experiment. In the experiment, the sample film was cast onto one side of the ATR prism and mounted into the liquid cell. Details of the films will be given in chapter 5. A 200 μm thick PTFE 'O' ring was placed directly onto the polymer film and held in place by

the clamping shut of the liquid cell. The PTFE 'O' ring creates an effectively infinite reservoir of liquid when filled. The system was tested for leakage, before the introduction of liquid, by injecting air into the liquid cell. If the syringes could both be moved upwards, away from the ATR prism, this meant that somewhere in the system there was a leak. If this occurred then the ATR prism was remounted and the 'o' ring reclamped in place.

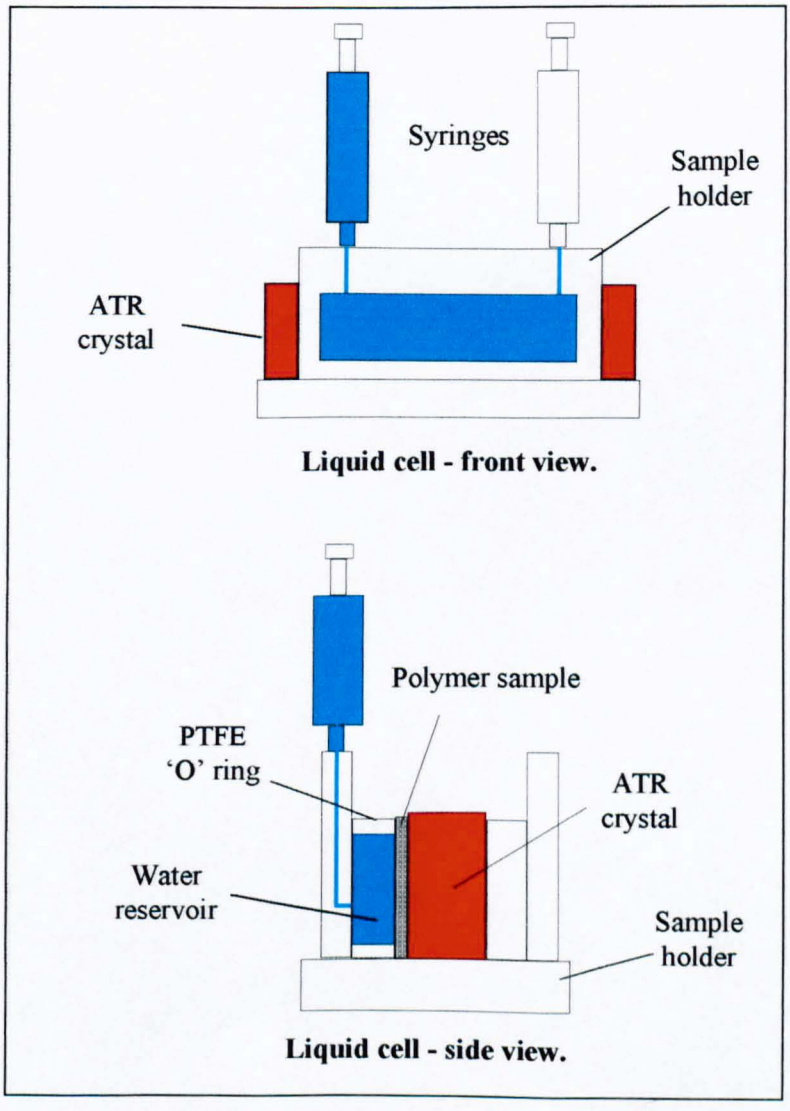

Figure 4.9. ***The experimental layout of the liquid ATR cell used in the diffusion experiment.***

Once the cell had been shown not to leak then the liquid cell was mounted onto the ATR accessory and the mirrors aligned so that the optimum throughput of radiation was reaching the detector.

Once the optimum throughput had been reached then the experiment was ready to begin. The spectra were recorded using a WinFirst macro program which recorded a spectrum every minute for the first thirty minutes of the experiment and every 5 minutes for the next 5 hours. It is important to note that the times quoted contain the time it took to acquire the data. Therefore the spectra obtained were an average over the time range (~42 seconds) that they were taken and were not spectra obtained instantaneously at the quoted time. The acquisition of timed spectra began once a key had been pressed, after the automatic acquisition of a background spectrum, in this case the dry film.

The instrumental parameters used for the diffusion experiment were contained in a datafile called 'CSD.dat' and are shown in table 4.1.

Resolution	4 cm^{-1}
Sample scans	25
Iris	25%
Signal gain	1
Mirror velocity	40 cm s^{-1}
Apodization function	Triangle

Table 4.1. Instrumental parameters used during the diffusion experiment.

The WinFirst macro program used to obtain the infrared data is shown.

```
% WinFirst macro to acquire infrared spectra
comment CSD.mac
let n 31
let d 18
comment Enter the title of the first spectrum including starting number
enter t

let p csd.dat
let b 0
increment b
test &b <= &n
goto done
mattscan parms = &p irdatatype = sbm actions = isq file &t
increment t

pause Inject the water and hit a key
label do_samp
        increment b
        test &b <= &n
        goto done
        mattscan parms = &p irdatatype = sbm actions = isq file &t
        increment t
        comment Run number &b completed
        comment System paused but active
        comment 1 minute scans
        test &b > &n
        sleep &d
        goto do_samp
label done

let n 60
let d 258
label do_sampa
        increment b
        test &b <= &n
        goto end
        mattscan parms = &p irdatatype = sbm actions = isq file &t
        increment t
        comment Run number &b completed
        comment System paused but active
        comment 5 minute scans
        test &b > &n
        sleep &d
        goto do_sampa
label end
comment Last spectrum = &t
exit
```

For the diffusion of water into PET, the integrated areas of the OH bands from the water were calculated from a macro written in WinFirst. The files were integrated between two points at 4000 and 2685 cm^{-1} with the baseline for the integration defined as a straight line between the two points. The program is listed below.

```
% WinFirst macro program to obtain absorbance data for diffusion experiments
enter n "Enter name of first file to integrate ( an .sbm )"
enter b "Enter name of background to use"
enter r "Enter number of files to ratio"
enter c "Enter starting wavenumber for integration"
enter d "Enter ending wavenumber for integration"
enter f "Enter the name of the file you want the results to go to"
G = buildstring f
fopen 1 G

For x = 1 to r step 1
begin
        F = buildstring n ".sbm"
        load F
        ratio b
        ras2abs
        save F
        A = integrate c d
        fprint 1 A
        increment n
end
fclose 1
```

The data from the WinFirst macro was then loaded into Excel where the corresponding times were added and the resulting data saved as a text file ('.txt') for use with the Matlab diffusion program. It was important to have the 'time data' in minutes and as the left-hand column in the text data or else the program would not work properly.

4.7. References

4.1. N. Schühler, A.S. da Silva Sobrinho, J.E. Klemberg-Sapieha, M. Andrews and M.R. Wertheimer, *Soc. Vacuum Coaters: 39th Annual Technical Conf. Proc.*, 285, (1996)

4.2. D. Langevin, J. Grenet and J.M. Saiter, *Eur. Polym. J.*, **30**, 3, 339, (1994)

4.3. M.J. Kloppers, F. Bellucci, R.M. Lantanision and J.E. Brennen, *J. Appl. Polym. Sci.*, **48**, 2197, (1993)

4.4. 'Diffusion in Polymers', (Eds J. Crank and G.S. Park), Academic Press, London. (1968)

4.5. 'Polymer Permeability', (Eds A.H. Windle and J. Comyn), Elsevier Applied Science Publishers, London, (1986)

4.6. 'The Mathematics of Diffusion', 2nd Ed., (Ed J. Crank), Clarenden Press, Oxford (1994)

4.7. N.E. Schlotter and P.Y. Furlan, *Polymer*, **33**, 16, 3323, (1992)

4.8. T. Alfrey, E.F. Gurnee and W.G. Lloyd, *J. Polym. Sci.*, **C12**, 249, (1966)

4.9. C. Miglaresi, L. Nicodemo, L. Nicolais and L. Paserini, *Polymer*, **23**, 687, (1984)

4.10. K.D. Yang, W.J. Koros, H.B. Hpfenberg and H, Stannet, *J. Appl. Polym. Sci.*, **31**, 689, (1986)

4.11. F. Bellucci and L. Nicodemo, *Corrosion*, **49**, 3, 235, (1993)

4.12. J.F. Westlake and M.J. Johnson, *J. Appl. Polym. Sci.*, **19**, 1745, (1975)

4.13. M.J. Johnson and J.F. Westlake, *J. Appl. Polym. Sci.*, **19**, 319, (1975)

4.14. G.S. Hartley, *Trans. Faraday Soc.*, **45**, 820, (1949)

4.15. N. Thomas and A.H. Windle, *Polymer*, **19**, 1195,(1977)

4.16. J. Klier and N.A. Peppas, *Polymer Bul.*, **16**, 359, (1986)

4.17. H.M. Tong, *J. Polym. Sci. Polym. Phys. Ed.*, **27**, 689, (1989)

4.18. R. Korsmeyer, *J. Polym. Sci. Polym. Phys. Ed.*, **24**, 409, (1986)

4.19. R.E. Cameron, M.A. Jalil and A.M. Donald, *Macromolecules*, **27**, 2708, (1994)

4.20. D.R. Rueda, A. Viksne, J. Kajaks, F.J. Balta-Cajella and H.G. Zachmann, *Macomol. Symp.*, **94**, 259, (1995)

4.21. D.R. Rueda and A Varkalis, *J. Polym. Sci. Part B: Polym. Phys.*, **33**, 2263, (1995)

4.22. H. Brandt and P. Reiger, *Exper. Technik Physik*, **32**, 413, (1984)

4.23. H. Brandt, *Exper. Technik Physik*, **33**, 423, (1985)

4.24. H. Brandt and K. Hemmelmann, *Exper. Technik Physik*, **35**, 349, (1987)

4.25. J.G. van Alsten and S.R. Lustig, *Macromolecules*, **25**, 5069, (1992)

4.26. J.G. van Alsten and J.C. Coburn, *Macromolecules*, **27**, 3752, (1994)

4.27. M.R. Pereira and J. Yarwood, *J. Chem. Soc., Faraday Trans.*, **92**, 15, 2731, (1996)

4.28. M.R. Pereira and J. Yarwood, *J. Chem. Soc., Faraday Trans.*, **92**, 15, 2737, (1996)

4.29. S. Hajatdoost and J. Yarwood, *J. Chem. Soc., Faraday Trans.*, **93**, 8, 1613, (1997)

4.30. C. Sammon, N. Everall and J, Yarwood, *Macromol. Symp.*, **119**, 189, (1997)

4.31. T.P. Skourlis and R.L. McCullough, *J. Appl. Polym. Sci.*, **52**, 1241, (1994)

4.32. N.E. Schlotter and P.Y. Furlan, *Vib. Spec.*, **3**, 147, (1992)

4.33. J.R. Xu and C.M. Balik, *Appl. Spec.*, **42**, 8, 1543, (1988)

4.34. G.T. Fieldson and T.A. Barbari, *Polymer*, **34**, 6, 1146, (1993)

4.35. G.T. Fieldson and T.A. Barbari, *Aiche J.*, **41**, 4, 795, (1995)

4.36. T. Nguyen, *J. Ahesion Sci. Tech.*, **5**, 9, 679, (1991)

4.37. T.L. Marshbanks, D.J. Ahn and E.I. Frances, *Langmuir*, **10**, 276, (1994)

4.38. E. Rosenberg and R. Keller, *R. 8th Int. Conf. on FT Spec.*, 346, (1991)

4.39. M. Fontyn, *J. Membrane Sci.*, **36**, 147, (1987)

4.40. N.J. Harrick, *J. Opt. Soc. Am.*, **55**, 851, (1965)

4.41. J.A. Horas and F. Nieto, *J. Polym. Sci. Part B: Polym. Phys.*, **32**, 1889, (1994)

4.42. M. Pereira, Thesis, Durham, (1994)

Chapter 5

Interactions of water molecules with PET at ambient temperature

5.1. Introduction

The sorption and transport of small molecules into polymers has been studied by numerous workers using numerous different methodologies (see chapter 4.4.). This work has used the *in-situ* ATR FT-IR methodology as it has been shown to be an elegant method for simultaneously obtaining both kinetic and structural information.

5.1.1. The study of the diffusion of water into PET

Diffusion coefficients for the sorption of liquid water and water vapour into PET have been calculated by various authors. Langevin and co-workers used differential scanning calorimetry (DSC) to examine the effects that water content has on the thermal properties of PET **[5.1]**. They also used a gravimetric technique to calculate the diffusion coefficient and work out the water content at equilibrium. The diffusion coefficient at 20°C was shown to be 4.5 x 10^{-9} cm^2s^{-1} and the water content at equilibrium was estimated at about 1% by weight. Energy minimised simulations were carried out with 1 water molecule per 10 repeating PET monomer units, to examine the distribution of water within the polymer matrix.

Electrochemical impedance spectroscopy (EIS) has been used to calculate the diffusion coefficient and the equilibrium water content of PET **[5.2, 5.3]**. The technique was validated by comparison to the traditional gravimetric method and found to be in good agreement. Diffusion coefficients calculated from this method varied from 2.11 - 9.97 x 10^{-9} cm^2s^{-1} for liquid water at 40°C and some thickness dependence was noted. Two of the samples were examined using the Payne cup gravimetric method and diffusion

coefficients were found to be higher but of the same order of magnitude. The amount of water in the samples at equilibrium was calculated at 0.54 & 0.95 % by weight for samples of 75 and 205 μm thick respectively.

Transmission FT-IR has also been used to study the diffusion of water vapour into PET and PEN as a function of crystallinity in two separate publications by Rueda et al [**5.4, 5.5**]. Samples ranging between 100 % amorphous and 29 % crystalline were examined and relationships between D values and crystallinity and between crystallinity and equilibrium water content were noted. Diffusion coefficients, at 25°C, ranging between 8.18 and 3.93 x 10^{-9} cm^2s^{-1} were calculated, decreasing with increasing crystallinity. The relationship was shown to follow a power law with an exponent of 0.5. The shape of the water band in the polymer is a doublet with centres at around 3630 cm^{-1} and 3550 cm^{-1}. This is quite different to the band of water in PET obtained from the ATR experiment. This is because the band in this system is due to gaseous monomeric water and the decoupled ν_{as}(OH) and ν_s(OH) have distinct vibrations. This is not the case for liquid water and will be discussed later. The mass of the samples was also measured to obtain percentage by weight of water at equilibrium. Values around 1 % by weight of water at equilibrium are given for amorphous material and 0.6 % by weight for 29 % crystalline. Difficulties in obtaining absolute values for the equilibrium water content were discussed due to the inherent errors in the stop-start procedure.

Yasuda and Stannet looked at a series of polymers including PET and calculated the diffusion rate of water vapour into them at 25°C, using the time lag technique [**5.6**]. They used a Mylar A sample and obtained a D value of 3.95 x 10^{-9} cm^2s^{-1}.

Schüler et al used the *in-situ* FT-IR ATR technique to monitor the diffusion of liquid water into PET and PET coated with thin (< 100 nm) SiO_2 layers [5.7]. They used films varying between 12 and 25 μm and obtained D values between 1.59 and 2.18 x 10^{-9} cm^2s^{-1} which agree well with previously calculated values. As stated in chapter 4, D values cannot be calculated directly from absorbance (A) versus $\sqrt{t}$ plots due to the convolution of the Fickian diffusion profile with the evanescent field. This work calculated the point of inflection of the A verses t plot and used the gradient of a tangent drawn through this point of inflection to obtain estimates for D. Perhaps not surprisingly the application of a SiO_2 layer drastically slowed down the diffusion process and a Fickian process was no longer observed.

5.1.2. The vibrational spectrum of liquid water

Recently literature on the interpretation of the ν(OH) band of pure liquid water based around new and more extensive data has been published [5.8-5.14]. The works have been based on the treatment of liquid water as a pseudo polymeric material composed of a mixture of defect and non-defect water molecules rapidly interchanging. The water band in polymeric matrices can be treated in the same way.

Intermolecular and intramolecular O-H oscillator coupling leads to a very complicated vibrational spectrum for liquid water. Coupling occurs between ν_s(OH) and ν_{as}(OH) vibrations and between the O-H oscillators on different molecules (ν_s(OH) and ν_{as}(OH) vibrations would occur in gas phase H_2O). The O-H oscillators on different molecules would need to be compared to totally decoupled O-H or O-D bands of HOD in the gas

phase, where isotopic substitution leads to the decoupling process. These coupling processes promote delocalisation in the liquid at room temperature which makes the isolation of different distinct O-H vibrations improbable. The liquid is subject to the breaking and reforming of intramolecular H-bonds on a pico second timescale (which is fixed on the vibrational timescale). Our interpretation of the water band is a hybrid of the mixture model of water; consisting only of a two-state, hydrogen bonding and non-hydrogen bonding water and the continuum model where the band is made up of a continuum of strengthening hydrogen bonds as the frequency lowers. The ν(OH) band can be deconvoluted into several components and each of the contributing components is generally quite broad. This width is consistent with a wide range of H-bonding distances and intermolecular bond angles within each of the major water types.

5.1.3. The structure of water adsorbed in polymer matrices

There is still a general lack of understanding of the effect of hydration on structural and dynamical properties and one way of trying to bridge this gap is to study the properties of bound water in polymer matrices. Water bound in a polymer matrix can be regarded as being quite different to pure liquid water, if only due to its restricted motion **[5.15-5.20]**. A great deal of work has been published in this area using spectroscopic techniques such as NMR **[5.20-5.22]**, neutron scattering **[5.17, 5.19]**, FTIR and Raman **[5.23-5.25]**, and light scattering **[5.26]**. One of the main difficulties that has needed to be overcome is the ability to distinguish between bound water from bulk water. It is with this in mind that selective probes **[5.19, 5.22]**, and spectral subtraction **[5.23, 5.24, 5.27]** have been used.

Vibrational spectroscopy with its high sensitivity to structural and conformational change is an ideal tool to examine water structure, but does have the disadvantage of saturation in thick (> 2μm) samples. The ATR FT-IR technique described earlier has great scope in this field as it circumvents the saturation problems by limiting the sampling thickness. Recent work on the perturbation of water close to an organic interface using this technique has been carried out on both microemulsions **[5.28, 5.29]** and polymers **[5.23-5.25, 5.27, 5.30]**

The water bands have been shown to change in frequency, intensity and shape. This in turn has been interpreted in terms of bound and free water **[5.28, 5.31, 5.32]**, water clustering **[5.30, 5.33-5.36]**, water orientation **[5.37]** and water networking **[5.36, 5.38-5.40]**. It has been questioned whether distinctly different electronically-perturbed states of water could be detected **[5.29, 5.31]** or whether the change in properties of non-bulk water is more gradual depending on the precise distance from the organic interface.

Kusanagi and Yukawa **[5.41]** and Rueda et al **[5.4, 5.5]** have looked at the state of water (from water vapour) in PET at equilibrium. The band is clearly seen to contain three components corresponding to the ν_s(OH), ν_{as}(OH) and the overtone of the carbonyl band. This is clearly different to the state of the liquid water observed during this work. Kusanagi and Yukawa postulate that the differences in water bands observed between a hydrophobic polymer such as PET and a hydrophilic polymer such as Nylon-6 (for the same experimental conditions) can be accounted for by water clustering. In the case of hydrophobic polymers no clustering occurs, hence a lack of coupling of the ν(OH) band leading to a simplified spectrum showing ν_{as}(OH) and ν_s(OH) components. In the case

of a hydrophilic polymer subsequent coupling of the ν(OH) oscillators, due to water clustering, results in a more complex 'liquid water' like spectrum.

Fukada et al used the near infrared region to look at water vapour sorbed in PET [5.42]. It was noted that the band at 7000 cm^{-1}, which can be attributed to the first overtones of the ν_{as}(OH) and ν_{s}(OH) bands, was shifted by around 100 cm^{-1} relative to that for liquid water, but was not in the region associated with gaseous water. The band was split into three components differing in the degree of hydrogen bonding. The three bands are termed sub-band I, I-II and II with the roman numerals indicating the number of hydrogen bonds each water molecule is involved in. It was stated that water molecules sorbed in PET interact less with each other than water molecules in liquid water. Estimates of the relative ratios of these water bands in PET and in pure liquid water were given as 60:30:10 % and 20:40:40 % respectively.

5.2. Experimental

The films used in this project were made in two different ways in order to obtain a range of crystallinities. All the films were made from extrusion grade PET chips containing pure PET (E47 polymer) and PET manufactured with 18 % isophthalic acid as a comonomer (E99 polymer). The structures of the polymers used are shown in chapter 1. Both types of PET were kindly donated, in extruded chip form, by ICI films (Wilton). All the films were cast from solution: the type of solution and the other treatments will be detailed in the next two sections. Some characteristics of the PET used are shown in table 5.1.

Name	Isophthalate content	M_w	T_g (polymer chips)
E47	0 %	70,000	73 °C
E99	18 %	60,000	67 °C

Table 5.1. Some characteristics of the PET samples used in this work

When preparing polymer films for diffusion experiments one of the most important things to consider is the uniformity of the film; i.e. is the film even? Is the film continuous ? Is the film flat ? Does the film look the same at all points ? If the film fails on any one of these counts, then the diffusion results obtained can be called into question. It is quite straight forward to characterise the films used in this work using a mixture of infrared spectroscopy, Raman microscopy and optical techniques.

Sometimes discontinuities in the films can be seen using the naked eye. It was found that solvent cast films with a high degree of crystallinity (>25 %) were often discontinuous. This seems to be due to spherulitic growth of the crystalline regions at the surface. This has been noted when trichloroethane (TCE) has been used as the solvent with E47 PET, making the manufacture of suitable films from this solvent without comonomer impossible. But when a film is cast, from *ortho*-chlorophenol (OCP), this seems to stop the formation of spherulites at the surface making the casting of films of higher crystallinity possible. The boiling point of OCP (175-176° C) is higher than that of TCE (121° C). The preferential formation of crystals in the faster evaporating solvent would seem to be counterintuitive. One would reasonably expect the solvent taking longer to evaporate encouraging the growth of crystals, whilst the quicker evaporating solvent would produce a more amorphous film. One possible explanation is that the polymer

dissolved in TCE is forming crystals in solution. If one leaves a freshly prepared stock solution of PET in TCE, within hours it becomes cloudy indicating crystal formation. PET in OCP on the other hand is stable for weeks. But the high boiling point of OCP also presents problems. It is necessary to anneal the polymers, at 60°C for at least 24 hr, to remove all of the solvent. TCE on the other hand will evaporate at room temperature overnight.

The uniformity of thickness can be measured by taking transmission infrared spectra at different regions using a 1 cm^3 aperture and comparing the band intensities.

The uniformity of conformation can be checked by doing a confocal Raman depth profile of the samples. The spatial resolution of the system was 2 μm and 1 μm size steps were used to obtain the profile.

5.2.1. Film preparation (Annealing).

For this set of experiments, the E99 PET polymer chips were used to give the films an initially low percentage of crystallinity. The rationale was then to anneal the films above the Tg (~73°C) to induce crystallinity. It has been found that the temperature of annealing is far more important than the length of time annealed for, in terms of degree of crystallinity induced [5.43]. Unfortunately the substrate used (ZnSe) is known to degrade at temperatures above 100°C, therefore relatively low temperatures (85-90°C) were used. This has the unfortunate side effect that only a small range of crystallinities can be produced using this method.

Films were prepared by dissolving the E99 PET (0.4g) in TCE (25 ml) under reflux (20 minutes) to give an approximately 2 % (w/w) solution. The solutions were allowed to cool for 30 minutes and 0.5 ml of solution was pipetted directly onto the clean surface of the ZnSe crystal. The solution was spread out, to evenly cover the ATR crystal with the pipette tip and allowed to dry at room temperature overnight.

The films were annealed at 85-90 °C for varying lengths of time to induce crystallinity. The crystallinity and the thickness of the film were calculated from infrared spectroscopy. The crystallinity was calculate using the method of Bellali and Vigoreux [**5.44**] described in chapter 5.1. The thickness was calculated from the calibration data described in chapter 5.3. A typical change in the CH_2 wagging region is shown for a sample of E99 before and after annealing in figure 5.1.

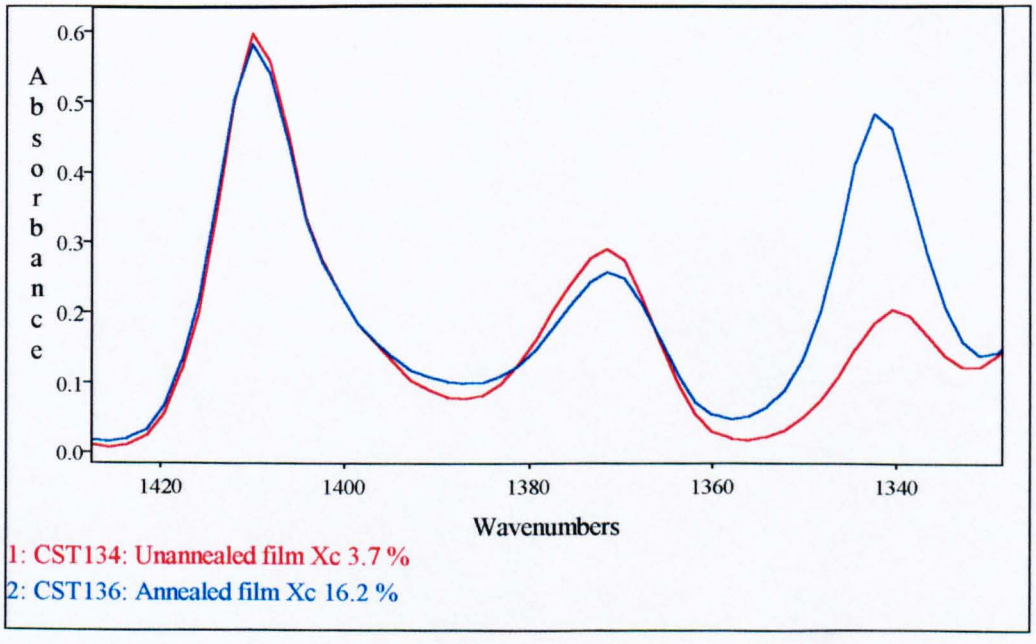

Figure 5.1. The change in crystallinity upon annealing at 85-90° C.

A range of samples were prepared in this way, table 5.2. shows a summary of the thicknesses and % crystallinities calculated for the films used in this work. Raman depth profiling showed no discernible differences in the morphology of the films on a 2 μm scale.

Film thickness / μm	Pre anneal % X_c	Anneal time / hrs	Post anneal % X_c
11.0 ± 0.2	4.0 ± 0.1	0	4.0 ± 0.1
8.7 ± 0.3	4.1 ± 0.1	0.25	6.4 ± 0.2
9.2 ± 0.2	5.0 ± 0.2	1	8.4 ± 0.2
8.0 ± 0.2	3.9 ± 0.3	3	10.1 ± 0.3
8.4 ± 0.1	4.2 ± 0.2	16	11.2 ± 0.2
8.2 ± 0.3	3.7 ± 0.1	6	12.7 ± 0.2
8.4 ± 0.1	3.6 ± 0.2	2	13.7 ± 0.3
8.6 ± 0.2	3.7 ± 0.2	8	16.2 ± 0.4

Table 5.2. Summary of the thicknesses and X_c of the films used for diffusion experiments annealed at 85-90° C.

5.2.2. Film preparation (*Trans* esterification).

In order to increase the range of crystallinity available in the solvent cast films other methods were sought. The main problem with the annealing procedure was the fragility of the ATR substrate. Two options were obvious to increase the range of film crystallinities; one was to change the substrate to Si, which was much more robust than ZnSe and use higher annealing temperatures. The other was to produce films with a range of crystallinities without the need for annealing. The former was tried, but the reduction in sampling depth (Si has a refractive index of 3.2 c.f. 2.54 for ZnSe) resulted in a loss in quality of the data produced - the water bands were much weaker and water

vapour presented a real problem during peak area integrations. The latter enabled a much more elegant method of sample preparation to be performed.

In section 1.3. it was described how the inclusion of an isophthalate group as a comonomer can reduce the degree of crystallinity in a PET sample by making the formation of *trans* conformers and subsequent chain alignment more difficult. Varying the level of isophthalate should also vary the degree of crystallinity. At high temperatures PET will readily *trans* esterify with another similar polyester to form a homogenous mixture of the two [5.45]. Therefore, by mixing E47 PET with E99 PET, in solution, at high temperatures it should be possible, by varying the ratios of the two polymers, to manufacture films with a whole range of crystallinities. As TCE had already been found to be a poor solvent for the manufacture of continuous films with a high degree of crystallinity, another solvent was tried. The solvent used was *ortho*-chlorophenol (OCP), which also now has the advantage of a higher boiling point. The mixing of the two polymers in OCP was found to produce a uniform film on casting (providing the solution was heated under reflux for a long enough period of time). Heating in excess of 12 hours with solutions of around 5 % w/w PET / OCP was found to be quite successful in this respect. Shorter periods of heating produced inhomogenous films with readily distinguishable strata of amorphous and crystalline phases. Films were prepared by heating the E99 PET and E47 PET mixture (total polymer mass, 0.4 g) in OCP (10 ml) under reflux (>12 hours) to give an approximately 5 % (w/w) solution. The solutions were allowed to cool for 5 minutes and 0.25 ml of solution was pipetted directly onto the clean surface of the ZnSe crystal. The solution was spread out, to evenly cover the ATR crystal with the pipette tip and allowed to dry

at room temperature overnight. The film was then annealed (60°C, >24 hours) to remove any excess solvent. The quality of films was found to be much better if the solution was cast whilst still hot onto a cool (ambient temperature) ZnSe ATR prism. Films which were cast from solutions which had cooled to ambient temperatures were sometimes patchy and inhomogenous in morphology. One possible explanation for this is a 'melt-quenching' type phenomenon where a rapid loss of hot solvent on casting, may decrease the mobility of the polymer solution by hastening film formation and stopping the formation of crystalline spherulites. If the solution is already cool on casting, the time it takes to 'set' is longer and therefore the probability of crystalline growth is that much greater. The films were characterised in the same way as the annealed films, with the crystallinities and thicknesses calculated using the methods described. The films manufactured are summarised in table 5.3.

Film thickness / μm	E47 : E99	X_c %
8.2 ± 0.1	0:1	4.9 ± 0.3
8.6 ± 0.3	1:3	8.4 ± 0.4
8.2 ± 0.2	1:2	11.2 ± 0.3
8.4 ± 0.2	1:1	18.2 ± 0.2
8.0 ± 0.2	1:0	25.0 ± 0.2

Table 5.3. ***Summary of the thicknesses and X_c of the films used for diffusion experiments(trans-esterified polymer).***

It is interesting to note that manufacture in this way does not seem to impair the film integrity. The variations in thickness and crystallinity along the film are comparable to those manufactured solely from E99 and then annealed (Chapter 5.2.1.). This method of film preparation does allow a slightly larger range of crystallinities to be produced, but does have the disadvantage of taking up to 3 times longer than the annealing method.

There may also be differences in the crystal sizes between the two systems. Annealing tends to increase the size of existing crystals, but varying the level of comonomer in the polymer solution may result in films of differing numbers of small crystals.

5.3. Thickness calibration

In order to calculate the diffusion coefficients for the sorption of small molecules into PET it was imperative to know the film thickness with some degree of accuracy. There are a number of different ways to calculate the thickness of polymer films, including mechanical measurement of the step height, elipsometry and infrared spectroscopy (making use of the Beer-Lambert law). This work has used an infrared technique calibrated using mechanical step height measurements to calculate the film thicknesses.

The step heights were calculated from a surface profiler (Laser Form Talysurf) which measures height as a function of distance along a predefined raster. In order for the step heights to be calculated it was necessary to remove 5 mm of the film, from the extremes, to give a good estimate of the baseline. The stage on which the samples were mounted can be moved in the x, y and z directions therefore it was not possible to calculate the absolute height of the films, only height relative to the baseline. The film edges were removed using a swab dipped in TCE. This often resulted in a sharp spike in the Talysurf output where some of the polymer had been moved rather than removed. This is obvious in figure 5.2. which shows the typical output from a surface profiler.

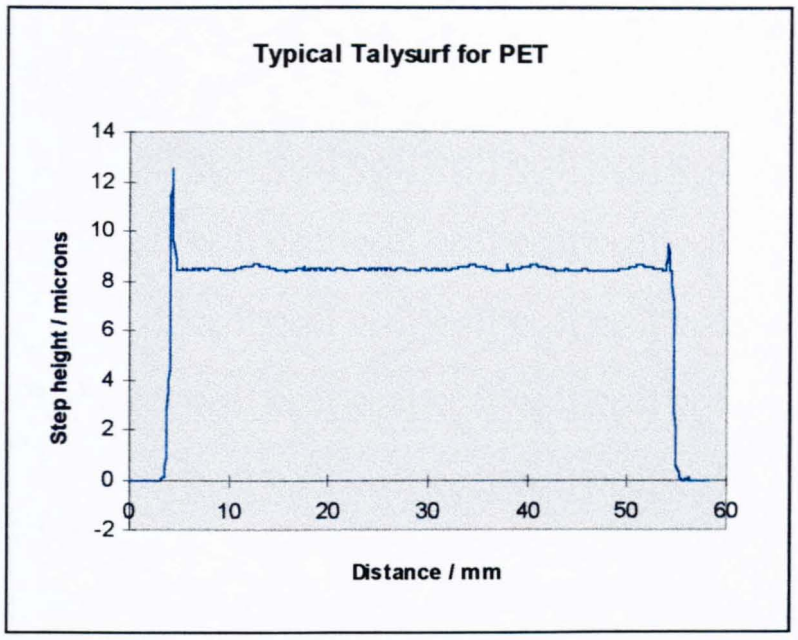

Figure 5.2. A typical surface profile output for PET cast onto a ZnSe ATR prism.

The thicknesses were calculated by taking the mean value, of the measured step height relative to the baseline, of 20 points along the profile.

It is not possible to use the films that thicknesses have been obtained for in a diffusion experiment. The removal of part of the film (for baseline purposes) means that the ATR prism would be directly exposed to the water reservoir. This makes distinction between water from the PET sample and water from the reservoir very difficult. Therefore it is necessary to use another means of calculating film thickness. Films of known thickness were therefore used to calibrate an absorbance versus thickness plot using transmission infrared.

The Beer-Lambert law will be obeyed in infrared for absorbances less than 1 Abs unit. In a spectrum such as PET there are many bands that are above this level for the thickness range used in this work. This instantly rules out bands at 1700, 1300 and 1100 cm^{-1} for

use as a calibration band. The search for a suitable band is also made more difficult by the fact that many bands are conformationally sensitive. In industry, a weak band at 1950 cm^{-1} is used for thickness calibration of films that are in excess of 100 μm thick. This band is too weak to be used with any confidence for the calibration of films between 6 and 15 μm thick, so another candidate was required. Numerous authors have used the band at 1410 cm^{-1} for the correction of ATR spectra in quantitative work where reproducibility of contact is difficult [5.46]. This band is found to be non conformationally sensitive, non dichroic in nature and not too strongly absorbing. It is with those reasons in mind that this band has been chosen for the calibration.

The calculation of band intensity, in this case band area, could not be achieved simply by integrating the area under the peak. The peak at 1410 cm^{-1} is situated very close to the conformationally sensitive CH_2 wagging modes at 1370 and 1340 cm^{-1}. This work involves the calculation of diffusion coefficients as a function of crystallinity, which means that the 'tails' of bands from the conformationally sensitive CH_2 wagging modes sufficiently overlap enough with the 1410 cm^{-1} band to cause variations in the band area if simple integration between two points is applied. Therefore a curvefit of the region is carried out with the area of the peak at 1410 cm^{-1} used in the calibration calculation. This same curvefit data is, incidentally, used in the calculation of the % crystallinity described earlier.

Figure 5.3. shows the effect of conformation on the intensity of the band at 1410 cm^{-1}. The spectra (CST112 and CST118) are the same E99 PET sample that has been annealed for three hours.

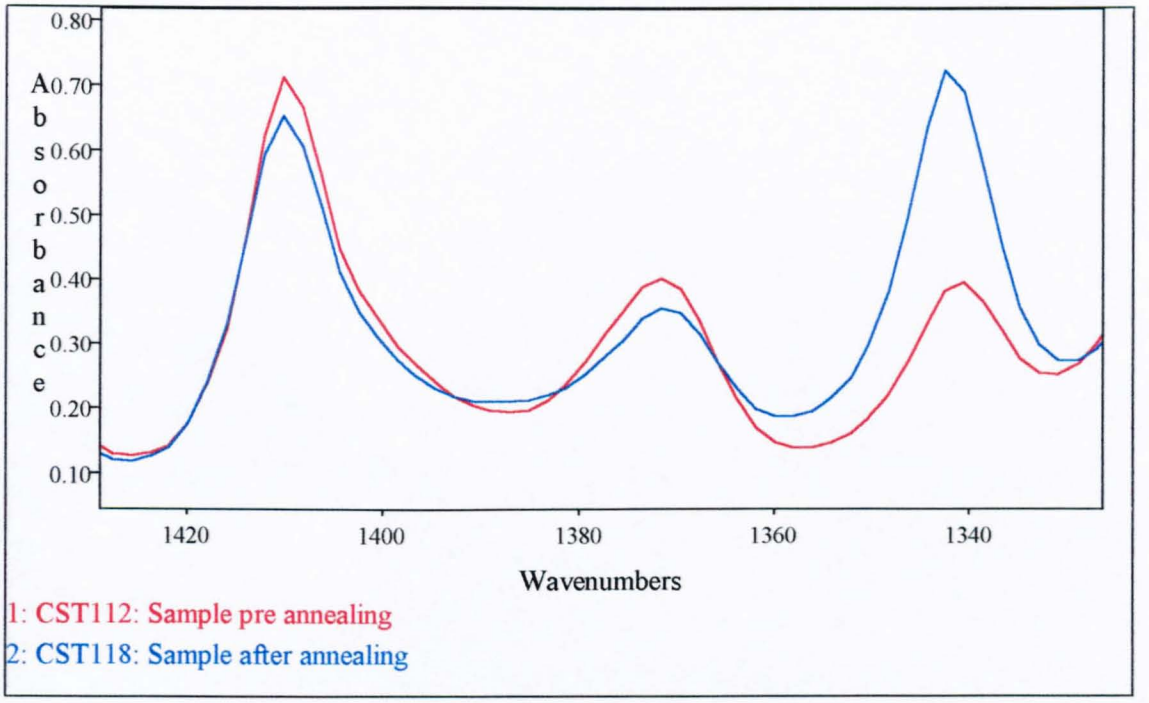

Figure 5.3. ***The effect of conformation on the intensity of the band at 1410 cm^{-1} used in the thickness versus integrated absorbance calibration plot.***

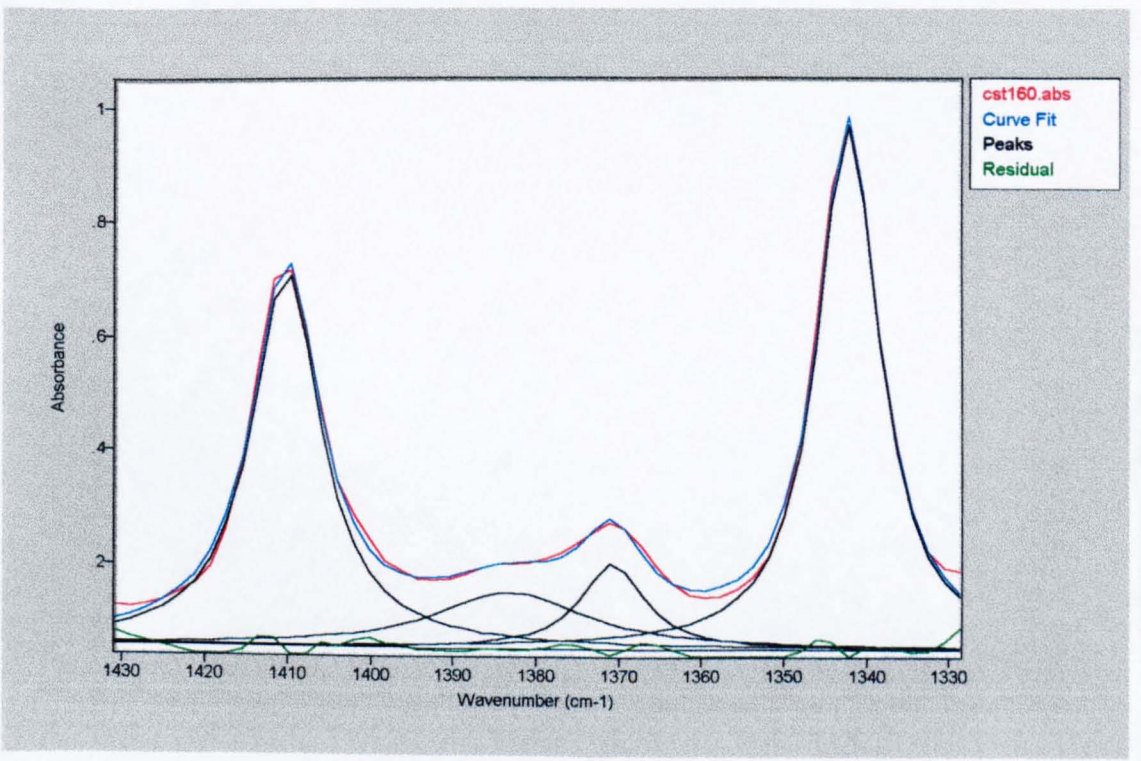

Figure 5.4. ***Typical curve fit of the CH_2 wagging modes of PET.***

The change in crystallinity, from 4 % to 10% represents a change in density from 1.33 g cm^{-3} to 1.37 g cm^{-3} [5.47]. For a 10 μm sample, the change in density would result in a change of thickness to 9.7 μm (Appendix 5.1). According to the Beer-Lambert Law, since the parameters changing are the thickness and concentration (i.e. density), no decrease in absorbance should be noted as they should compensate for each other. Integrating between two points (1485 to 1386 cm^{-1}) gives relative areas of 6.95 and 6.12 cm^{-1} respectively. This equates to a 12 % change in area. Using a curve fitting procedure one obtains peak areas of 10.1 and 9.9 cm^{-1} respectively. This equates to a 2 % change in peak area which is closer to no change which is expected. This difference could be accounted for by the slightly different regions that one has sampled. It is very difficult to sample the exact same spot each time. Therefore in order to minimise errors the peak areas from curve fitting procedures were used. Spectra were recorded by sampling, using a $1cm^3$ diameter aperture, at 5 different points along the ZnSe crystal. The mean and standard deviation of values obtained using curve fitting procedures were used to provide data for the calibration.

Thickness measurements (Talysurf) / μm		Curve fitting data / cm^{-1}	
Mean	Standard deviation	Mean	Standard deviation
0	0	0	0
2.5	0.45	3.21	0.51
4.4	0.32	6.4	0.42
6.5	0.35	9.6	0.31
8.1	0.36	11.9	0.22
8.4	0.37	12.56	0.31
8.6	0.26	12.74	0.22
9.8	0.36	14.2	0.29
12.3	0.54	17.5	0.41
16.3	0.89	22.69	1.12
19.6	1.26	26.58	1.06
20.6	1.39	28.36	1.24

Table 5.4. Thickness calibration data for cast PET films

From figure 5.4. it is clear that the 1410 cm^{-1} band fits all the criterion required for a good calibration. The errors involved appear to be accentuated at thicknesses higher and lower than 10 μm. For thicker films the concentration of the polymer solution was relatively high. This could cause problems of the polymer beginning to 'drop' out of solution. The films > 15 μm thick were in general more uneven and less uniform in thickness than films of 8-12 μm. Films around the 8 μm thickness mark were highly reproducible and of uniform thickness throughout. The thinner films were not really of use for the diffusion work, as the films were required to be thicker than the effective sampling depth of the ATR experiment (in this case ~ 3 μm) in order to avoid the sampling of the bulk water in the reservoir.

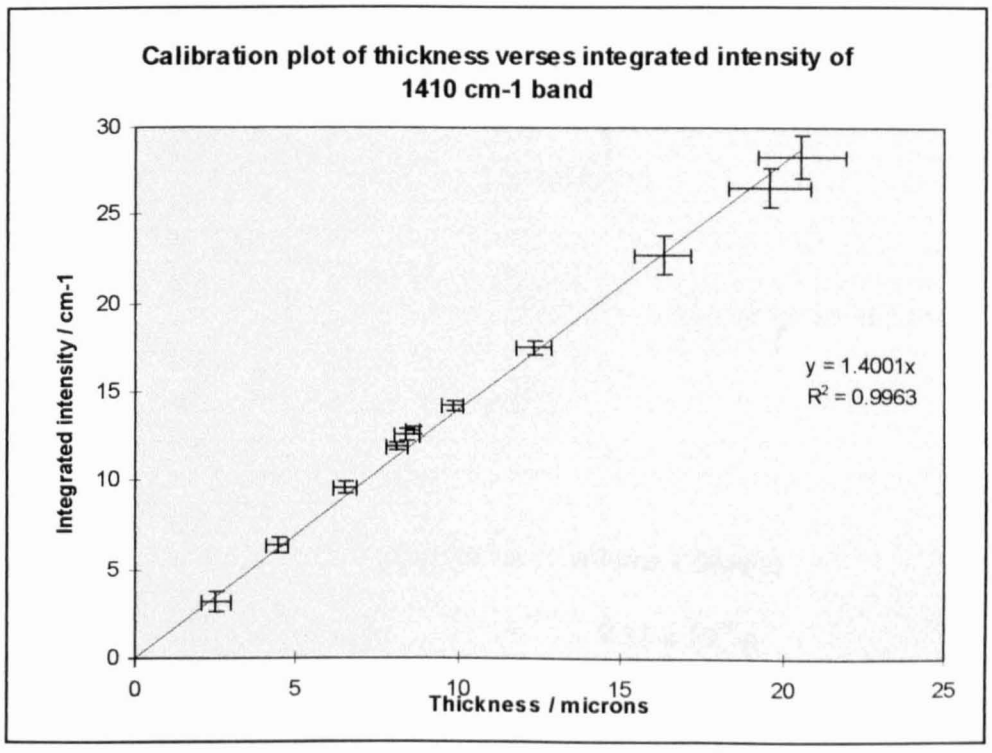

Figure 5.5. Calibration plot for thickness versus integrated absorption for cast PET films

Linear regression analysis of the mean values plotted in figure 5.4. shows that the data can be fitted to a simple (y = 1.4001x) relationship between 0 and 21 μm, with a

Linear regression analysis of the mean values plotted in figure 5.4. shows that the data can be fitted to a simple ($y = 1.4001x$) relationship between 0 and 21 μm, with a correlation coefficient (R^2) of 0.9963. This means that the thickness (in μm) of any of the films used during this work could simply be calculated by multiplying the curve fitted peak at 1410 cm^{-1} by 1.4001. But this does not take into account the density change for different crystallinities.

Figure 5.4. shows the plot of the integrated intensity of the 1410 cm^{-1} band as a function of thickness for amorphous PET. Amorphous PET has a density of 1.33 g cm^{-3}. For samples with a higher degree of crystallinity, therefore a greater density, the thickness, calculated from the calibration plot, will be higher than the real value. This can be corrected for by using a density correction. For a given crystallinity, the density of PET is known. If one simply multiplies the calculated thickness by the ratio of the density change, then the corrected thickness can be obtained.

Appendix 5.1

ZnSe ATR prism has a surface area of 7 x 1 cm^2.

Film of thickness 10 μm (1 x 10^{-3} cm);

Total mass of PET for density of 1.33 g cm^{-3} is ∴ volume x density

$7 \times 1 \times 10^{-3}$ cm^3 x 1.33 g cm^{-3} = 9.31×10^{-3} g

On crystallising density increases (to 1.37 g cm^{-3}), but total mass is the same ∴ thickness

9.31×10^{-3} g ÷ (1.37 g cm^{-3} x 7 cm^2) = 9.70×10^{-4} cm

= 9.70 μm

Morphologically it is likely that three key elements will determine the rate of diffusion of liquid through a semi-crystalline film. The first will be the degree of crystallinity. This is obvious as crystallites have been shown to be impermeable to penetrant solvents. The second is the crystal domain size. There may well be differences in the diffusion kinetics of systems with small crystal sizes and systems with large crystals, due to the boundaries of the crystals having different properties to the bulk. Finally the packing and orientation of the crystals is also important, as the direction of crystal orientation with respect to the direction of diffusional flux will play a prominent role in dictating the overall diffusion rate.

The two polymer systems used in this work may well contain different sets of crystal sizes. To begin with, the systems use different solvents. It is known that solvent type plays an important role in crystal formation in polymers. Secondly, the differing degree of comonomer concentration will also play an important role in determining the crystal sizes. Introducing more comonomer effectively introduces more point defects therefore limiting the crystal size and lamellar thickness. It would seem most likely that annealing the polymer containing a higher level of comonomer will produce a structure containing many small crystals, where producing a film from solution containing a lower level of comonomer will produce larger crystals. From these two systems it is feasible to have two films with the same overall level of crystallinity, but with different crystal sizes which may have an effect on the rate of diffusion.

5.4.1. Results and discussion.

The spectra were obtained on a Mattson Polaris FTIR spectrometer, using a Mattson Macro program described in chapter 4.5. The instrumental parameters and other details of the diffusion experiment are given in chapter 4.5. The diffusion coefficients were calculated from a Matlab program based on a program originally written in Pascal by Dr. Marcia Pereira [5.48] described in chapter 4.6. Examples of simulated outputs from the program are given in chapter 4.6. along with an explanation of its use.

A summary of the diffusion coefficients calculated for the annealed samples is given in table 5.5 and figure 5.6. shows a plot of the calculated diffusion coefficients as a function of measured crystallinity.

Film thickness / μm	X_c %	D / x 10^{-9} cm^2s^{-1}
11.0 ± 0.2	4.0 ± 0.1	8.57 ± 0.33
8.7 ± 0.3	6.4 ± 0.2	6.87 ± 0.48
9.2 ± 0.2	8.4 ± 0.2	5.84 ± 0.26
8.0 ± 0.2	10.1 ± 0.3	4.54 ± 0.23
8.4 ± 0.1	11.2 ± 0.2	4.05 ± 0.30
8.2 ± 0.3	12.7 ± 0.2	3.77 ± 0.10
8.4 ± 0.1	13.7 ± 0.3	2.92 ± 0.22
8.6 ± 0.2	16.2 ± 0.4	1.80 ± 0.11

Table 5.5. Tabulated thicknesses, % crystallinity and diffusion coefficients for annealed PET samples

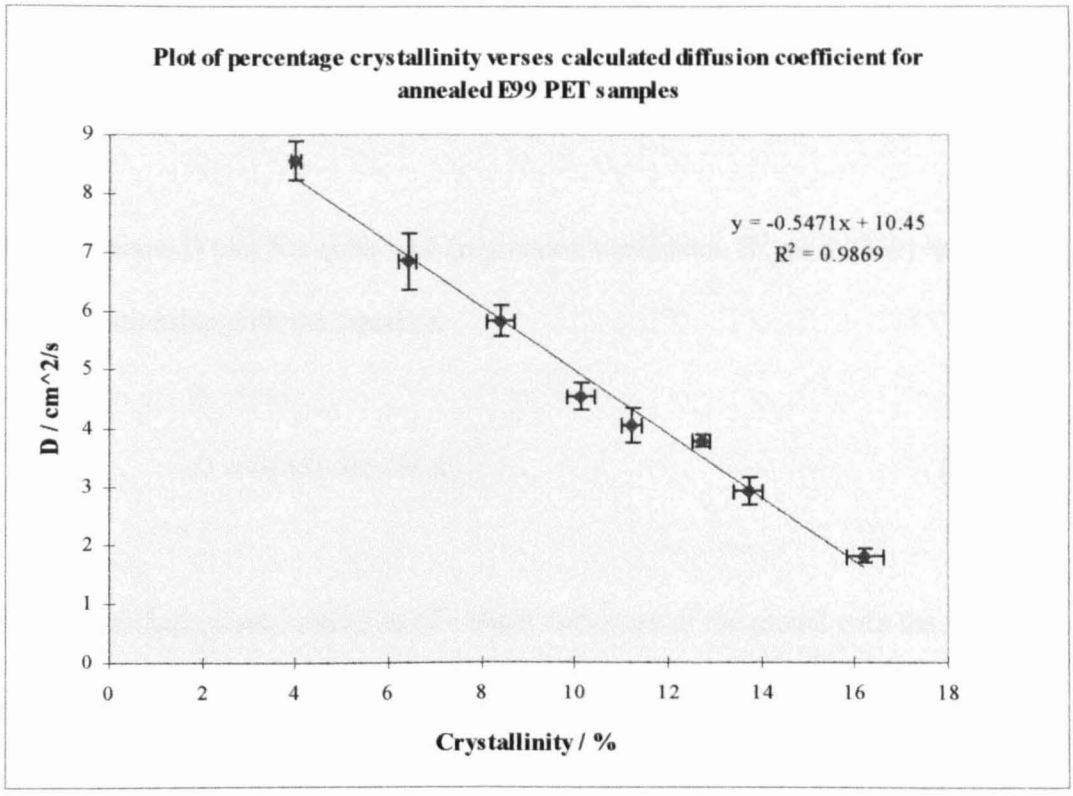

Figure 5.6. Plot of D versus % crystallinity for annealed PET samples.

As crystallinity increases the diffusion rate decreases. From a simple perspective, this is expected to be due to diffusion being limited to amorphous regions, with the crystalline regions acting as a barrier [**5.30, 5.49**] reducing the volume available to allow transport. At greater levels of crystallinity it is believed that other effects can become important [**5.30**]. These include crystallite anchoring points perturbing the polymer relaxations thereby reducing the ability of the polymers to flex and allow small molecules through. The essentially linear nature of the X_c versus D plot (figure 5.6.) seems to suggest that only a reduction of free volume space effect is seen for this set of experimental data. It known that orientation can greatly affect the rate of diffusion [**5.49**]. This system can simply be thought of as small pockets of crystalline regions in a matrix of amorphous

material. However, inducing crystallinity by annealing does not impart any preferential orientation on the system.

The X_c versus D plot fits quite well (regression coefficient, R^2, of 0.9869) to a simple linear relationship with the equation

$$D = 10.45 - 0.5474 X_c \qquad \text{(eq. 5.1)}$$

There is perhaps some indication of a slight curvature of the model with the more highly crystalline samples (> 12 %) having a calculated D value higher than predicted by equation 5.1. Table 5.6. shows the comparison between predicted (from the simple linear model) and calculated diffusion coefficients.

X_c %	Calculated D / x 10^{-9} cm^2s^{-1}	Predicted D / x 10^{-9} cm^2s^{-1}
4.0 ± 0.1	8.57 ± 0.33	8.26 ± 0.05
6.4 ± 0.2	6.87 ± 0.48	6.94 ± 0.09
8.4 ± 0.2	5.84 ± 0.26	5.85 ± 0.11
10.1 ± 0.3	4.54 ± 0.23	4.92 ± 0.16
11.2 ± 0.2	4.05 ± 0.30	4.32 ± 0.11
12.7 ± 0.2	3.77 ± 0.10	3.50 ± 0.11
13.7 ± 0.3	2.92 ± 0.22	2.95 ± 0.16
16.2 ± 0.4	1.80 ± 0.11	1.58 ± 0.22

Table 5.6. ***Comparison of the calculated and expected D values for a given % crystallinity for annealed PET samples***

The output diffusion profiles are shown in figures 5.7. - 5.14.

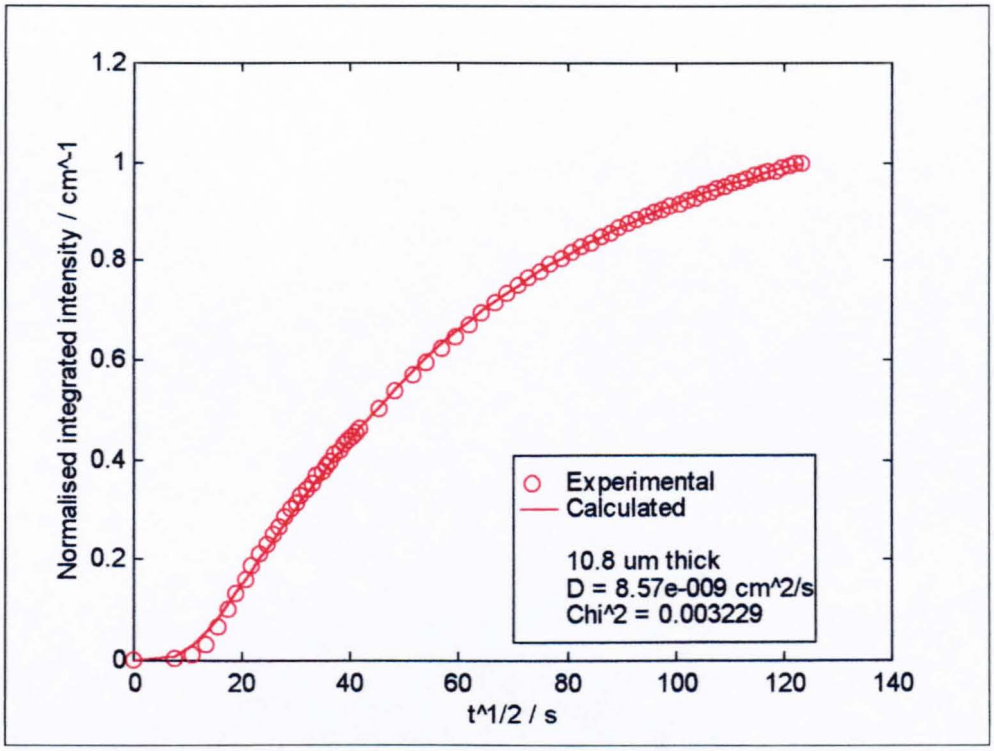

Figure 5.7. Experimental and calculated diffusion profile for 4% crystalline PET.

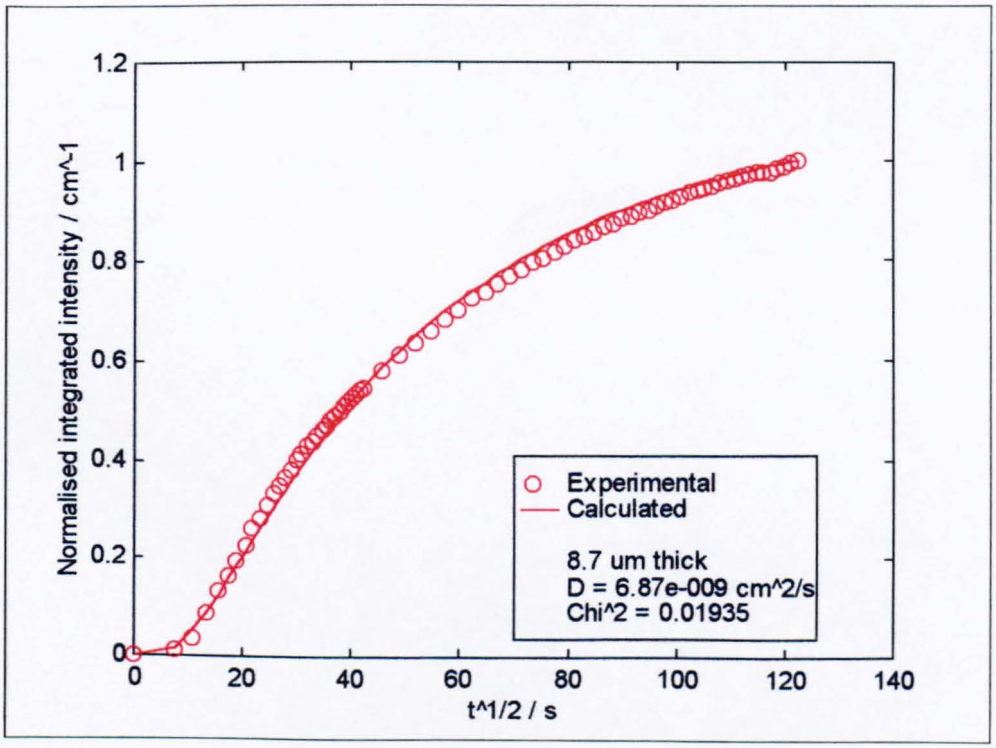

Figure 5.8. Experimental and calculated diffusion profile for 6.4 % crystalline PET.

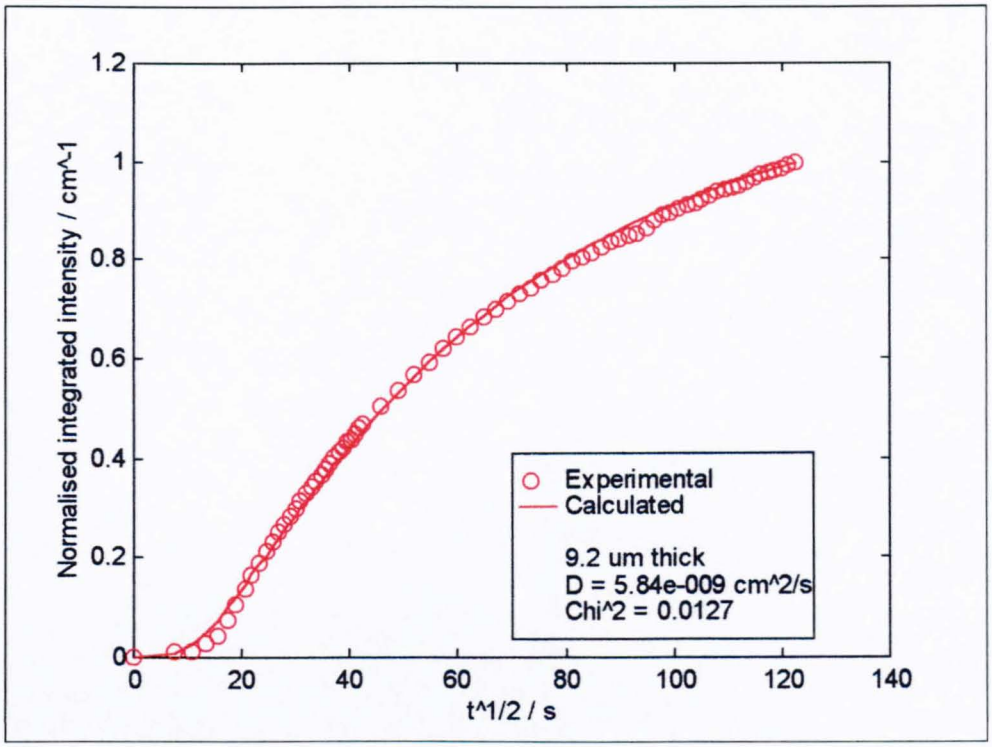

Figure 5.9. Experimental and calculated diffusion profile for 8.4 % crystalline PET.

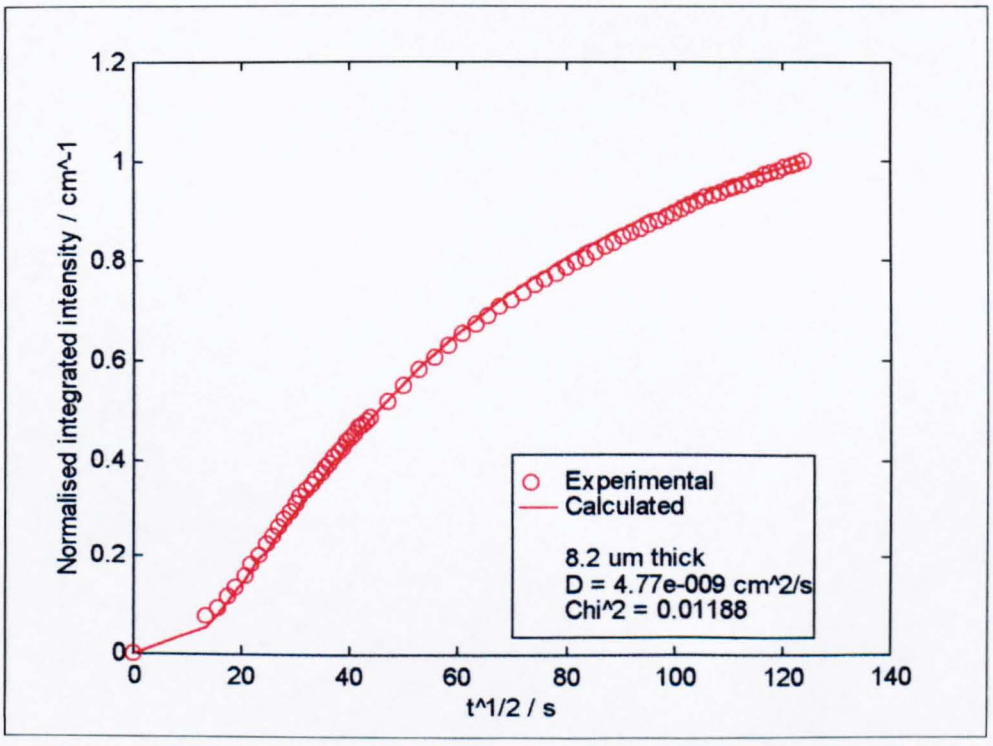

Figure 5.10. Experimental and calculated diffusion profile for 10.1 % crystalline PET.

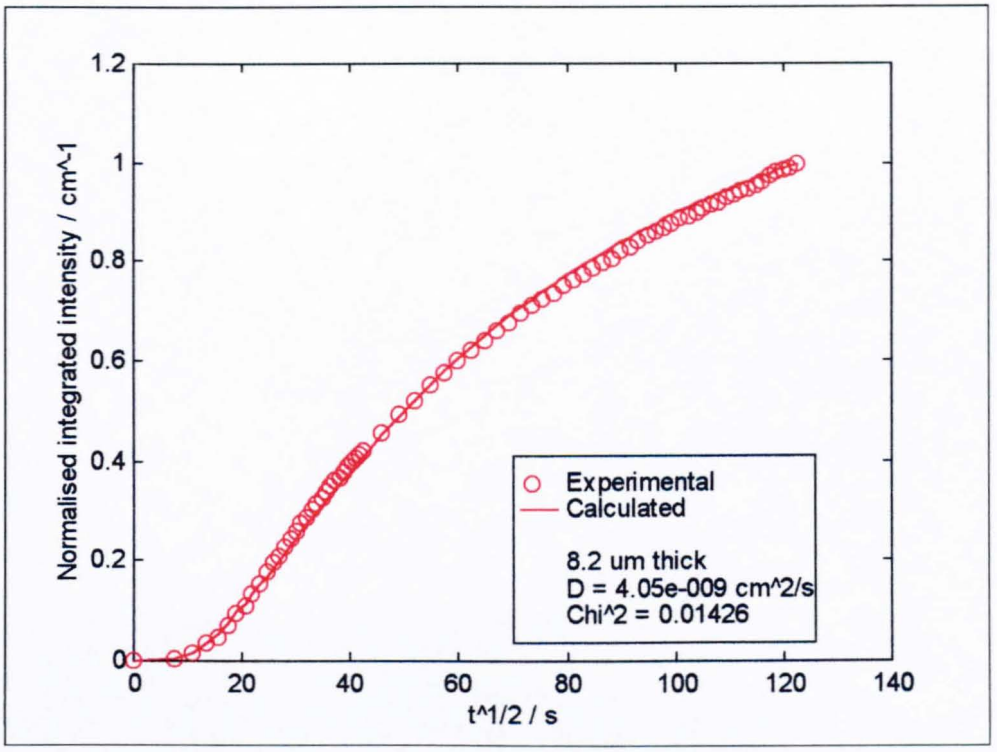

Figure 5.11. Experimental and calculated diffusion profile for 11.2 % crystalline PET.

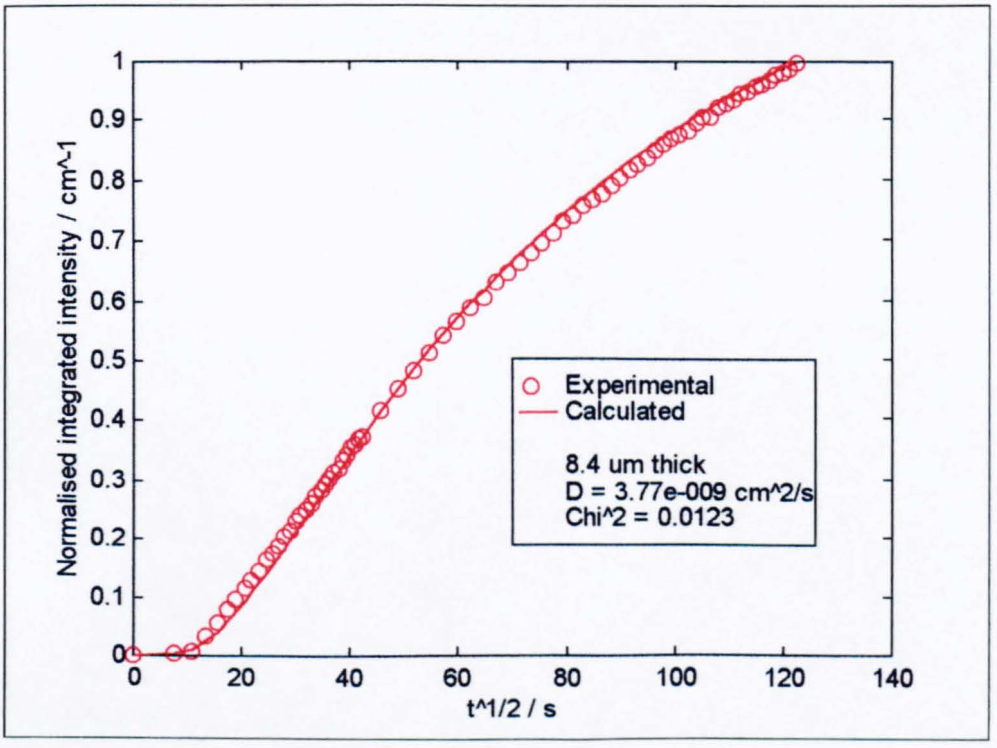

Figure 5.12. Experimental and calculated diffusion profile for 12.7 % crystalline PET.

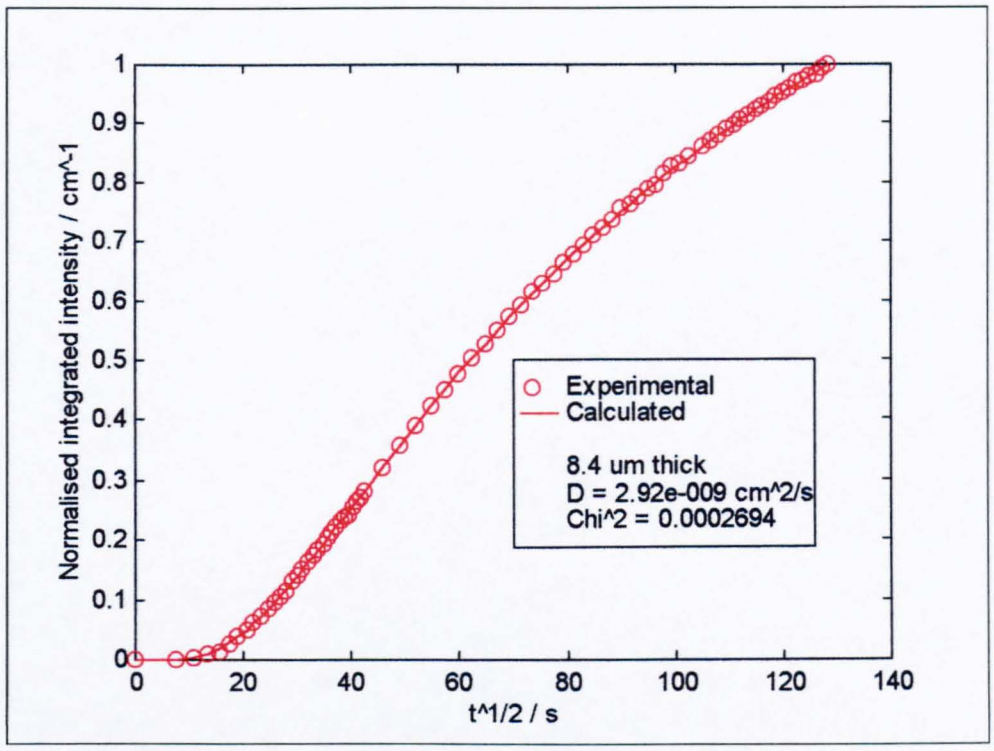

Figure 5.13. Experimental and calculated diffusion profile for 13.7 % crystalline PET.

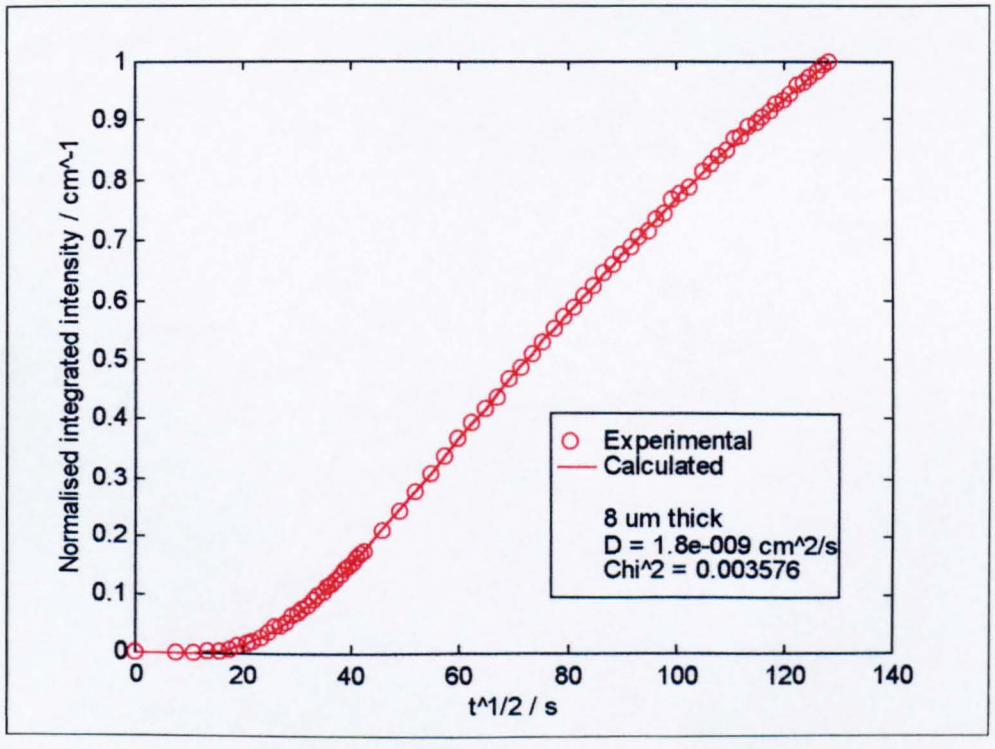

Figure 5.14. Experimental and calculated diffusion profile for 16.2 % crystalline PET.

As described earlier, the output from an ATR diffusion experiment is a convolution of the evanescent wave with the liquid diffusion profile. The most distinguishing feature for of such data is the apparently low intensity at shorter times producing an 'S' shape to the curve. This is a direct result of the exponential decay of the evanescent wave. As the penetrant moves further into the evanescent field the response is therefore itself more exponential in nature than linear.

For more amorphous films, at shorter time periods, the fit of the model is poorer than at longer times. A better fit at these shorter times would be obtained using a slower diffusion coefficient. This is clearly shown in figures 5.7 - 5.9. This is not seen in figures 5.11. - 5.14. This 'tail' is caused by the time it takes for the sample penetrant to enter the evanescent field. Comparison with the simulated diffusion profiles in chapter 4, suggests that longer 'tails' are associated with slower diffusion rates. It appears that the best fit to a purely Fickian model gives a diffusion constant higher than that expected from the data at shortest times.

One possible explanation for these observations is an increase in crystallinity at the surface, forming a barrier to the diffusant. This crystallinity difference has been shown by Hayes et al using XPS [5.50]. As crystallinity increases throughout the film (figures 5.11. - 5.14.), and the bulk crystallinity approaches that of the surface, this makes differences between calculated and experimental less noticeable. Since the comonomer is incorporated in order to reduce the crystallinity, by introducing 'kinks' into the polymer backbone, it may be that it is not possible to induce more crystallinity at 85 - 90° C than

is already present at the surface, where less restricted motion is allowed during film formation. Other workers such as Walls et al [5.46, 5.51] and Hayes et al [5.50] have noted difference in the surface crystallinity to the bulk. It is interesting to note that the Raman microprobe with its 2 μm depth resolution was unable to pick out any discernible differences between the bulk and surface crystallinity. Walls on the other hand used sampling depths of 0.5 and 1.5 μm during his ATR experiment and differences in morphology were noted. This suggests that if any differences in morphology are present between the surface and the bulk then they are in the top 0.5 μm of the film.

It is also possible that the initially slower diffusion constant is due to a plasticisation effect of the water on the polymer chains allowing greater mobility. The fact that this only occurs on samples that are lower in crystallinity (< 8.5 %) seems to place doubt on this theory. Indeed, Van Alsten and Coburn [5.30] have postulated that the increased amount of water in the bulk may restrict the motions of the polymer chains reducing D values. We have not detected this in our work.

A summary of the diffusion coefficients calculated for the *trans* esterification samples is given in table 5.7. and figure 5.15. shows a plot of the calculated diffusion coefficients as a function of measured crystallinity.

Film thickness / μm	X_c %	D / x 10^{-9} cm^2s^{-1}
8.2 ± 0.1	4.9 ± 0.3	8.35 ± 0.11
8.6 ± 0.3	8.4 ± 0.4	5.58 ± 0.31
8.2 ± 0.2	11.2 ± 0.3	3.88 ± 0.24
8.4 ± 0.2	18.2 ± 0.2	1.35 ± 0.21
8.0 ± 0.2	25.0 ± 0.2	0.52 ± 0.24

Table 5.7. ***Tabulated thicknesses, % crystallinity and diffusion coefficients for trans-esterified PET samples***

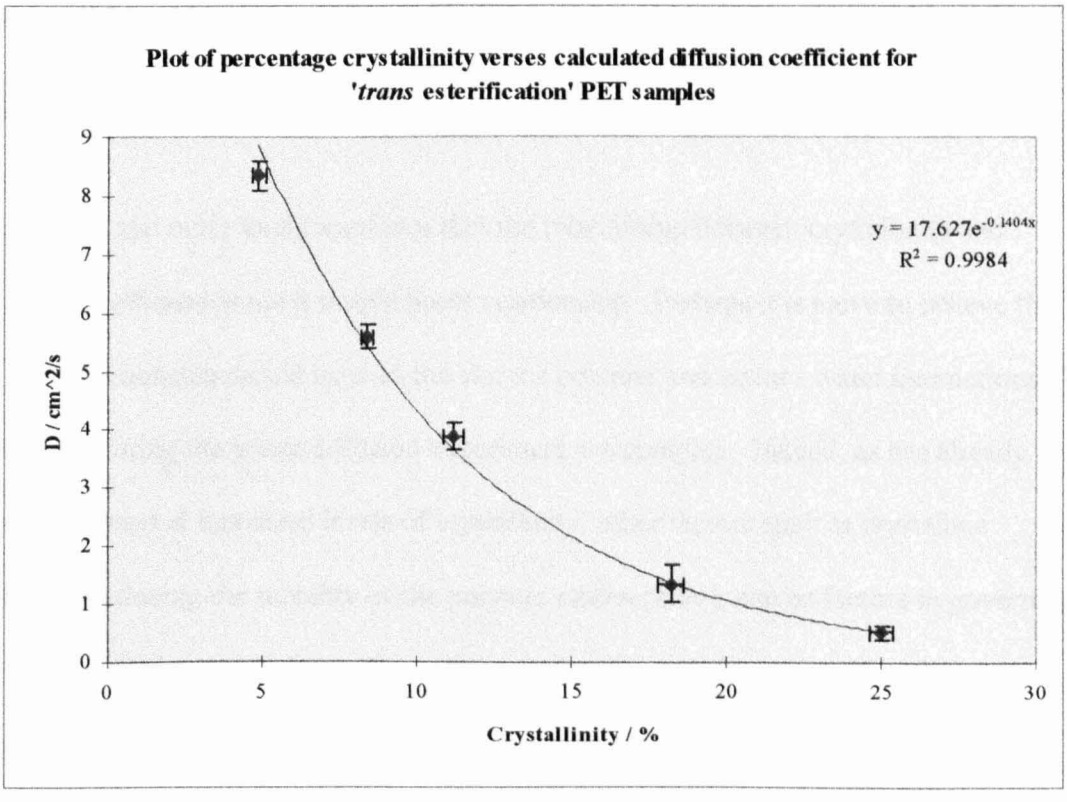

Figure 5.15. ***Plot of calculated D values for measured % crystallinity for PET.***

In a similar fashion to the data from annealed PET samples the D values decrease with increasing X_c. The same arguments vis á vis lower volumes of free space within the polymer matrix and increased barrier density can again be applied. This time the

relationship is not linear. The D values for higher crystallinities are higher than expected for the linear model used earlier. This could be accounted for in several ways. Firstly the diffusion of water may not be limited to just the amorphous regions but may occur at a reduced rate through the crystalline regions. The idea that water may diffuse in crystalline regions is in stark disagreement to work published elsewhere [5.49]. If this were to be the case then the diffusion profiles would not fit a pure Fickian model, but may be accounted for by a dual-sorption type model with two diffusion coefficients. The output diffusion profiles as shown in figures 5.16. - 5.20. generally fit the Fickian model very well. Therefore one can discount this idea.

The second and more likely answer is that the relationship between crystallinity and diffusion coefficient is not a simple linear relationship. Perhaps it is naive to believe that a simple relationship would exist as the water / polymer and water / water interactions that occur during the water diffusion experiment are complex. Indeed, as has already been mentioned at increased levels of crystallinity, other factors such as crystalline anchoring reducing the mobility of the polymer chains [5.30], can be factors in governing the water diffusion coefficient. These other factors would perhaps manifest themselves as an even greater reduction of the diffusion coefficient with increased crystallinity, not seen in this work.

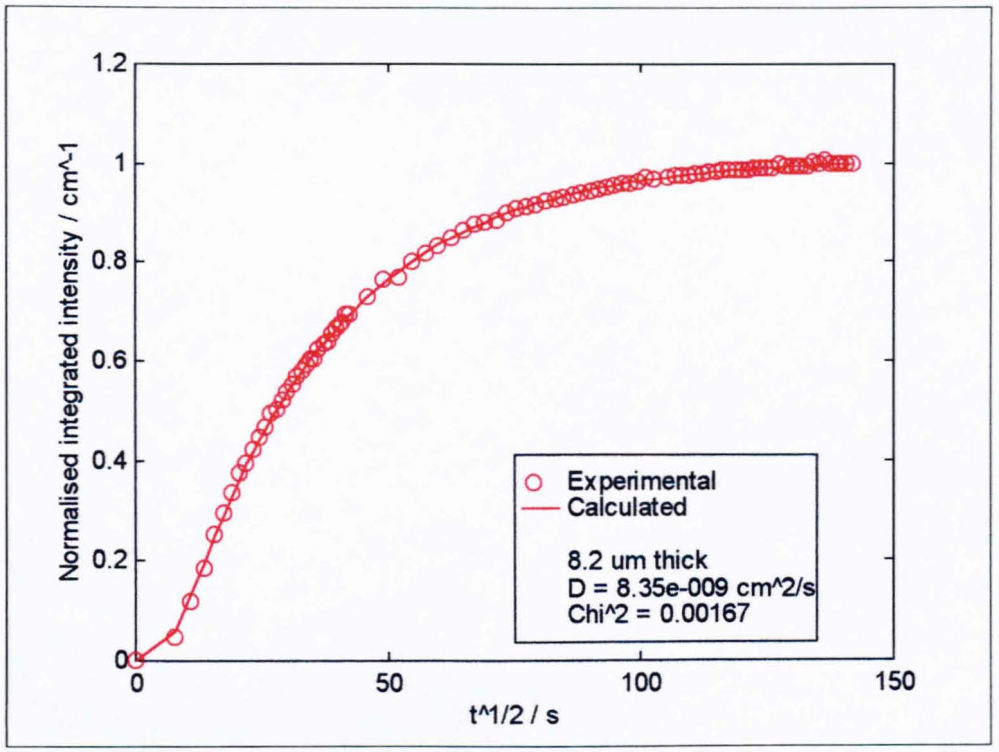

Figure 5.16. Experimental and calculated diffusion profile for 4.9 % crystalline PET.

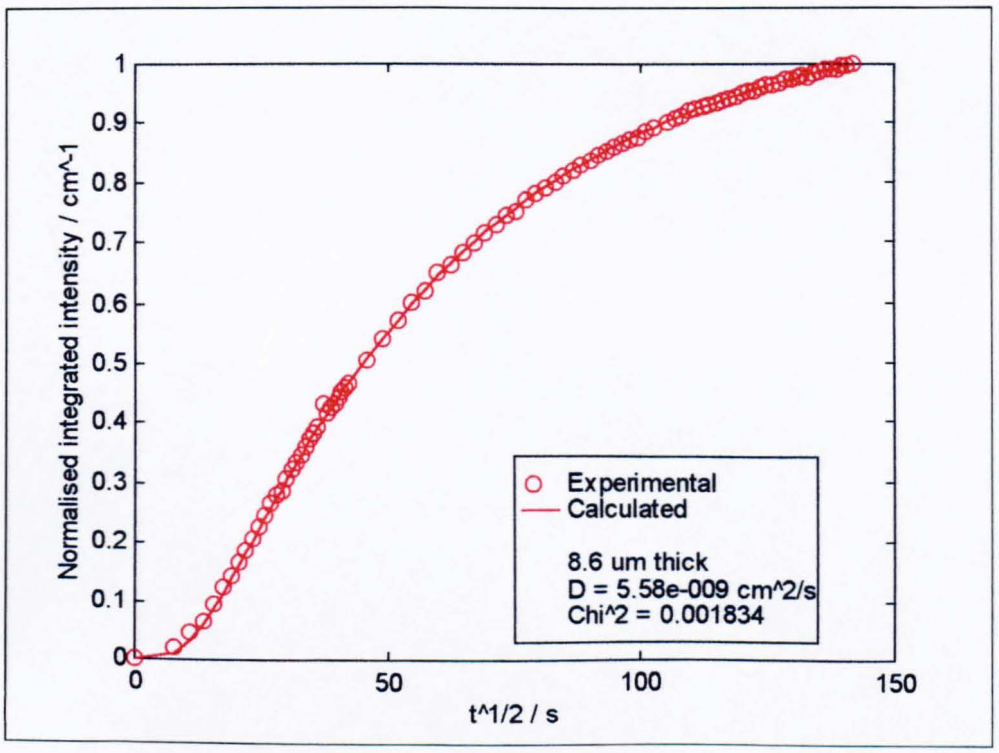

Figure 5.17. Experimental and calculated diffusion profile for 8.4 % crystalline PET.

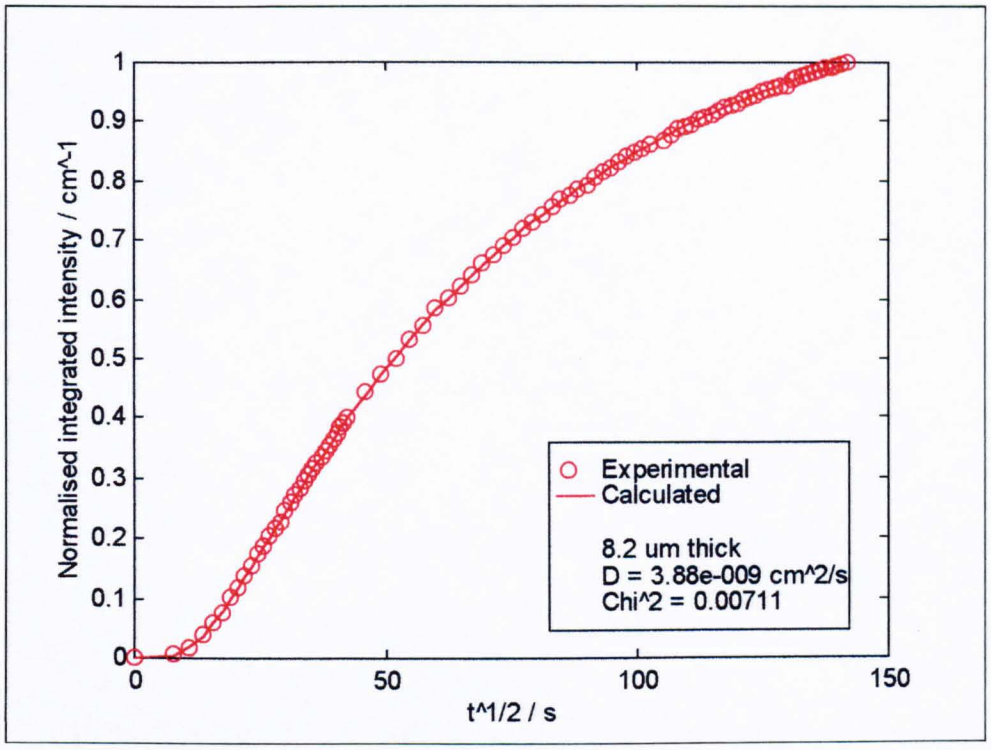

Figure 5.18. Experimental and calculated diffusion profile for 11.2 % crystalline PET.

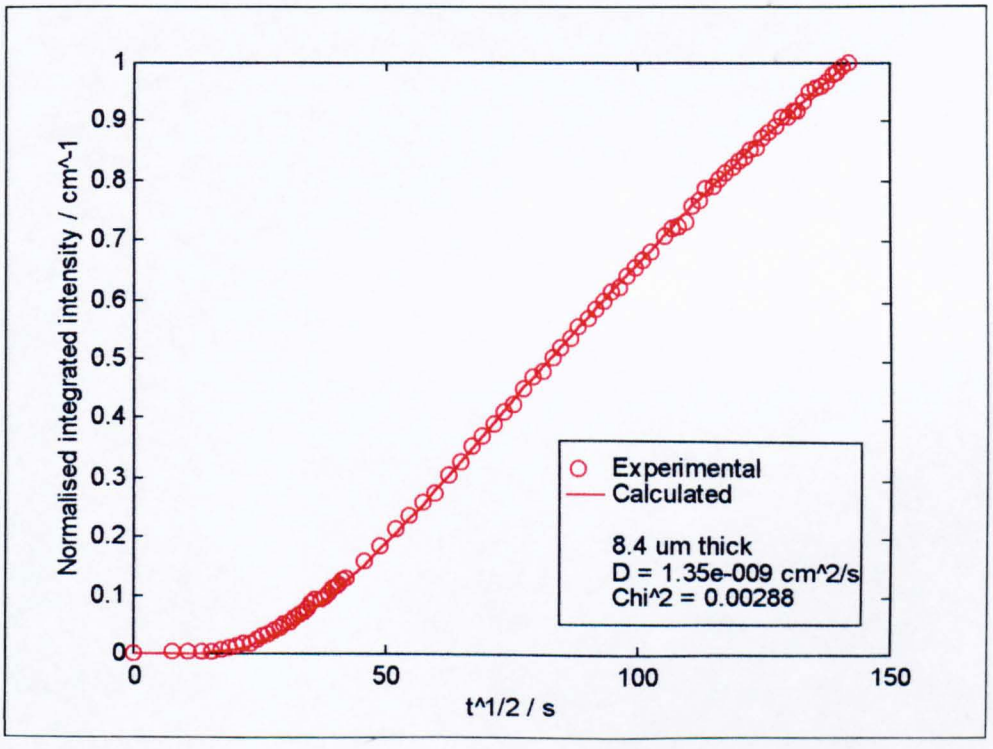

Figure 5.19. Experimental and calculated diffusion profile for 18.2 % crystalline PET.

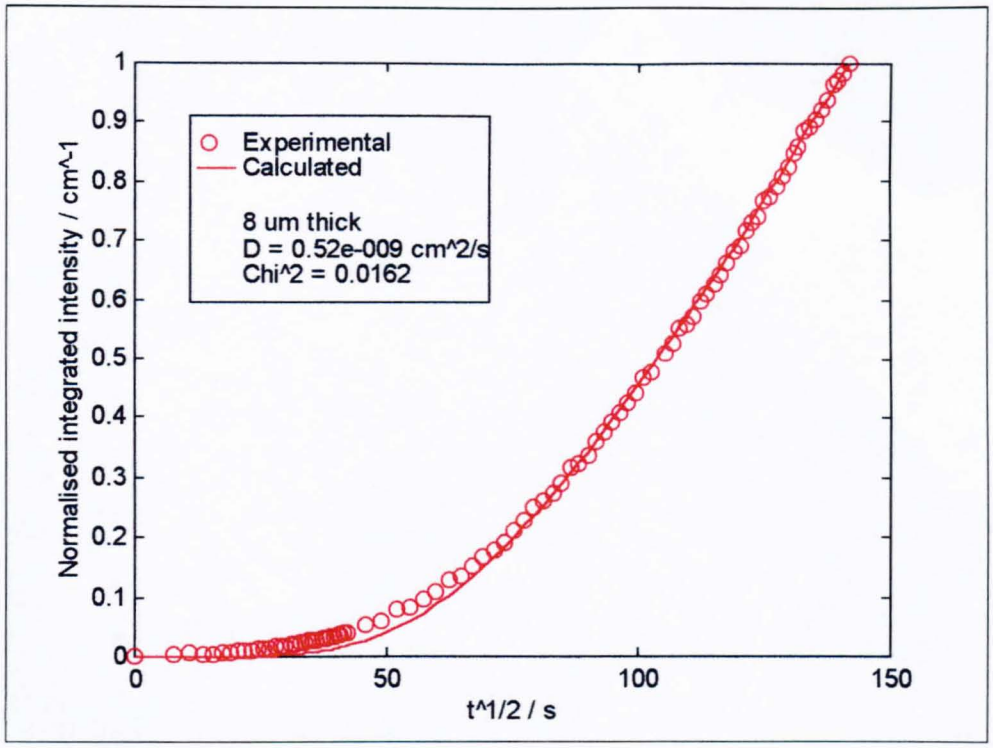

Figure 5.20. Experimental and calculated diffusion profile for 25.0 % crystalline PET.

Figures 5.16. - 5.20. show the calculated and experimental diffusion outputs from the ATR experiments. It is interesting to note that the poor fitting at short times for lower crystallinities observed in the annealing work, is not present in this data. This implies that the surface crystallinity effect may be more marked in TCE, i.e. is solvent dependent. As mentioned earlier, TCE appeared to encourage the formation of crystals in solution, indeed the highly crystalline films shown in chapter 1 were manufactured by allowing the polymer solution to stand for several days.

The most interesting feature of the diffusion profiles, for *trans* esterification samples, is an effect opposite to the 'slower diffusion rate at shorter times' effect seen in annealed samples. For the 25 % crystalline sample (figure 5.20.) and less so for the 18.2 % crystalline sample (figure 5.19.) the diffusion constant at shorter times seems to be more

rapid than that in the bulk. This feature could be accounted for by slight discontinuities, on a microscopic scale, allowing the more rapid diffusion of water into the sample at the surface. The manufacture of continuous reproducible films of higher degrees of crystallinity (>25 %) is a batch dependent phenomenon. 'Pores' at the surface would perhaps lead to such an effect. This more rapid diffusion at shorter times will undoubtedly have some bearing on the overall calculated D value, since the calculated D is simply a 'D of best fit'. This calculated D will therefore be higher than the real D, though perhaps not enough to indicate a linear relationship between X_c and D.

Figure 5.15. tentatively fits the relationship between Xc and D to an exponential function the equation of which is shown.

$$D = 17.627 \exp(-0.1404 X_c) \qquad \text{(eq. 5.2)}$$

The correlation coefficient (R^2) for this model is 0.9984 which is very good. It is interesting to note that the model also agrees well with the results obtained from the annealing work. The model is not valid for values of crystallinity less than ~ 5 % but appears to be very reasonable for other values of crystallinity within both data sets.

Table 5.8. shows expected D values fitted to this exponential model compared to calculated D values. The values are in very good agreement.

X_c %	Calculated D / x 10^{-9} cm^2s^{-1}	Predicted D / x 10^{-9} cm^2s^{-1}
4.9 ± 0.3	8.35 ± 0.11	8.85 ± 0.38
8.4 ± 0.4	5.58 ± 0.31	5.41 ± 0.32
11.2 ± 0.3	3.88 ± 0.24	3.65 ± 0.15
18.2 ± 0.2	1.35 ± 0.21	1.36 ± 0.03
25.0 ± 0.2	0.52 ± 0.24	0.52 ± 0.03

Table 5.8. ***Comparison of the calculated and predicted D values for a given % crystallinity for annealed PET samples***

Figure 5.21. shows a plot of all the percentage crystallinity calculations plotted the against D values obtained, in both the annealing and *trans* esterification experiments.

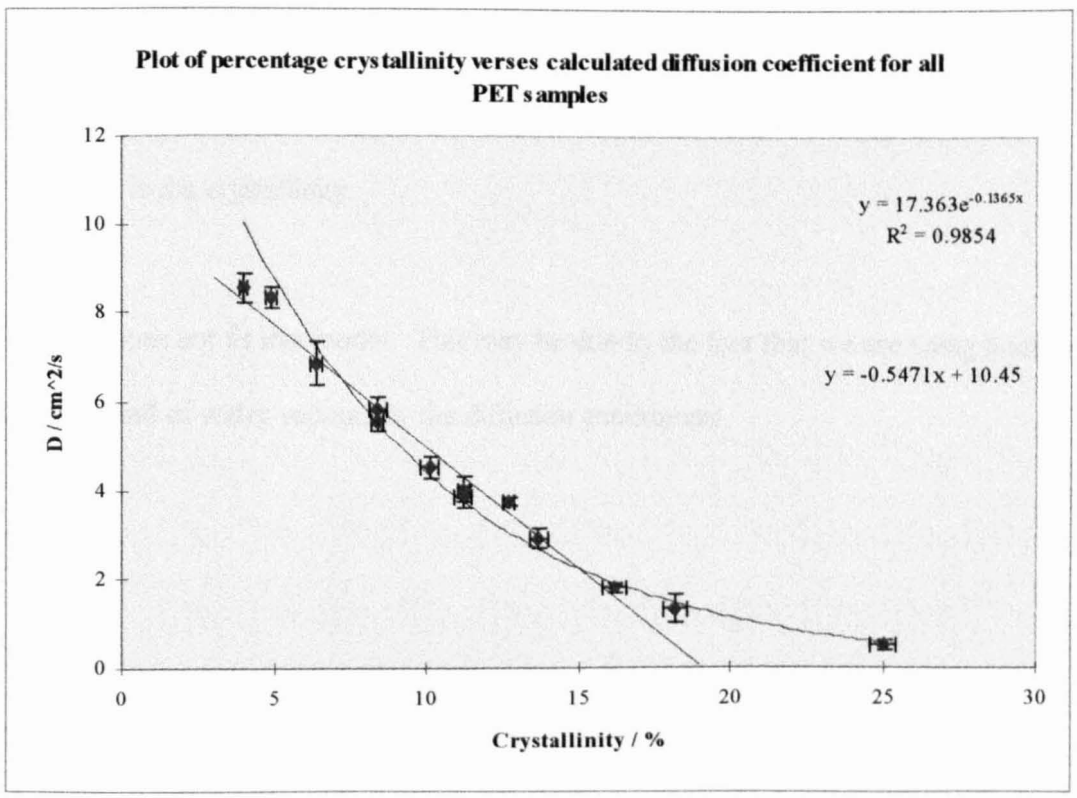

Figure 5.21. ***Plot of measured % crystallinity for calculated D values for PET.***

When all the percentage crystallinity versus calculated diffusion coefficients are placed on the same plot, the modelling outcome is quite interesting. The data seem to fit only a linear model for values of X_c less than ~ 6 %. For data with a higher crystallinity than ~ 16 % an exponential model is more appropriate. For data between 6 and 16 % crystallinity both models give a reasonable estimate of the diffusion coefficient for a given percentage crystallinity. The actual relationship between percentage crystallinity and D is most likely a convolution of the two models.

Rueda and Varkalis have used a power law to model the D values versus crystallinity for water vapour diffusion [5.5]. They find that

$$D = D_0\left(1 - \psi_c^{0.5}\right) \qquad \text{(eq. 5.3.)}$$

Where D_0 is the diffusion coefficient of 100 % amorphous PET.

Ψ_c is the crystallinity.

Our data does not fit this model. This may be due to the fact that we are using liquid water instead of water vapour for the diffusion experiment.

5.5. The perturbation of water in PET.

Figure 5.22. shows the comparison between the water bands of PET at equilibrium and the water band of pure water. The top diagram shows a real scale allowing comparison of intensity differences and the bottom shows an expanded scale for shape differences.

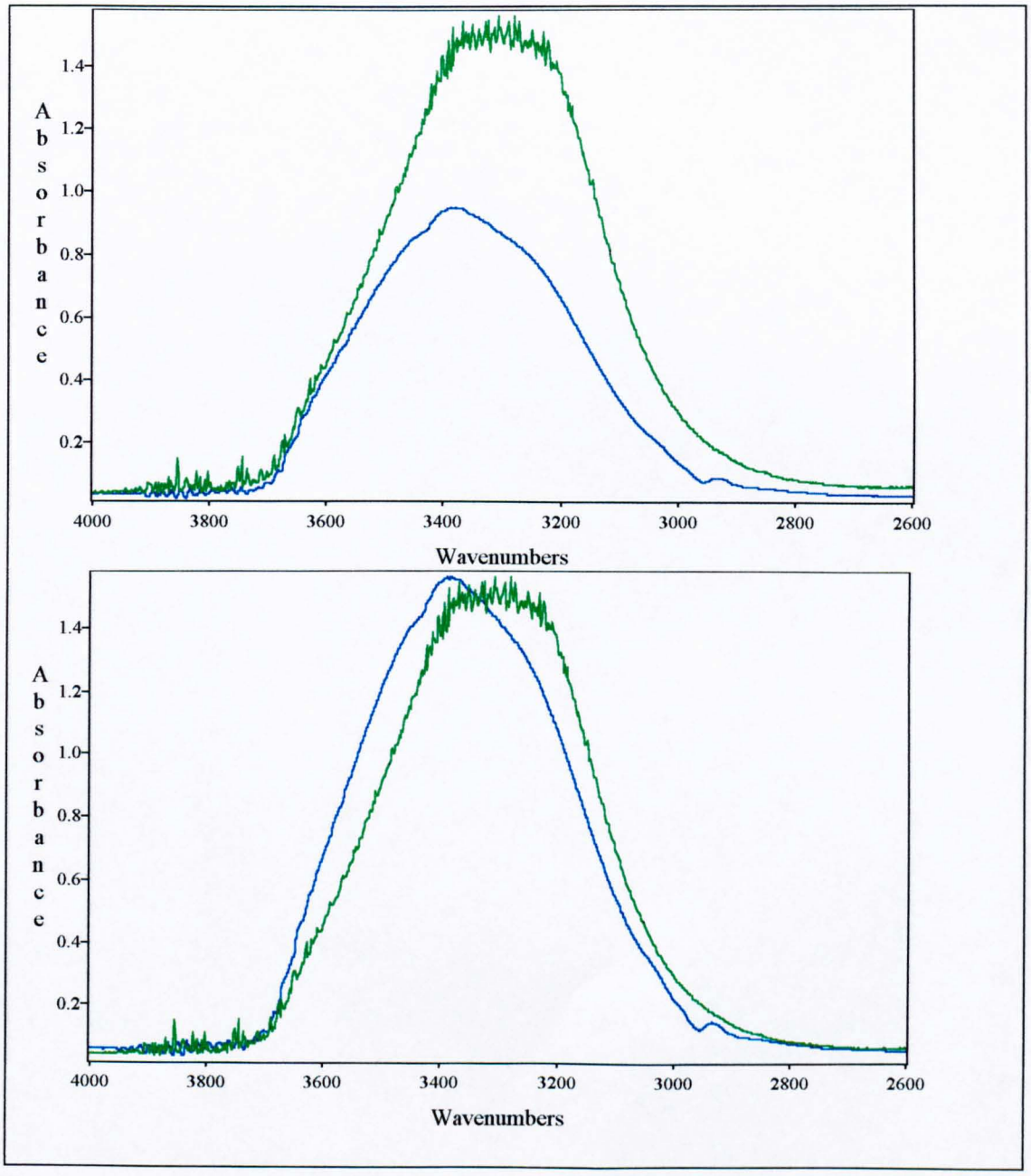

Figure 5.22. Comparison of the ν(OH) band of water at equilibrium in PET and pure water.

During the diffusion of water into PET the ν(OH) band of water, undergoes quite drastic changes in shape. It is the aim of this section to try to interpret the changes occurring to the water band in terms of interactions with the polymer and hence 'types' of water. Figure 5.23. shows the intensity change of the ν(OH) band with time for a predominantly amorphous (4 % crystalline) PET film. The equilibrium value was obtained at about 48 hours.

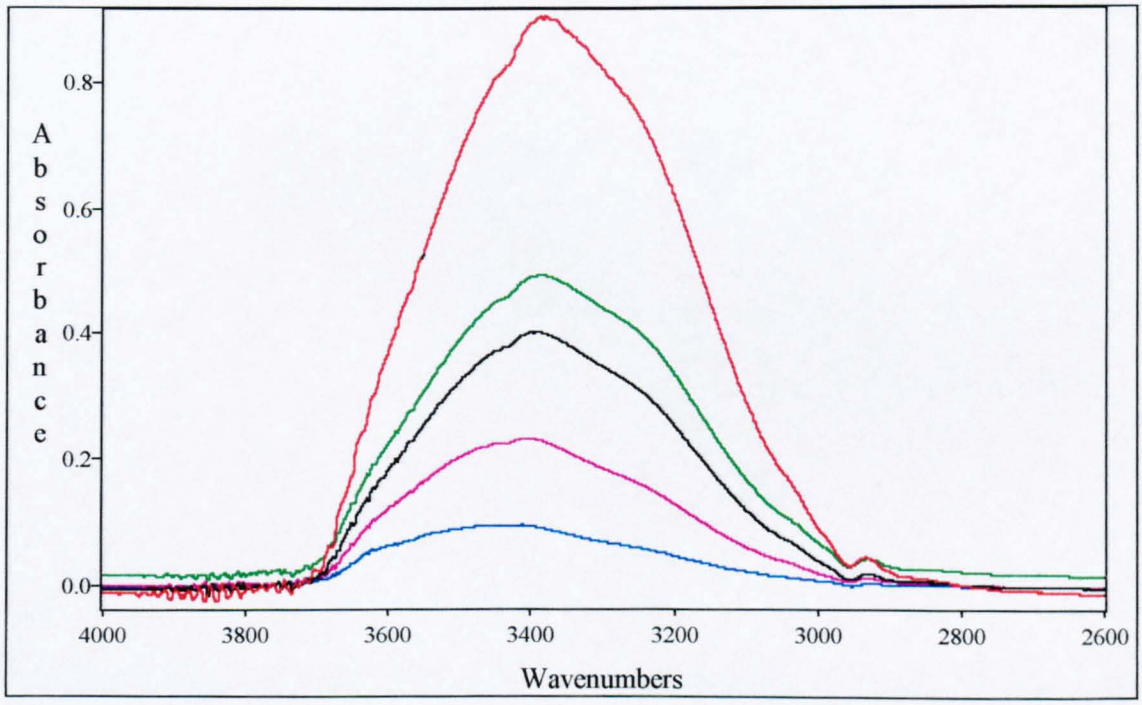

Figure 5.23. The change in intensity of the ν(OH) band of water in PET at 10, 30, 60, 90 minutes and equilibrium (~ 2 days).

The kinetic data described in the previous section can be obtained by simply integrating the area under the peak as a function of time. Figure 5.24. shows the change in shape for the water band as a function of time. The intensities of the bands are expanded to fit on the same absorbance scale.

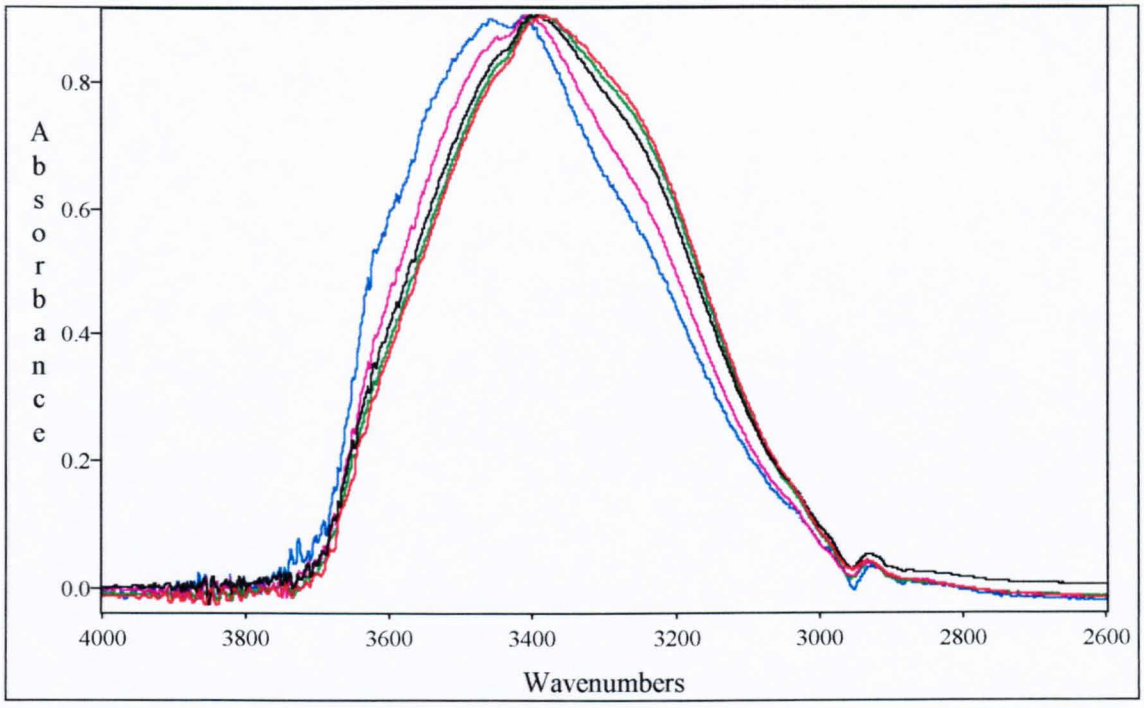

Figure 5.24. The change in shape of the ν(OH) band of water in PET at 10, 30, 60, 90 minutes and equilibrium (~ 2 days).

The shape of the water band in PET is different as a function of time and quite different to that of pure water (figure 5.23.). The whole water profile containing the symmetric and antisymmetric ν(OH) modes has shifted to high frequency compared to that of pure water.

The dramatic change in band shape as a function of time, hence water concentration, within the polymer matrix is clearly shown in figure 5.24. The water band in PET has been deconvoluted to 4 constituent bands (figure 5.25.), which have frequencies and relative intensities similar to those of described by Libnau et al for pure water [**5.12**, **5.13**]. The spectra show relatively weakly hydrogen bonded molecules with a band around 3600 cm^{-1} as is found in pure water. The other three bands correspond to water molecules engaged in different degrees of hydrogen bonding with themselves or the polymeric membrane. The band centres obtained are close, but not identical to those

obtained from curve fitting procedures. The results from curve fitting procedures will be discussed later in the chapter.

It has generally been found for a wide number of organic systems that water dissolved in an organic medium is on average more weakly hydrogen bonded than water molecules in a pure water network [**5.27, 5.30, 5.33-5.41**]. This is probably due to a number of reasons, such as the breaking up of the water network into smaller clusters and the fact that the hydrogen bonding between water and the polymer is weaker than water hydrogen bonded to another water molecule.

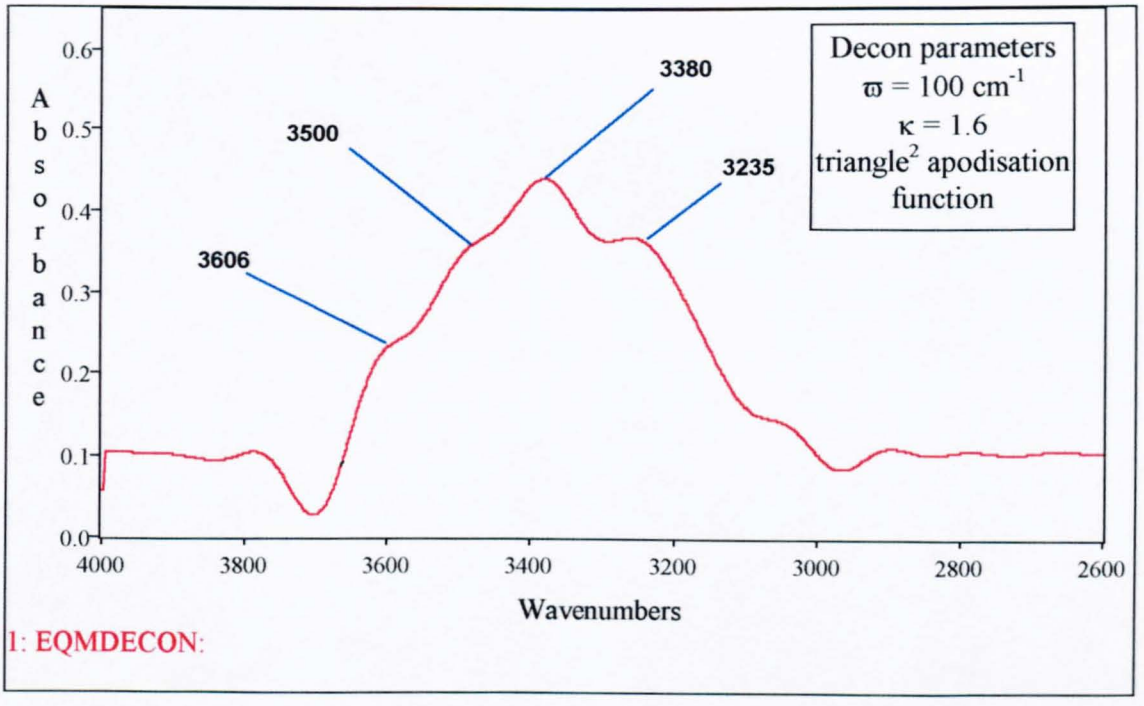

Figure 5.25. Fourier deconvolution of the equilibrium water in amorphous PET

The changes in the band positions and intensities will now be discussed in more detail. For ease of presentation this discussion will be split into two parts; water as a function of time / concentration and equilibrium water as a function of crystallinity.

As stated earlier the ν(OH) band of water in a polymeric material changes dramatically as a function of time / concentration. Although the change is continuous until equilibrium is reached the most dramatic changes occur at short time, hence at low concentrations. Figure 5.26. shows the ν(OH) band of water during the first 5 minutes and at 10 minutes of a diffusion experiment. The spectra have been expanded to fit on the same y axis. For the first three minutes of the diffusion the splitting of the ν_{as}(OH) and the ν_{s}(OH) are clearly visible. This can be interpreted as the water being in a pseudo 'monomeric' form or water interacting with the carbonyl band, i.e. forming hydrogen bonds. Figure 5.27. suggests that interactions between the water and the ester carbonyl are occurring.

The water band after 1 minute (green) is a doublet and looks very similar to the water band in PET after treatment with water vapour [5.5]. These have been assigned as the ν_{as}(OH) and ν_{s}(OH) modes at 3630 and 3550 cm^{-1} respectively, i.e. 'free' uncoupled water. The frequencies are shifted lower in frequency than those expected for water vapour, true uncoupled water. This we have attributed to hydrogen bonding with the carbonyl band in PET.

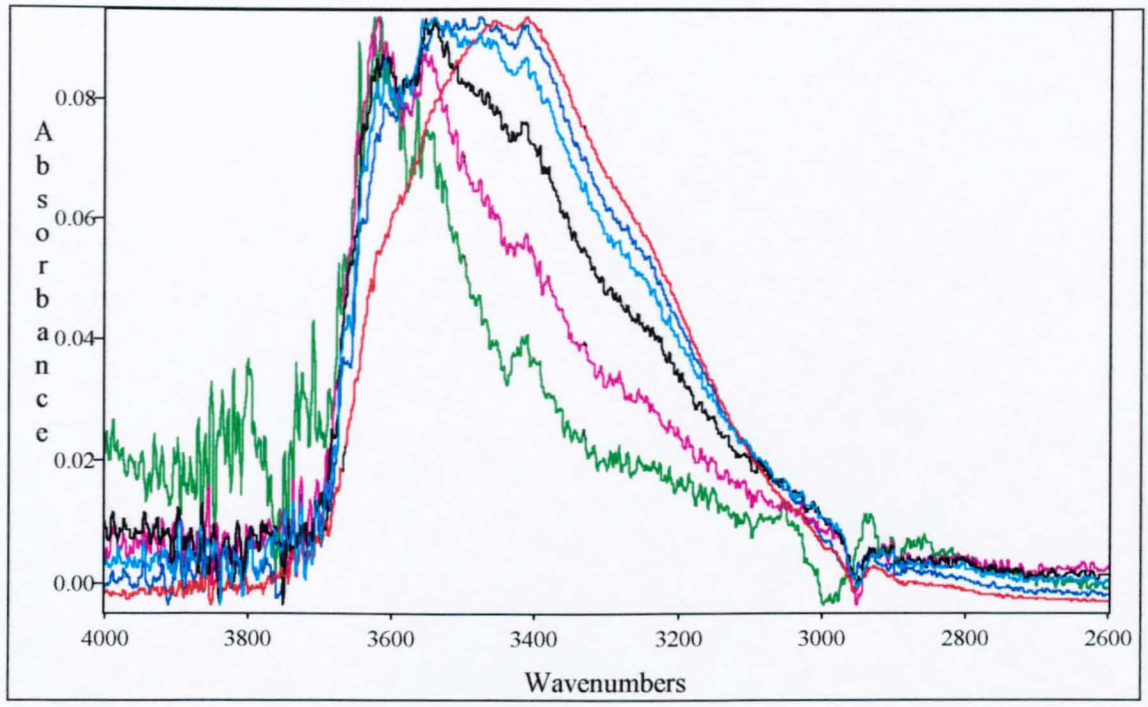

Figure 5.26. The change in shape of the ν(OH) band of water in PET at 1, 2, 3, 4, 5 and 10 minutes.

As the concentration increases the water band gains more pure water like character resulting in a shift to lower frequency. Subsequent coupling with other ν(OH) oscillators as clustering increases results in the loss of the doublet and formation of a broad complex band that can only be broken down to its constituent parts with the aid of spectral manipulation techniques such as Fourier deconvolution, band fitting and second derivative spectroscopy. The clustering of the water means the frequencies tend towards, but do not reach, the frequencies that have been defined for pure water [**5.12, 5.13**].

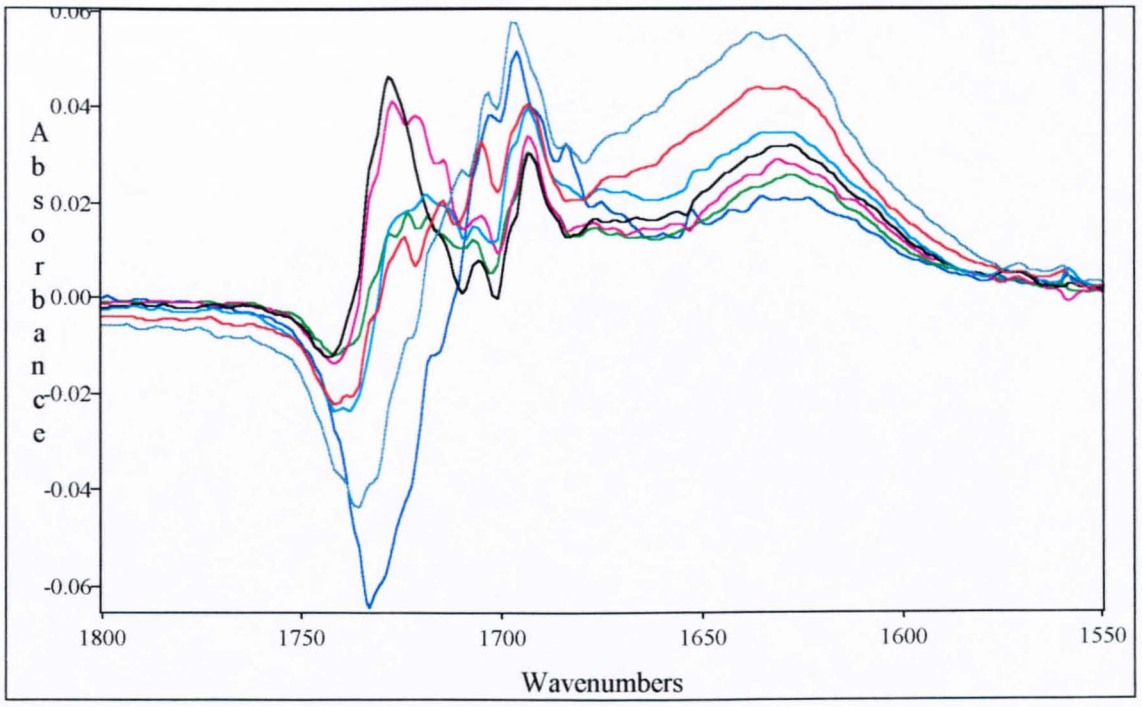

Figure 5.27. The interactions of water with the ν(C=O) in PET at 1, 2, 3, 4, 5, 10 and 15 minutes.

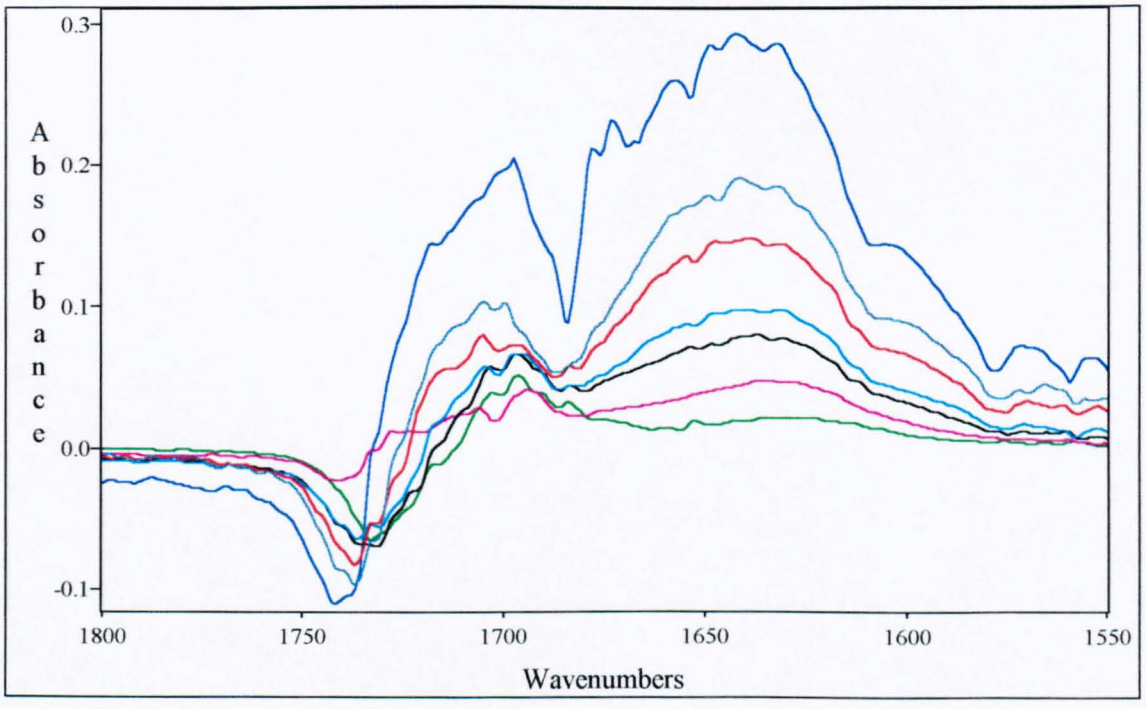

Figure 5.28. The interactions of water with the ν(C=O) in PET at 1, 10, 30, 60, 120, 480 minutes and equilibrium (~ 2 days).

Figures 5.27 and 5.28 show the effect of the interaction of the water with the carbonyl band of PET. The spectra of water were produced by ratioing the single beam spectrum of the wet film against the single beam spectrum of the dry polymeric film. If no interactions between the water and the PET membrane were occurring then one could expect to see a flat line in all regions where there is no water spectrum. In this region one can clearly see the γ(OH) (bending mode) at 1635 cm^{-1} but there is also a negative band at 1735 cm^{-1} which corresponds to the carbonyl band in PET and a positive band at around about 1695 cm^{-1} which may be assigned to the ester carbonyl hydrogen bonded to the sorbed water. The band at 1695 cm^{-1} is always positive in the wet film and increases with concentration, but the band at 1735 cm^{-1} changes both frequency and intensity with concentration. After 1 minute (figure 5.27) the band is (relatively) strongly negative but loses (negative) intensity after 2 minutes and gains a derivative type shape. As the concentration of water sorbed in the film increases so the intensity of this (negative) feature at 1735 cm^{-1} increases. After 30 minutes (figure 5.28) the intensity of the negative feature at 1735 cm^{-1} is greater than that observed after 1 minute, as are the band at 1695 cm^{-1} and the γ(OH) band.

These complex changes in intensity may be due to the different carbonyl environments within the polymeric matrix. The molar extinction coefficient, ε, of the carbonyl band is dependent on the environment, with perturbations due to hydrogen bonding not uncommon. There is evidence of strong interactions between water and the ester carbonyl at low water concentrations in the ν(OH) region. The ν(OH) band is shifted to high frequency, indicating a 'breaking up' of the water network due to interactions with the polymer film.

As the concentration of the water in the film increases so does the tendancy of the sorbed water molecules to cluster. This is shown by a shift to lower frequncy of the ν(OH) band (figures 5.24 and 5.26). This may also explain the decrease in (negative) intensity of the feature at 1735 cm^{-1} as the sorbed water molecules interact with other water molecules, rather than solely with the polymeric membrane. The interactions between the clustered water and the ester carbonyl are 'weaker' and the perturbation of the carbonyl band is less. But as the concentration of the water sorbed in the polymer increases, so does the number of these 'weak' interactions, leading to an increase in (negative) intensity of the feature at 1745 cm^{-1}.

5.5.1. Deconvolution of the ν(OH) band of water using curve fitting procdures.

To detail changes in the water band, the curve fitting procedures used to calculate band positions and peak intensities in the last section were applied to the water band at different times. Figures 5.29. - 5.33. show the results of curvefitting the equilibrium ν(OH) band of water in PET and figure 5.34, shows the band fitting of pure water for comparison..

Band fitting was achieved by using the curve fitting routine provided in the Grams-32 software package. The band shape was fixed at 50 % Gaussian / 50 % Lorentzian but all other parameters (peak magnitude, band-width and frequency) were allowed to vary upon iteration. The statistical parameters defined in the user manual were used as a guide to the 'best fit'. The results of the band fitting are shown in table 5.8.

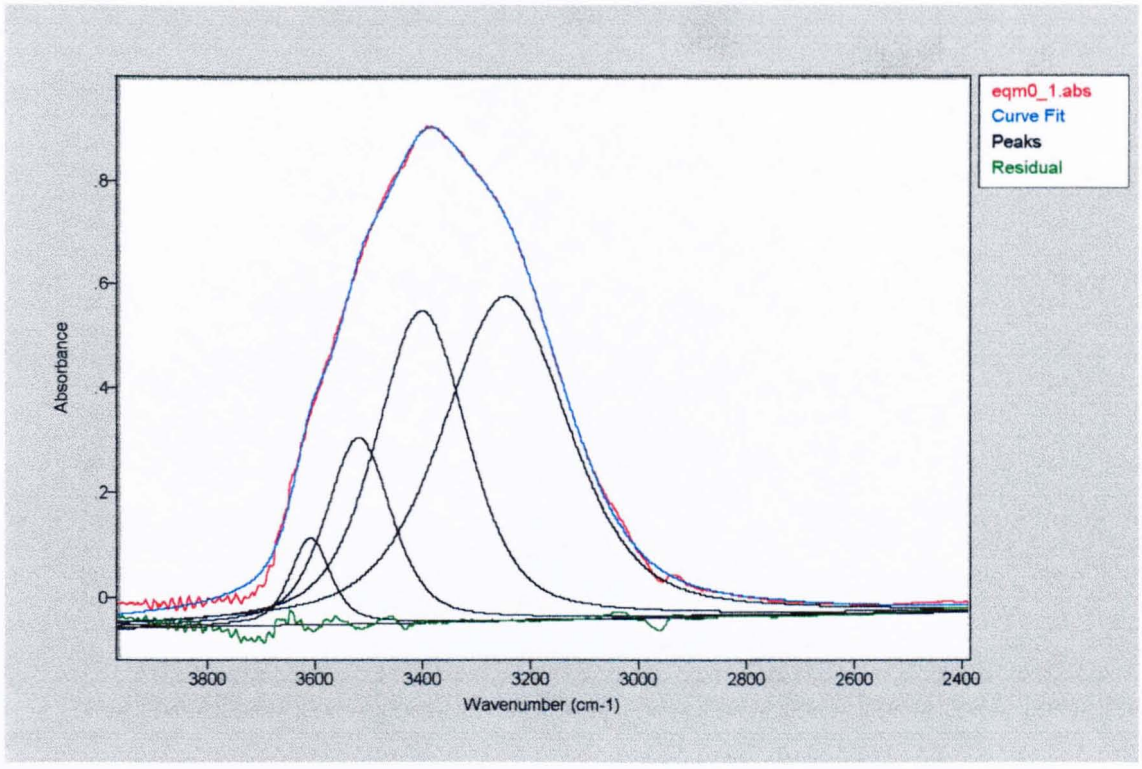

Figure 5.29. The four 50% Gaussian / 50% Lorentzian component bands fitted to the equilibrium ν(OH) band of water in 4.9% crystalline PET.

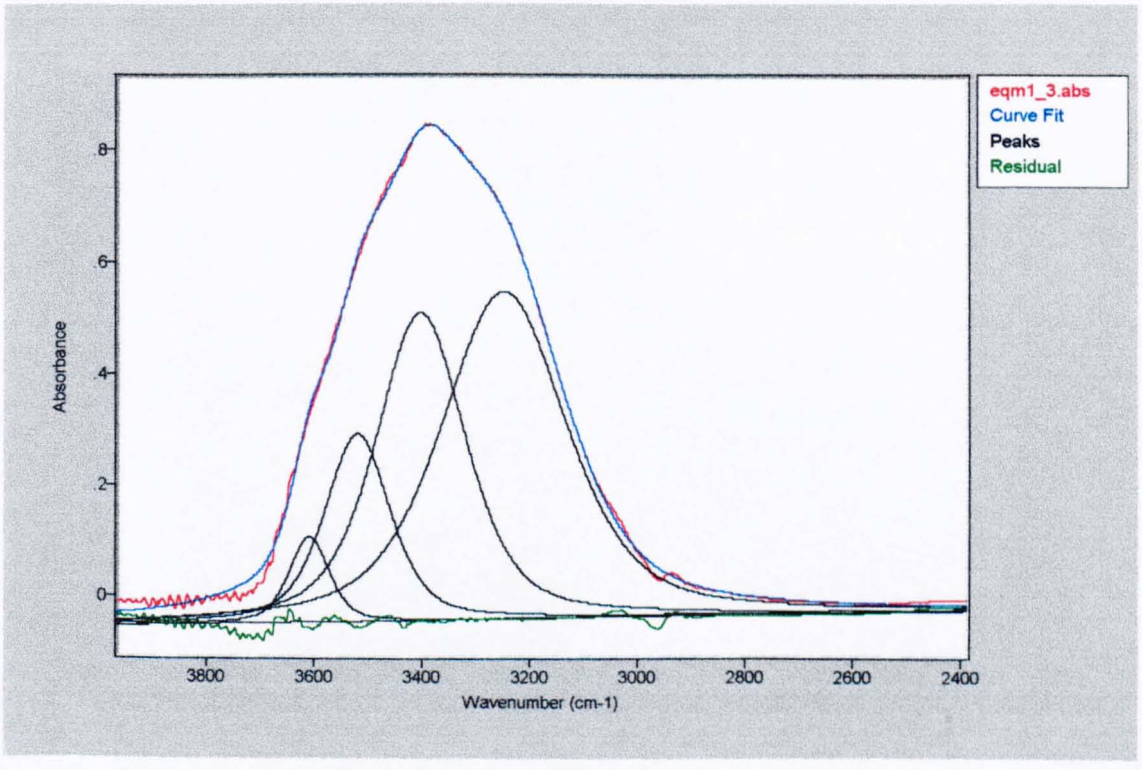

Figure 5.30. The four 50% Gaussian / 50% Lorentzian component bands fitted to the equilibrium ν(OH) band of water in 8.4% crystalline PET.

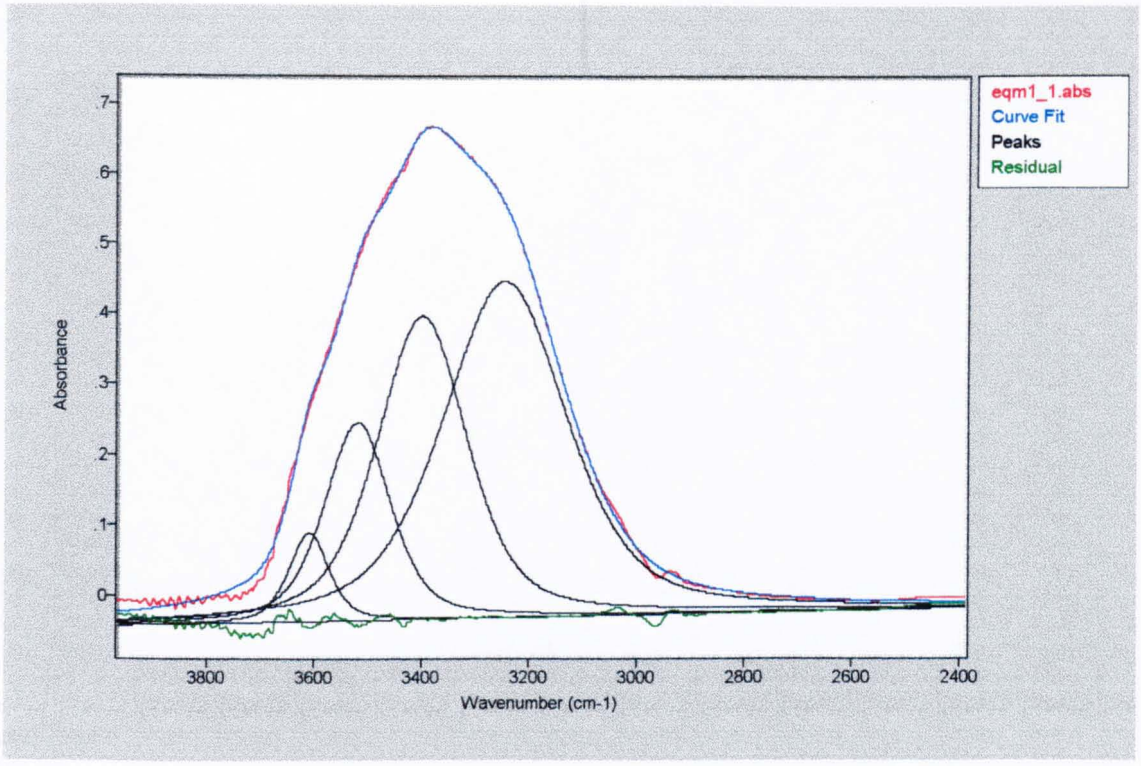

Figure 5.31. The four 50% Gaussian / 50% Lorentzian component bands fitted to the equilibrium ν(OH) band of water in 11.2% crystalline PET.

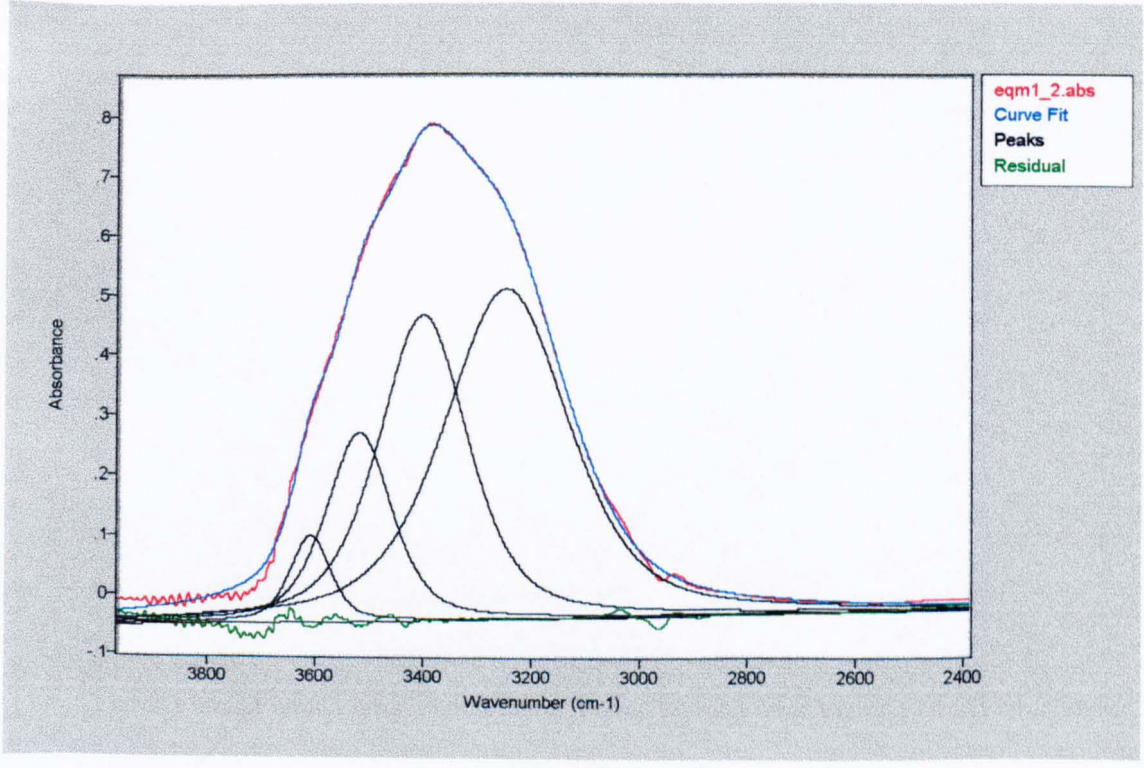

Figure 5.32. The four 50% Gaussian / 50% Lorentzian component bands fitted to the equilibrium ν(OH) band of water in 18.2% crystalline PET.

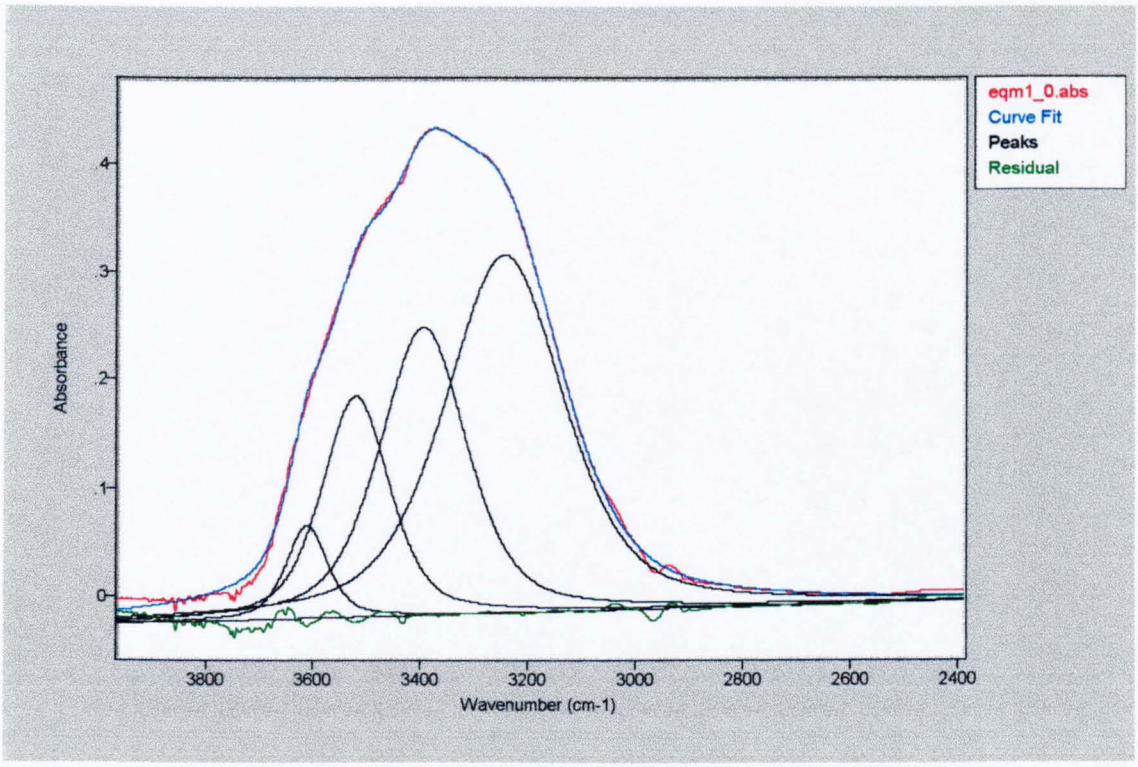

Figure 5.33. The four 50% Gaussian / 50% Lorentzian component bands fitted to the equilibrium ν(OH) band of water in 25% crystalline PET.

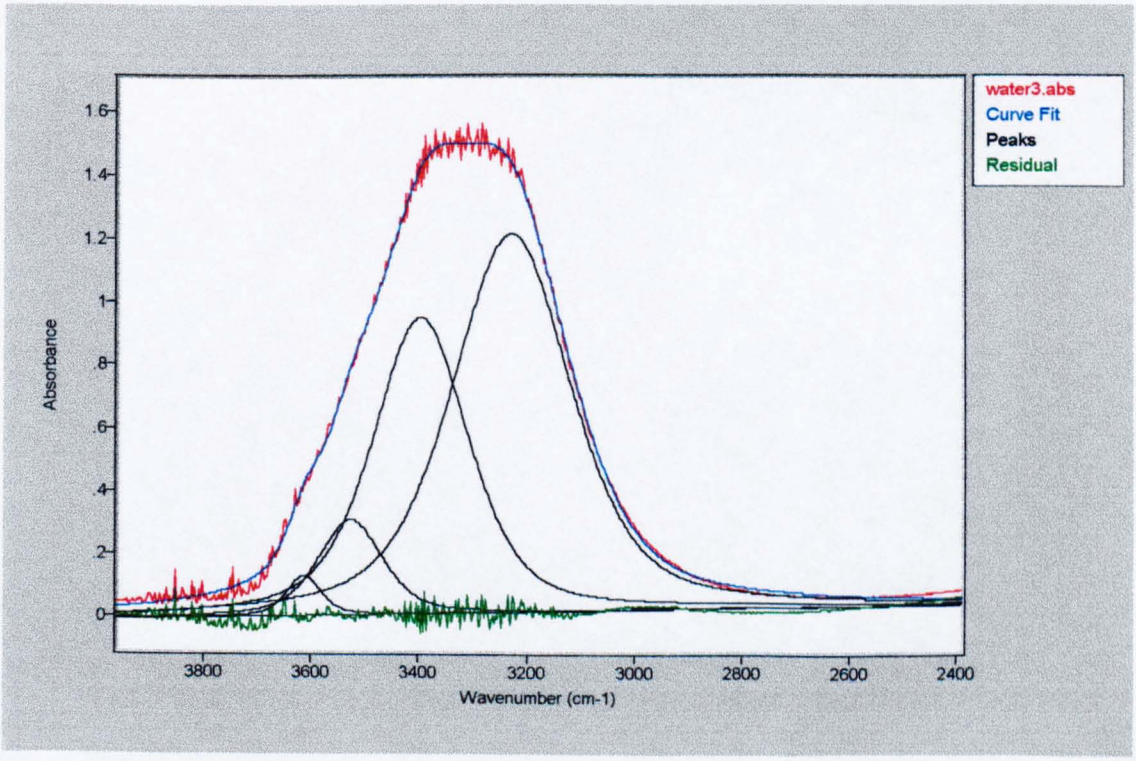

Figure 5.34. The four 50% Gaussian / 50% Lorentzian component bands fitted to the ν(OH) band ofpure water.

Figures 5.35. - 5.38. show the frequency shifts upon diffusion that are occurring to the component bands within the PET membrane. The components are termed, weakly H-B, moderately weak H-B, moderately strong H-B and strongly H-B depending on the frequency of the band. All of the bands show an initial shift in frequency as the water network breaks up and then reforms into clustered, coupled water.

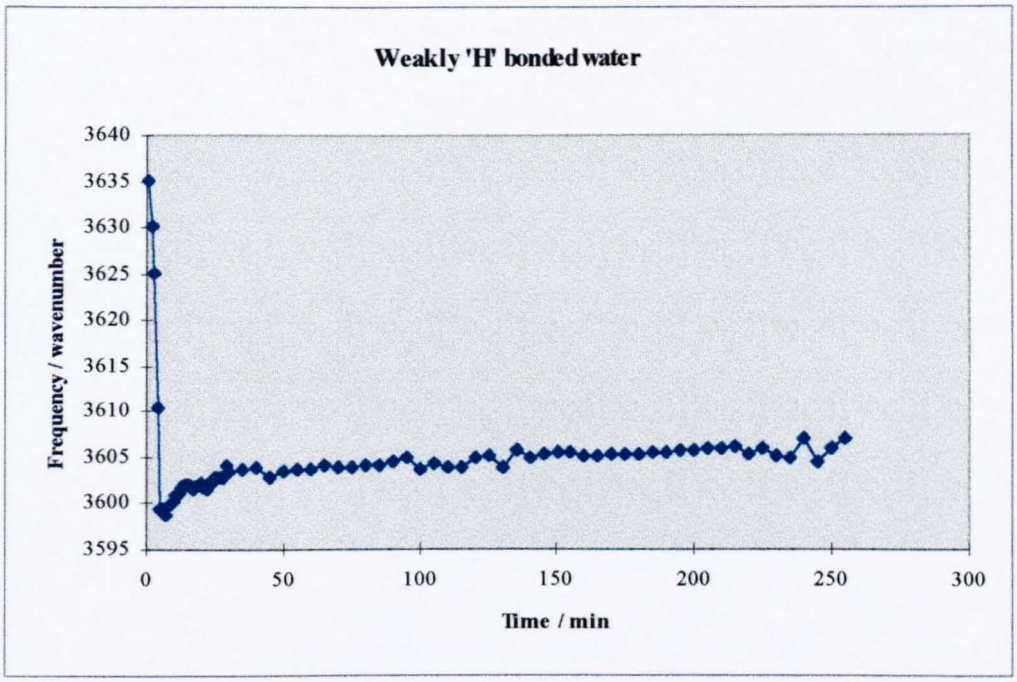

Figure 5.35. The frequency shift of the weakly hydrogen bonded water component in PET with time.

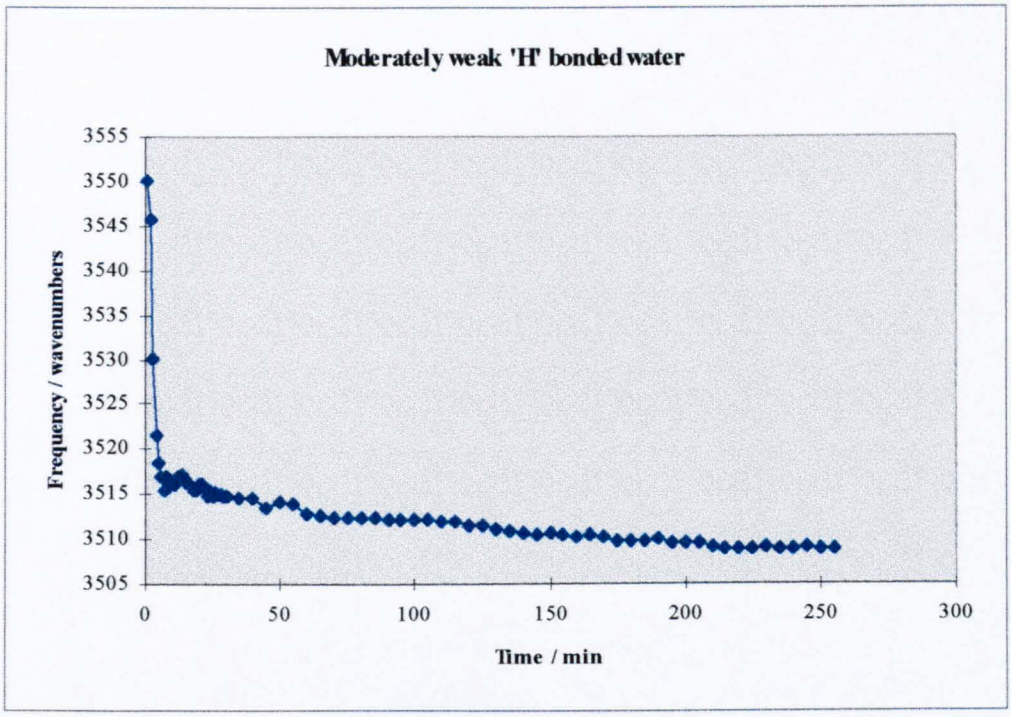

Figure 5.36. The frequency shift of the moderately weak hydrogen bonded water component in PET with time.

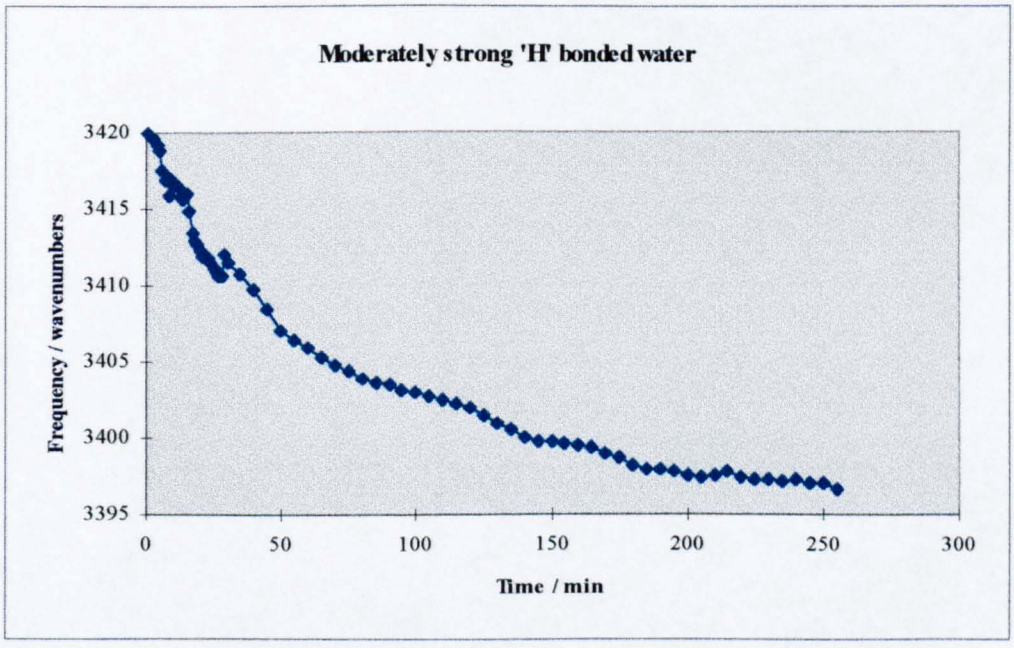

Figure 5.37. The frequency shift of the moderately strong hydrogen bonded water component in PET with time.

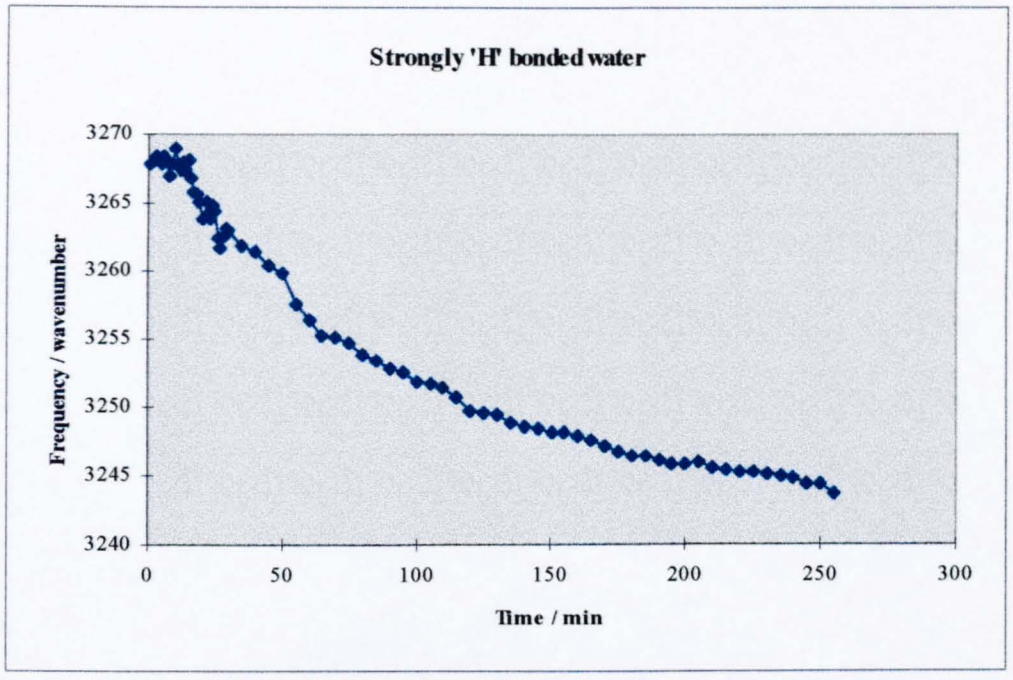

Figure 5.38. The frequency shift of the strongly hydrogen bonded water component in PET with time.

Figure 5.35. show an extremely interesting feature. The initial shifts are from what has been described as pseudo 'monomeric water' bound just to the polymer, to water in small clusters. This initial shift to lower frequency of 25 - 30 cm^{-1} occurs in the first 3 minutes of the diffusion and can be related to this clustering phenomenon. During the rest of the diffusion there is a small but gradual shift to higher frequency indicating a weakening of the hydrogen bonding. This may well suggest that the 3610 cm^{-1} water band can be associated to a water hydrogen bonded to the polymer, (i.e. water of hydration). The relationship between water concentration (i.e. clustering) and frequency is shown in figure 5.39.

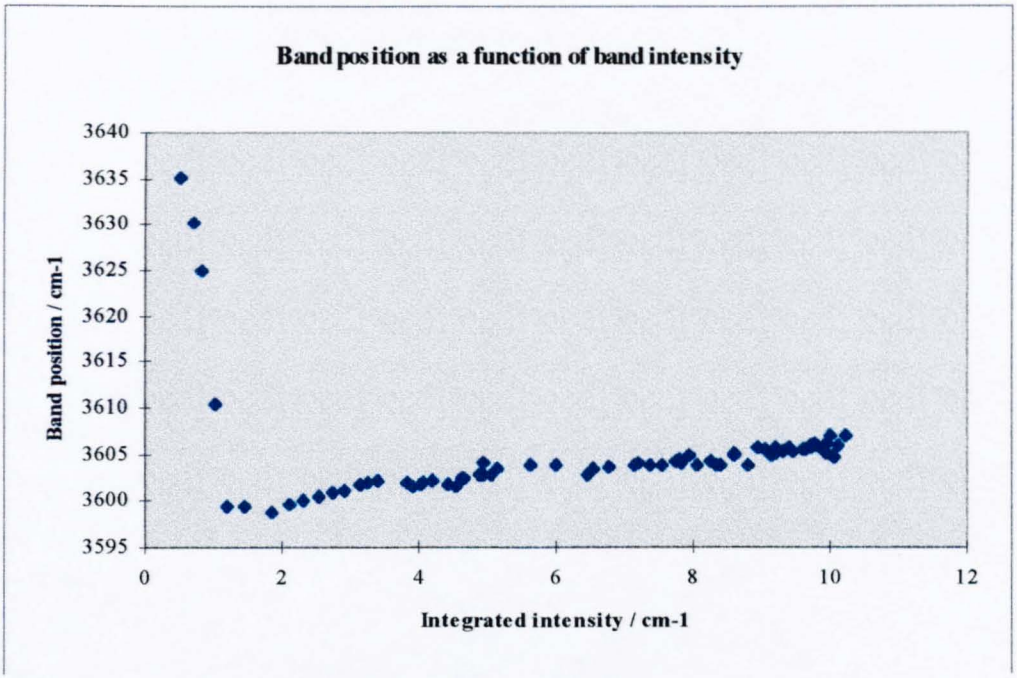

Figure 5.39. The frequency of the weakly hydrogen bonded water as a function of band intensity

Figure 5.36. shows the band at 3510 cm^{-1} also undergoes a dramatic shift at short times (low concentrations). This may well be because at short times in the monomeric type water, this band is attributed to the symmetric O-H stretch. Upon increasing in concentration, with the subsequent clustering and coupling to the other O-H vibrators, it is highly improbable that this band can be attributed to the ν_a(OH). The spectrum of pure water has a band in this position and as the band in PET approaches equilibrium, the shifts to lower frequency imply that this is a water environment involved in progressively strong hydrogen bonding to itself as the concentration of water increases. This is clearly shown in figure 5.40.

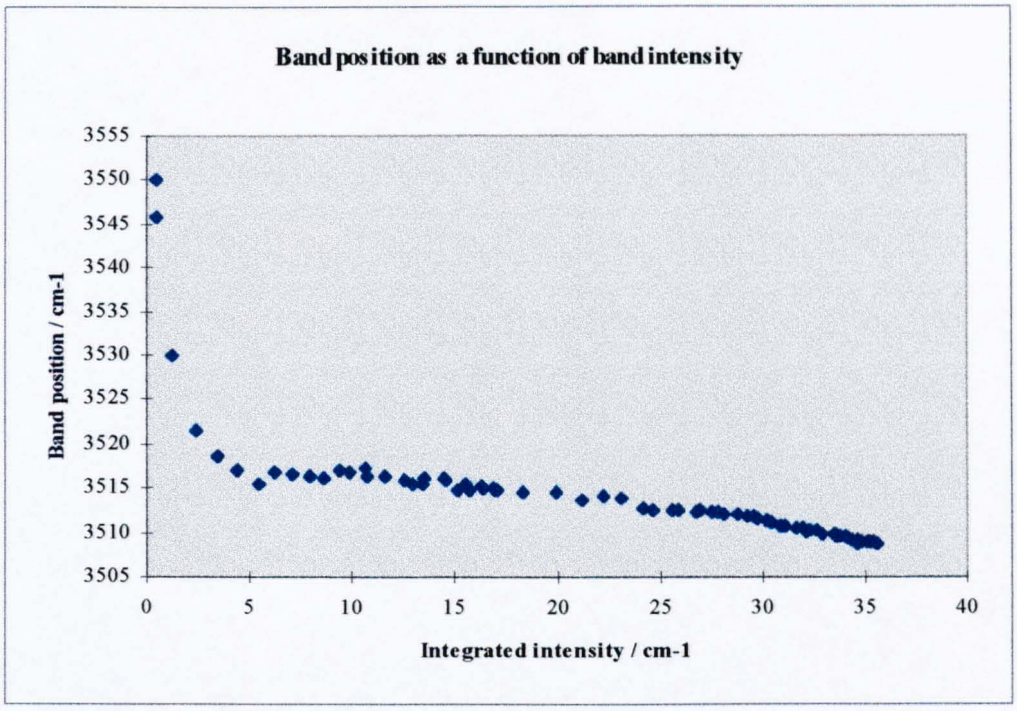

Figure 5.40. The frequency of the moderately weak hydrogen bonded water as a function of band intensity

Figures 5.39. and 5.40. show the shift to lower frequency of the two most strongly hydrogen bonded water environments with an increase in water content (i.e. time). The implications are that at lower concentrations of water, the water network is broken to such an extent that the water molecules are arranged in smaller clusters within the polymer microstructure. These clusters then increase in size as the water reaches saturation. Figures 5.41. and 5.42. show that as the intensity of the component bands increase, the frequency shifts towards that of pure water, strongly indicative of the increase in water cluster size with concentration.

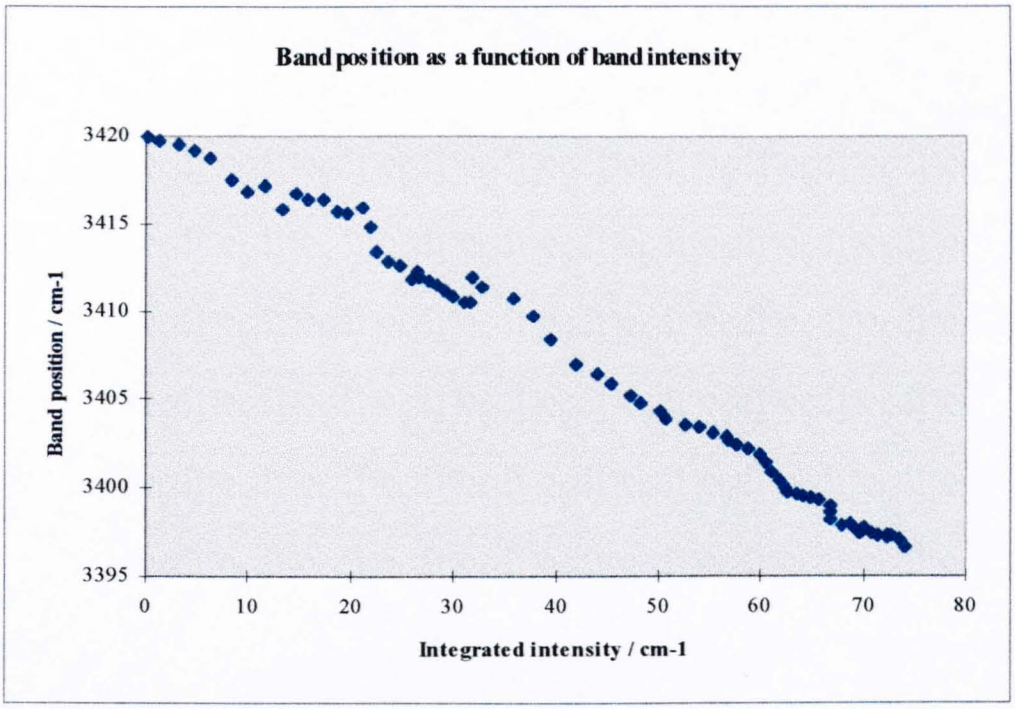

Figure 5.41. The frequency of the moderately strong hydrogen bonded water as a function of band intensity

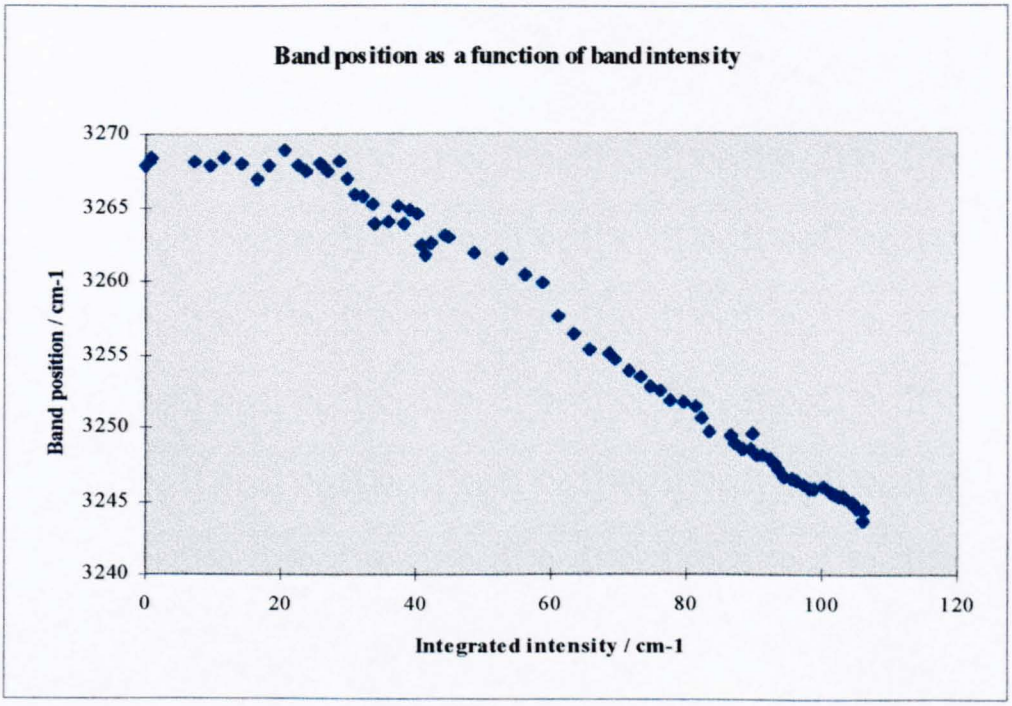

Figure 5.42. The frequency of the strongly hydrogen bonded water as a function of band intensity

Figure 5.43. shows the change in intensity of the equilibrium ν(OH) band of PET as a function of crystallinity for the *trans* esterification diffusion results. It is interesting to note that the change in intensity between the equilibrium ν(OH) bands is quite dramatic. An increase in crystallinity of 20 % results in a halving of the absorbance. The absorbance at equilibrium of the amorphous sample is indeed comparable to that of pure water in the same cell, with a supposedly much lower concentration of water. This suggests that the molar extinction coefficient of water changes dramatically in a polymer matrix [**5.52**].

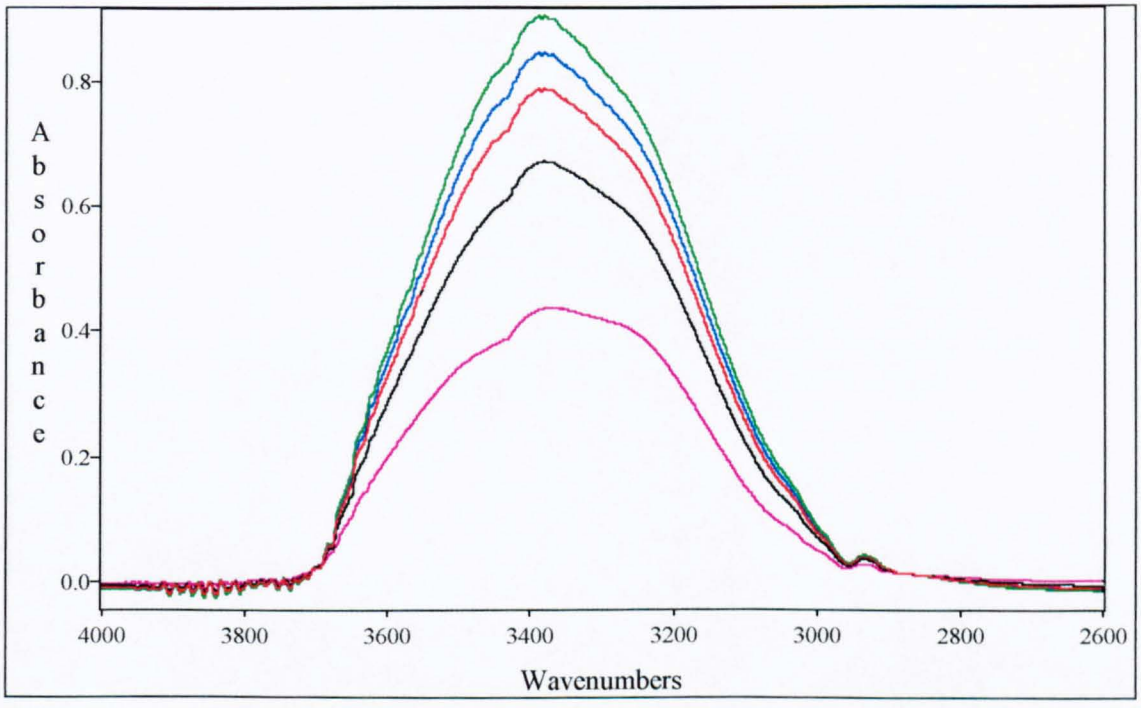

Figure 5.43. The intensity of the equilibrium ν(OH) bands of water in PET of 4.9, 8.4, 11.2, 18.2 and 25 % crystallinity.

Figure 5.44 shows the band shift in the equilibrium water as a function of crystallinity. The water bands in figure 5.44. are expanded to fit on the same y axis to allow easier

comparisons of the band shapes. It is shown that as crystallinity increases the overall band is slightly broader. This broadening indicates that although less water is in the more crystalline polymer, the hydrogen bonding network of the water is stronger than that of the water in the more amorphous polymer. This suggests that there is less interaction between the sorbed water and the polymer in more highly crystalline samples.

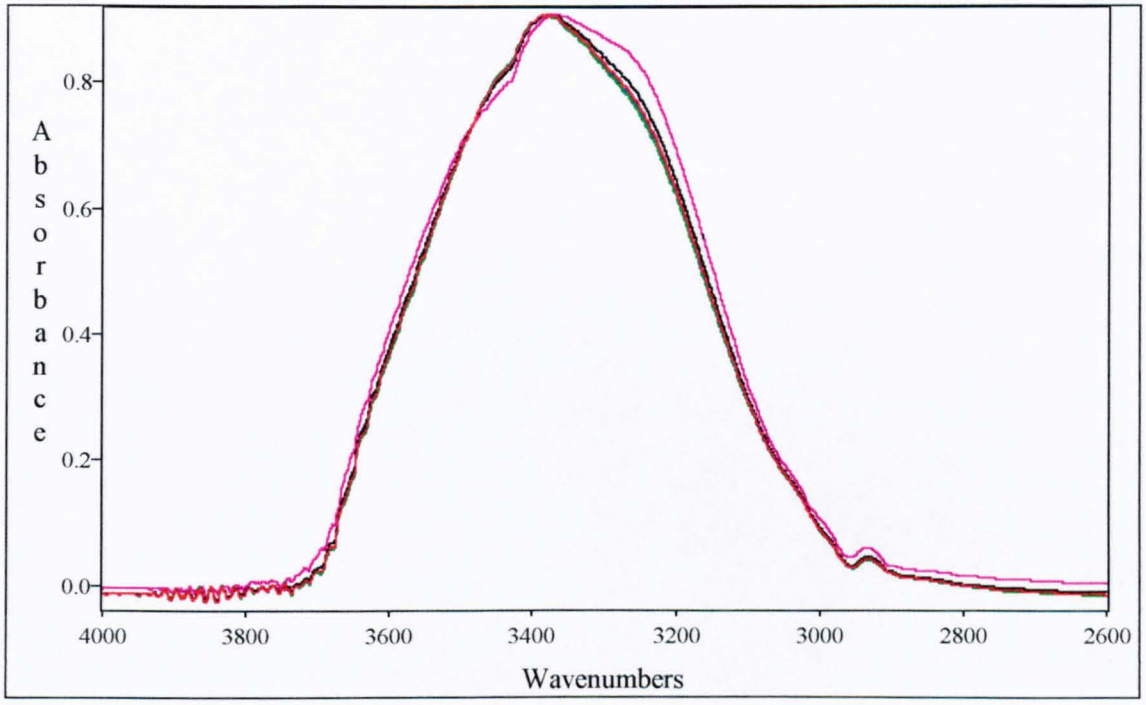

Figure 5.44. The band shape of the equilibrium ν(OH) bands of water in PET of 4.9, 8.4, 11.2, 18.2 and 25 % crystallinity.

For an ATR experiment it has been shown [**5.53, 5.54**] that the absorbance of a particular band can be given by

$$Abs = \log\left(\frac{I_0}{I}\right)_{\bar{\nu}} = \varepsilon C d_e \qquad \text{(eq. 5.3.)}$$

Where ε is the molar extinction coefficient

C is the concentration

d_e is the effective thickness

In ATR the effective thickness can be calculated from well known equations [5.54], assuming that the actual thickness of the film is much greater than the penetration depth. This is known as the semi-infinite thickness case. The corresponding band integrated intensity, which can be approximated from the measured band area, is given by

$$B = \int \varepsilon_{\bar{\nu}} d\bar{\nu} = \frac{Abs}{Cd_e} \qquad \text{(eq. 5.4.)}$$

Equation 5.4. can be used to calculate the percentage of water in the PET film at equilibrium, by using data obtained from figure 5.22, assuming that the molar extinction coefficient (ε) remains constant. Using d_e values of 0.7604 and 1.2955 μm for pure water and the water / PET system respectively, a PET density of 1.33 g cm^{-3} and the integrated intensities of the bands in figure 5.22. the percentage of water, by weight, in the polymer film at equilibrium is calculated to be 25 %. This value is very high compared to literature values obtained via gravimetric techniques, which suggest an equilibrium water content of around 1 % by weight. Therefore one may conclude that the water is highly perturbed in the polymer membrane.

For pure water the values of ε and B are well documented and are known [5.23, 5.24, 5.29] to depend critically on the molecular environment i.e. perturbation. The ν(OH) bands, both in the polymer and pure water can be deconvoluted into their component bands. Comparison of the recalculated ε and B (using the literature concentrations of

water in PET) for each of the component bands will give us a quantitative measure of the perturbation.

Using ideas proposed by Maeda et al [5.38-5.40]

$$\frac{\varepsilon_p}{\varepsilon_w} = \underline{P} \qquad \text{(eq. 5.5.)}$$

Where $\underline{P}$ is some measure of the oscillator perturbation due to sorption in the polymer

In order to calculate the perturbation, $\underline{P}$, all that is required is equation 5.4. and values of the water concentration obtained from the literature. Several assumptions are made,

1. There is a homogenous distribution of water molecules within the polymer matrix.
2. Changes of ε are due only to network 'perturbation' and / or interaction with the polymer.
3. Component bands of similar frequency both in pure water and water in the polymer correspond.

In this calculation only intensity ratios obtained under identical conditions have been used. No attempt to calculate the absolute infrared intensities has been made. The factor $\underline{P}$ can be calculated from the following equation

$$\underline{P} = \left(\frac{C_w}{C_p}\right)\left(\frac{d_w}{d_p}\right)\frac{area_p}{area_w} \qquad \text{(eq. 5.6)}$$

Where C_w and C_p are the water concentrations in pure water and the polymer respectively.

d_w and d_p are the sampling depths of the water and polymer containing water.

$area_w$ and $area_p$ correspond to the integrated areas of the ν(OH) band for the pure water and the water in the polymer matrix.

From table 5.8. it is clear that there is a distinction in the degree of perturbation (P factors) between the weakly hydrogen bonded water species (bands at ~3606 and 3517 cm^{-1}) and the more strongly hydrogen bonded species (bands at 3397 and 3243 cm^{-1}). This is as expected as the weakly hydrogen bonded species are most likely involved in hydrogen bonding with the polymer. The P factors are generally between 11 and 43. These are the result of a severe intensity or transition moment ($\partial\mu / \partial q$) enhancement when the water is sorbed in the polymer. This may well be due to the 'breaking up' of the tetrahedral network in pure water and is supported by the differences in the P values between the lower frequency (strongly interacting) and higher frequency (weakly interacting) bands.

Position / cm^{-1}	Area / cm^{-1}	width / cm^{-1}	Relative %	$\varepsilon \times 10^{-7}$ / cm mol^{-1}	P
Ratio (0:1) - 4.9% crystalline sample - 0.95% water					
3606	18.8	88	4.2	81.1	43.0
3517	63.5	142	14.3	65.8	34.9
3399	151.2	201	34.1	32.0	17.0
3243	210.0	276	47.4	29.8	15.8
Ratio (1:3) - 8.4% crystalline sample - 0.89% water					
3606	17.6	87	4.2	81.0	43.0
3516	61.8	144	14.9	68.3	36.3
3399	136.9	198	32.9	34.2	18.1
3244	199.0	276	47.0	30.2	16.0
Ratio (1:2) - 11.2% crystalline sample - 0.84% water					
3607	16.5	88	4.3	80.5	42.8
3516	58.3	144	15.1	68.3	36.3
3398	126.4	198	32.6	30.3	16.1
3244	185.8	274	48.0	29.8	15.8
Ratio (1:1) - 18.2% crystalline sample - 0.75% water					
3607	14.6	90	4.4	79.6	42.3
3517	51.5	145	15.5	67.6	35.9
3397	105.6	196	31.9	28.3	15.0
3243	159.2	271	48.1	28.6	15.2
Ratio (1:0) - 25.0% crystalline sample - 0.60% water					
3608	10.3	93	4.7	70.3	37.3
3517	38.4	149	17.6	62.9	33.5
3391	62.8	189	28.7	21.1	11.2
3241	107.1	261	48.0	24.1	12.8
Pure water / 20° C					
3613	12.7	77	1.8	1.883	-
3526	52.8	140	7.5	1.883	-
3395	258.4	216	36.4	1.883	-
3224	385.3	263	54.3	1.883	-

Table 5.8. ***Quantitative results from the curvefit of equilibria water bands in PET. (The % water was estimated from reference [5.5])***

Table 5.8. shows changes in the state of the water at equilibrium in PET films with different degrees of crystallinity. If one plots the P factor against the degree of crystallinity (figure 5.45.) then one can see that there is a general trend for perturbation to decrease with increased crystallinity. This implies that the water network has more pure water-like character in the more crystalline samples. This is reflected in the water

bandshape where the shift to higher frequency is not as great as that observed in the ν(OH) band of water in more amorphous PET (figure 5.43.).

Table 5.8. also illustrates that the degree of perturbation becomes systematically less significant for bands of increasing hydrogen bond strength regardless of the crystallinity of the polymer film.

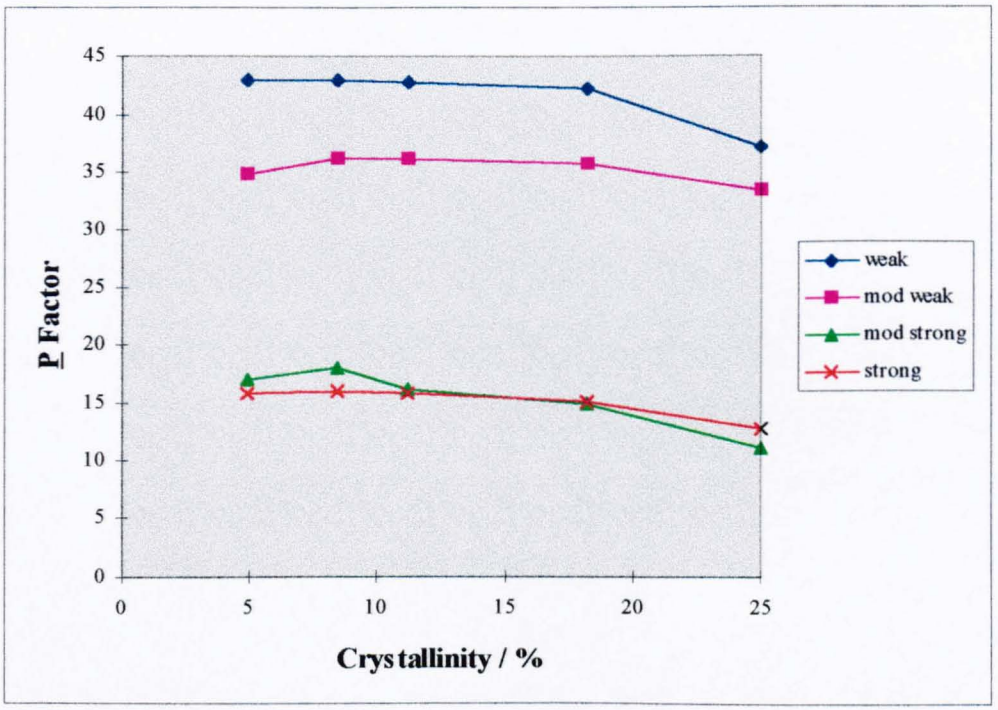

Figure 5.44. The change in P factor with crystallinity.

It is also interesting to note patterns in the relative percentage of each of the components of the water band. The proportion of high frequency and low frequency components remains essentially constant regardless of the morphology of the film. But the two intermediate components vary systematically with changes in crystallinity. The proportion of 'moderately weak' hydrogen bonded component increases with

crystallinity. The proportion of 'moderately strong' hydrogen bonded component decreases with crystallinity. There is also a marked difference in the proportions of the four components between pure water and water in PET. As expected, the proportion of water involved in strong hydrogen bonding (with itself) is much greater in pure water, whilst the proportion of weaker hydrogen bonding species is greater in the water in PET, a clear indication of the interactions between the water and the ester carbonyl.

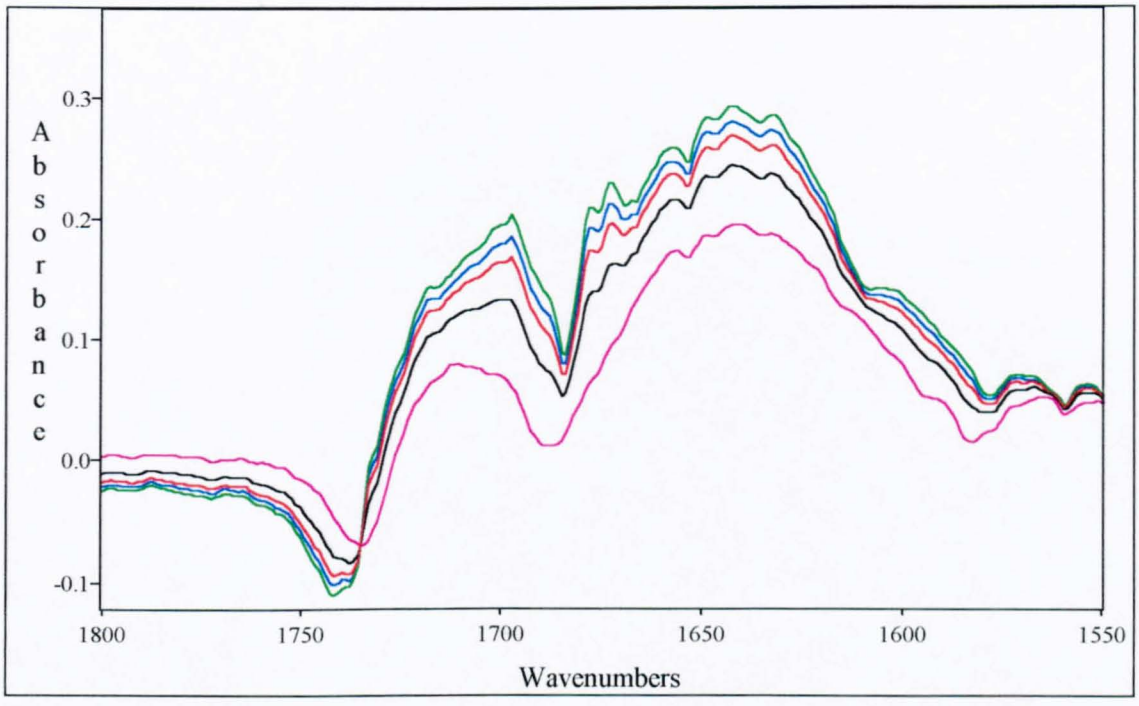

Figure 5.45. The band shape of the ν(C=O) bands of 4.9, 8.4, 11.2, 18.2 and 25 % crystalline PET containing water at equilibrium.

Further evidence of interaction between the sorbed water and the ester carbonyl can be obtained by examination of the carbonyl region (figure 5.45.). From figure 5.45. it is clear that interactions between the sorbed water and the ester carbonyl do occur with a 'derivative' type peak and the bending mode of the sorbed water clearly visible. The

negative component at ~ 1730 cm^{-1} is probably the non-interacting ester carbonyl, whilst the positive component at ~ 1695 cm^{-1} may be assigned to the ester carbonyl strongly hydrogen bonded with the sorbed water.

5.6. Summary.

The diffusion of water into PET has been successfully followed *in-situ* by using the technique of FT-IR ATR. The technique has allowed kinetic and structural information to be obtained simultaneously.

The diffusion of water into PET was shown to be classically Fickian in nature. The diffusion coefficients were shown to decrease with an increase in crystallinity, with the crystalline regions thought to be acting as a barrier. The reduction of free volume space within the polymer matrix, upon an increase in crystallinity, may also have a reductive effect on the diffusion rate. A plot of the diffusion coefficients verses crystallinity produced an exponential type curve, with the equation $y = 17.636\exp(-0.136x)$ describing the data with a correlation coefficient (R^2) of 0.9854.

A detailed study of the state of the sorbed water was carried out both during the diffusion and when equilibrium water levels had been reached. The water network was shown to be highly disrupted at lower concentrations of water in the polymer matrix, with high frequency species dominating the spectrum. This we have interpreted as water molecules hydrogen bonding to the ester carbonyl. The 1800 - 1650 cm^{-1} region of the spectrum indicated that the ester carbonyl was indeed involved in hydrogen bonding. As

the concentration of the sorbed water increased, the frequency of the ν(OH) shifted towards that of pure water. This we have interpreted as the clustering of water molecules within the polymer matrix. The frequency of the ν(OH) band of water in PET remained higher than that of pure water, even after equilibrium water content had been reached.

A systematic deconvolution of the ν(OH) band of sorbed water (based on the mixture model), both as a function of time and at equilibrium was carried out, using curve-fitting techniques. The ν(OH) band was 'broken down' to 4 component bands, which we termed; weak hydrogen bonded, moderately weak hydrogen bonded, moderately strong hydrogen bonded and strong hydrogen bonded. Changes in the frequencies of the components during the diffusion were noted as a function of time. Shifts in the higher frequency components (weak and moderately weak hydrogen bonded) were especially pronounced at low concentrations (short times) indicating interactions between the water molecules and the ester carbonyls. As the water content increased there was a general shift to lower frequency of the components, indicating clustering of the sorbed water, an increase in pure water like character and a strengthening of the hydrogen bonding network. The one exception to this general trend was the weak hydrogen bonded component, which after an initial shift to lower frequency in the first 5 minutes, tended to higher frequency, indicating a weakening of the hydrogen bonding. This may be indicative of an interaction between water that is already hydrogen bonded with an ester carbonyl (which would tend to give a high frequency species) and clusters of sorbed water (which would tend to give a lower frequency species). As the size and numbers of these water clusters increased, with increasing water content, so the interactions with water hydrogen bonded to the ester carbonyl would tend to increase.

The magnitude of the ν(OH) band of the water sorbed in PET at equilibrium was shown to be much greater than expected. This we have attributed to the breaking up (perturbation) of the tetrahedral network of water within the polymer matrix. We have attempted to quantify this perturbation, P, by comparing the intensities of each of the components of pure water with components of water sorbed in PET. Molar extinction coefficients and perturbation factors, P, for each of the components were calculated. The perturbation of the high frequency components was shown to be much greater than the lower frequency components, which one would expect as these components represent interactions between sorbed water and the polymer.

Examination of the P factors for equilibrium levels of sorbed water as a function of crystallinity indicated less perturbation (i.e. less interaction) in more highly crystalline polymers. This could account for the non-linear decrease in magnitude of the ν(OH) band of sorbed water at equilibrium for films of increasing crystallinity.

5.6. References

5.1. D. Langevin, J. Grenet and J.M. Saiter, *Eur. Polym. J.*, **30**, 30, (1994)

5.2. M.J. Kloppers, F. Bellucci, R.M. Lantanision and J.E. Brennen, *J. Appl. Poyml. Sci.*, **48**, 2197, (1993)

5.3. F. Bellucci and L. Nicodemo, *Corrosion*, **49**, 3, 235, (1993)

5.4. D.R. Rueda, A. Viksne, J. Kajaks, F.J. Balta-Cajella and H.G. Zachmann, *Macomol. Symp.*, **94**, 259, (1995)

5.5. D.R. Rueda and A Varkalis, *J. Polym. Sci. Part B: Polym. Phys.*, **33**, 2263, (1995)

5.6. H. Yasuda and V. Stannett, *J. Polym. Sci.*, **57**, 907, (1962)

5.7. N. Schühler, A.S. da Silva Sobrinho, J.E. Klemberg-Sapieha, M. Andrews and M.R. Wertheimer, *Soc. Vacuum Coaters: 39th Annual Technical Conf. Proc.*, 285, (1996)

5.8. G.E. Walrafen, M.R. Fischer, M.R. Hakmatadi and W.H. Yang, *J. Chem. Phys.*, **85**, 6964, (1986)

5.9. G.E. Walrafen, M.R. Fischer, M.R. Hakmatadi and W.H. Yang, *J. Phys. Chem.*, **92**, 2433, (1988)

5.10. G. D'Arrigo, G. Mansano, F. Mallamace, P. Migliardo and F. Wanderlingh, *J. Chem. Phys.*, **75**, 4264, (1981)

5.11. C.I. Ratcliffe and D.E. Irish, *J. Phys. Chem.*, **86**, 4897, (1982)

5.12. F.O. Libnau, A.A. Christy, O.M. Kvalheim, *Appl. Spec.*, **49**, 1431, (1995)

5.13. F.O. Libnau, O.M. Kvalheim, A.A. Christy and J. Toft, *Vib. Spec.*, **7**, 243, (1994)

5.14. D.E. Hare and C.M. Sorensen, , *J. Chem. Phys.*, **95**, 25, 6954, (1990)

5.15. W. Doster, A. Bachleitner, R. Dunau, M. Heibl and E. Lüscher, *Biophys. J.*, **50**, 213, (1986)

5.16. J. Teixera and H.E. Stanley, *J. Chem. Phys.*, **73**, 3404, (1980)

5.17. M. Settles and W. Doster, *Faraday Disc.*, **103**, 269, (1996)

5.18. V.J. McBriety, J.M.D. Coey and N.G. Boyle, *Chem. Phys. Lett.*, **86**, 16, (1993)

5.19. G. Otting, E. Liepnish and K. Wuthrich, *J. Amer. Chem. Soc.*, **113**, 4363, (1991)

5.20. J.M. Goodfellow, M. Knaggs, M.A. Williams and J.M. Thornton, Faraday Disc., **103**, 339, (1996)

5.21. J.A. Ernst, R.T. Chubb, H.X. Zou, A.M. Grogenhorn and G.M. Clore, *Science*, **267**, 1813, (1995)

5.22. V. Denisov and B. Halle, *Faraday Disc.*, **103**, 227, (1996)

5.23. Y. Marachel and A. Chamel, *J. Phys. Chem.*, **100**, 8551, (1996)

5.24. Y. Marachel and A. Chamel, *Faraday Disc.*, **103**, 349, (1996)

5.25. Q.T. Nguyen, E. Byrd and C. Lin, *J. Adhesion Sci. Techn.*, **5**, 697, (1991)

5.26. N.J. Tao, S.M. Lindsay and A. Rupprecht, *Biopolym.*, **28**, 1019, (1989)

5.27. M. Falk, *Can. J. Chem.*, **58**, 1495, (1980)

5.28. G. Ononi and A. Sanctucci, *J. Phys. Chem.*, **97**, 5430, (1993)

5.29. D.J. Christopher, B.P. Hills, P.S. Belton and J. Yarwood, *J. Coll. Int. Sci.*, **152**, 465, (1992)

5.30. J.G. van Alsten and J.C. Coburn, *Macromolecules*, **27**, 3752, (1994)

5.31. P.D. Moran, G.A. Bowmaker, R.P. Cooney, J. Bartlett and J.L. Woofrey, *Langmuir*, **11**, 738, (1995)

5.32. A. D'Apprano, A. Lizzio, V. Turco-Liveri, F. Aliotta, C. Vasi, E. Bardez, D.I. Donato, B. Larrey and P. Migliardo, *J. Phys. Chem.*, **92**, 4436, (1988)

5.33. D. Murphy and M.N. Dephinho, *J. Membrane Sci.*, **106**, 245, (1995)

5.34. P. Sutander, D.J. Ahn and E.I. Frances, *Macromolecules*, **27**, 7316, (1994)

5.35. P. Sutander, D.J. Ahn and E.I. Frances, *Thin Solid Films*, 263, 134, (1995)

5.36. J.R. Scherer, M.K. Go and S. Kint, *J. Phys. Chem.*, **78**, 1304, (1974)

5.37. Z. Bashir, S.P. Church and D. Waldron, *Polymer*, **35**, 967, (1995)

5.38. Y. Maeda, N. Tsukida, H. Kitano, T. Terada and J. Yamananka, *J. Phys. Chem.*, **97**, 3619, (1993)

5.39. Y. Maeda, N. Tsukida, H. Kitano, T. Terada and J. Yamananka, *Spectro Chimica Acta*, **51**, 2433, (1995)

5.40. Y. Maeda, N. Tsukida, H. Kitano, T. Terada and J. Yamananka, *Macromolecular Chem. Phys.*, **197**, 1681, (1996)

5.41. H. Kusanagi and S. Yukawa, *Polymer*, **35**, 26, 5637, (1994)

5.42. M. Fukada, H. Kawai, N. Yagi, O. Kimura and T. Ohta, *Polymer*, **31**, 295, (1990)

5.43. P.D. Richards, E. Weitz, A.J. Ouderkirk and D.S. Dunn, *Macromolecules*, **26**, 1254, (1993)

5.44. R. Belali and J.M. Vigoureux, *Appl. Spec.*, **48**, 4, 465, (1994)

5.45. E. Anderssen and H.G. Zachmann, *Colloid Polym. Sci.*, **272**, 11, 1352, (1994)

5.46. D.J. Walls, *Appl. Spec.*, **45**, 7, 1193, (1991)

5.47. P. Lapersonne, D.I. Bower and I.M. Ward, *Polymer*, **33**, 6, 1277, (1992)

5.48. M. Pereira, Thesis, Durham, (1994)

5.49. N.E. Schlotter and P.Y. Furlan, *Polymer*, **33**, 16, 3323, (1992)

5.50. N.W. Hayes, G. Beamson, D.T. Clark, D.S-L. Law and R. Raval, *Surface and Interface Analysis*, **24**, 19, 723, (1996)

5.51. D.J. Walls and J.C. Coburn, *J. Polym. Sci. Part B: Polym. Phys.*, **30**, 887, (1992)

5.52. C. Sammon, C. Mura, J. Yarwood, N. Everall, R. Swart and D. Hodgson, (in press)

5.53. F.M. Mirabella, *Appl. Spec. Rev.*, **21**, 45, (1985)

5.54. 'Internal Reflection Spectroscopy', (Ed F.M. Mirabella), Marcel-Dekker, New York, (1993)

Chapter 6

The Degradation of PET in water.

6.1. Introduction.

It is well-known that aqueous coatings applied to PET films have an adverse effect on the reclaimability of the film [**6.1**]. The coatings can affect the optical clarity, melt viscosity and colour of the recycled film, the reasons for which are poorly understood despite the work carried out in this field [**6.2-6.17**]. During coating application in film manufacture, the film is exposed to both water and elevated temperatures in excess of 200°C. Recently, techniques such as ESCA (SIMS) have shown that even at lower temperatures, of around 50°C in water, the uppermost surface i.e. < 2 nm of PET undergoes hydrolysis [**6.18**]. The aim of this chapter was to mimic the top 100 nm of a PET film and look at the effects of water on its structure using infrared spectroscopy. The rationale is that, whilst ESCA (SIMS) gives one information on the uppermost surface (<5nm), it provides no real gauge as to how deep the degradation penetrates at these lower temperatures. Reflection absorption infrared spectroscopy (RAIRS) is an ideal tool for looking at films of around 100 nm thickness and has been discussed in section 2.7.3.

The hydrolysis of PET is known to occur significantly in moist, wet or humid conditions at temperatures above the T_g. The results include an increase in carboxylic and alcoholic end groups and an increase in smaller chain fragments [**6.2-6.17**] probably by reverse esterification [**6.8**]. The presence of acid or basic conditions increases the rate of hydrolysis significantly, but the mechanism is thought to be similar [**6.8**]. Although apparently simple, the mechanism for the hydrolysis of PET is not fully understood and

at least four different kinetic schemes have been proposed [6.2-6.5]. It is thought that the water diffuses into the amorphous regions of the polymer and it is here that hydrolysis occurs. The rate will obviously depend on the polymer morphology and degree of crystallinity, and on the relative humidity and temperature. The kinetics have also been shown to have some autocatalytic character [6.4, 6.12, 6.13]. The role of the carboxylic end groups presents a problem. Some authors have chosen to ignore the role of end groups [6.2, 6.5] whilst others have reasoned that the autocatalytic effect and the increasing hydrophilicity effects of the acid must be significant [6.12, 6.13].

One proposed mechanism for the hydrolytic degradation of PET in water is a reverse *trans*-esterification process at random ester carbonyls in the polymer chain. This is shown in figure 6.1.

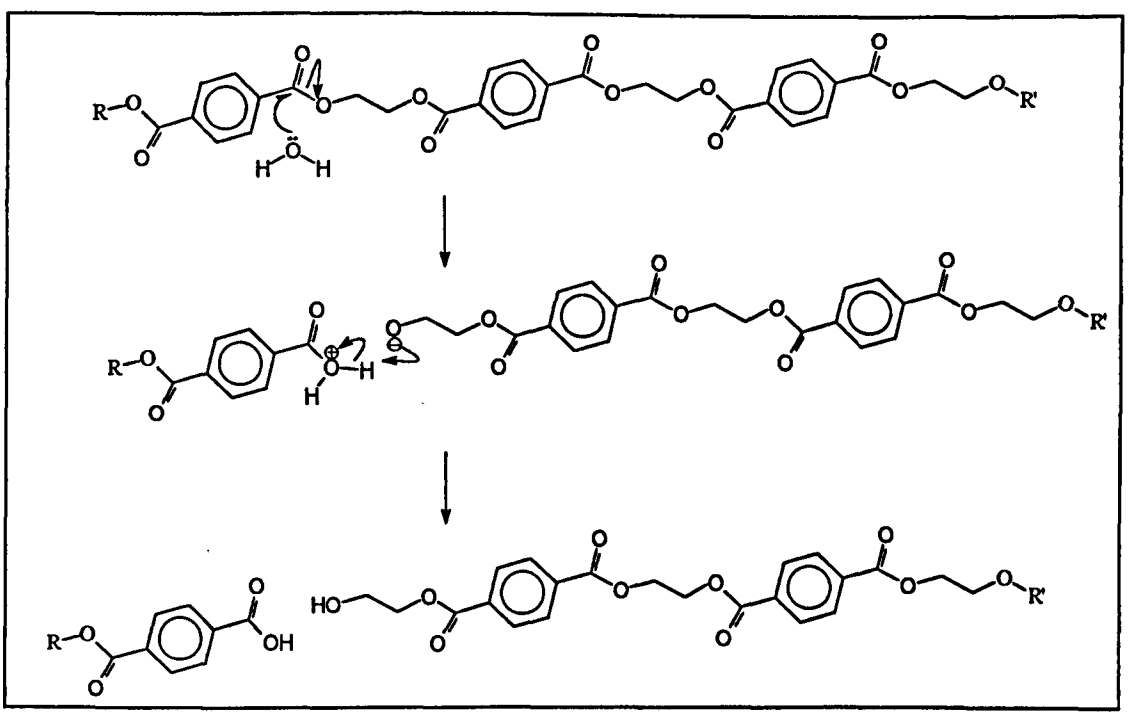

Figure 6.1. One proposed mechanism for the hydrolysis of PET involving random in-chain scission

During the degradation process numerous authors have reported density changes [**6.8-6.12, 6.16, 6.17**] which have been attributed to a so-called 'chemicrystallisation' process. The idea is that the chain scissions will only be occurring in the amorphous regions, leading to small chain segments with enough mobility to realign and therefore crystallise. It is interesting to note that the chemicrystallisation effect has also been seen during oxidative degradation [**6.19**]. Crystallinity changes occurring during degradation are extremely important as the morphology governs things such as small molecule transport and tensile strength. It has also been found by numerous workers that the initial degree of crystallinity greatly affects the rate of hydrolysis [**6.2, 6.4, 6.8-6.11**].

Ballara and Verdu [**6.6**] have looked at the hydrolysis of PET foils in water at 100°C using gravimetric, transmission IR and microcalorimetric techniques. They reasoned that the hydrolysis of a straight chain ester should result in significant weight gain (assuming no loss of water soluble molecules) which could readily be measured on a laboratory balance. The rate of hydrolysis was determined by the measurement of the carboxyl end groups as a function of time. The increase in crystallinity was measured via density measurements. Two explanations for the increase in crystallinity are given. Firstly, the extraction of low molecular weight compounds and secondly chemicrystallisation. The effects of chemicrystallisation were calculated and estimated to incorporate 5 to 6 monomer units into the crystalline phase per chain scission. They suggest that increasing the number of end groups increases the hydrophilicity allowing more water in the system giving some auto catalytic character to the kinetics.

The results could still not account for the chain end effects which other authors have claimed [**6.6**]. Ballara postulates that the existence of weight loss points towards a

preferential hydrolysis at the terminal rather than 'internal' ester groups leading to the formation of small, water soluble products.

Allen et al have tried to circumvent the 'water solubles' loss problems by looking at degradation of different types of PET in humid conditions in a number of publications [6.8-6.11]. This has the disadvantage of taking several hundred days to perform an experiment, but was perhaps a more realistic approach to examining the stability of archive film, as was the intention. The works cited here also examined UV and thermal degradation processes which will occur at the same time in a real system. Intrinsic viscocities were measured and related to molecular weights, density was measured and related to crystallinity and the end groups were calculated using an infrared technique developed at ICI Wilton [6.20].

They found that during the early stages of hydrolytic ageing of PET there was an initial 'rapid' increase in crystallinity (in amorphous samples) due to the plasticisation effects of the water vapour, followed by a slower crystallisation effect caused by the degradation and chemicrystallisation effects. They conclude that the crystallisation and main chain scission are not necessarily related, which may make the correlation of mechanical properties difficult. The initial crystallinity was shown to play an important role in the rate of hydrolysis as was the relative humidity and temperature used. The role of wet soil in degradation was also examined and this was found to have a marked affect on the hydrolytic ageing rate. Metal ions in the soil were suggested to be acting as degradands. It was interesting to note that hydrolysis was found only to be dominant above the glass transition temperature of the polyester and in highly humid conditions [6.8-6.11].

One of the main aims of this work was to follow up the work done by Hodgson and fellow workers, who have examined the surface of degraded PET using ESCA SIMS [6.16]. They have found evidence for degradation at low (<60° C) temperatures in the top surface of a thick PET film. The aim of this project was to use a 100-200 nm PET film to simulate the top surface of a thick film undergoing different treatments in water.

6.2. Experimental

This section will deal with the manufacture and treatment of suitable PET samples for examination using RAIRS. The theory of RAIRS is detailed in section 2.7.3. but the reader is reminded that the technique involves a single external reflection, requiring a reflective (metallic) substrate and thin (< 1 μm) sample.

The reflective substrates were made from metal coated glass slides. Initially it was hoped to use aluminium to form a reflective surface, as this was cheap and gave a high reflective throughput, but as will be discussed later in section 6.3.1. this was found to be unsuitable for later experiments due to the reactive nature of aluminium. The search for a more robust reflective surface resulted in using a glass slide coated first with chromium, then with gold. The chromium acted as a 'primer' by binding strongly both with the silicon oxide in the glass and the gold. Simple avaporated gold coatings were found not to bind very well directly on to the glass and were easily removed by brushing or submerging in hot water.

The glass slides were kindly donated by Pilkington Glass plc. The gold was bought in a wire form from Advent Research Materials Limited and was 99.99 % pure. The

aluminium wire was bought from Advent Research Materials Limited and was 99.99 % pure. The chromium was retrieved as filings from the engineering workshop.

The glass slides were coated in an Edwards Coating System E306A evaporation coater. The geometry of such a system is shown in figure 6.2.

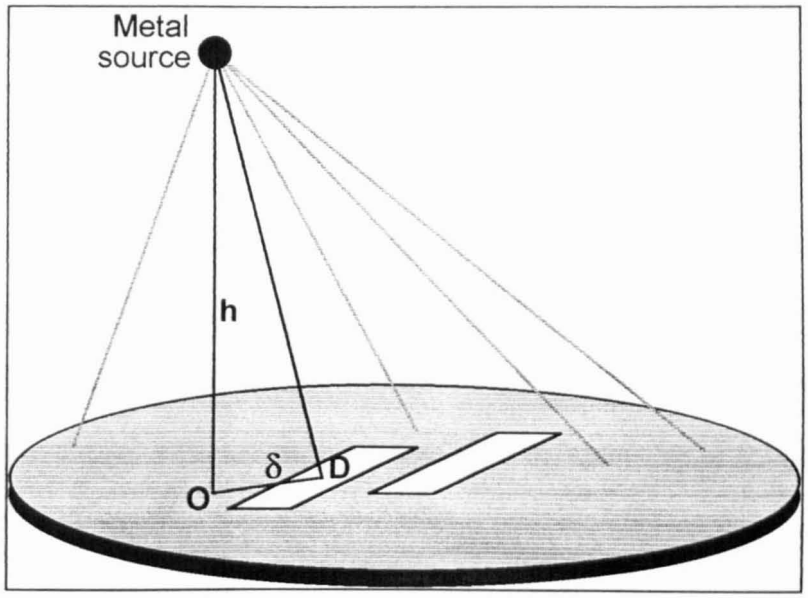

Figure 6.2. The geometric layout of the evaporation coater.

The distance from the point metal source (h) can be used to calculate the thickness (t_0) at the point O, vertically underneath the source, by the following relationship

$$t_0 = \frac{m}{4\pi\rho h^2} \qquad \text{(eq. 6.1.)}$$

Where m is the total mass of the metal evaporated,

ρ the density of the metal

h is the height of the metal source from the slide

The thickness at any point, D, at a distance δ from point O is given by

$$t(D) = t_0 \frac{1}{\left[1+\left(\frac{\delta}{h}\right)^2\right]^{\frac{3}{2}}} \qquad \text{(eq. 6.2.)}$$

It is obvious that the coverage of metal will not be uniform, but the greater the height (i.e. δ/h tends to 0), the more uniform the coating will be. It was found that by using 0.25g of gold a thickness of around 100nm was obtained. The thickness of the coating was not deemed to be an issue as long as a good reflection was obtained. Gold coatings on a precursor of chromium prepared in this way were found to be adequate. The precursor of Chromium was prepared in the same way using 0.02g of metal to produce a 10nm film which is adequate to form a binding layer. A schematic of the resulting slide structure is shown in figure 6.3.

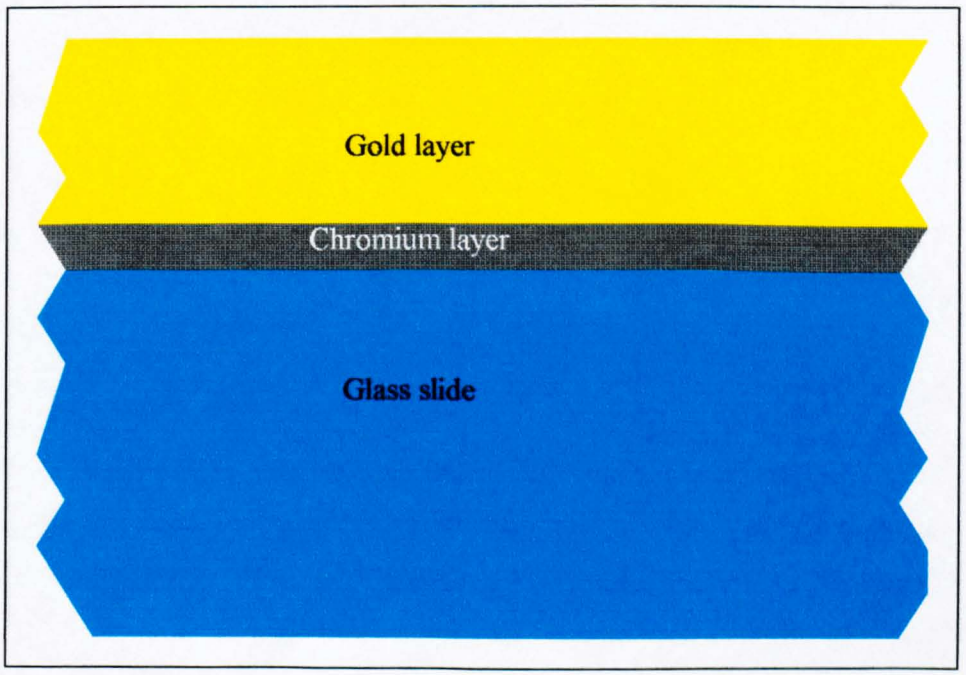

Figure 6.3. Schematic of the slides manufactured for the RAIRS experiments.

6.2.1. Film preparation

All the films were manufactured from solutions made using extrusion grade E47 PET donated by ICI, Wilton. All solvents were spectroscopy grade and purchased from Aldrich. Films were prepared in a number of ways and each one evaluated. Films were prepared by dipping in a 5% PET / trichloroethane (TCE) solution, spin cast from hexafluoroisopropanol (HFIP) and spin cast from *ortho*-chlorophenol (OCP). The film thicknesses and to a certain extent the uniformity were gauged from the elipsometry results, some of which are shown in section 6.2.2.

The spin coated films were made by dropping around 0.5 ml of solution onto a metal coated slide and spun at 4000 RPM for 10 seconds on an in-house manufactured spin coater. The films were left to dry for 30 minutes.

6.2.2. Film characterisation

The film thicknesses were determined on a Sentech SE400 multiangle elipsometer equipped with an automated stage and the roughness determined on a WYCO Systems white light interferometer. Sample elipsometry output are shown in figures 6.4. to 6.6. and an example of the WYCO output is shown in figure 6.6.

Figure 6.4. shows some interesting features. Firstly the film coating from 5% polymer in HFIP is quite even between 200 and 220 nm. There are some areas on the slide where there appears to be no sample. These have been shown to be areas where the aluminium

has fallen off the slide. There is poor adhesion between the aluminium and the glass so this is quite a common phenomenon.

Figure 6.5. shows the sample manufactured from 5% polymer in OCP. This procedure produces the best quality of samples which are even in thickness on a nm scale. It is thought that the viscous nature and the relatively high boiling point of the solvent aid film formation. The samples manufactured using HFIP are found to be much rougher, due to the high volatility of solvent which is thought to evaporate in some areas before the spinning has had a chance to produce an even coating This roughness is shown on the WYCO output (figure 6.6.) which uses white light interferometry to determine roughness parameters.

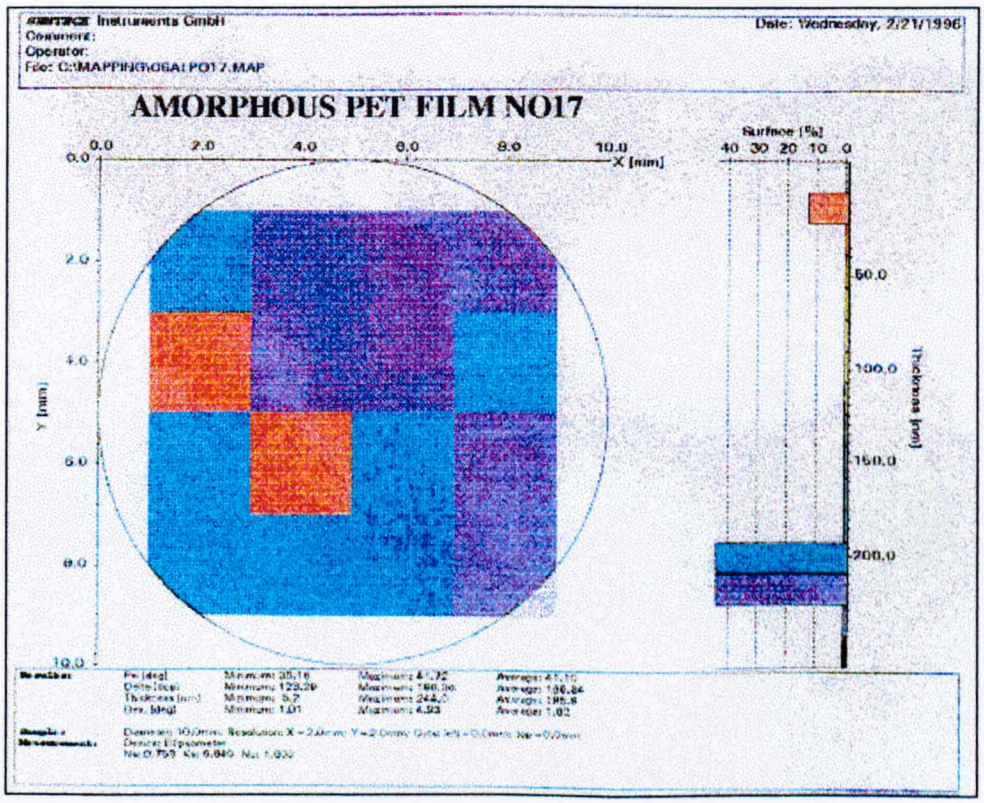

Figure 6.4. PET spin coated from 5% HFIP on aluminium coated glass.

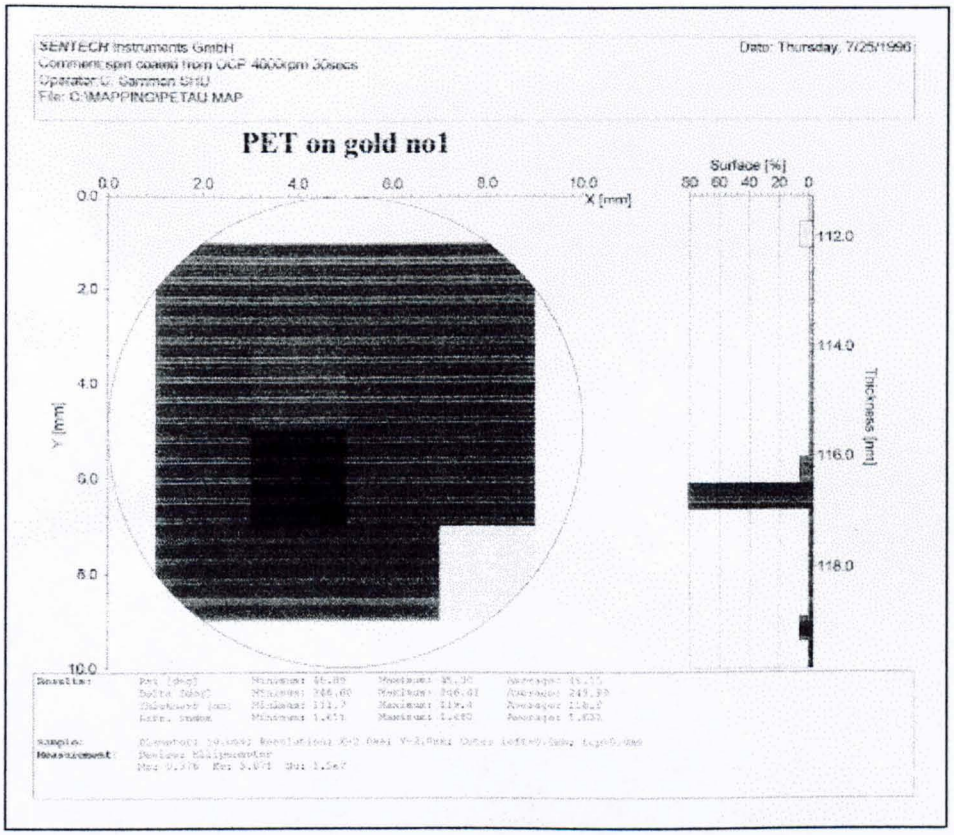

Figure 6.5. PET spin coated from 5% OCP on gold coated glass.

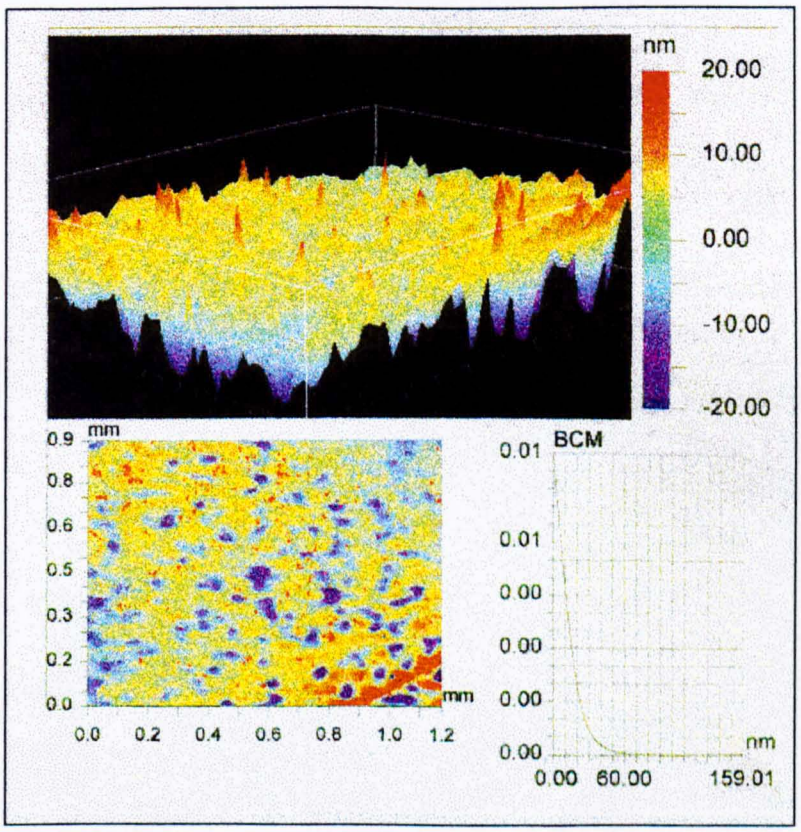

Figure 6.6. WYCO of PET spin coated from 5% HFIP on gold coated glass.

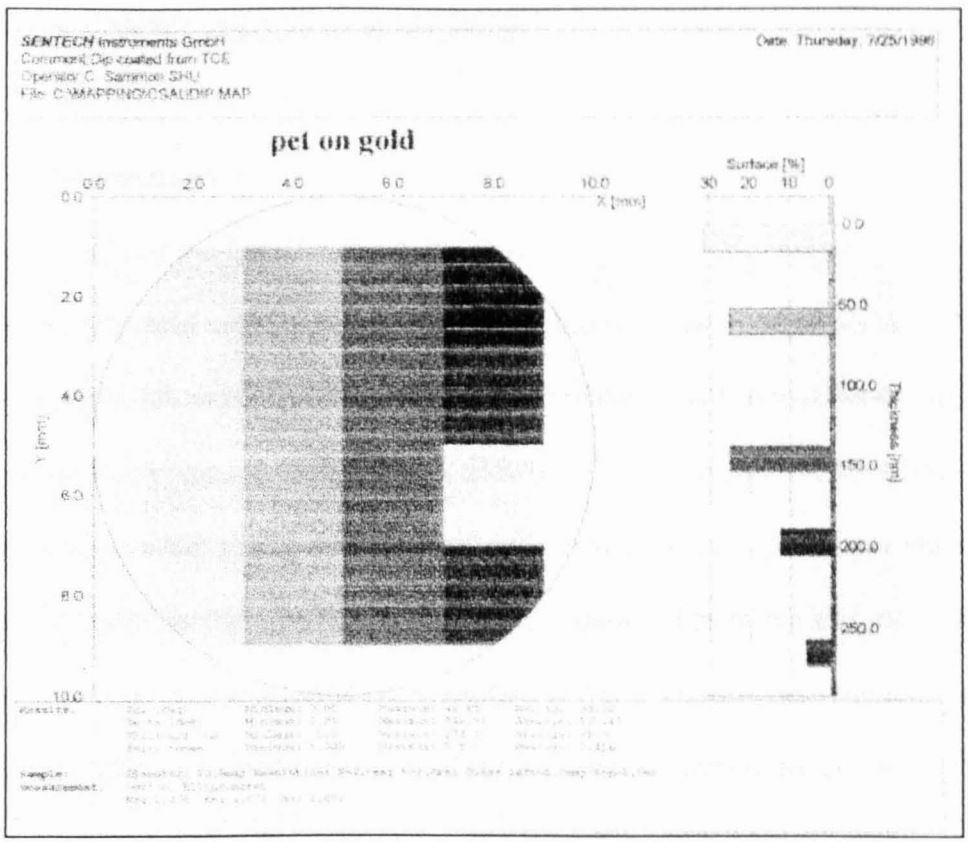

Figure 6.7. PET dip coated from 5% TCE on gold coated glass.

Figure 6.7. clearly illustrates the fact that the dipping procedure is unsuitable for the manufacture of even PET films. It shows the rippling effect that is noticeable even with the naked eye, where refractive index changes due to the ripples create a 'rainbow' pattern on the slide.

The films that were examined during this work were therefore manufactured from 5% OCP solution and spun at 4000 RPM for 10 seconds.

The crystallinity was calculated from infrared measurements described in section 5.3. Differences in the crystallinities between films spin cast from OCP and HFIP were noted.

The films spin cast from HFIP had ~1-2 % crystallinity whilst those spin cast from OCP were found to be between 4 and 5 % crystalline.

6.2.3. Film treatment.

All films were treated in the same manner. Deionised water was placed in a clean 150 ml screw topped bottle and placed in a water bath at the designated temperature. The temperature of the water in the bottle was allowed to equilibrate for at least 4 hours. The samples were completely immersed in the water and the top replaced and the timer started. It was found that treating a sample for 1 hour and then taking a spectrum had the same effect as treating a sample in water for two separate half hours and then taking a spectrum. This meant that it was possible to use the same sample for all the measurements at the specified conditions. The following tables summarises the experimental conditions of the data. Table 6.1. shows the experimental conditions used in the study of the plasticisation effects of water. Table 6.2. shows the experimental conditions used to examine the degradation of PET in water.

	Temperature					
Time / Minutes	**52° C**	**62° C**	**70° C**	**80° C**	**80° C (air)**	**90° C**
0	✓	✓	✓	✓	✓	✓
5	✓	✓	✓	✓	✓	-
10	✓	✓	✓	✓	✓	✓
20	✓	✓	✓	✓	✓	✓
30	✓	✓	✓	✓	✓	✓
60	✓	✓	✓	✓	✓	✓
120	✓	✓	✓	✓	✓	✓
240	-	-	-	✓	-	✓
360	-	-	-	✓	-	-
480	-	✓	✓	✓	-	-

Table 6.1. Temperatures and times of treatment of RAIRS samples in water.

Time Days	Temperature / 90° C
1	✓
2	✓
3	✓
4	✓
5	✓
6	✓
7	✓
8	✓

Table 6.2. Temperatures and times of treatment of RAIRS samples in water.

Time hours	Temperature / 90° C, 1% KOH
1	✓
2	✓
3	✓
4	✓

Table 6.3. Temperatures and times of treatment of RAIRS samples in 1% KOH.

An attempt was also made to simulate stenter conditions, whereby a PET sample was coated with water and placed in the oven at 200° C until the water had evaporated.

6.3. The effects of water on PET at elevated temperatures.

6.3.1. Plasticisation effects of water.

It is known that water can act as a plasticiser, giving polymer molecules mobility with which to rearrange and form different conformers. During the early stages of this project whilst looking for the mildest conditions at which one could observe degradation on a reasonable timescale, several films were looked at, in water, at temperatures below and around the glass transition temperature (80° C). It was noted that these films underwent *gauche* to *trans* conversion at temperatures below those that one would expect. This finding was interesting but it was something of an 'aside' from the initial goals of this section of the project and as such not much work has been done obtaining things such as rate constants and activation energies of the conversions. Attempts to fit the polymer crystallisation data to the Avrami model, which has been used in the past to describe crystallisation rates **[6.21]**, proved to be unsuccessful due to the E_A of crystallisation being dependent on the *trans* conformer content **[6.22]**.

Figures 6.9 - 6.12 show the effect of water on the crystallinity versus time profiles for PET at 80° C and table 6.4 gives a summary of the recorded crystallinity changes in PET as a function of submersion in water at sub T_g temperatures.

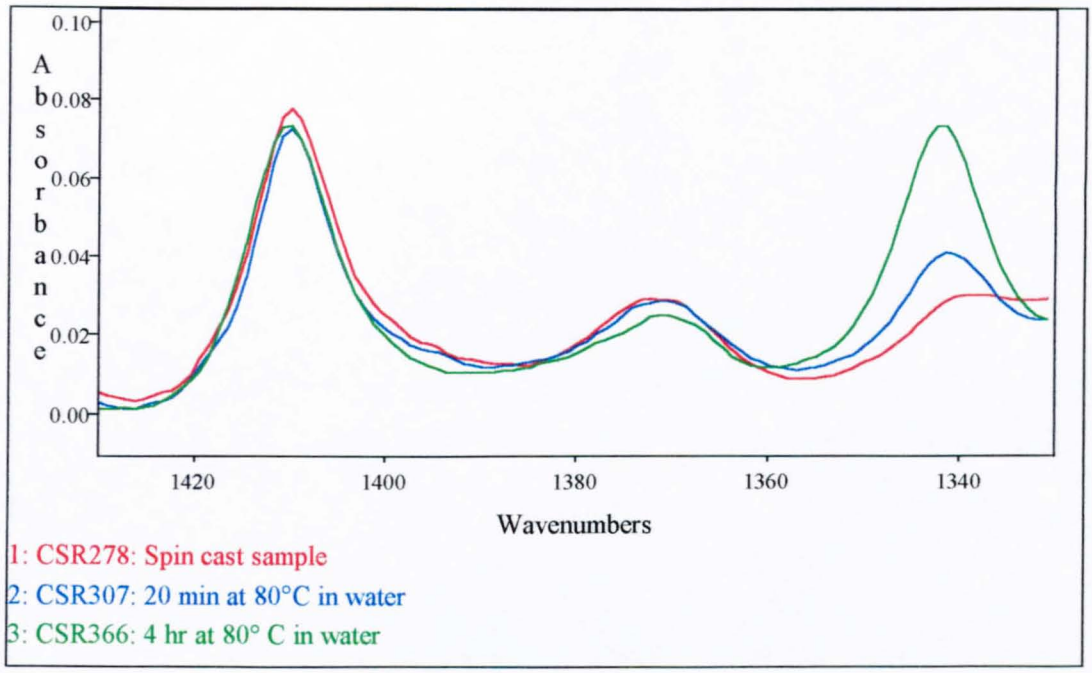

Figure 6.9. CH_2 wagging region of PET treated at 80° C in water.

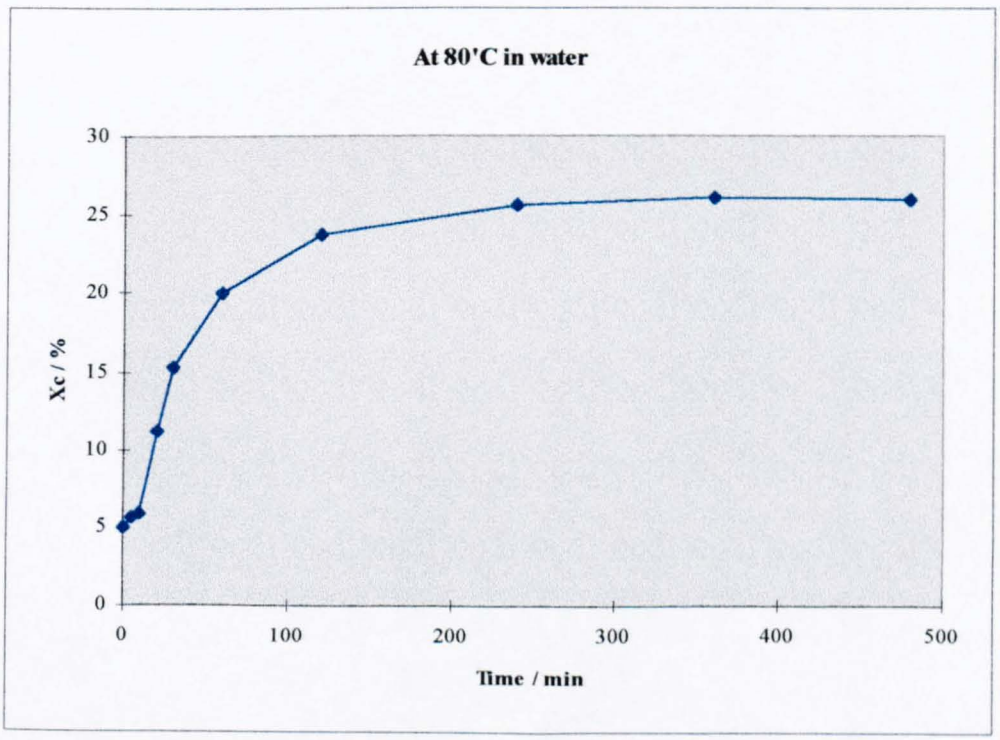

Figure 6.10. Plot of PET crystallinity versus time of treatment at 80° C in water.

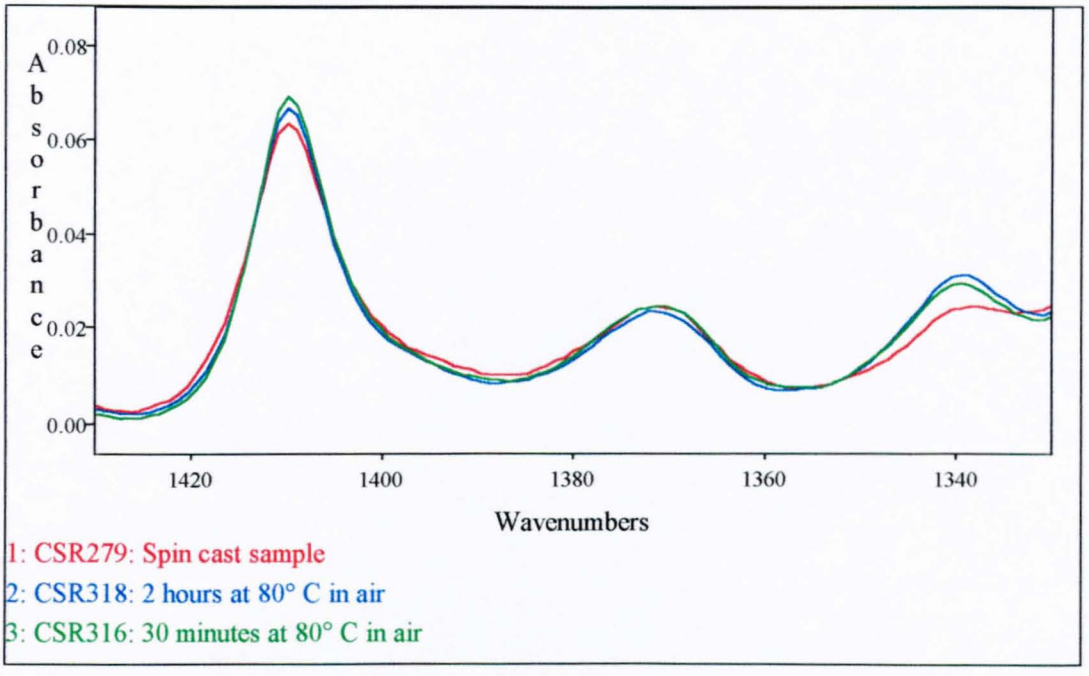

Figure 6.11. CH_2 wagging region of PET treated at 80° C in air.

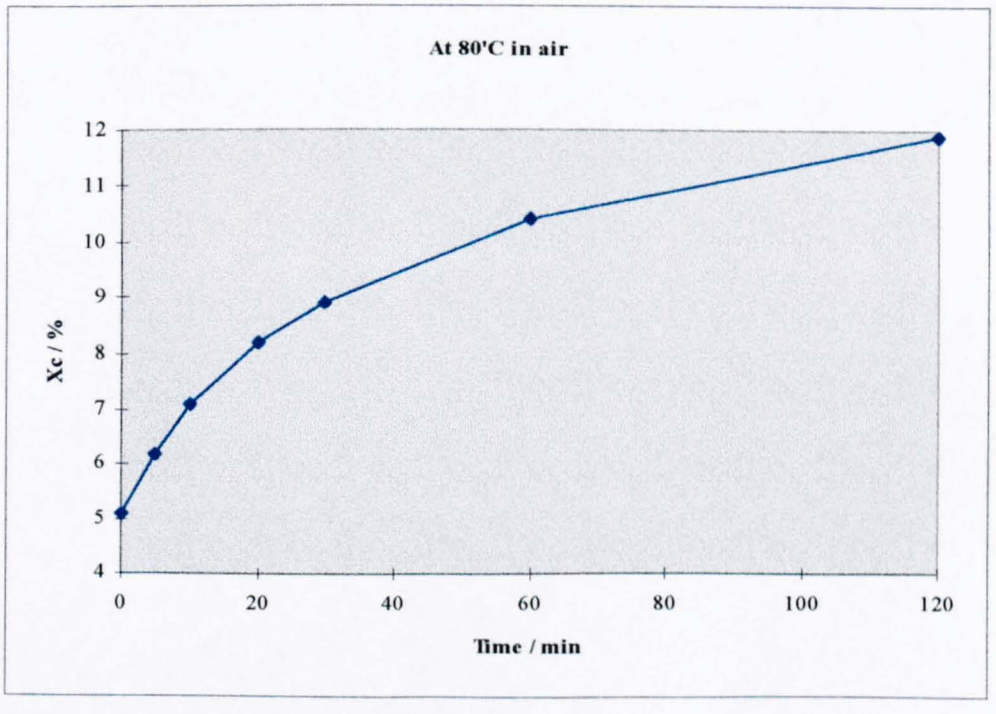

Figure 6.12. Plot of PET crystallinity versus time of treatment at 80° C in air.

	X_C / %					
Time / Minutes	**52° C**	**62° C**	**70° C**	**80° C**	**80° C (air)**	**90° C**
0	0.7	5	5.1	5	5.1	6.8
5	1.5	5.1	5.3	5.6	6.2	-
10	2.1	5.2	5.4	5.8	7.1	11
20	2.3	5.3	5.7	11.2	8.2	18.6
30	2.4	5.6	6.4	15.3	8.9	24
60	2.5	5.7	6.8	20.1	10.4	32
120	2.4	5.8	7.2	23.8	11.9	36
240	-	-	-	25.7	-	38
360	-	-	-	26.1	-	-
480	-	6.3	7.3	26	-	-

Table 6.4. Crystallinity versus time for PET at various temperatures.

Lin and Koenig looked at the *gauche-trans* isomerism in PET as a function of temperature in air between 75 and 240° C [**6.22**]. A two phase process was suggested, one phase involving an essentially constant activation energy at low levels of *trans* conformer content. The second process, which occurs at higher *trans* content, shows a linear increase in activation energy with *trans* content. These experimental conditions were different to those examined during this work and the difference may be further heightened by the fact that this work was also examining a 'surface' effect rather than a 'bulk' effect.

6.3.2. The hydrolytic degradation of PET.

This next section will examine the complex changes that occur to a PET film placed in water at 90° C. As stated in section 6.1. the exact nature of the hydrolysis of PET is not fully understood. It is however thought to produce carboxyl and alcoholic end groups in equal proportions and shorter polymer chain lengths. As far as we are aware there has been no detailed study published on the conformational changes occurring in the polymer chains during hydrolysis using infrared spectroscopy. Published work has tended to focus on infrared spectroscopy for end group analysis and viscometry for density changes **[6.6-6.12]**. Changes in the density have been interpreted as a chemicrystallisation process with the shorter chains having greater mobility and freedom to form denser crystalline structures. It should also be noted that the examination of conformational changes has in the past been hampered by the thickness of the films studied. Sections 1.4 and 1.5 have dealt with the conformational changes occurring in PET upon annealing and this touched upon sampling difficulties (i.e. saturation problems) associated with studying thick films using traditional infrared techniques. By using thin (~100nm thickness) films, this work circumvents the saturation problems associated with transmission and ATR (strong bands such as the carbonyl and ester bands) and allows a detailed look at the structural changes that occur within the polymer matrix.

Figure 6.13. shows the full mid infrared spectrum of PET before and after 8 days of treatment at 90° C in water. Figures 6.13. - 6.21. show the spectral changes that occur with time during the hydrolysis of PET. The spectra shown are as recorded, with adjustments made in the absorbance scale so that comparisons can be easily made, except

in the case of figures 6.13., 6.16. and 6.17. where different slopes in the baseline made comparison of the OH region difficult. In this instance the baseline was corrected by

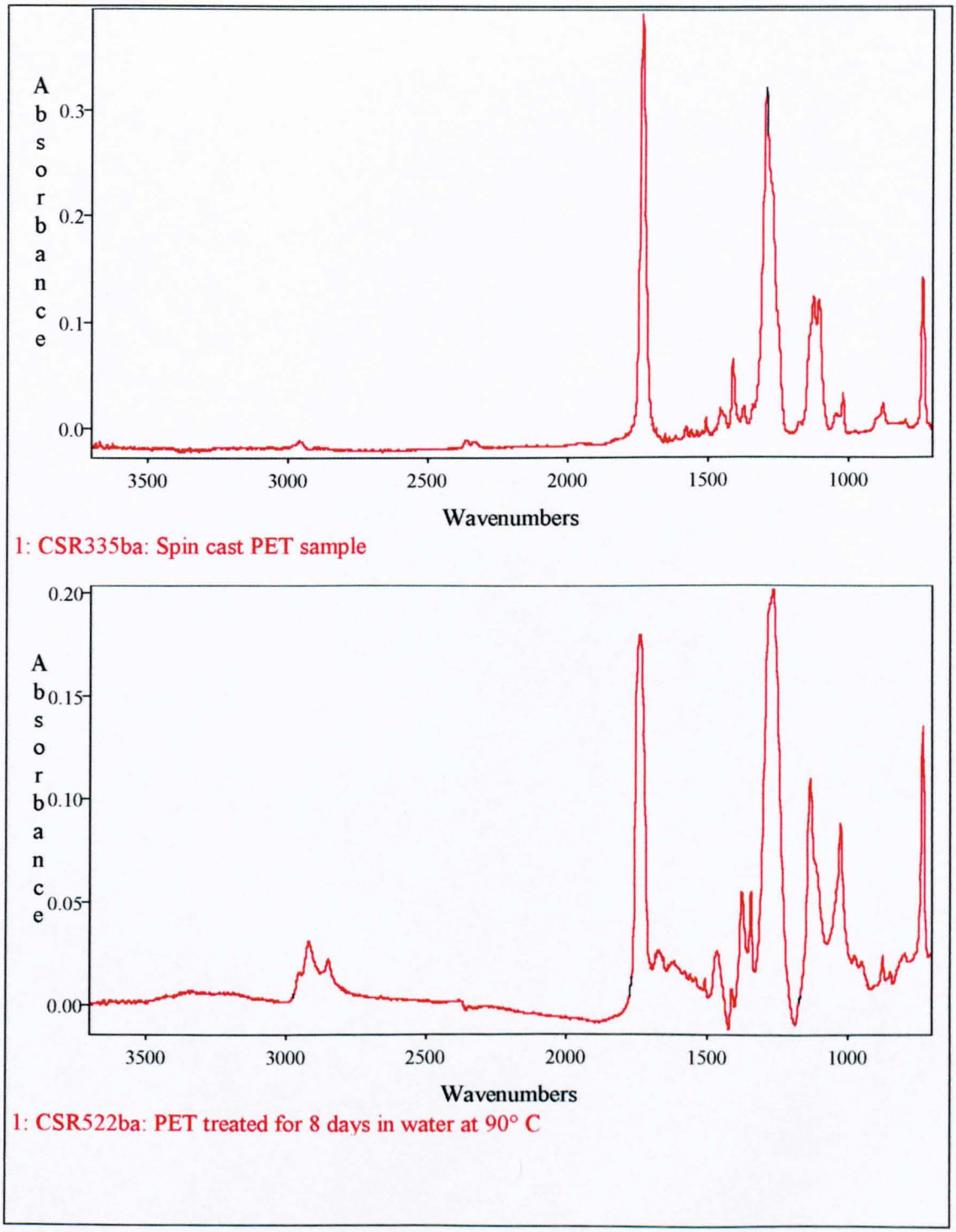

Figure 6.13. The full mid-infrared spectrum of PET before and after 8 days treatment in 90° C water.

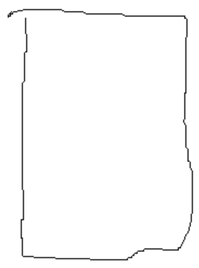

PAGES ARE MISSING IN ORIGINAL

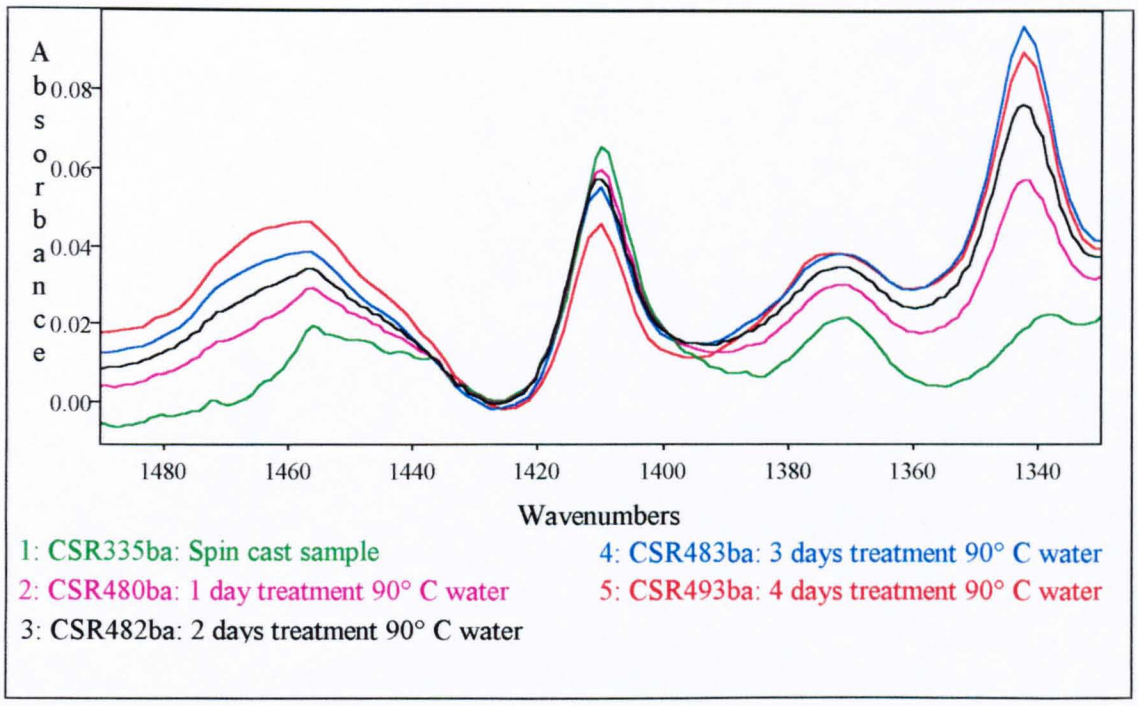

Figure 6.14. The CH_2 wagging modes and acid C-O stretch of PET treated in pure water.

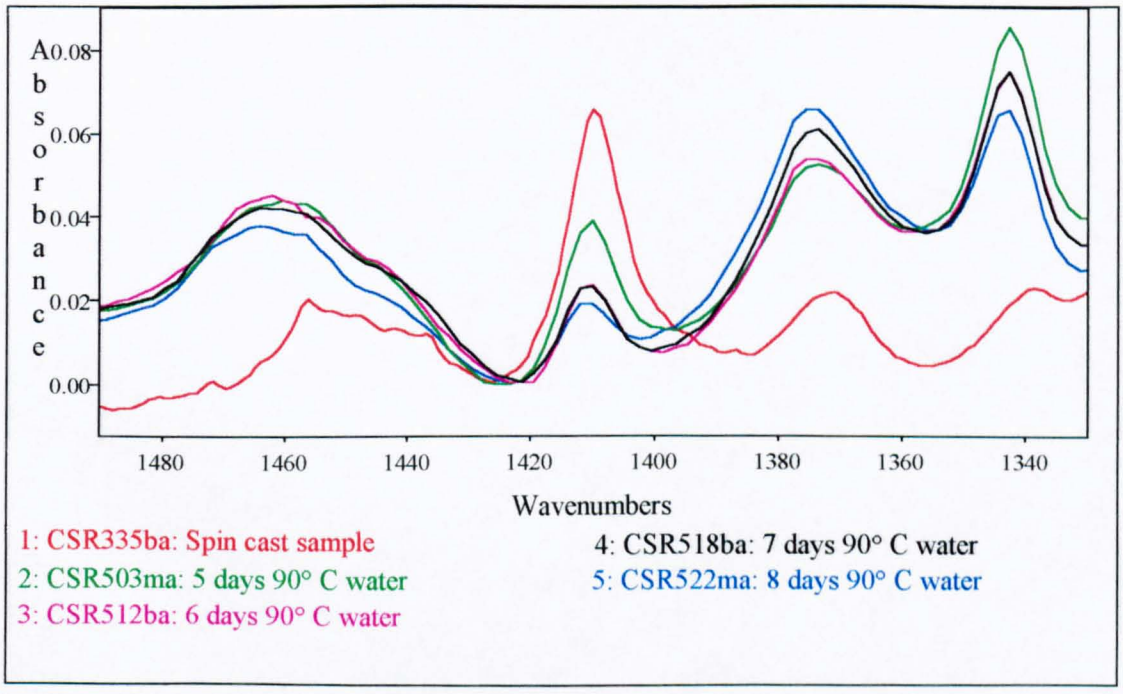

Figure 6.15. The CH_2 wagging modes and acid C-O stretch of PET treated in pure water.

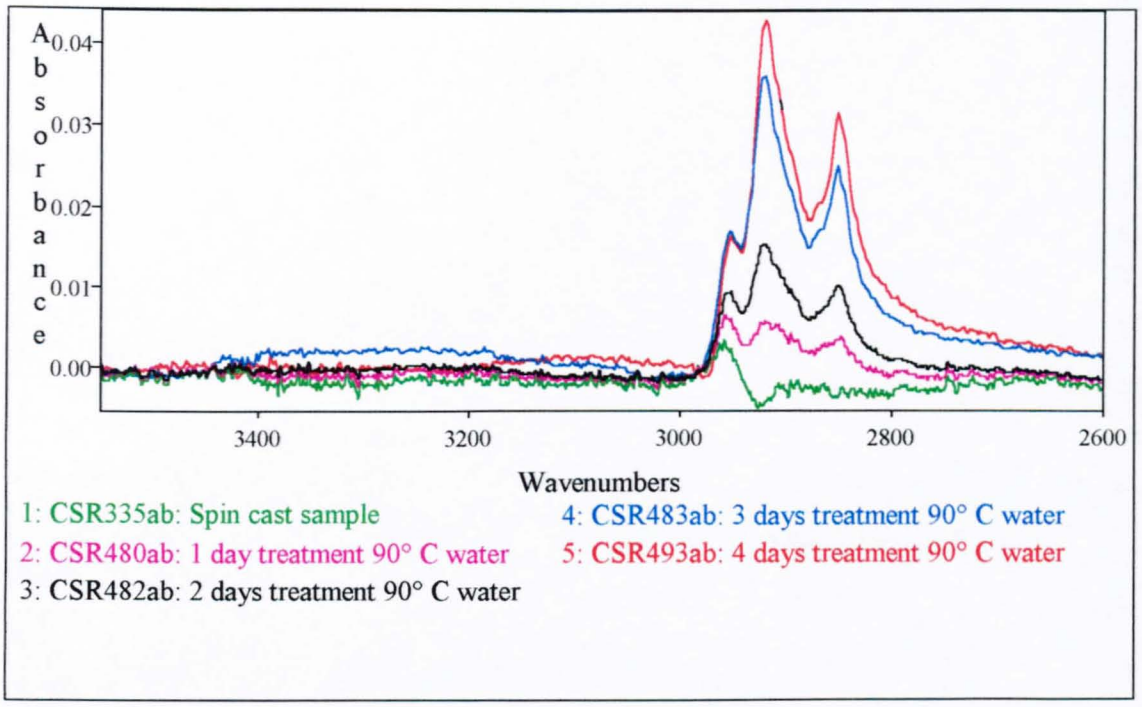

Figure 6.16. The CH and OH stretching regions of PET treated at 90° C in water.

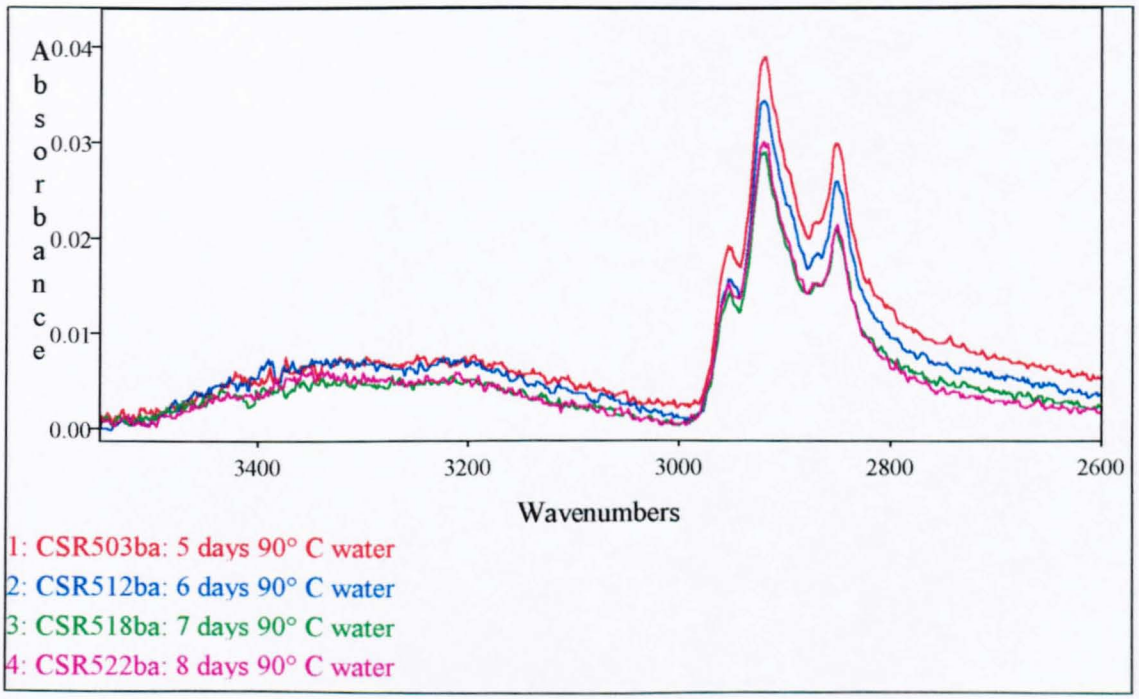

Figure 6.17. The CH and OH stretching regions of PET treated at 90° C in water.

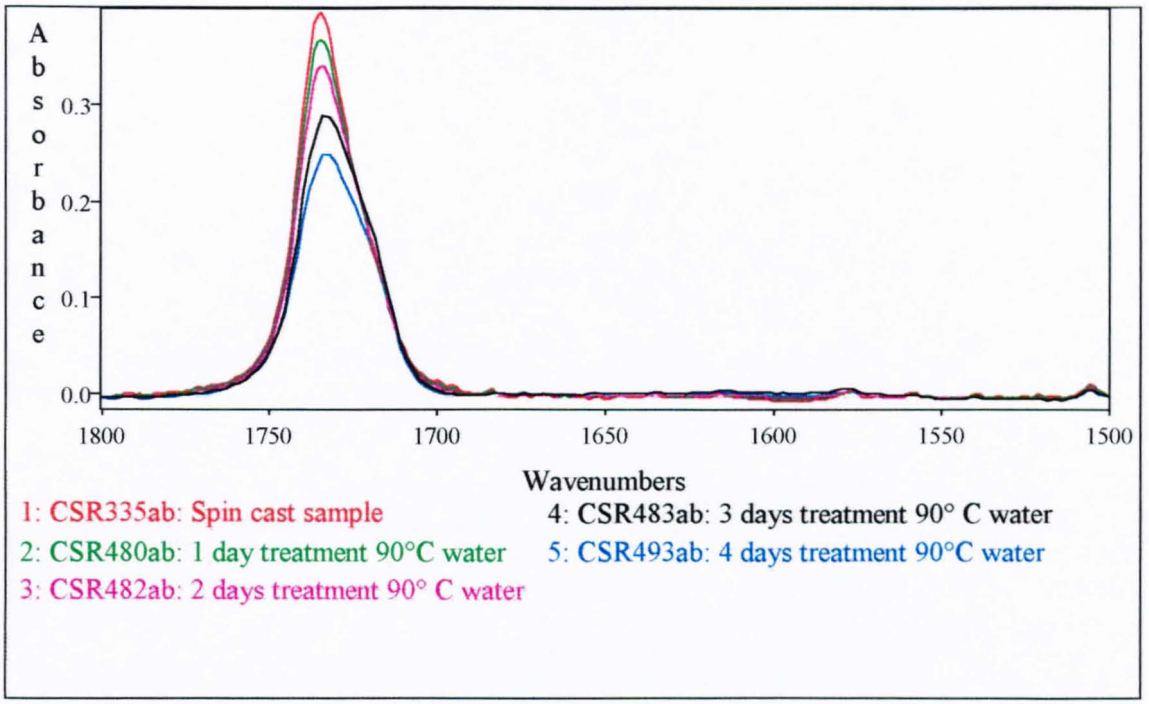

Figure 6.18. The carbonyl region of PET treated at 90° C in water.

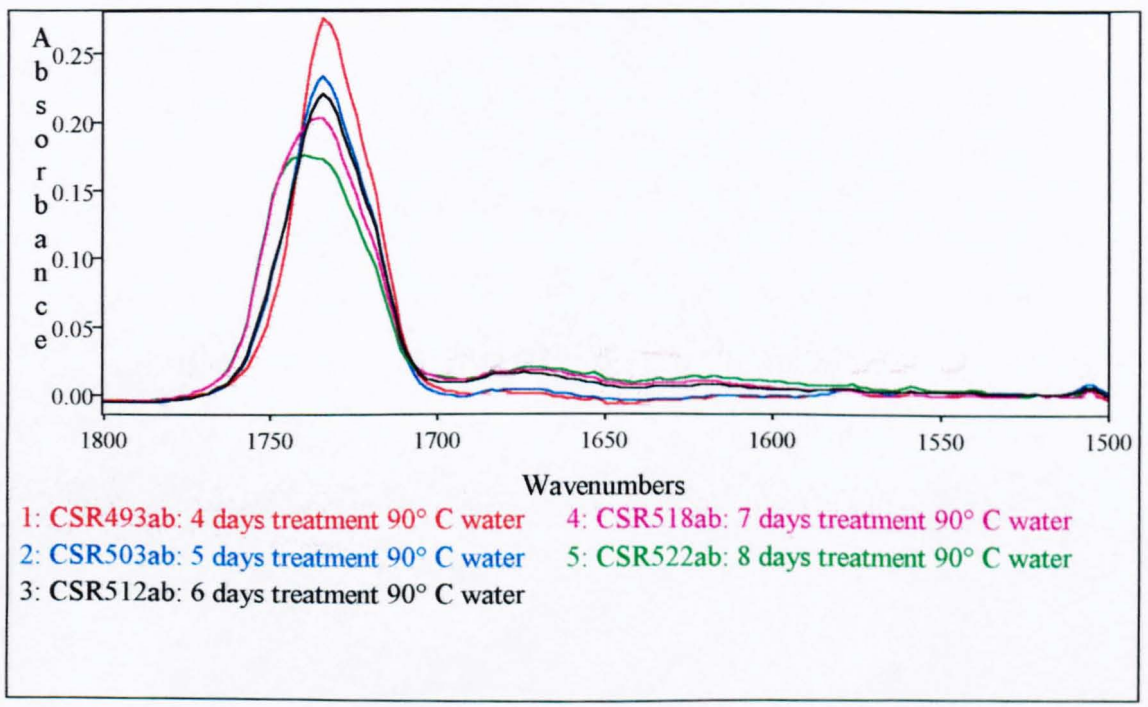

Figure 6.19. The carbonyl region of PET treated at 90° C in water.

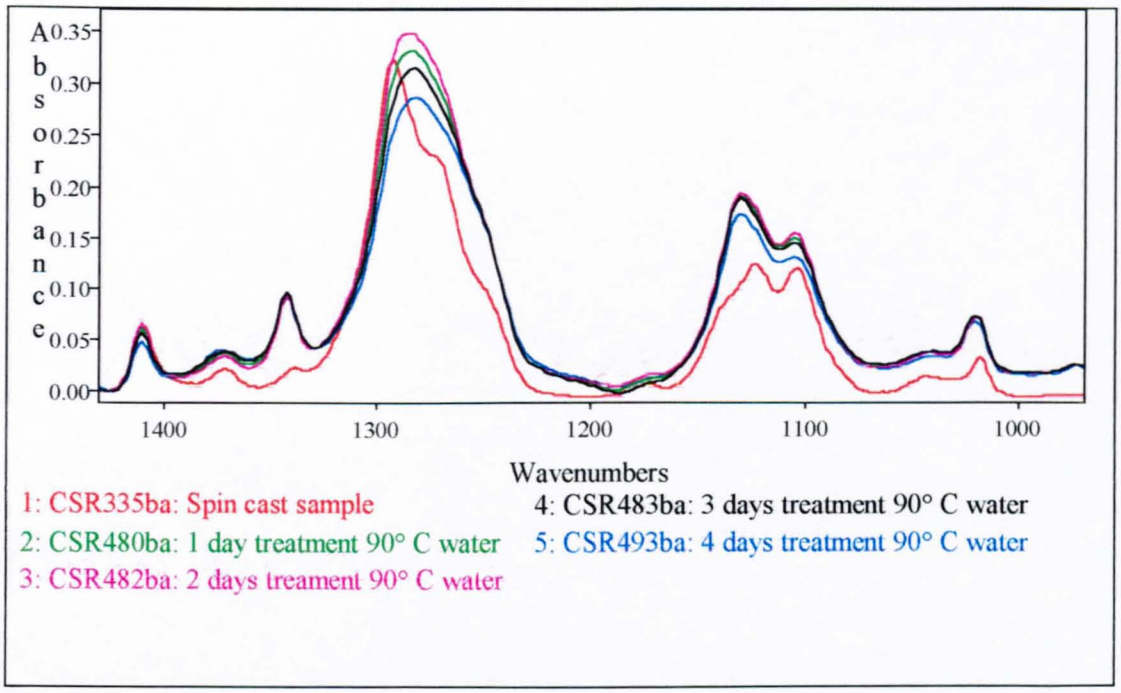

Figure 6.20. The wagging modes and ester bands of PET treated at 90° C in water.

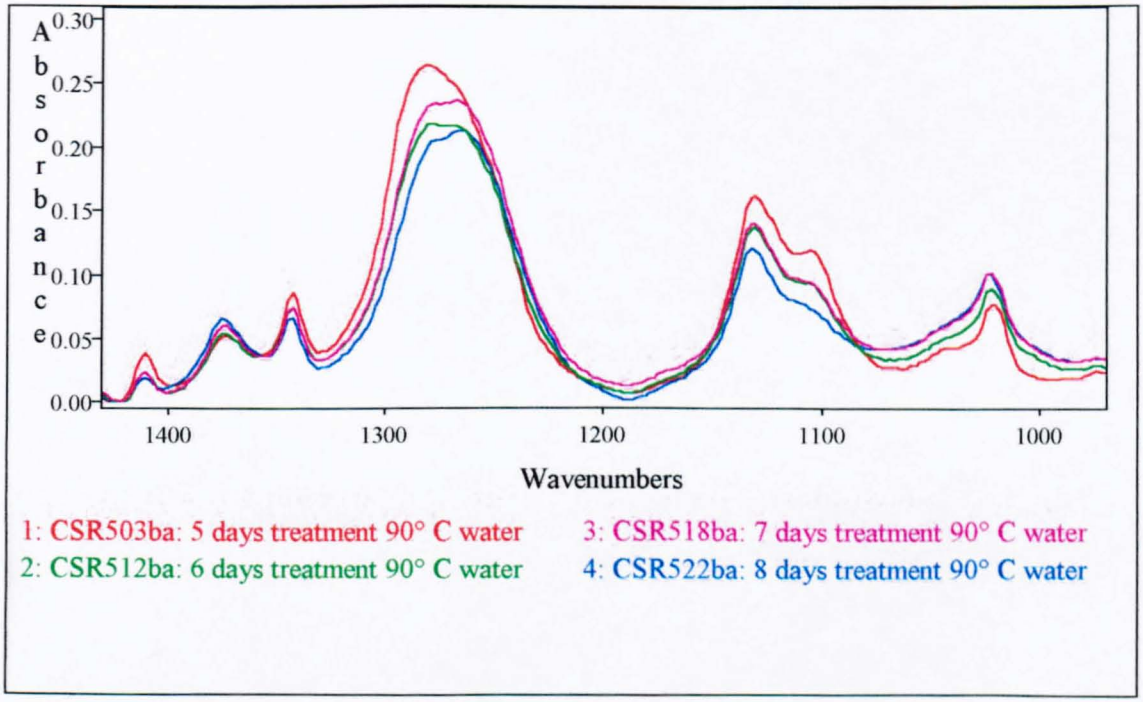

Figure 6.21. The wagging modes and ester bands of PET treated at 90° C in water.

Within the first day the crystallinity has changed from around 6% initially, to 36%. This is indicated by the changes in the 1340 cm^{-1} and 1370 cm^{-1} bands (figure 6.15.). There is also a shift to lower wavenumber in the carbonyl band (figure 6.18), this is again indicative of an increase in crystallinity.

There is also a loss in intensity of the carbonyl band, which cannot be explained by a loss of sample into solution. This may be due to the realignment of the electric dipoles of the carbonyl band in the plane of the substrate, which would result in a weakening of response in the RAIRS experiment. The structure of PET in an all *trans* crystalline conformation is one where the benzene rings are co-planar, with the carbonyls in the same plane as the ring and the ethylene glycol section displaced by 18° out of the plane of the rings [**6.23**]. If the benzene rings were lying parallel to the plane of the substrate this may give the effect observed.

Perhaps the most difficult changes to explain are those in the CH stretching region. Figure 6.16. shows that within the first day the CH stretching region has been dramatically changed, from 2 weak bands at around 2970 cm^{-1} and 2880 cm^{-1} to at least 3 or 4 bands with greater intensity.

Very little work is available in the literature on the effects of conformation on the CH stretching region in PET. There is no evidence of any significant degradation (i.e. carboxyl and OH end groups) at this stage, so one may assume that the changes are either orientational or conformational.

Figure 6.22. shows the conformational changes that occur in amorphous PET after annealing in air at 200° C. This results in a sample of around 36% crystallinity, similar in level to that seen in the water treated samples under discussion. It is interesting to note that the CH stretching region shows no significant change i.e. still two weak bands. This suggests that the effect noted in this work is not an annealing effect but a function of the immersion in water, be it orientational or chemical.

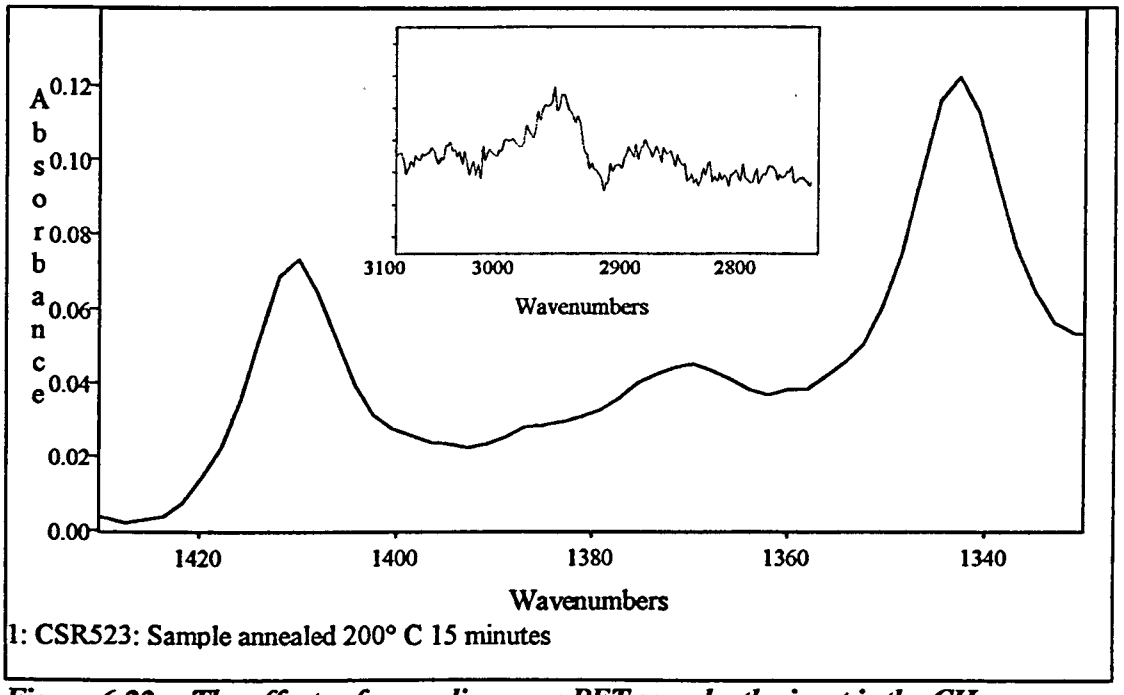

Figure 6.22. The effects of annealing on a PET sample, the inset is the CH stretching region.

One possible explanation for the changes in the CH stretching region could be a realignment of the polymer chains such that the electric dipoles associated with the CH stretching modes preferentially aligned perpendicular to the surface of the substrate, thus enhancing the RAIRS effect. This seems counter intuitive, as it implies in the extreme case, that before treatment, there was a preferential orientation of the dipoles in the plane of the substrate, or at least a dramatic increase in the overall average orientation of the CH stretching modes. There is an argument for, and one argument against this idea. Firstly from the spectroscopic evidence the sample is essentially amorphous, i.e. conformationally random. This implies no preferential orientation of the dipoles associated with the CH stretches. Conversely it could be possible that the spinning has some sort of orientational effect upon the film as it is deposited; forcing the polymer chains to be conformationally random (i.e. amorphous) but ultimately oriented, flat against the substrate.

Perhaps the most rational explanation for this drastic change in character is the fact that it relates to a different type of CH stretch, i.e. not a CH_2 attached to an ester (CH_2-O-CO-R) but a CH_2 attached to an alcohol (CH_2-OH). In this instance this would be highly indicative of the formation of more alcohol end groups. An increase in alcohol end groups would manifest itself in a correlation between the intensity of the CH stretching region with the intensity of the OH stretching region. Figure 6.23. shows a plot of the integrated intensities of the whole of the OH stretching region against the integrated intensities of the whole of the CH stretching region. One could say there is a general trend that increased OH correlates with increased CH. The error bars correspond to ± 1 standard deviation from the mean. It could be argued that the point corresponding to t =

0 in figure 6.23. is not of the same data set as the others as this has not been immersed in water and hence is an outlier.

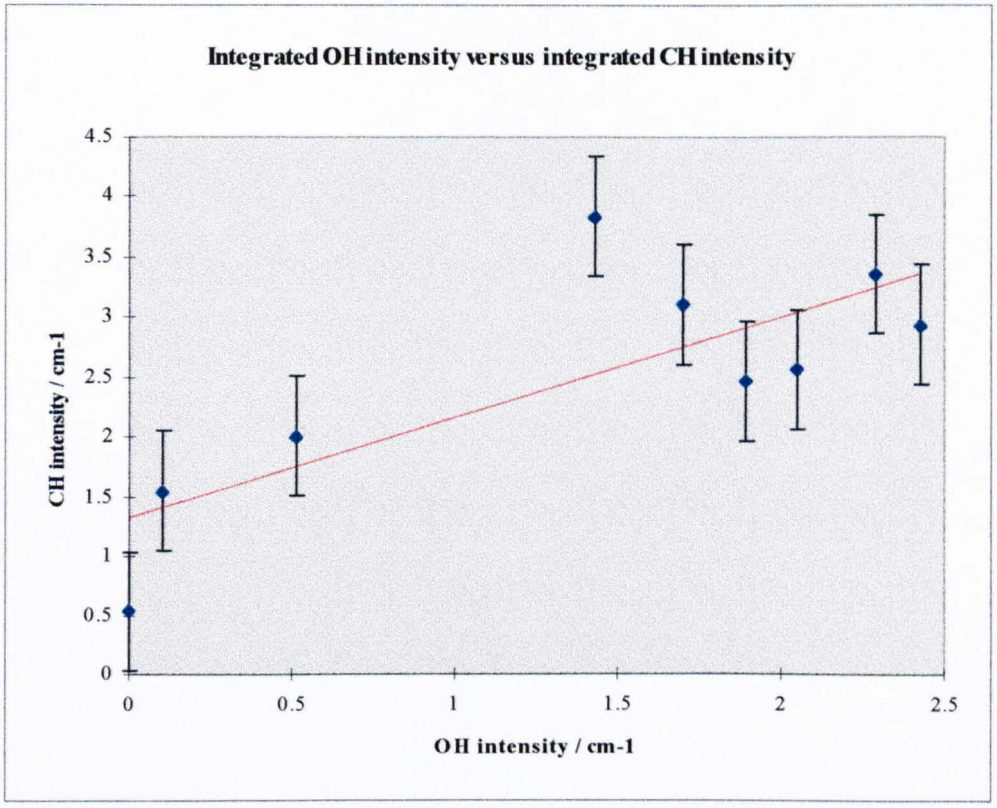

Figure 6.23. ***Plot of the integrated intensities of the OH stretching region against the integrated intensities of the CH stretching region from figures 6.16. and 6.17.***

Pozefsky and Coggeshall [**6.24**] have shown that the extinction coefficient of the ν(CH) of a CH_2 attached directly to an oxygen is different to that of an alkane. Dramatic reductions in the intensities compared to those of the corresponding alkane are observed when a CH_2 is directly attached to or in close proximity to a carbonyl and this would explain the weak nature of the ν(CH) in PET. Mirone and Fabbri [**6.25**] have shown that the intensities of the ν(CH) of a CH_2 attached to a primary alcohol are stronger than those associated with other alcohols. Bellamy states that the involvement of the oxygen in hydrogen bonding can result in shifts of the ν(CH) frequency [**6.26**].

The fact that we see a shift in frequency and an increase in intensity in the CH stretching region perhaps indicates that we are seeing the formation of more primary alcohols (end groups) which would very probably be involved in hydrogen bonding. The increase in intensity would arise from the CH_2 being directly attached to a primary alcohol rather than an ester. The frequency shifts could be a result of hydrogen bonding, although it seems probable that the stretching frequency of a CH_2 attached to an alcohol would be different to that of a CH_2 attached to an ester

Changes also occur in the ester bands (figure 6.20.). The ester band at 1300 cm^{-1} goes from a definite 3 component band to a broader one with, according to Cole **[6.27]**, up to 5 components. These changes are seen during annealing processes and are indicative of an increase in crystallinity. Both this band and the band at 1150 cm^{-1} contain both ester and ring mode components but the actual number of components and complete assignments have yet to be fully published. Perhaps it is a little over ambitious to attempt to obtain too much information from this region of the spectrum in such a complex system !

There is however some evidence for an increase in acid end groups from the acid C-O stretching band at 1470 cm^{-1} shown in figure 6.14. This band is not seen in amorphous PET, but in crystalline PET there is a CH_2 bending mode in close proximity, which further complicates the matter. The CH_2 bending mode is a known crystalline band **[6.28]**.

Initially the increase in intensity of the 1470 cm^{-1} band can be attributed to an increase in crystallinity. But as the crystallinity decreases, as shown by the CH_2 wagging modes at 1370 and 1340 cm^{-1}, this band is seen to continue to increase. The explanation for this is that there is also a band associated with the delocalised C-O stretch from the acid end group at the same frequency. Contributions from CH_2 bending mode must decrease as degradation continues, therefore the increase in the intensity of this band must be attributed to an increase in acid end group.

After 2 days of treatment there is a further increase in the bands associated with the CH stretching modes (figure 6.16.) but a decrease in the crystallinity as shown by the CH_2 wagging modes (figure 6.14.). This is contrary to evidence given in the literature, where using density measurements, and correlating this to crystallinity, there is an increase in crystallinity over and above that associated with annealing which has been attributed to a chemicrystallisation process. This perhaps suggests that the polymer may not be in a crystalline phase normally associated with PET i.e. not all *trans* conformers, but may be some dense amorphous phase. Figure 6.16. indicates that there may be the beginnings of some features in the OH stretching region, but there is no evidence of any terminal COOH carbonyl (figure 6.18.). There is a further decrease in the intensity of the carbonyl band which could be indicative of an orientational effect or the conversion of carbonyl to carboxyl. If the molar extinction coefficient of the terminal carboxyl is not as large as that of the carbonyl (a very strong band) then perhaps it would not be surprising to see a decrease in the intensity of the carbonyl without a subsequent increase in carboxyl.

The band at 1410 cm^{-1} (figure 6.14.) can be used as a guide for film thickness. Although the calibration for the thickness of films using transmission infrared spectroscopy described in section 5.3. is not valid for this system due to the different sampling technique. The band has been shown to be insensitive to changes in morphology [**6.29, 6.30**] and therefore, is still a good marker for relative thickness. Just looking at the spectra can be misleading as there are contributions from other bands in close proximity. Therefore the intensities must be obtained using curve fitted data described earlier in section 5.3. Using this band as a marker for film thickness (hence a marker for loss of water soluble components) it is possible to state that after 2 days there is little or no loss of polymer as water soluble smaller molecules.

After 3 days there is a further increase in the intensities of the CH stretching modes (figure 6.16.), a decrease in crystallinity as indicated by the CH_2 wagging modes (figure 6.14.) and definite signs of OH (figure 6.16.). There is a further decrease in carbonyl intensity (figure 6.18.) but still no real signs of carboxyl end groups, where they were expected at 1680 cm^{-1}. The decrease in intensity of the 1410 cm^{-1} band suggests that there is a loss of water soluble components. The fact that this occurs whilst only observing slight signs of hydrolysis backs up the suggestion of Ballara and Verdu that carbonyls close to chain ends are a preferred site of hydrolytic attack [**6.6**].

The changes in the spectra that occur after 3 days are more dramatic. By the fourth day the CH stretching modes reach their maximum intensity (despite an apparent loss of material into the water) and the existence of an OH band is no longer in doubt (figure 6.17.). There is a further loss in carbonyl intensity (figure 6.19.) and the beginnings of a terminal carboxyl carbonyl more clearly seen at 1680 cm^{-1} (red sample in figure 6.19). It

is important to note that the sample in figure 6.18. and 6.19. (CSR493ab) is the same sample but on a different absorbance scale. It was not convenient to have all the spectra in the same figure as it made distinguishing between them extremely tiresome. The carbonyl band now has 3 components, the new component at 1747 cm^{-1} which is higher in frequency than one would normally expect for PET. This component is clearly shown in figure 6.24. which shows the Fourier deconvolution of the carbonyl bands as a function of time treated. This clearly suggests that there is a formation of a new species within the polymer.

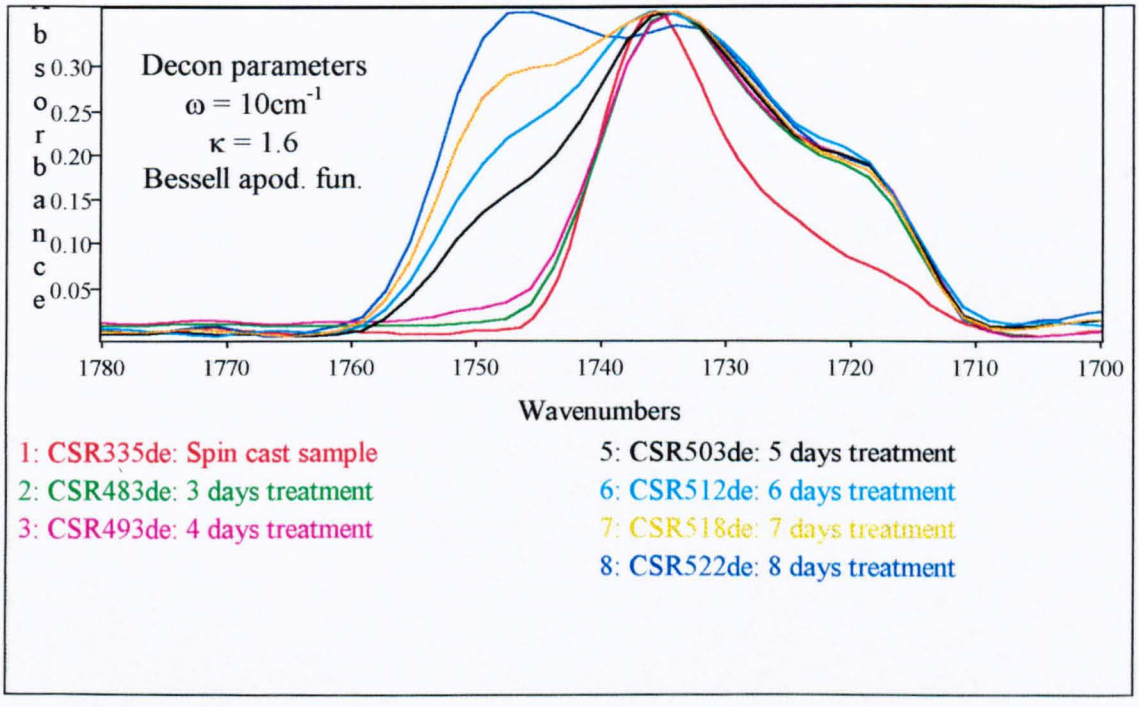

Figure 6.24. The Fourier deconvoluted carbonyl bands of PET undergoing hydrolysis.

In an attempt to identify this species, model compounds were spin cast onto Cr / Au coated glass slides and examined using RAIRS. These included a PET oligomer, a dimer and a possible monomer.

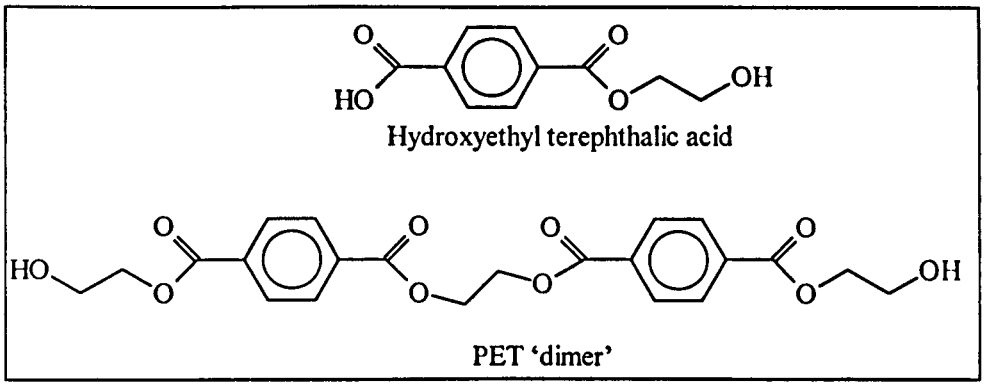

Figure 6.25. Model compounds used to identify possible degradation products.

The resulting spectra unfortunately do not resemble the spectra of the degraded samples, nor do any of the carbonyl frequencies coincide. One interesting feature is the increased intensity (relative to the other bands) of the ν(CH) in the hydroxyethyl terephthalic acid sample. This perhaps lends weight to the argument that the changes in the ν(CH) band seen during the hydrolysis are indeed due to an increase in the CH_2-OH species (in this sample half of the CH_2 groups are directly attached to an OH group as opposed to an ester). Differences in frequency may well be accounted for by differing levels of hydrogen bonding between the two systems as this can have an effect on the frequency of the ν(CH) band.

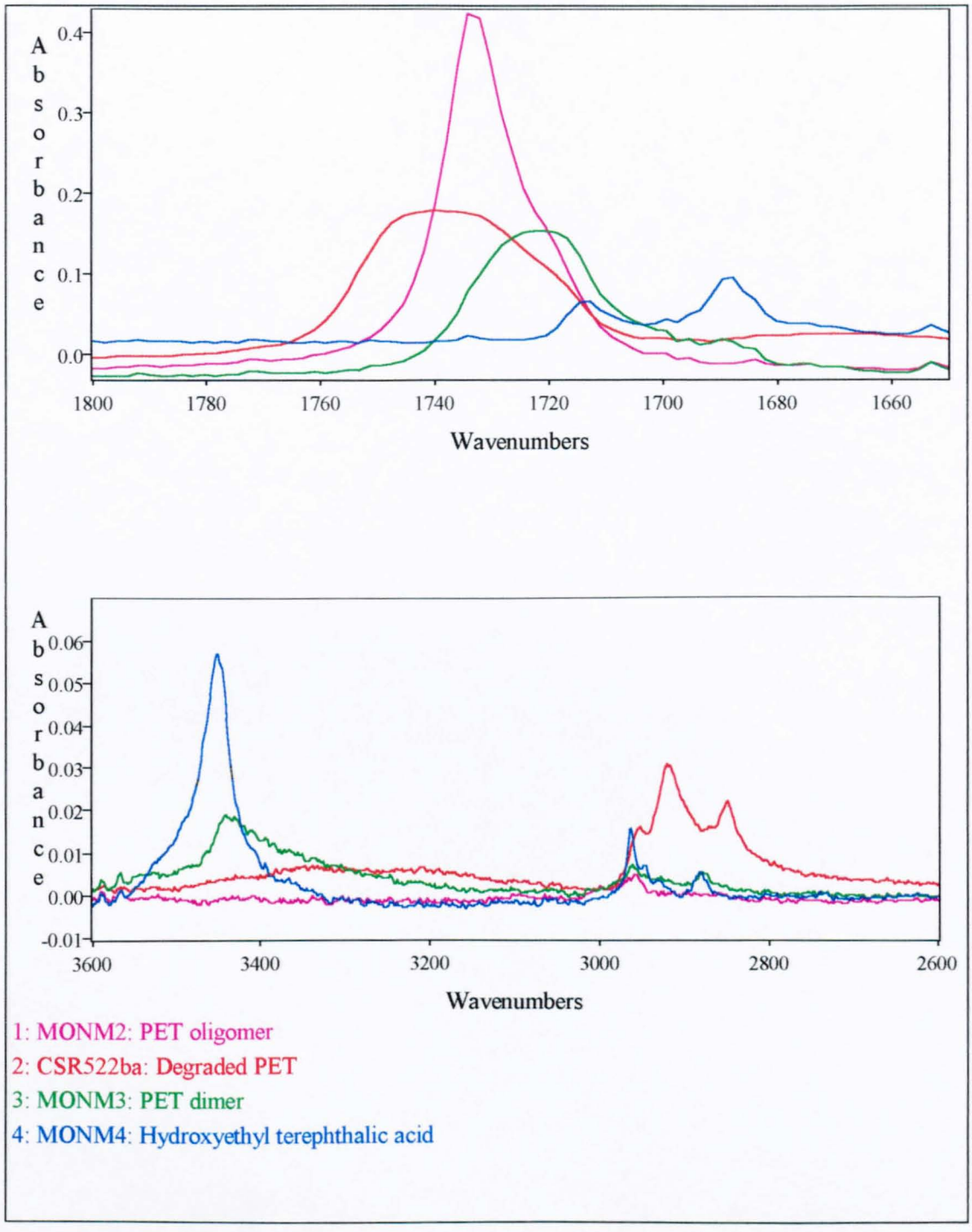

Figure 6.26. Comparison of RAIRS of possible degradation products with degraded PET in the ν(C=O) and ν(CH) regions.

If one examines the spectra for days 5 to 8 together it is possible to identify numerous trends. Firstly there is a general decrease in intensity of all bands, which is indicative of a loss of material into solution. Secondly there is a broadening and blue shift of the

carbonyl band. The broadening is readily explained by an increase in the number of 'types' of carbonyl within the system. This shift to higher wavenumber is unusual and either suggests a new species or hydrogen bonding involving the 'alcoholic' oxygen rather than the carbonyl oxygen [**6.31**]. Possible 'new species' may include strained rings formed by intramolecular hydrogen bonding. Figure 6.27. shows two possible scenarios which would give rise to a blue shift of an ester carbonyl.

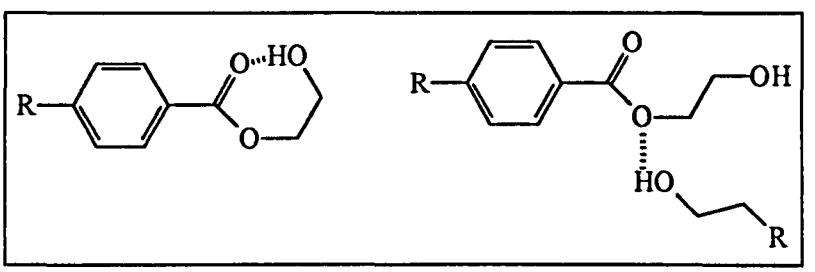

Figure 6.27. Possible moieties leading to the emergence of a band at 1747 cm^{-1}.

Examination of the OH stretching region (figure 6.19.) suggests a possible doublet, with components at 3200 and 3350 cm^{-1} which is quite different to the values quoted for end group analysis (c.f. ν_{OH}(OH) 3542 cm^{-1} and ν_{COOH}(OH) 3252 cm^{-1}). These values quoted are for isolated alcohol or carboxyl end groups which is perhaps not viable for this system. If one examines the shape of the OH band observed during these experiments it is very broad suggesting a 'polymeric' type structure i.e. one with extensive hydrogen bonding and widely distributed hydrogen bonding types. One can expect hydrogen bonding between the alcohol groups and the carboxyl groups, the carboxyl groups and other carboxyl groups, carboxyl groups with ester carbonyl, alcohol OH with other alcohol OH, etc. etc. This is a complex system with many interactions probable. One may therefore suggest that the two bands observed may well be the ν_{OH}(OH) and the

ν_{COOH}(OH) shifted lower in frequency due to the extensive hydrogen bonding network present.

Differences in the shapes and positions of the bands in the OH stretching region could be explained by the fact that we were examining 'surface' based material, which could differ dramatically from the 'bulk' based polymer described in the literature.

Another explanation could be that this work looked at a small amount of material (< 200 nm) which has heavily degraded. It may be that the material examined in published work may not be so heavily degraded. To examine a thick film (>100 μm) with this amount of degradation may be difficult as the material would be very brittle. In our system the material would be supported by the metal coated glass slide.

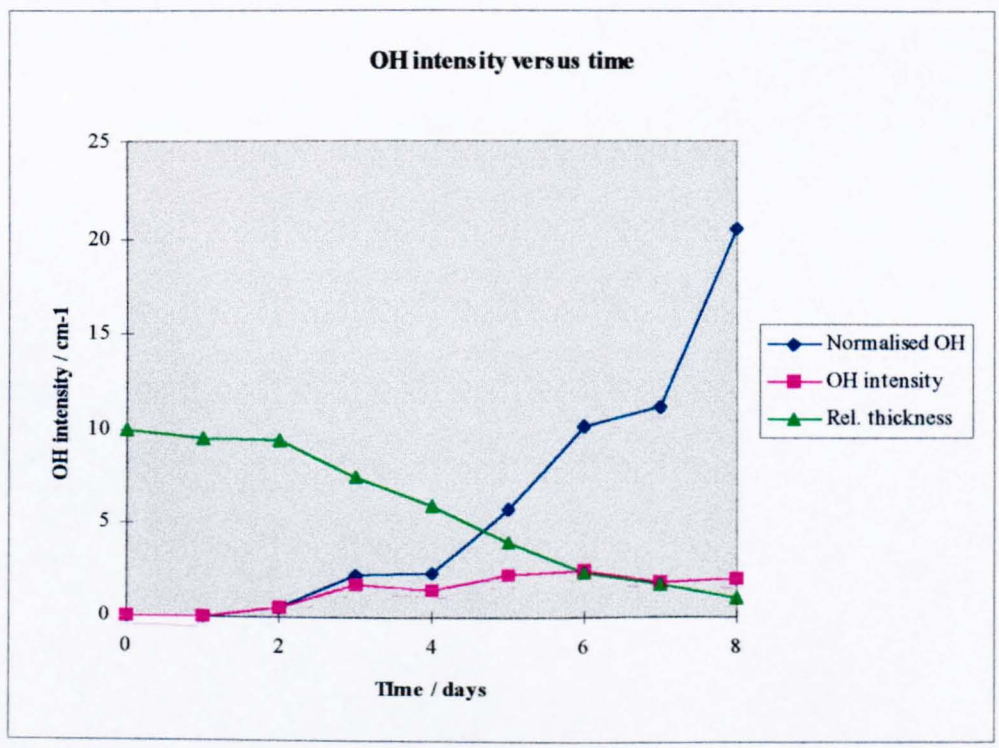

Figure 6.28. Plot of the change in intensity of the OH stretching region with time of PET treated at 90° C in water.

The simple plot of the intensity of the OH band with time can be quite misleading due to the loss of material into solution. The intensity of the OH stretching band can be corrected to take into account of the loss of material by normalising using the 1410 cm^{-1} band. Figure 6.28. shows the normalised OH intensity (i.e. the intensity of the OH stretch ratioed against the intensity of the 1410 cm^{-1} ring mode for that particular time) versus time.

From figure 6.28. there is some evidence of autocatalytic behaviour as the slope of the OH intensity versus time plot appears to become steeper as time progresses. This agrees with the findings of other workers **[6.4, 6.12, 6.13]** The same plot also includes the integrated intensity of the 1410 cm^{-1} band (in green) to give some measure of the loss of water soluble or small mobile species into the surrounding water. The loss of material is almost linear with time after 2 days of treatment.

The decrease in the ratio of the bands at 1340 and 1370 cm^{-1} (Figure 6.15.) shows the further increase in amorphous nature within the polymer. There are two possible explanations for this phenomenon; firstly that we are indeed seeing a loss of crystallinity, which is perfectly reasonable as the conditions during hydrolysis are very harsh compared to those one would encounter in film manufacture (i.e. immersed in water at 90° C for several days, compared to sprinkled with water then heated at 200° C for two hours) and to expect the conformational order to remain intact would seem to be counter intuitive. A second possible explanation is that, because so much complex chemical degradation is occurring, the bands are no longer simply *trans* and *gauche* CH_2 wagging modes of PET, but a mixture of wagging modes from related species e.g. monomers, oligomers, cyclic moieties. This would perhaps make the use of the equation proposed by Bellali and

Vigoreux [6.32] subject to error for the calculation of crystallinity of PET degraded under these conditions. It seems likely that both of the arguments hold true to a certain extent. Generally in the literature, crystallinity has been measured by the correlation with density measurements during degradation. With known phenomena such as amorphous ageing [6.33], where the polymer becomes more dense without an increase in *trans* glycol content, this simple correlation must also be flawed.

If one imagines a less crystalline, yet still quite dense, phase where the close proximity of the polar, potential hydrogen bonding end groups to one another means that interaction is inevitable, then many of the interactions suggested would be possible; the polymer would be dense, the sample would be more amorphous and a strong hydrogen bond network could exist.

Figure 6.30. shows a schematic of the possible structure of PET during treatment with water at 90° C.

The first stage, which is rapid, is the incorporation of the water molecules into the amorphous polymer. The state of the water at ambient temperatures has been discussed in section 5.5. and as no *in-situ* work has been carried out in RAIRS one can only speculate on the state of the water at 90° C. There is likely to be more 'free' water at 90° C, i.e. not hydrogen bonded to other water molecules, due to the increased energy in the system changing the equilibrium between different states of water. This 'free' water could readily interact with the polymer chains. The water will be incorporated into the polymer network and have a plasticising effect [6.34]. This, coupled with the higher

temperature has the effect of crystallising the polymer (converting *gauche* glycol conformers to *trans* conformers) and aiding a more dense packing of the polymer chains.

Once water has been incorporated into the polymer it is able to attack the polymer chains. It would appear that the sites of attack are part random, resulting in shorter polymer chains and part preferential at sites near the chain ends resulting in a loss of small water soluble materials. The creation of more end groups results in more potential hydrogen bonding species, increasing the likelihood of a hydrogen bonding network, the evidence for which is seen in the OH stretching region of the spectrum of the degrading polymer. The spectroscopic evidence from the CH_2 wagging modes (figure 6.15.) indicates that during this phase of hydrolysis there is a decrease in the crystallinity of the polymer. Figure 6.29. shows the calculated crystallinity versus time during degradation.

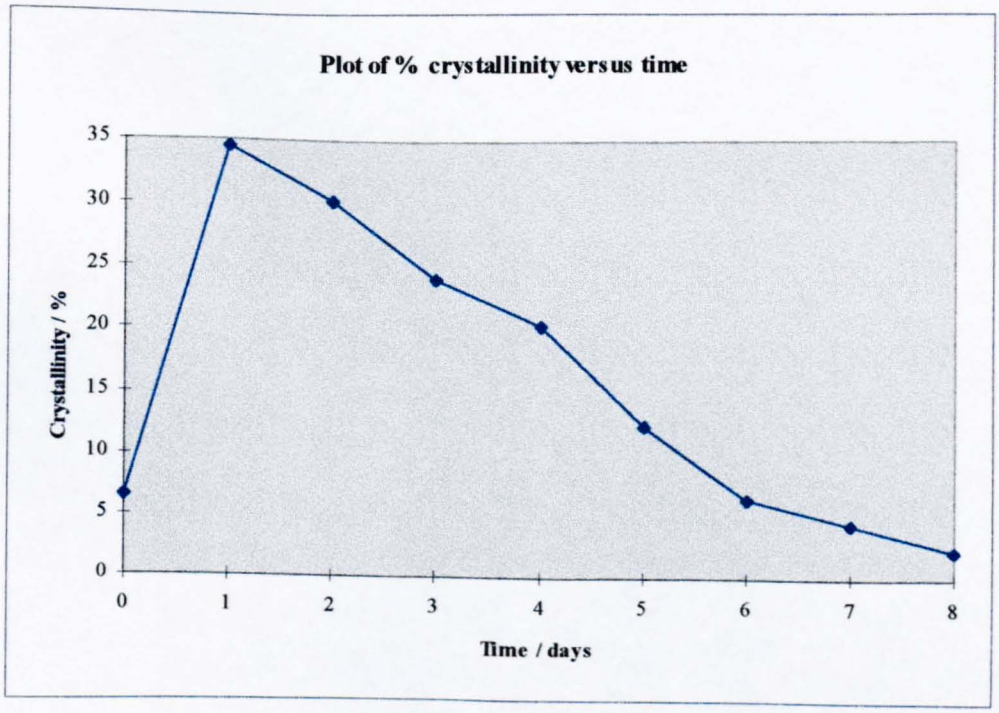

Figure 6.29. Calculated crystallinity for PET during degradation.

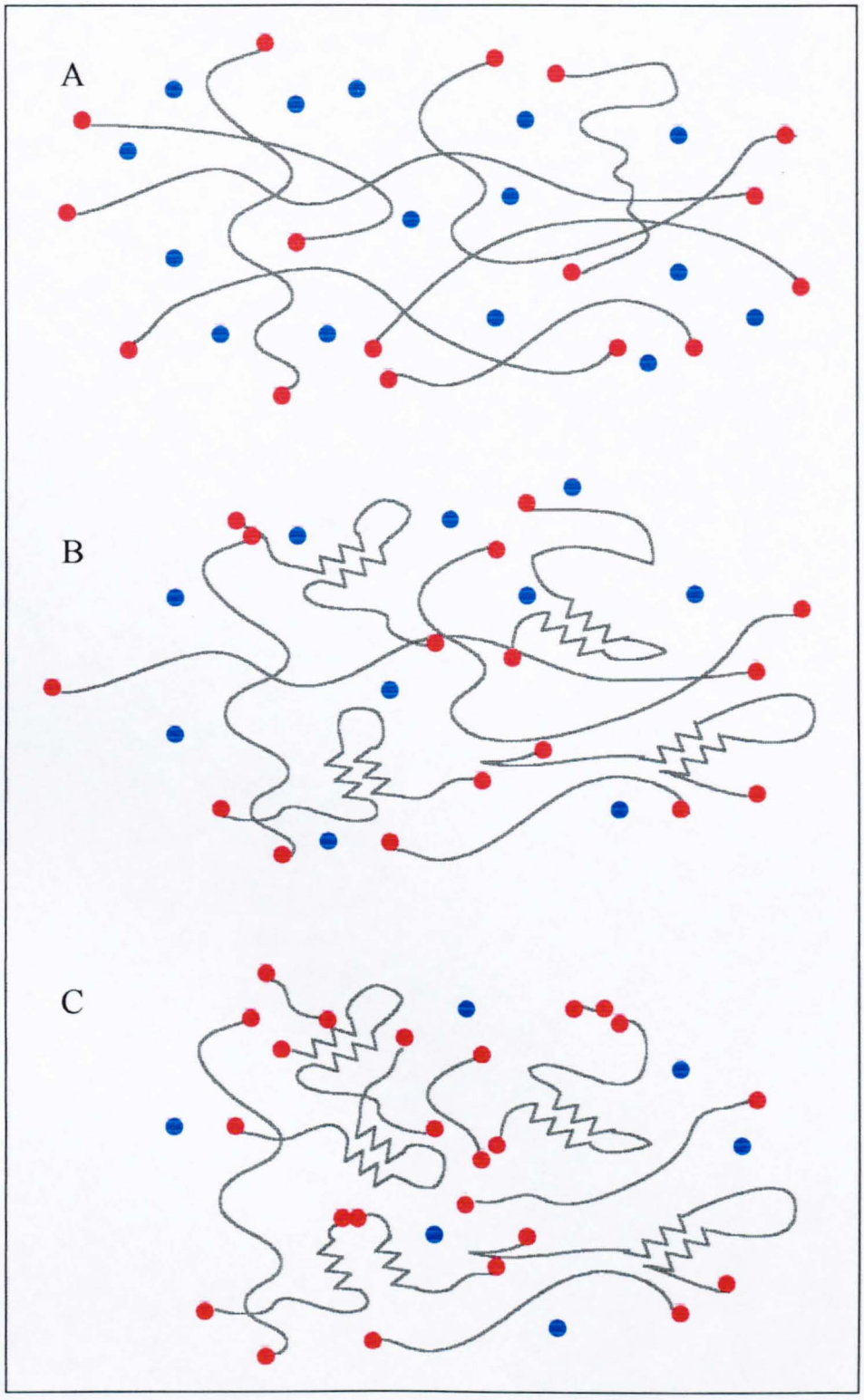

Figure 6.30. Schematic of the polymer chains during hydrolysis.
A) Amorphous polymer containing water molecules.
B) Plasticised polymer.
C) Hydrolised polymer.
Where ● is a water molecule
and ● is a hydrophillic end group.

Further light may be cast on the degradation mechanism by looking at hot alkaline degradation. If we examine the spectra associated with the hydrolysis of PET in hot alkali solution (1%) the following observations can be made. As the hydrolysis progresses intensity increases in the CH stretching and OH stretching regions are observed. The correlation between OH stretching and CH stretching is more systematic, i.e. there is an increase of the CH stretching modes and with an increase in the OH stretching modes (figure 6.32.). This leads to the conclusion that the increase in the CH stretching band intensity is related to an increase in the OH end groups. This increase in intensity is due to the CH_2 directly attached to an alcohol and lend support to the previous speculation for PET hydrolysed in water. The shape of the CH stretching band is very similar to that of PET hydrolysed in pure water (figure 6.17.) but quite different to that of unadulterated PET (figure 6.16.). This implies that the same species is present in both water hydrolysed PET and alkaline hydrolysed PET.

The changes that occur to the carbonyl band are also quite straight forward (figure 6.33.). There is a decrease in intensity of the carbonyl band corresponding to a loss of material into solution. There is also the emergence of a band at 1715 cm^{-1} which appears as a shoulder and can be assigned to the acid end group cyclic dimer [**6.35**].

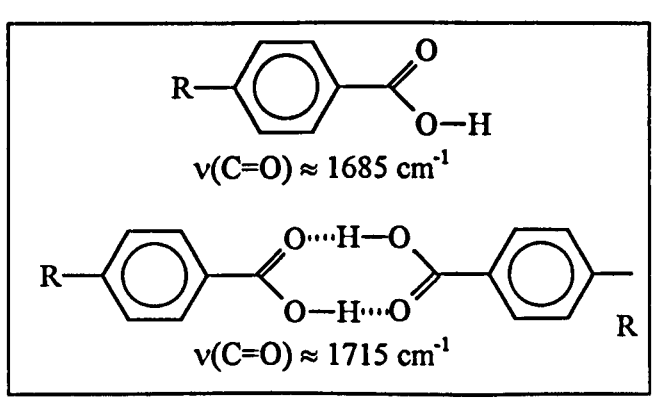

Figure 6.31. Approximate frequencies of acid end groups in PET.

This has quite important implications pertaining to the hydrolysis in pure water. This band is not observed during hydrolysis in water. It may be that the more severe conditions imposed during hydrolysis in 1% KOH cause much more chain scission, leading to shorter more mobile oligomer chains more easily able to rearrange and form cyclic dimers. It is worth while noting that generally, the dimer is the most common form of a carboxylic acid in liquid solution unless the concentration is very low. It may also be that the formation of carboxyl end groups is not so prevalent in the pure water system. This would imply that the small molecular weight species that are lost during hydrolysis contain the carboxylic acid portion of the two new end groups. Equally valid is the fact that the more harsh reactive conditions, hydroxyl anions rather than oxygen lone pairs, may lead to a more random hydrolytic attack, unlike that involving pure water where Ballara and Verdu [6.6] have noted a preference for groups close to the chain ends.

The CH_2 wagging modes, as indicators of crystallinity, once more show an initial increase in crystallinity (i.e. an annealing effect) followed by a shift in the ratio of *trans* to *gauche* conformers, suggesting a decrease in crystallinity as greater degradation occurs (figure 6.34.). This is very similar to the phenomenon seen in pure water.

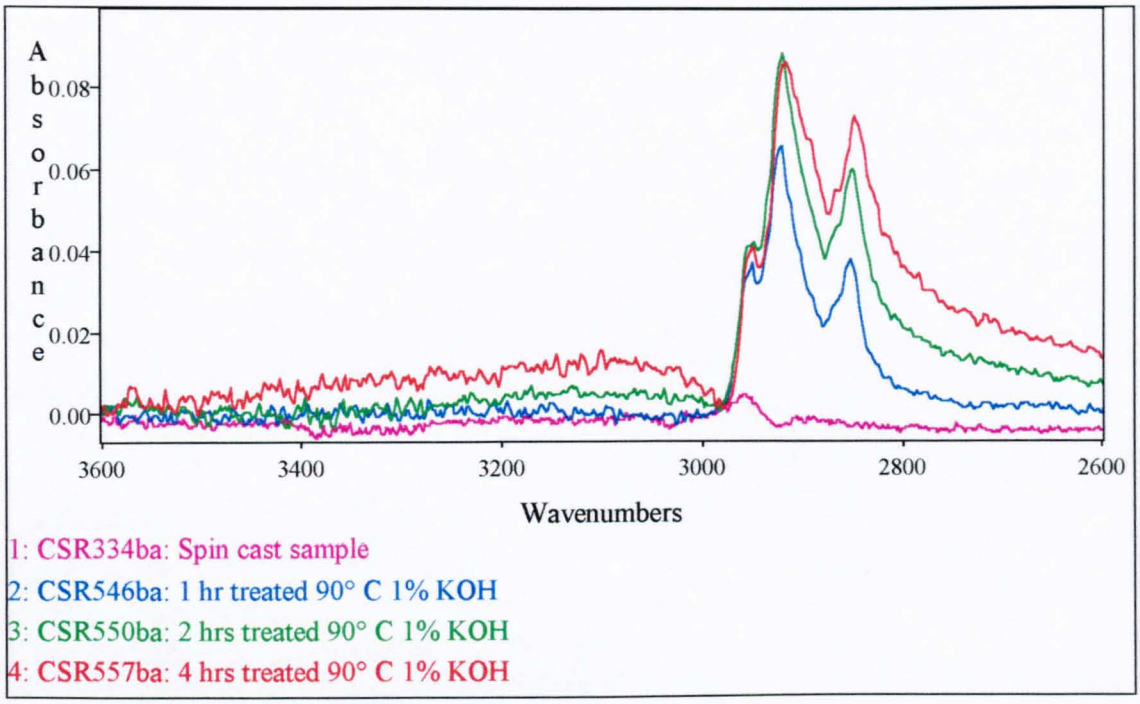

Figure 6.32. The OH and CH stretching mode regions of PET treated at 90° C in 1% KOH.

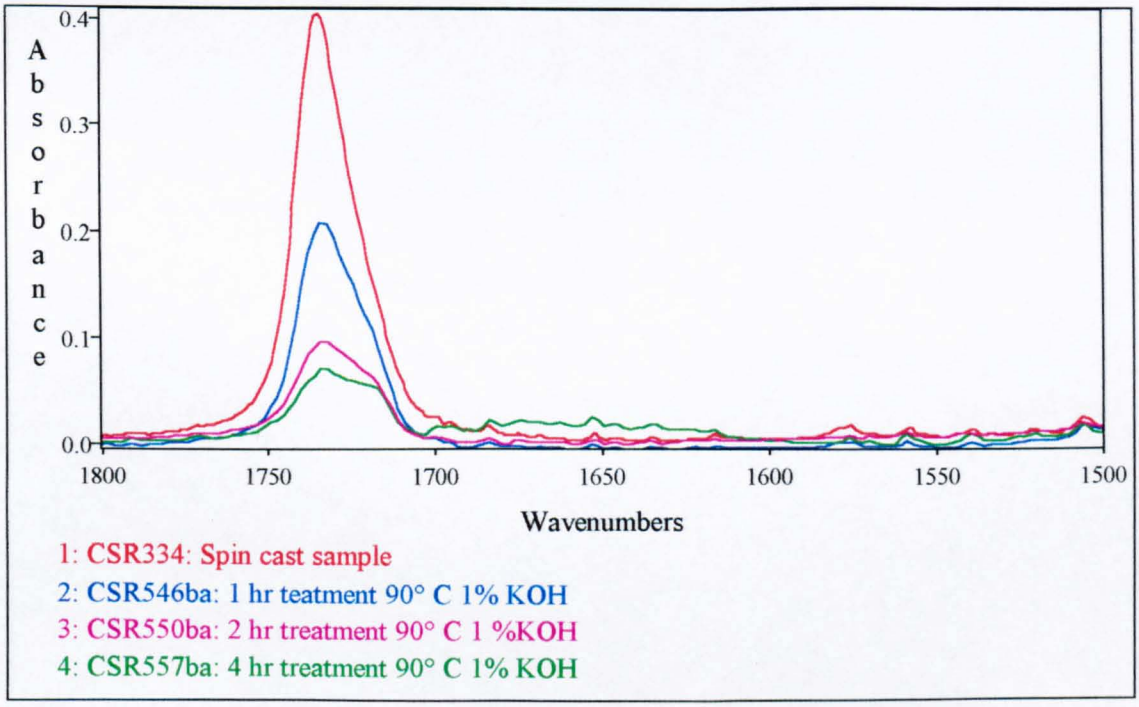

Figure 6.33. The carbonyl region of PET treated at 90° C in 1% KOH.

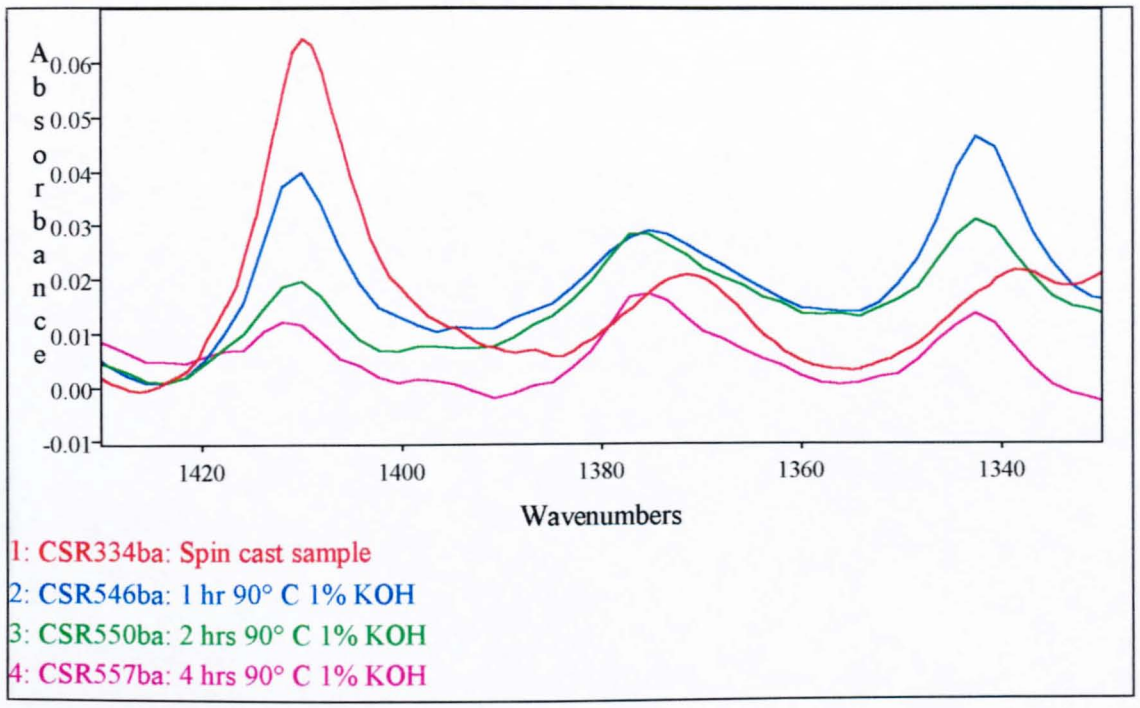

Figure 6.34. The CH_2 wagging mode region of PET treated at 90° C in 1% KOH.

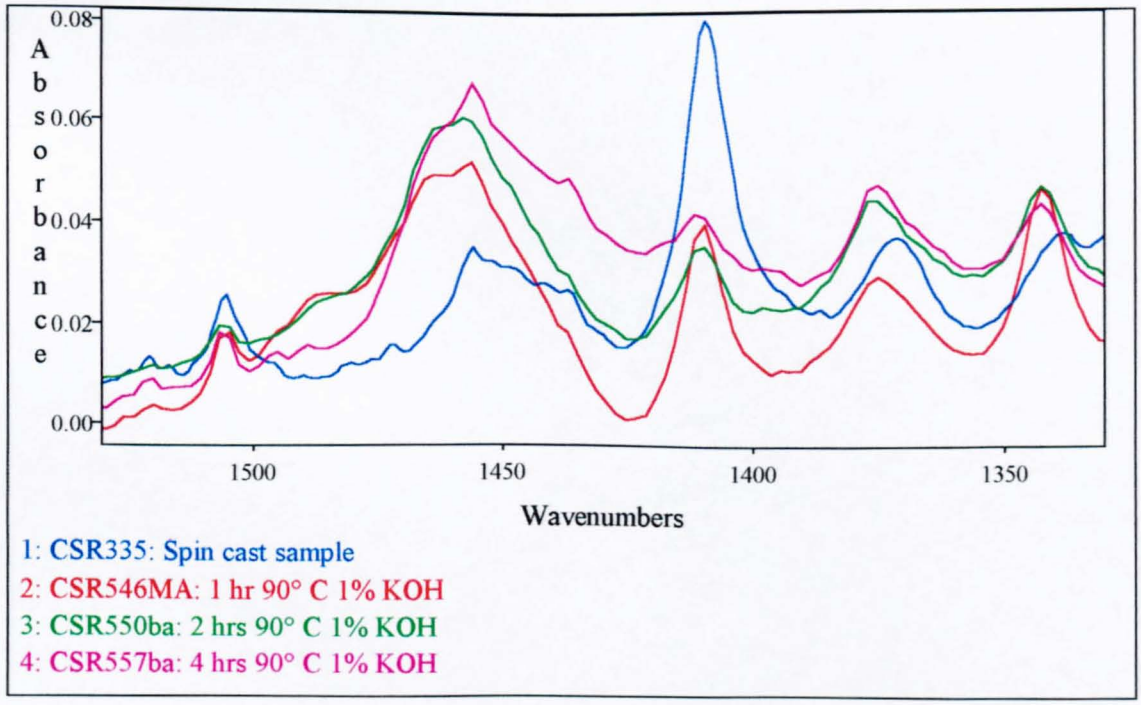

Figure 6.35. The CH_2 wagging mode and acid C-O stretching region of PET treated at 90° C in 1% KOH.

Figure 6.35. shows the increase in the acid C-O stretching band at 1470 cm^{-1}; further evidence of an increase in acid end groups. As stated previously, this band is complicated by a CH_2 bending mode at the same frequency. It is difficult to determine the composition of this band by a spectral resolution enhancement technique, such as Fourier self deconvolution, as the water vapour acts as noise in this region of the spectrum and Fourier self deconvolution and second derivative spectroscopy are noise limited. Used in conjunction with other bands, such as the CH stretching modes, it is possible to assess whether the changes in this region are due to conformational changes or due to degradation. Changes arise from a mixture of the two effects after one hour, but the contribution of the crystalline CH_2 bending mode decreases with increased degradation and decreased in crystallinity.

6.4. Summary and proposed mechanism.

The hydrolysis of thin (<200 nm) PET films in water at 90° C can be summarised as follows.

1. Initial stages (i.e. during the first few hours) show a marked increase in crystallinity, indicated by the increase of the *trans* CH_2 wagging mode band at 1370 cm^{-1}, a shift of the carbonyl band and numerous changes to the complex ester bands at 1300 and 1100 cm^{-1}.
2. The first markers for hydrolytic degradation are the C-H stretching modes, which show dramatic changes in intensity and frequency that we have assigned to an

increase in CH_2 directly attached to alcohol end groups. This is noted after 1 to 2 days.

3. As hydrolysis continues to occur we see a loss of material, denoted by a general decrease in the intensity of most bands especially the 1410 cm^{-1} in-plane C-H bending mode which is supposedly impervious to structural change. This implies a preferred site of attack of the terminal ester carbonyl, which allows the formation of small mobile molecules which can diffuse into the water matrix.
4. We see the emergence of a broad doublet at 3300 cm^{-1} that we have assigned to the alcohol and carboxyl end groups in a strongly hydrogen bonded network. The broad nature of the band implies many different species of OH with different degrees of hydrogen bonding. The plot of the integrated area of this band normalised against the intensity of the 1410 cm^{-1} band, shows an auto catalytic increase in intensity with time.
5. Finally we see a decrease in the ratio of the 1370 to 1340 cm^{-1} CH_2 wagging modes which is indicative of a decrease in crystallinity.

From the evidence it is possible to say that the proposed mechanism in figure 6.1. needs some slight modification. 'Random in chain scission' will undoubtedly be occurring, but the loss of smaller mobile molecules, implies that this will be occurring at a lower rate than the scission occurring at terminal ester carbonyls shown in figure 6.36.

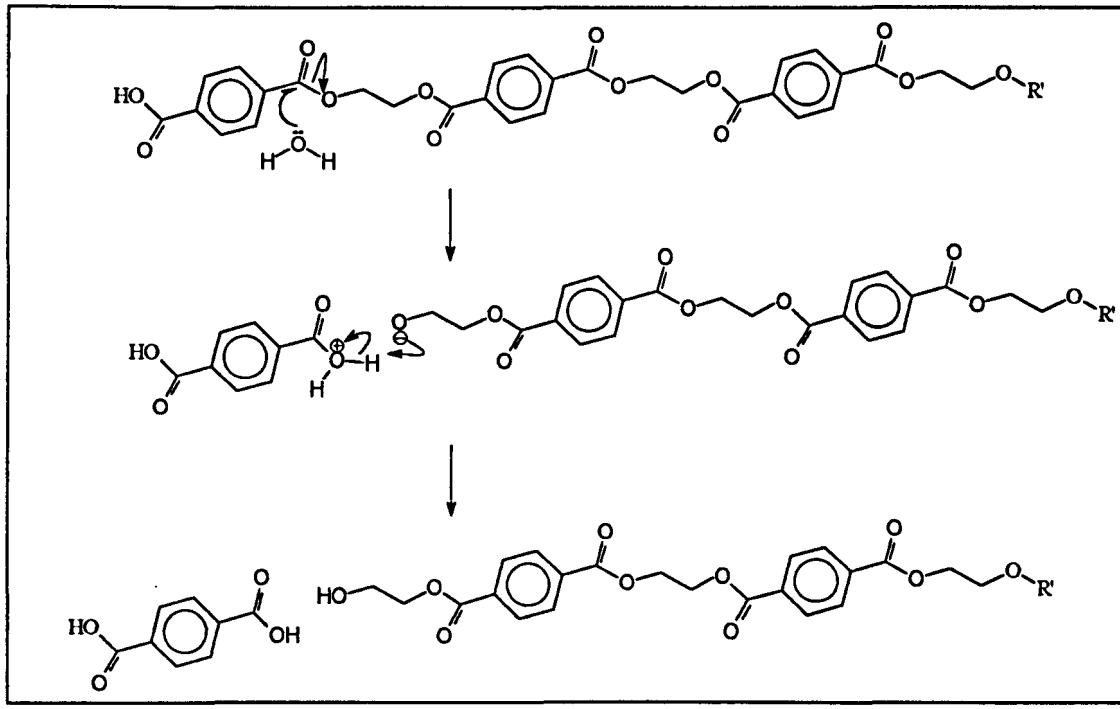

Figure 6.36. Nucleophillic attack of water at the terminal ester carbonyl in PET.

6.5. Simulation of the Stenter conditions.

Having examined in detail, the structural changes that occur in a thin PET film during hydrolytic degradation, it was time to approach the problem first set, 'on a 100 nm thickness scale, how much degradation can one observe under "film manufacture" type conditions ?'.

In order to do this a sample film was simply covered with deionised water at room temperature, and placed in an oven at 200° C for 10 minutes, until the water had evaporated. Figures 6.37. - 6.40. show the spectra of the film before and after treatment.

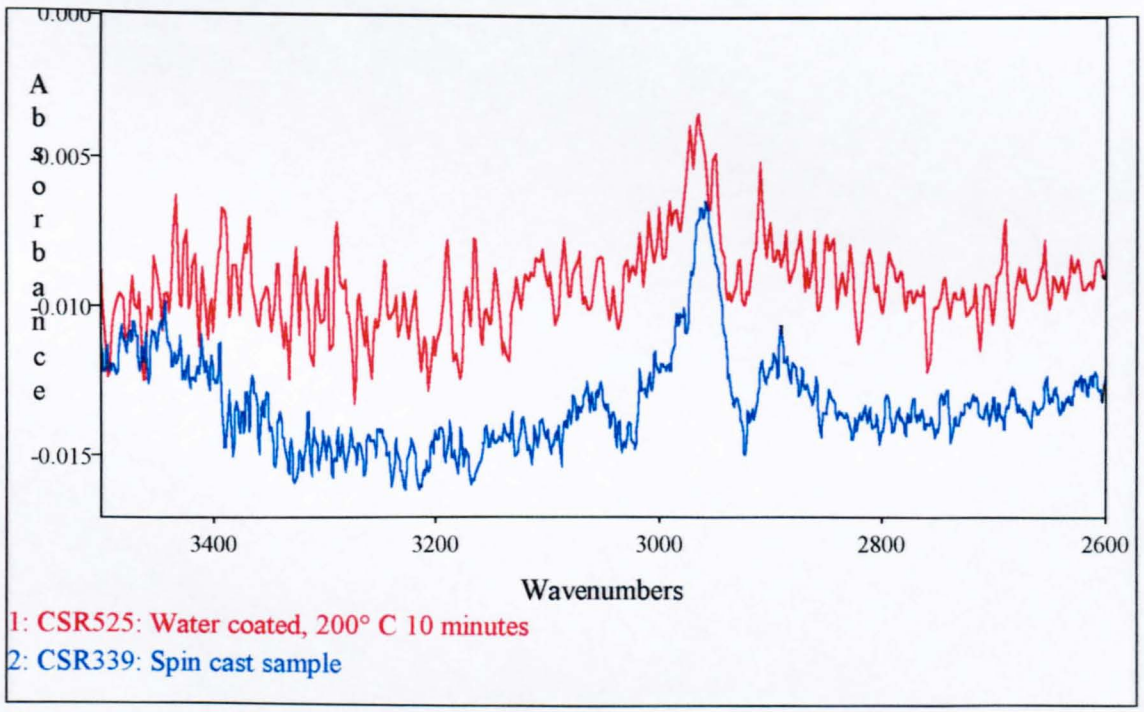

Figure 6.37. The ν(OH) and ν(CH) regions of PET from the stenter simulation experiment.

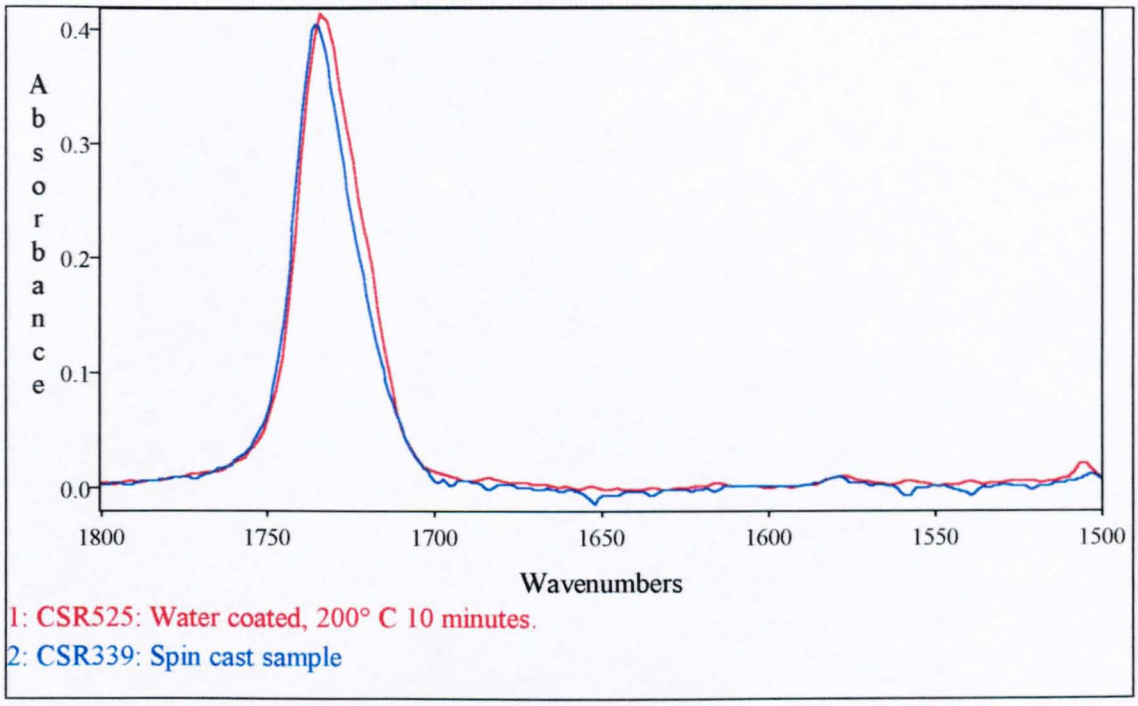

Figure 6.38. Carbonyl stretching region of PET from the simulated stenter experiment.

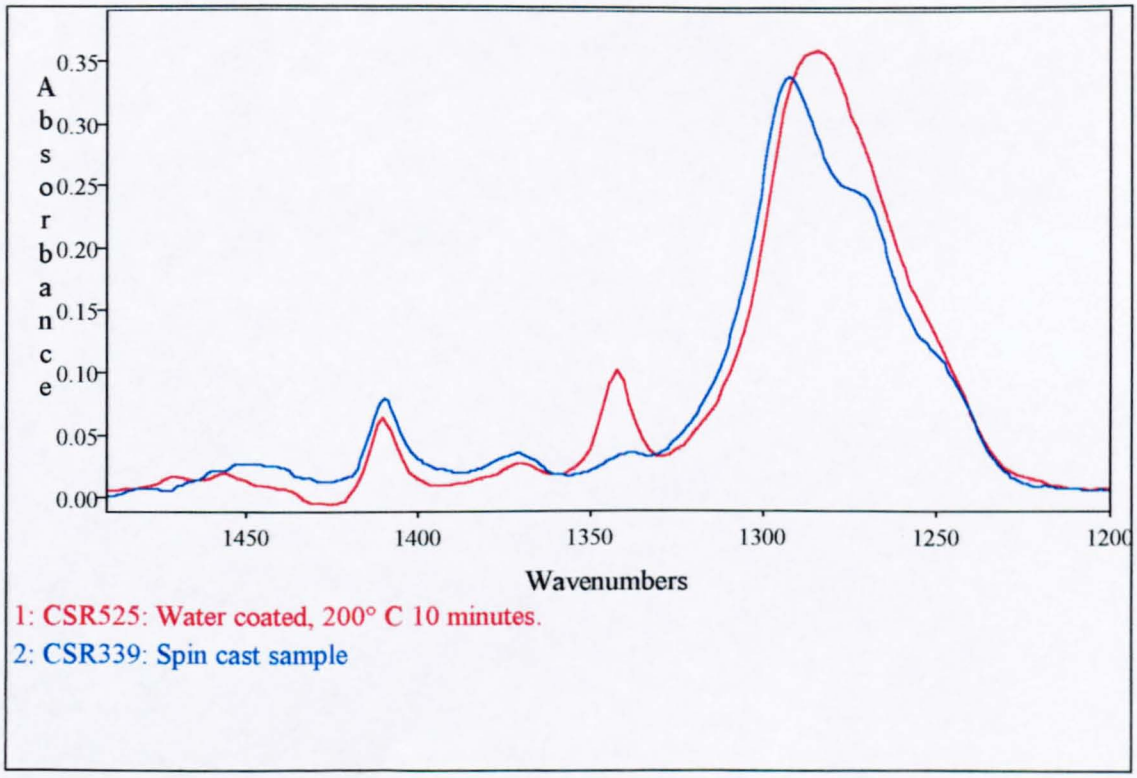

Figure 6.39. CH_2 wagging modes and ester modes of PET from the simulated stenter experiment.

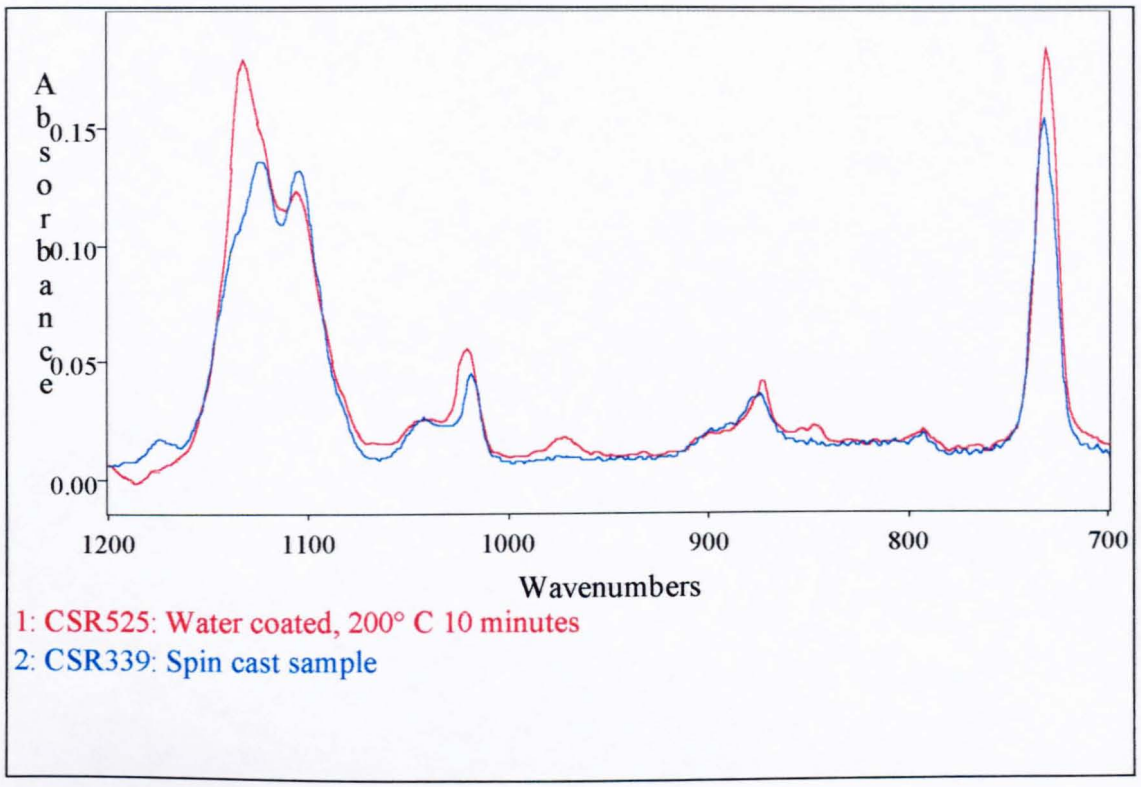

Figure 6.40. 'Fingerprint' region of PET from the simulated stenter experiment.

Figures 6.37. - 6.40. show that on a 100 nm thickness scale, for the experimental conditions used, there is little or no evidence that much hydrolysis has occurred. Hodgson et al have seen evidence for degradation on a much smaller thickness scale (< 5 nm) using ESCA SIMS at lower temperatures [**6.18**].

The changes in the spectra, between the spin coated sample and the treated sample can be explained by annealing effects. Figure 6.38. shows the shift to lower wavenumber of the carbonyl band. Figure 6.39. shows the change in relative intensity of the CH_2 wagging modes at 1340 and 1370 cm^{-1} and the changes occurring in the 1300 cm^{-1} ester band. Figure 6.40. shows the intensity, width and frequency changes occurring in another of the ester bands at ~ 1100 cm^{-1} and the intensity changes of the $\nu(O\text{-}CH_2)$ mode at 972 cm^{-1} and the $\gamma_r(CH_2)$ mode at 850 cm^{-1}. All these spectral changes can be attributed to an increase in the crystallinity of the PET film.

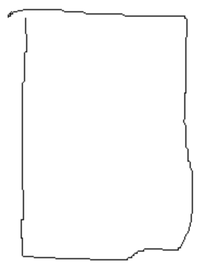

PAGES ARE MISSING IN ORIGINAL

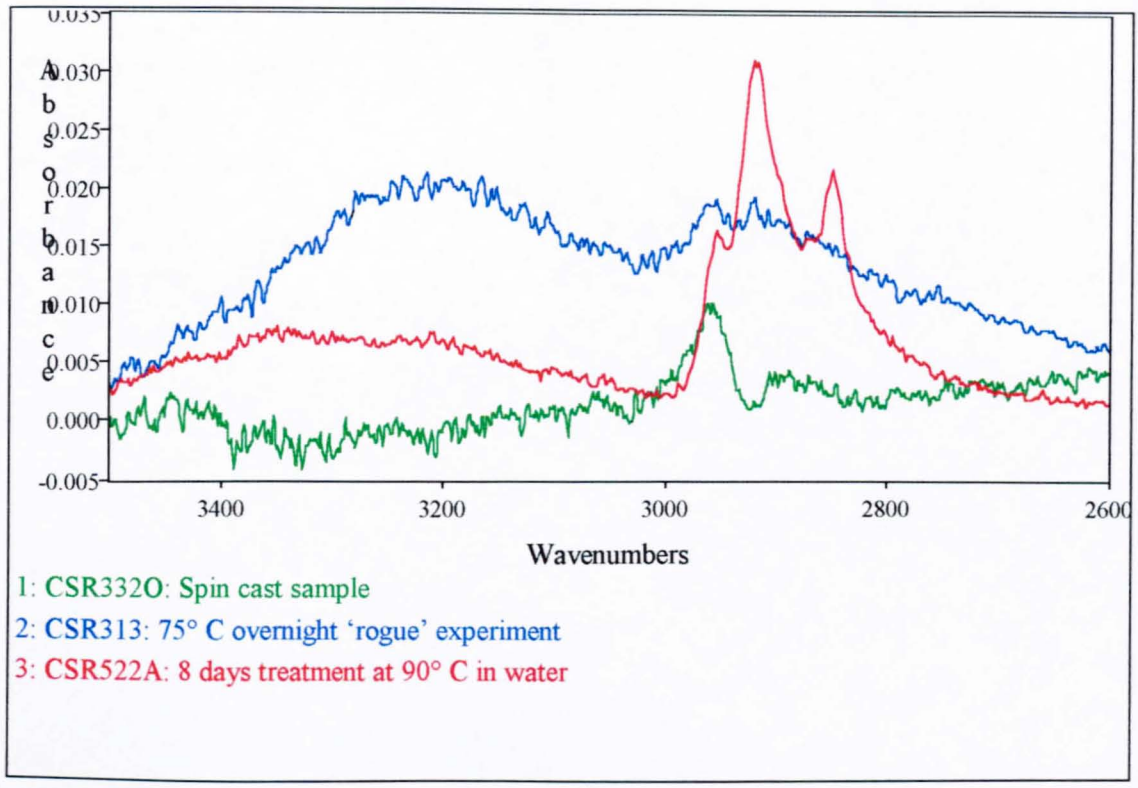

Figure 6.41. ***Comparison of the v(OH) and v(CH) regions of PET from the 'rogue' and 'normal' hydrolysis experiment***

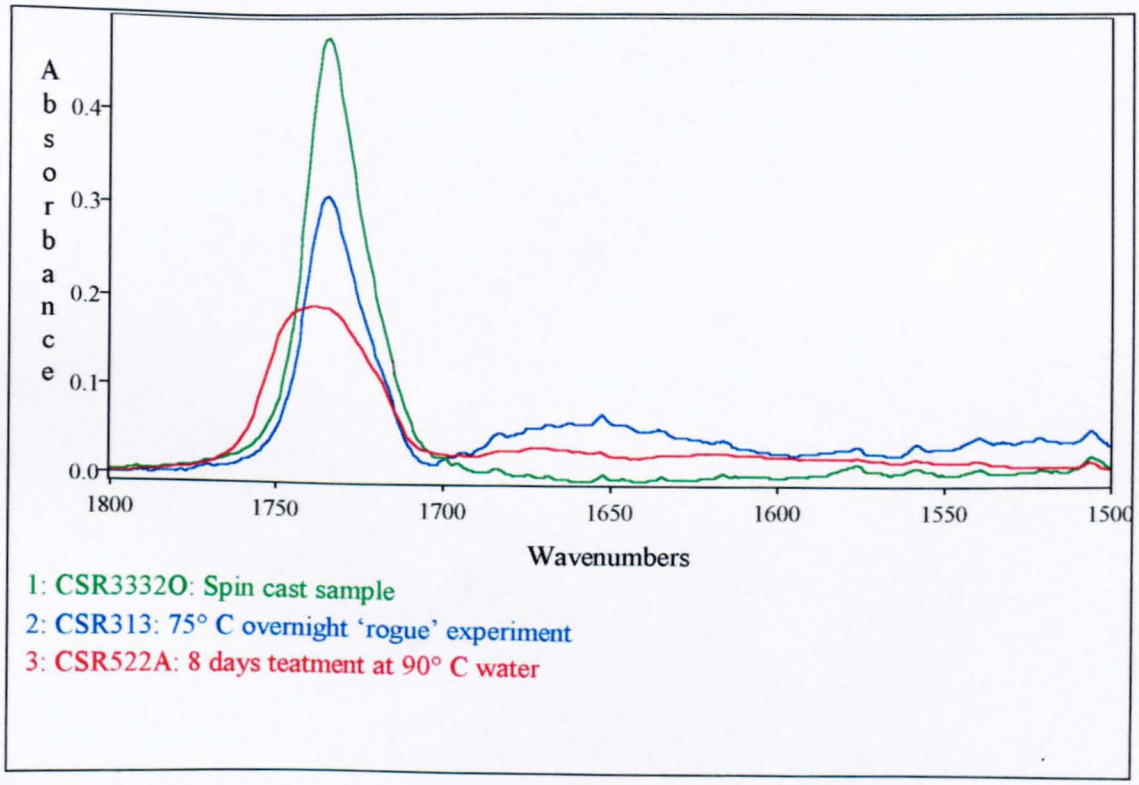

Figure 6.42. ***Carbonyl stretching region of PET from the 'rogue' and 'normal' hydrolysis experiment.***

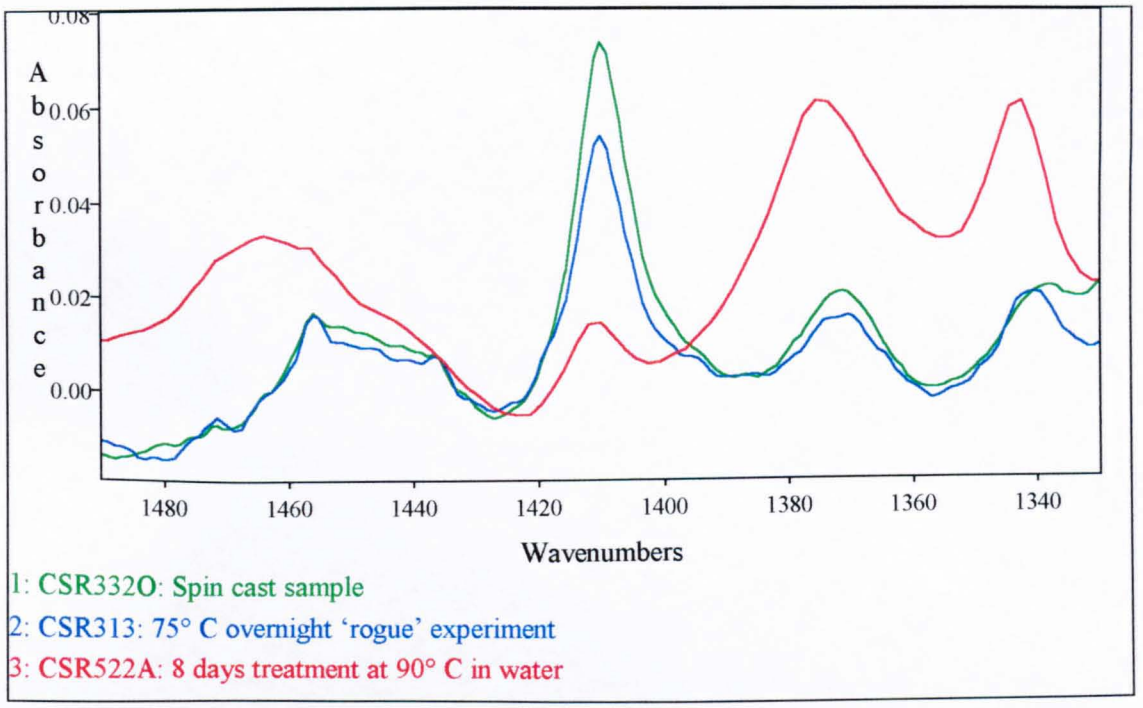

Figure 6.43. CH_2 wagging modes of PET from the 'rogue' and 'normal' hydrolysis experiment.

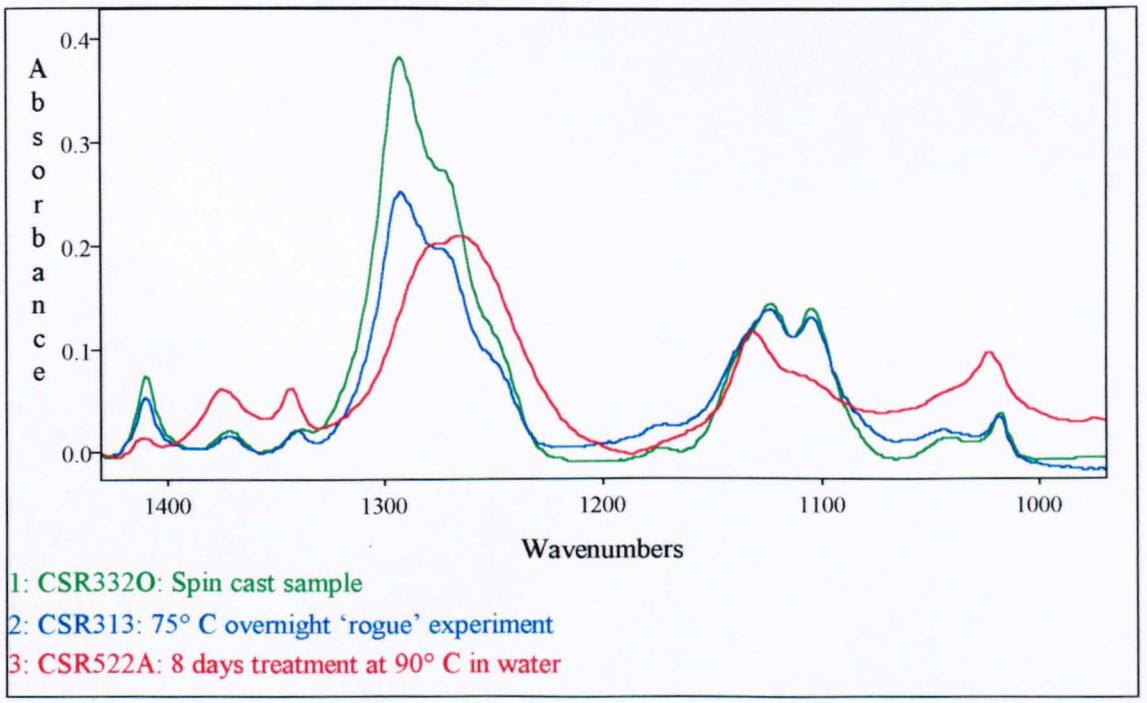

Figure 6.44. Ester band modes of PET from the 'rogue' and 'normal' hydrolysis experiment.

As figures 6.41 - 6.44. show the structure of the PET that has undergone 'rogue' hydrolysis is very different to that which has undergone 'normal' hydrolysis. Firstly the ν(CH) and ν(OH) are quite different (figure 6.41.). The position of the ν(OH), 3215 cm^{-1}, is much closer to the acid ν(OH) band position of 3256 cm^{-1} used in acid end group analysis. These two pieces of evidence perhaps indicate that this sample does not contain as much of the CH_2-OH group that the 'normal' hydrolysis product appears to have.

Figure 6.43. shows very little change in crystallinity has occurred during the 'rogue' hydrolysis according to the CH_2 wagging modes. Also it is shown that the 1470 cm^{-1} band that is very prominent in the 'normal' hydrolysis, which has been assigned to the crystalline δ(CH_2) and the delocalised acid ν(C-O) does not change dramatically in the 'rogue' experiment. This gives contrary evidence to the position of the ν(OH) band which seemed to point to a large increase in acid end groups.

Further work on the causes and mechanism of the 'rogue' degradation is clearly required, as there are too many unknowns in the system to reach any clear conclusions.

6.7 References.

6.1. M. Hodgson, Internal Report, Durham, (1995)

6.2. R.C. Golioke and S.W. Lasoski, *J. Phys. Chem.*, **64**, 895, (1960)

6.3. T. Davies, P.L. Goldsmith, D.A.S. Ravens and I.M. Ward, *J. Phys. Chem.*, **66**, 175, (1962)

6.4. D.A.S. Ravens and I.M. Ward, *Trans. Faraday Soc.*, **57**, 150, (1960)

6.5. W. McMahon, H.A. Birdsall, G.R. johnson and C.T. Camilli, *J.Chem. Eng. Data*, **4**, 75, (1959)

6.6. A. Ballara and J. Verdu, *Polym. Deg. Stability*, **26**, 361, (1989)

6.7. A. Launay, F. Thominette and J. Verdu, *Polym. Deg. Stability*, **46**, 319, (1994)

6.8. M. Edge, M. Hayes, M. Mohammadian, N.S. Allen, T.S. Jewitt, K. Brems and K. Jones, *Polym. Deg. Stability*, **32**, 131, (1991)

6.9. N.S. Allen, M. Edge, M. Mohammadian, and K. Jones, *Eur. Polym. J.*, **27**, 12, 1373, (1991)

6.10. N.S. Allen, M. Edge, M. Mohammadian, and K. Jones, *Polym. Deg. Stability*, **41**, 191, (1993)

6.11. N.S. Allen, M. Edge, M. Mohammadian, and K. Jones, *Polym. Deg. Stability*, **43**, 229, (1994)

6.12. H. Zhang and I.M. Ward, *Macromolecules*, 28, 7622, (1995)

6.13. H. Zimmermann and N. T. Kim, *Polym. Eng. Sci.*, **20**, 680, (1980)

6.14. J.R. Campanelli, M.R. Kamal and D.G. Cooper, *J. Appl. Polym. Sci.*, **48**, 443, (1993)

6.15. M. Nagata, T. Kiyotsukuri, S. Manami, N. Tsutsumi and W. Sakai, *Polym. Int.*, **39**, 83, (1996)

6.16. M.S. Ellison, *J. Appl. Polym. Sci.*, **27**, 247, (1982)

6.17. A. Miyagi and B. Wunderlich, *J. Polym. Sci. Polym. Phys. Ed.*, **10**, 2073, (1972)

6.18. M. Hodgson and J. Robinson (unpublished results)

6.19. G. Papet, L. Jirackova-Audouin and J. Verdu, *J. Radiat. Phys. Chem.*, **29**, 65, (1987)

6.20. ICI Standard Analytical Method, SAM/IR/12

6.21. 'Polymer Handbook', 3rd edition, (Eds. J. Brandrup and E.H. Immergut), Wiley-Interscience, Ney York, (1989)

6.22. S-B. Lin and J.L. Koenig, *J. Polym. Sci. Polym. Phys. Ed.*, **21**, 2365, (1983)

6.23. R.P. Daubney, C.W. Bunn and C.J. Brown, *Proc. R. Soc.* (London), **A226**, 531, (1954)

6.24. K. Pozefsky and H. Coggeshall, *Anal. Chem.*, **23**, 1611, (1951)

6.25. G. Mirrone and R. Fabbri, *Gazz. Chim.*, **84**, 187, (1954)

6.26. J. Francis, *J. Chem. Phys.*, **18**, 861, (1950)

6.27. K.C. Cole, J. Guèvremont, A. Ajji and M.M. Dumoulin, *Appl. Spec.*, **48**, 12, 1513, (1994)

6.28. A. Miyake, *J. Polym. Sci.*, **38**, 479, (1958)

6.29. D.J. Walls, *Appl. Spec.*, **45**, 7, 1193, (1991)

6.30. D.J. Walls and J.C. Coburn, *J. Polym. Sci. Part B: Polym. Phys.*, **30**, 887, (1992)

6.31. 'Infrared Spectra of Complex Molecules, Volume 2', (Ed L. J. Bellamy), Chapman and Hall, London, 172, (1975)

6.32. R. Belali and J.M. Vigoureux, *Appl. Spec.*, **48**, 4, 465, (1994)

6.33. A. Aref-Azar and J.N. Hay, *Polymer*, **23**, 1129, (1982)

6.34. D. Langevin, J. Grenet and J.M. Saiter, *Eur. Polym. J.*, **30**, 3, 339, (1994)

6.35. N. Everall, (personal communication)

Chapter 7.

The diffusion of organic molecules into PET.

7.1. Introduction.

The diffusion of organic liquids into and out of PET has important implications with regard to recycling. As environmental pressures to recycle packaging materials are increased, the economic rewards to find a suitable market for the use of recycled materials are all too obvious. Currently, there are restrictions on the use of reclaim for food and drug packaging [7.1], as there is not enough information on the extent to which impurities may or may not migrate into food upon contact with reclaimed materials. Further research will indicate whether these restrictions are warranted [7.2].

Generally, the diffusion of organic molecules has implications further afield, with small molecules playing important roles in the polymer industry as plasticisers, fillers and biocides. Organic solvents are also used to remove small impurities and oligomers from PET films for use as high specification substrates [7.3].

It is hoped that by observing the vibrations of sorbed hydroxylated organic molecules we may gain a better understanding of the interactions between PET and hydrogen bonding species. It was for this reason that the alcohol, methanol and the diol, ethylene glycol were chosen for this study.

The diffusion of organic liquids into polymers is generally non-Fickian in nature [7.4] for several reasons. Firstly, it is often accompanied by swelling, which can change the diffusion coefficient by increasing the free volume space [7.5]. Secondly, strong

interactions between the polymer and diffusant, may cause deviations from Fickian diffusion [7.6]. Thirdly, in systems where diffusion is accompanied by chemical reaction, anomalous diffusion is also dominant [7.7-7.10].

The inclusion of small amounts of organic molecules can lower the T_g of semicrystalline polymers to below ambient temperatures, thus enabling changes in crystallinity [7.10-7.12]. It has been shown that samples tend to reach a maximum degree of induced crystallinity depending on the conditions used [7.13]. Durning et al in several publications [7.10, 7.11, 7.13-7.15] and Liu and Neogi [7.16] have examined the effects of methylene chloride vapour on PET and the levels of crystallinity have been shown to increase in the polymer matrix after sorption.

The diffusion of methanol into PET and its effects on the polymer structure have been examined by a number of workers [7.7, 7.10, 7.11, 7.17, 7.18]. The diffusion of methanol is accompanied by crystallisation and Durning et al have proposed a mathematical model [7.10, 7.11]. The diffusion of 'interactive diluents' has also been likened to non-Fickian diffusion in noncrystallisable glassy polymers [7.10], which have been fitted to a dual sorption model in the past [7.19-7.21]. The kinetics of liquid induced crystallisation have been shown to be very rapid [7.7, 7.17, 7.18] and the resulting polymer left opaque to visible light, due to the spherulite sizes being of the order of the wavelength of light [7.17, 7.22, 7.23].

The diffusion of ethyl laurate and ethanol vapours through oriented PET membranes has been examined using a radio tracer technique by Barson and Dong [7.24]. In this work

the diffusion process was accompanied by swelling and the amount of swelling determined the apparent diffusion coefficient.

Nir et al [7.2] looked at the sorption of series of organic liquids into amorphous and oriented PET. They used gravimetric methods and using a 'pseudo-Fickian' analysis of the data and obtained estimated diffusion coefficients for the sorption of benzyl alcohol and toluene. The sorption of toluene into amorphous PET, was estimated to have a diffusion coefficient of ~ 4 x 10^{-9} cm^2s^{-1} and ~ 11.5 % weight gain at equilibrium. When the same analysis was applied to the sorption of toluene into oriented PET, the D value quoted was ~ 4 x 10^{-10} cm^2s^{-1} with an equilibrium weight increase of ~ 9.5 %. There was even more contrast for benzyl alcohol sorption, the diffusion coefficient went from ~ 1 x 10^{-8} cm^2s^{-1} for amorphous PET, to ~ 4 x 10^{-10} cm^2s^{-1} for oriented PET. With the equilibrium weight gains being quoted as ~22 % and 13.5 % for amorphous and oriented PET respectively. Neither PET sample was shown to absorb liquid or swell when placed in heptane or 1,2-propanediol.

Popoola has looked at the retention of organic liquids in PET fibres of differing crystallinity [7.25]. It was found that pre-treatment of the fibres at 200° C increased the amount of liquid retained after sorption in DMF and benzaldehyde and subsequent 'drying' at 60° C. The sorption of a series of alcohol vapours (methanol, ethanol, propanol, butanol and isopropanol) into amorphous PMMA was studied by Sfirakis and Rogers [7.26]. The rate of sorption was seen to decrease with an increase in size of the alcohol. Sadler et al [7.27] looked at the permeability of organic contaminants including benzene through PET samples into a headspace for volatile components and a liquid medium for non volatiles, utilising GC detection. It was found that in mixtures of

contaminants, that faster diffusing components could 'drag' slower diffusing components with them.

7.2. Experimental.

For this set of experiments, all films were 'hot' cast from OCP onto a ZnSe ATR prism and characterised using the methods described in chapter 5. Only the most highly crystalline and highly amorphous films that we were able to prepare were examined, which means that films were manufactured from, 100 % E47 and 100 % E99, i.e. normal PET and PET containing 18 % isophthalate comonomer, to give one essentially amorphous and one semi-crystalline film. All films were annealed at 60° C for at least 24 hours to remove the residual solvent. Film thicknesses and percentage crystallinity were calculated using methods described in chapter 5. Table 7.1. shows the characteristics of the films used during this work.

Diffusant	Film type	Thickness / μm	% crystallinity
Methanol	E99	9.2 ± 0.3	5 ± 0.1
Methanol	E47	8.7 ± 0.2	27 ± 0.2
Ethylene glycol	E99	8.2 ± 0.2	4.7 ± 0.1
Ethylene glycol	E47	8.0 ± 0.2	29 ± 0.3

Table 7.1. Characteristics of the films used for the diffusion experiments.

Data was collected and treated using the methods described in chapter 4. Due to the swelling of the polymer creating negative bands in the CH stretching region, the integrated intensities of the ν(OH) band were obtained by integration between 4000 and 3050 cm^{-1}.

7.3. Results and discussion.

The spectra were obtained on a Mattson Polaris FTIR spectrometer, using a Mattson Macro program described in section 4.5. The instrumental parameters and other details of the diffusion experiment are given in section 4.5. The diffusion coefficients were calculated from a program written in Pascal by Marcia Pereria [**7.28**].

7.3.1. The diffusion of liquid methanol into PET.

Figure 7.1. shows the FT-IR ATR spectrum of pure methanol. The ν(OH) band of methanol can be interpreted as containing a whole range of hydrogen bond strengths and angles, and as such, is similar to the ν(OH) band of water. However, unlike the relatively simple spectrum of water, methanol also has many other bands in its spectrum which will complicate the examination of the polymer structure during diffusion.

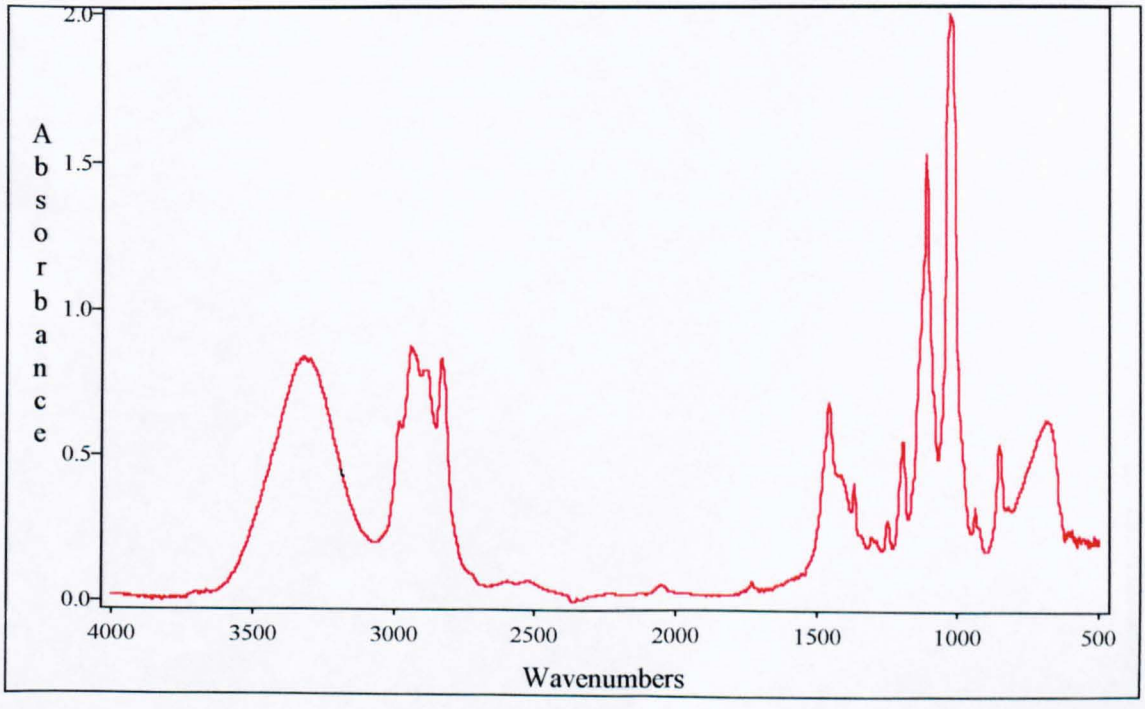

Figure 7.1. The FT-IR ATR spectrum of pure methanol.

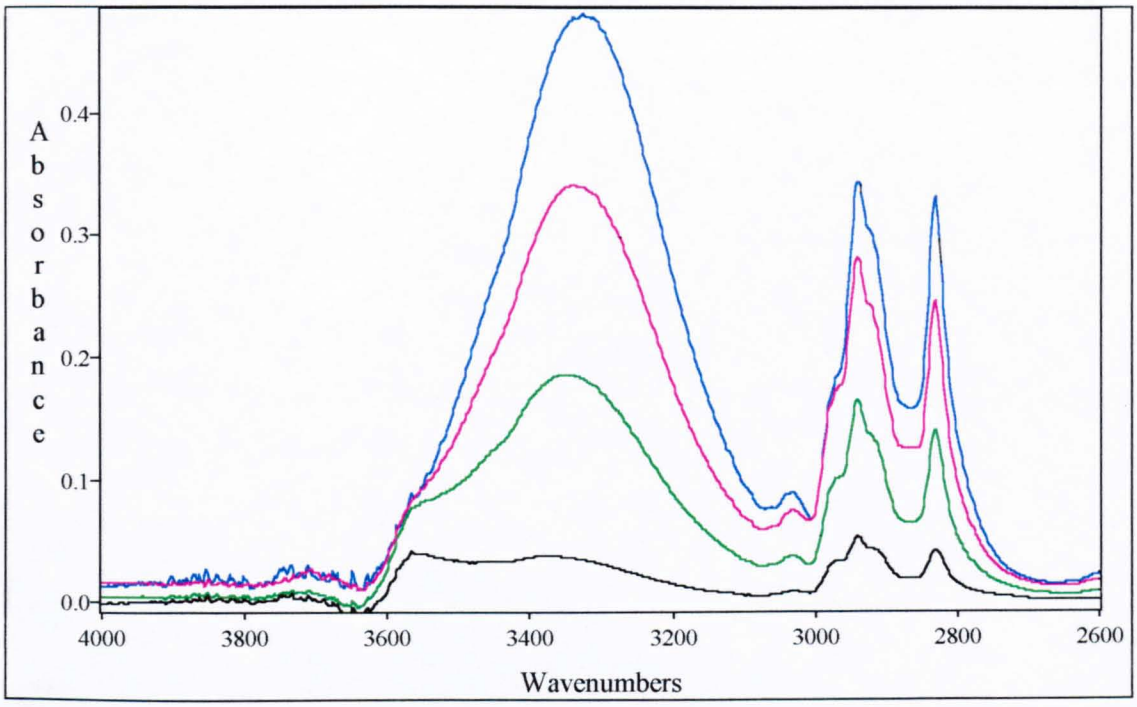

Figure 7.2. ***The ν(OH) and ν(CH) regions of methanol diffusing into 5 % crystalline PET at 1, 2 and 10 minutes and at equilibrium (4 hours)***

Figure 7.2. shows the growth of the ν(OH) band, as methanol diffuses into a 5 % crystalline PET film. In a manner not unlike that described in chapter 5 for water, there are drastic changes occurring to the shape of the ν(OH) band as a function of concentration of methanol in the polymer. At shorter times, i.e. lower concentrations, there are at least two ν(OH) bands clearly distinguishable, without the need for resolution enhancement techniques.

The high wavenumber feature at ~ 3565 cm^{-1} could be assigned to methanol interacting with or hydrogen bonded to the polymer. This would result in a weakening of the methanol hydrogen bonding and a shift to higher wavenumber of the ν(OH). As the concentration of the methanol in the polymer increased, this high wavenumber feature

became less pronounced (figure 7.2.). This phenomenon was noted by Fieldson and Barbari [**7.29**].

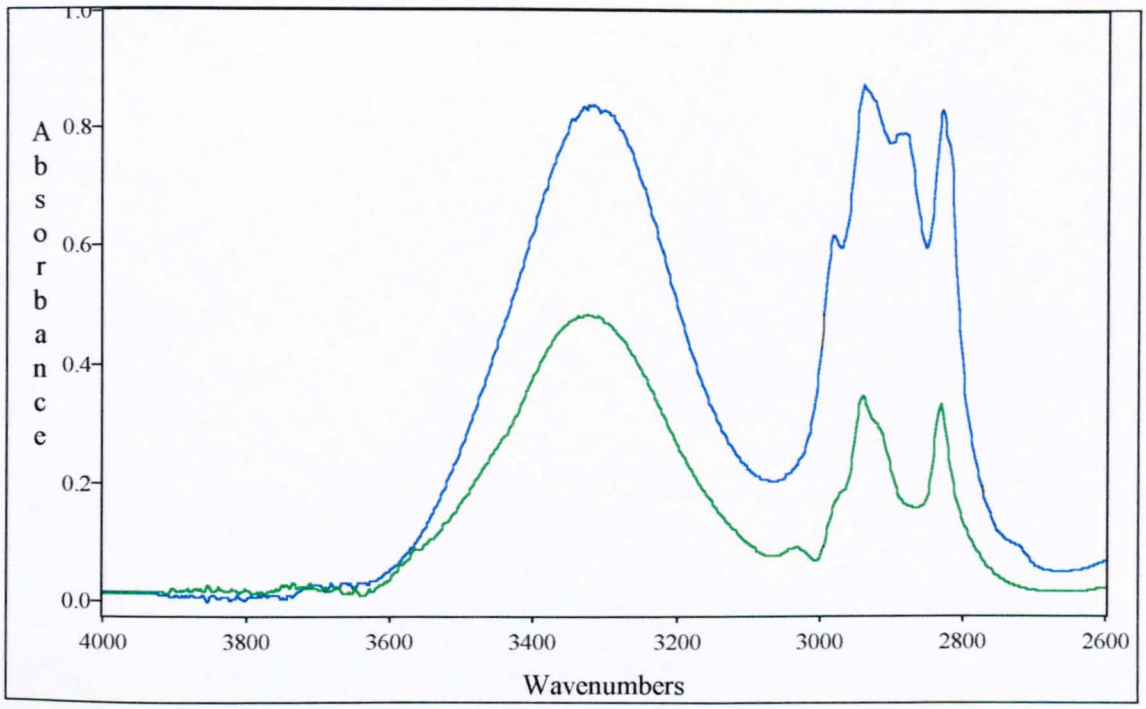

Figure 7.3. ***Comparison of the ν(OH) and ν(CH) regions of pure methanol and methanol at equilibrium in 5 % crystalline PET.***

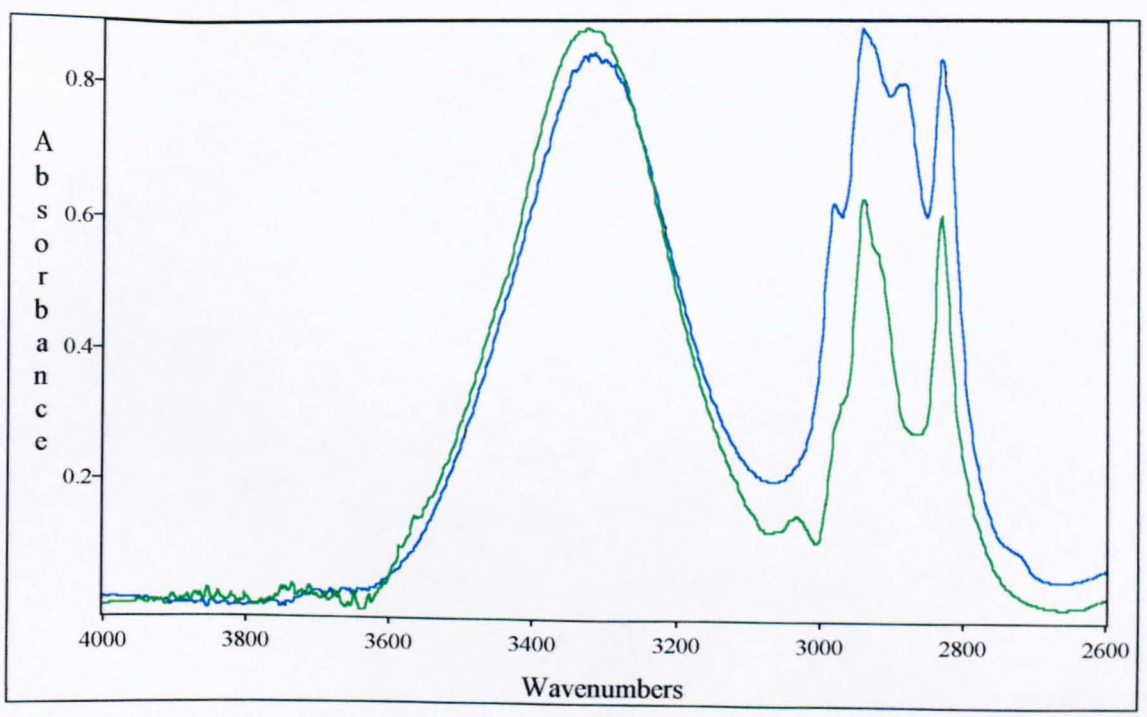

Figure 7.4. ***Comparison of the ν(OH) and ν(CH) regions of pure methanol and (on an expanded scale) methanol at equilibrium in 5 % crystalline PET.***

Figures 7.3. and 7.4. show the comparison of the ν(OH) regions of pure methanol and methanol in 5 % crystalline PET. Figure 7.3. shows the difference in intensity between the two ν(OH) bands, whilst expanding the scale of the equilibrium methanol in figure 7.4. allows easier comparison of the bandshapes.

Figure 7.4. shows that the ν(OH) band has shifted slightly to higher wavenumber in the 'methanol in PET' spectrum. The perturbation of the ν(OH) band at equilibrium is not as pronounced as the ν(OH) band seen with liquid water sorbed in PET. But the perturbation of the ν(OH) band at lower concentrations is just as dramatic as that seen in liquid water. This is consistent with the fundamental ideas behind the dual sorption model [**7.19-7.21, 7.30**]. The dual sorption model is generally used to explore the kinetics of diffusing systems with strong interactions between the penetrant and polymer. If one considers that at short times, i.e. low concentrations, one is essentially observing the 'filling' of vacant sites in the polymer matrix, this would explain the prominence of the high wavenumber species in the ν(OH) band of methanol in these spectra. As the possible hydrogen bonding sites get 'filled', one can observe the increase in the 'pure methanol like' nature of the ν(OH) band. As there are only a finite number of sites for hydrogen bonding between the methanol and the polymer, one may expect to see the proportion of methanol adsorbed / bound to these hydrogen bonding sites to decrease with increased concentration. Another factor is that methanol may prefer to interact with other methanol molecules instead of the polymer. At lower concentrations this may not be possible, but as the concentration of methanol increases so does the likelihood of interactions between methanol molecules.

If one examines the Fourier self deconvolution (FSD) of the methanol in PET at equilibrium compared with the FSD of pure methanol (figure 7.5.) then one can see some very interesting features.

The FSD of methanol in PET shows that the band at 3565 cm^{-1} is still present in the equilibrium ν(OH) band. This lends support to the proposal that the band at 3565 cm^{-1} is associated with methanol that is interacting with or hydrogen bonded to the polymer. Another band that is observed in the FSD of the methanol in the polymer, but not in pure methanol, occurs at 3458 cm^{-1} which is very similar in frequency to the first overtone of the ester carbonyl in PET.

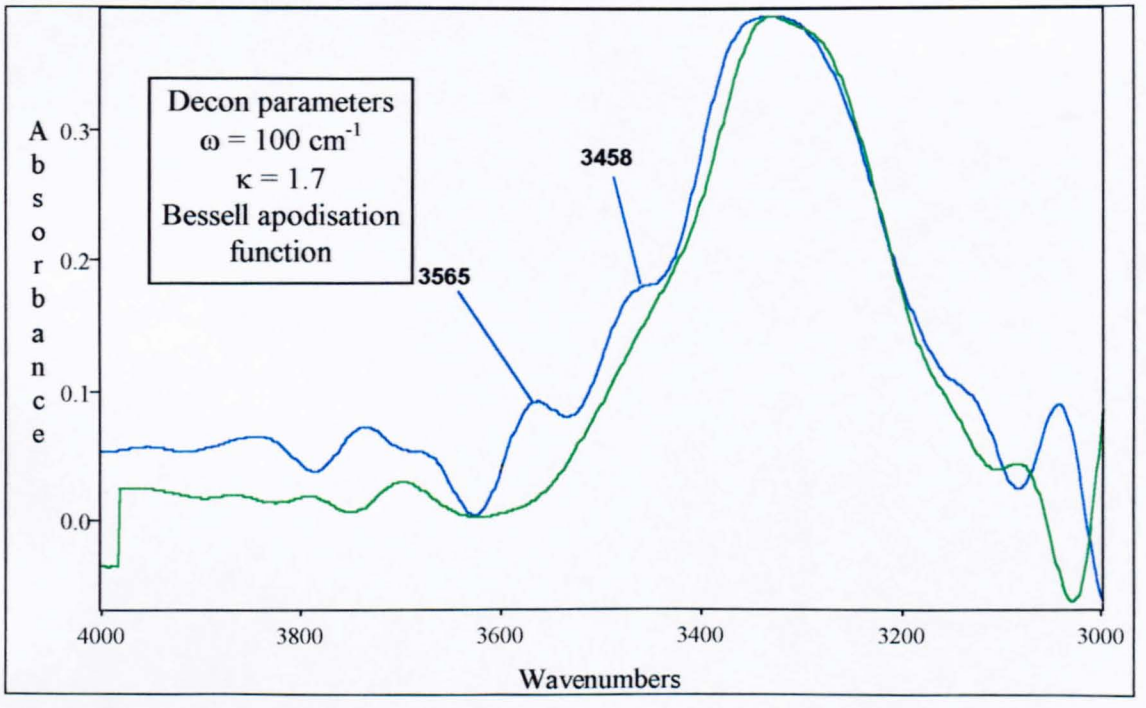

Figure 7.5. ***Comparison of the Fourier self deconvolution of the ν(OH) regions of pure methanol and (on an expanded scale) methanol at equilibrium in 5 % crystalline PET.***

More evidence for strong interactions between the polymer and the penetrant can be gleaned from the ν(C=O) region of the spectrum. Figure 7.6. gives interesting information on both the interactions of the methanol and the ester carbonyl, and the swelling that occurred simultaneously during diffusion. It was not possible to directly examine the carbonyl band of PET for films >2 μm thick, using FT-IR ATR, due to the saturation of the ν(C=O) band in the spectrum. But, since the spectra were obtained by ratioing against a dry film in these experiments, differences between the carbonyl bands with time show up.

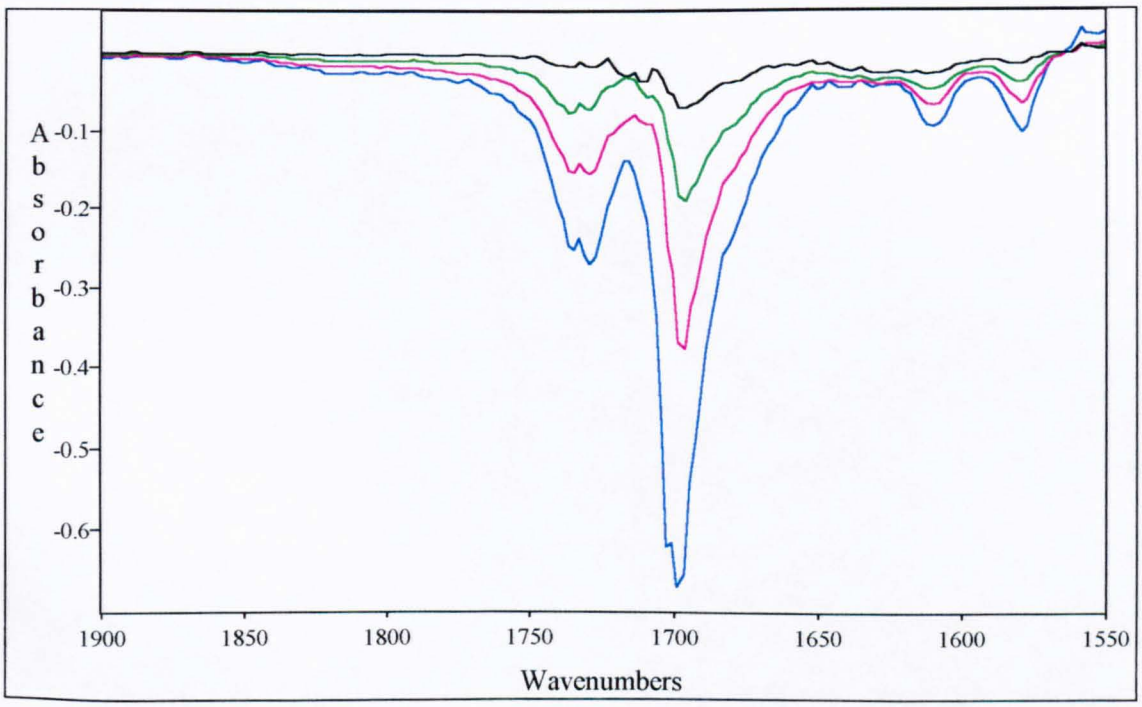

Figure 7.6. The ν(C=O) region of methanol diffusing into 5 % crystalline PET at 1, 2 and 10 minutes and at equilibrium (4 hours).

Figure 7.6. shows the ν(C=O) region of spectra of methanol in PET, ratioed against the dry polymer film. In this figure, negative bands relate to the swelling of the polymer. The larger the negativity of the bands, the greater the swelling. The shape of the band can also be used to give indications of interactions that may be occurring.

The negative carbonyl band shown in figure 7.6. is clearly a doublet. This has some interesting implications. The carbonyl band of PET contains at least two components **[7.31]**. In the presence of methanol, some of the components of the carbonyl band are clearly perturbed more than the others, hence a doublet rather than a normal negative asymmetric peak. The frequencies of the bands of the doublet are 1732 and 1700 cm^{-1}. The band positions for the peaks in the doublet may be somewhat misleading, for example, if some components in the carbonyl band are increasing as the others are decreasing this could result in a distortion of the bands after ratioing against the dry film.

The 'normal' ν(C=O) band of amorphous PET has a frequency of 1730 cm^{-1}, the frequency does lower upon crystallisation to around 1716 cm^{-1}, but changes in crystallinity alone, which do occur during methanol sorption **[7.10, 7.11, 7.13-7.15]**, cannot account for the low frequency negative band at 1700 cm^{-1}. If the effect observed was simply a shift in frequency, due to a crystallinity change, then one could expect to see a 'differential type' band. Additional effects may include swelling and interactions between the methanol OH and PET carbonyl. These will further complicate the carbonyl bandshape. Another consideration is the growth of the (very weak) methanol band at 1725 cm^{-1} which may have an effect on the shape of the ν(C=O). It would appear that the negative bands observed during the diffusion of methanol into essentially amorphous PET, are a combined result of crystallisation, swelling, interactions between PET carbonyl. The band at ~ 1700 cm^{-1} may well be as a result of the carbonyl and alcohol interaction in PET.

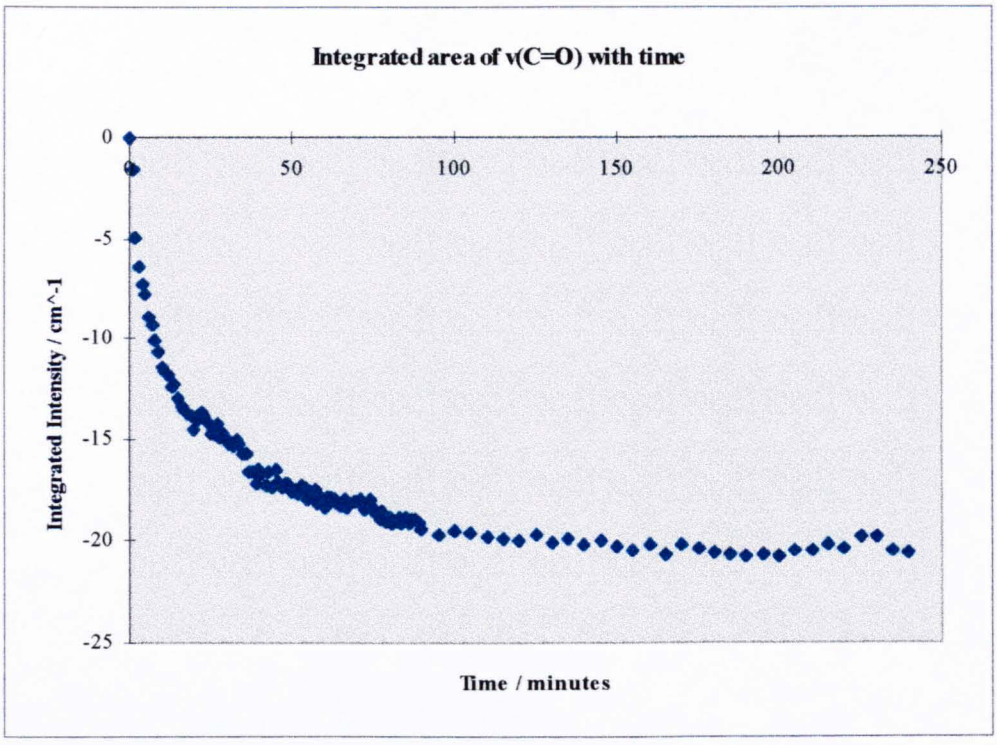

Figure 7.7. The integrated area of the decrease of the ν(C=O) band of 5 % crystalline PET as methanol diffuses in.

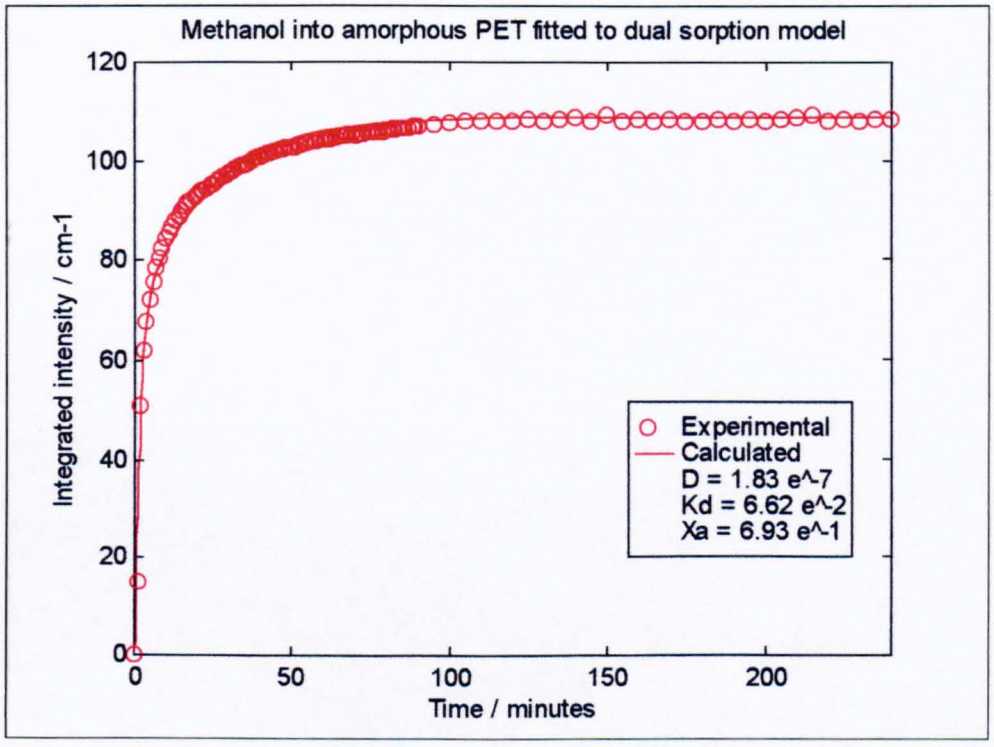

Figure 7.8. The plot of ν(OH) intensity versus time for methanol diffusing into 5 % crystalline PET fitted to a dual sorption model.

The area of the carbonyl band can be used as a crude indicator of swelling with time. This is shown in figure 7.7. It is interesting that the shape of the curve associated with swelling is like a mirror image of the sorption curve shown in figure 7.8. which suggests correlation between swelling and the diffusion rate.

Due to the interferences from bands associated with the methanol diffusant, it was not possible to use the technique of Belali and Vigoreux [7.32] to calculate the crystallinity. Another method, for example density measurements, Raman spectroscopy or XRD, would be necessary which would mean that the experiment would no longer be able to be carried out *in-situ*. Because of this no calculation of the increase in crystallinity with time has been undertaken during this work.

The experimental data fits well to the dual sorption model described in chapter 4. The kinetics of the sorption will be discussed later in this section and compared to results obtained with a more crystalline film.

Figure 7.9. shows the ν(OH) and ν(CH) of methanol diffusing into 27 % crystalline PET. The ν(OH) bandshape is very similar to that of methanol diffusing into amorphous PET at shorter times, probably due to the concentration of methanol involved. Both experiments show that the shape of the ν(OH) for methanol in PET is highly dependent on the concentration of methanol within the polymer.

It was noticeable that equilibrium had not been reached after 4 hours in this sample, unlike for the 5 % crystalline sample, which is a clear indication that the diffusion rate is slower for the more crystalline sample, as one would expect.

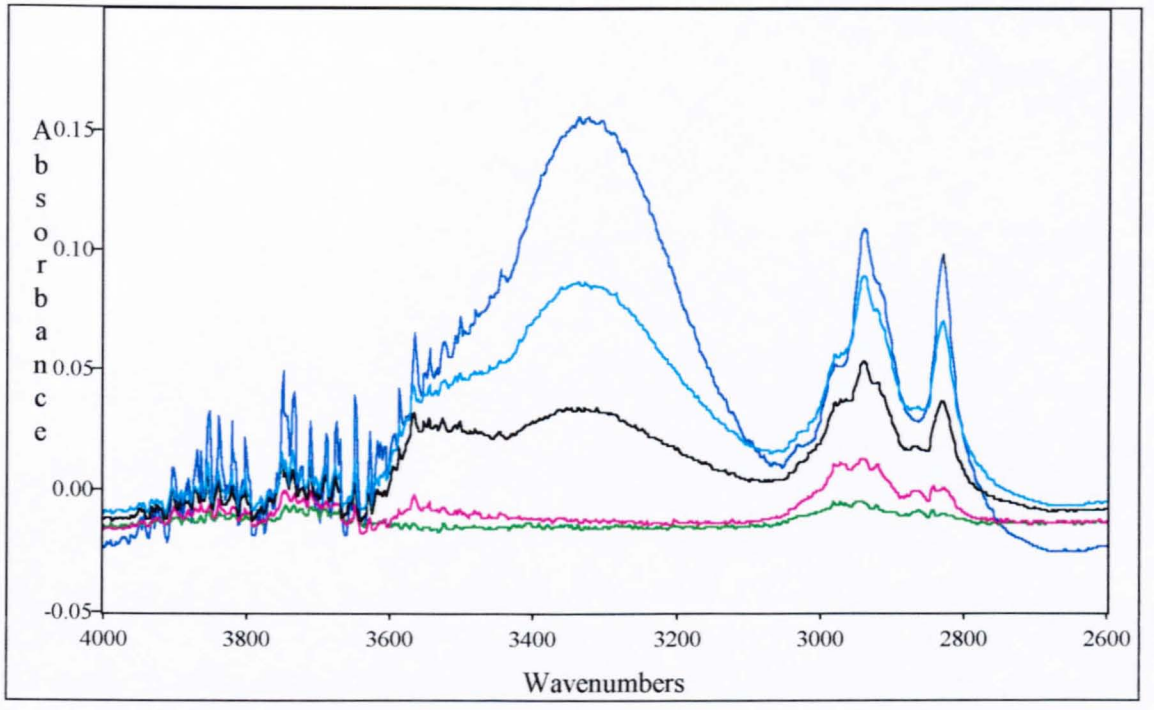

Figure 7.9. The ν(OH) and ν(CH) regions of methanol diffusing into 27 % crystalline PET at 1, 10, 30, 120 and 240 minutes.

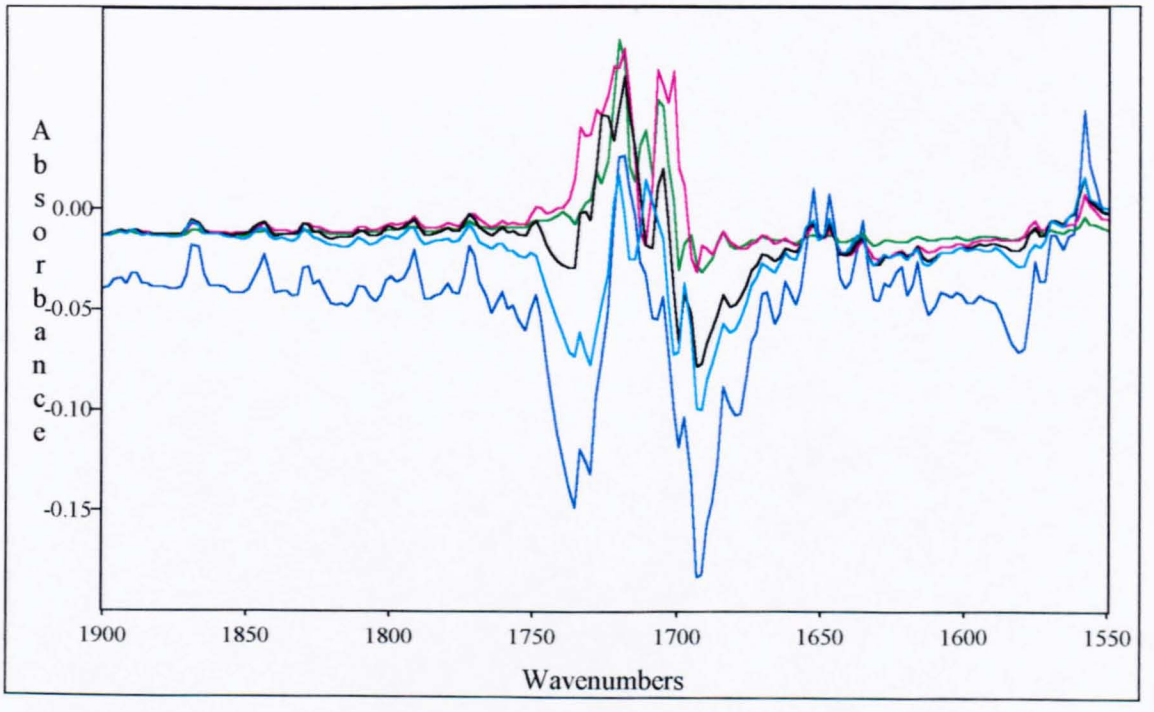

Figure 7.10. The ν(C=O) region of methanol diffusing into 27 % crystalline PET at 1, 10, 30, 120 and 240 minutes.

Figure 7.10. shows the negative carbonyl band for methanol diffusing into 27 % crystalline PET. Figure 7.10. indicates that swelling appears to be much less prevalent in the polymer with higher crystallinity. This may be due to the increased rigidity of the polymer chains hindering chain segmental motion. It is also noticeable that both negative and positive bands are shown in this region, c.f. for the 5 % crystalline sample where only negative bands were observed.. The most simple explanation of the ν(C=O) band is that the negative peak at around 1730 cm^{-1} corresponds to ester carbonyl that is not interacting or is weakly interacting with methanol and the negative peak at 1700 cm^{-1} corresponds to ester carbonyl that is hydrogen bonded to the sorbed methanol. Other factors that may influence the shape of the band include changes in crystallinity and interferences from methanol bands.

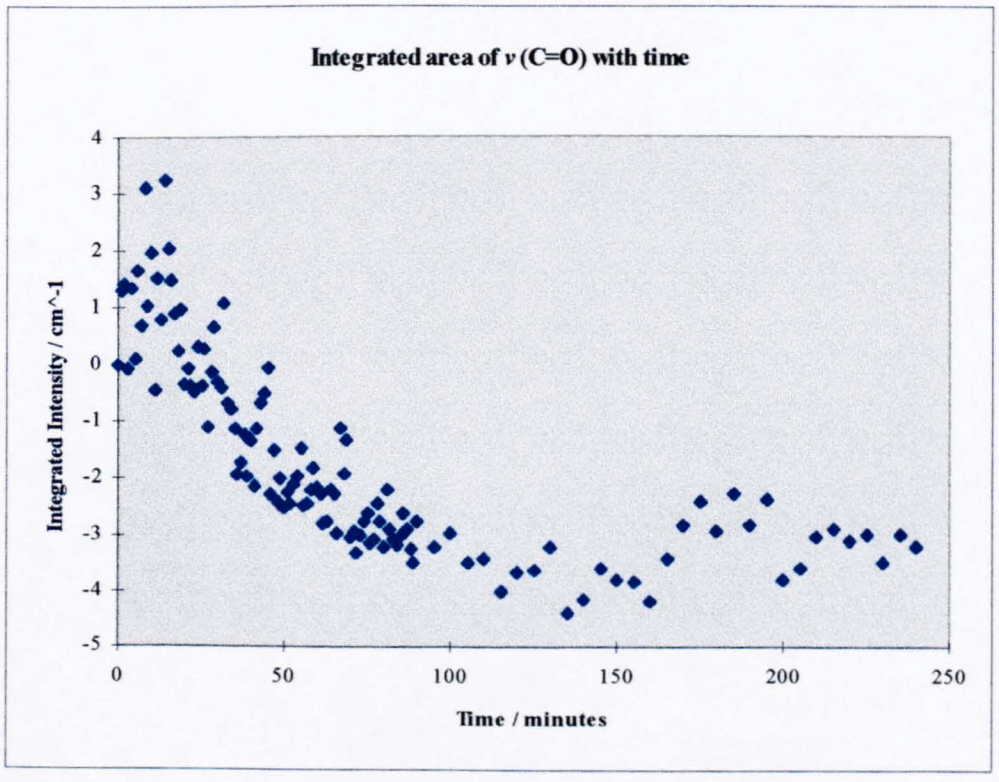

Figure 7.11. The integrated area of the ν(C=O) band of 27 % crystalline PET as methanol diffuses in.

Figure 7.11. shows the integrated area of the ν(C=O) band as a function of time. The initial positive values of the integrated areas, are interesting. This strongly suggests that interactions between methanol and the PET carbonyl occurs very rapidly, causing a shift in the carbonyl band which manifests itself as a distorted band (see green band in figure 7.10.). This interaction / binding, which is predicted by the dual sorption model, is then followed by swelling, as the decrease in the integrated intensity to negative values indicates. It would appear that the swelling is;

1. More rapid in the amorphous polymer, no initially positive bands were observed in the ν(C=O) region for the 5 % crystalline film.
2. Much more widespread in the amorphous polymer, the magnitude of the negative bands are much greater in the amorphous PET film than the more crystalline one.

Both these phenomena can be explained by the increase in the rigidity of the polymer chains as crystallinity increases. It may also be argued that the crystalline regions may also be impermeable (or at least less permeable) to the methanol, which would mean that there was less polymer involved in swelling in the more crystalline film.

The experimental data was once again fitted to a dual sorption model and the produced output is shown in figure 7.12. The fit of the more crystalline film data to the model is not as good as the fit of the amorphous PET data to the same model. This could be due to the model no longer being an accurate description of the diffusion process or that the fact that equilibrium had not been reached during data acquisition has an effect on the computer fitting process or both these factors. At shorter times the model fits the data very well.

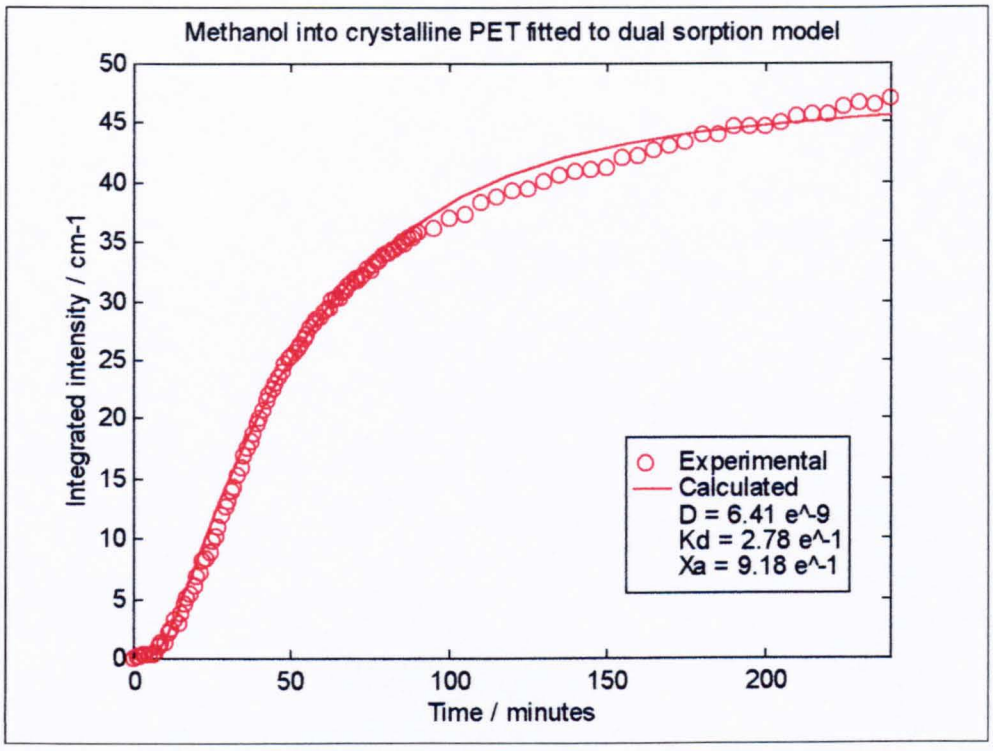

Figure 7.12. The plot of ν(OH) intensity versus time for methanol diffusing into 27 % crystalline PET fitted to a dual sorption model.

As stated previously, even a cursory glance at the diffusion profiles (figures 7.8. and 7.12.) for the diffusion of methanol into PET, would suggest a dramatic difference in the kinetics between the two polymer films examined. Table 7.2. shows the calculations of the diffusion coefficients and the fraction of strongly 'bound' diffusant.

Sample	5 % crystalline	27 % crystalline
D_1 / x 10^{-8} cm^2s^{-1}	18.3 (± 0.22)	0.64 (± 0.09)
D_2 / x 10^{-8} cm^2s^{-1}	1.21 (± 0.09)	0.18 (± 0.07)
X_a	0.69 (± 0.03)	0.92 (± 0.04)

Table 7.2. Calculated diffusion coefficients and fraction of 'bound' penetrant for methanol diffusing into PET.

The diffusion coefficient, D_1, represents the rate at which the penetrant enters the polymer film and becomes 'bound' at sites within the polymer matrix, possibly forming a gel. The diffusion coefficient, D_2, represents the rate at which the penetrant front of the

diffusant (i.e. the gel) moves through the polymer. The fraction of strongly 'bound' penetrant is given by X_a and is always <1.

From table 7.2. it is clear that both the initial adsorption of the methanol and the subsequent diffusion of the penetrant are significantly hindered by the increase in crystallinity. Indeed, the initial diffusion of the methanol penetrant is 1-2 orders of magnitude slower in the more crystalline PET film. This can be explained by the morphological differences between the polymers, the decrease in the flexibility of the polymer chains with increased crystallinity. The fact that some regions of the polymer matrix may be inaccessible to the penetrant due to the crystallites acting as a barrier, may also influence the rate of diffusion. Swelling is thought to increase the rate of diffusion by creating a larger free volume for molecules to penetrate within the polymer matrix [7.6]. If the swelling is reduced, as appears to be the case when the crystallinity is increased, then this rate enhancement is not observed.

The effect of the crystalline regions on the movement of the penetrant front is not as marked as the initial sorption, but is still just under 1 order of magnitude greater in the less crystalline polymer. Similar arguments *vis à vis* chain mobility can be applied to explain the differences.

Another factor which has not been mentioned during this discussion is the role of the penetrant in chain mobility. As mentioned earlier, the sorption of methanol into PET is accompanied by crystallisation. It is thought that the presence of methanol can sufficiently lower the T_g to allow enough mobility in chain segments for them to form crystallites. This should have a greater effect on the sample with lowest crystallinity

because, as mentioned in section 6, the T_g in PET, is dependent on the crystallinity. Samples generally tend to reach a maximum level of crystallinity, depending on the conditions. Therefore it is not unlikely that more crystallinity will be induced in the amorphous film than in the more crystalline film and as the conditions for both samples were identical, then the final degrees of crystallinity should be the around the same. But the important point here, is that as well as allowing greater chain mobility for the formation of crystallites, the increase in chain mobility would allow a more rapid diffusion. Unfortunately as mentioned earlier, it was impossible to calculate the levels of crystallinity of the two PET samples from the infrared spectra, due to spectral interferences from the sorbed methanol. Attempts at spectral subtraction proved to be unsuccessful.

The parameter X_a, which indicates the fraction of penetrant which is strongly 'bound' also differs, between the two samples. The model estimates that around 69 % of the methanol is 'bound' in the 5 % crystalline sample and 92 % in the 27 % crystalline PET sample. Whilst on first impressions these numbers seem high, the spectra of the ν(OH) bands (figures 7.2. and 7.9.) do indicate that there are differences in the relative proportions of strongly 'bound' and 'unbound' or 'bulk liquid' methanol within the polymer matrices. If one accepts the proposal that the high wavenumber feature at ~ 3565 cm^{-1} can be attributed to methanol interacting / bound to / hydrogen bonded to the PET matrix, then observing that the sample with a higher X_a value does indeed have a greater proportion of this high wavenumber feature would support this claim.

The fact that the samples apparently contain a greater proportion of strongly 'bound' rather than 'bulk' methanol would suggest that the molar extinction coefficients between

the strongly 'bound' and 'bulk' methanol ν(OH) are dramatically different, when one examines the shape of the bands. If these values for X_a were indeed correct then the molar extinction coefficient for the 'bulk' methanol ν(OH) is much greater than that for strongly 'bound' methanol ν(OH).

On a microscopic scale, the idea that the more crystalline sample contains a greater proportion of 'bound' methanol does seem reasonable, if one assumes that in a film with larger free volume spaces, the methanol can form clusters in which some of the molecules may have no interactions with the surrounding polymer matrix. Conversely, in a system with smaller free volume spaces or voids, then the methanol has little or no choice but to interact with the polymer matrix. Although the proportion of 'bound' molecules appears to be greater in the more crystalline sample, it is important to point out that overall there is much more methanol in the less crystalline sample. This may reflect on the relative size of the voids within the polymer matrices.

To summarise,

1. The rate of the diffusion of methanol into PET is highly dependent on the morphology of the film.
2. The state of the methanol in the polymer film is dependent on both the concentration of penetrant and the morphology of the film.
3. Diffusion is accompanied by both swelling and crystallisation, both of which are more prominent in the amorphous sample.
4. Increasing the crystallinity of the PET film, decreases the rate of diffusion, decreases the amount of swelling, decreases the total amount of sorbed methanol and increases the proportion of methanol directly bound to the polymer within the PET matrix.

7.3.2. The diffusion of liquid ethylene glycol into PET.

The FT-IR ATR spectrum of pure ethylene glycol is shown in figure 7.14. The broad ν(OH) can once again be said to contain a wide range of hydrogen bond strengths and angles. Again, unlike the diffusion of water into PET, many bands associated with the ethylene glycol will overlap with bands associated with the polymer, making interpretation of the structural changes to the PET matrix very difficult.

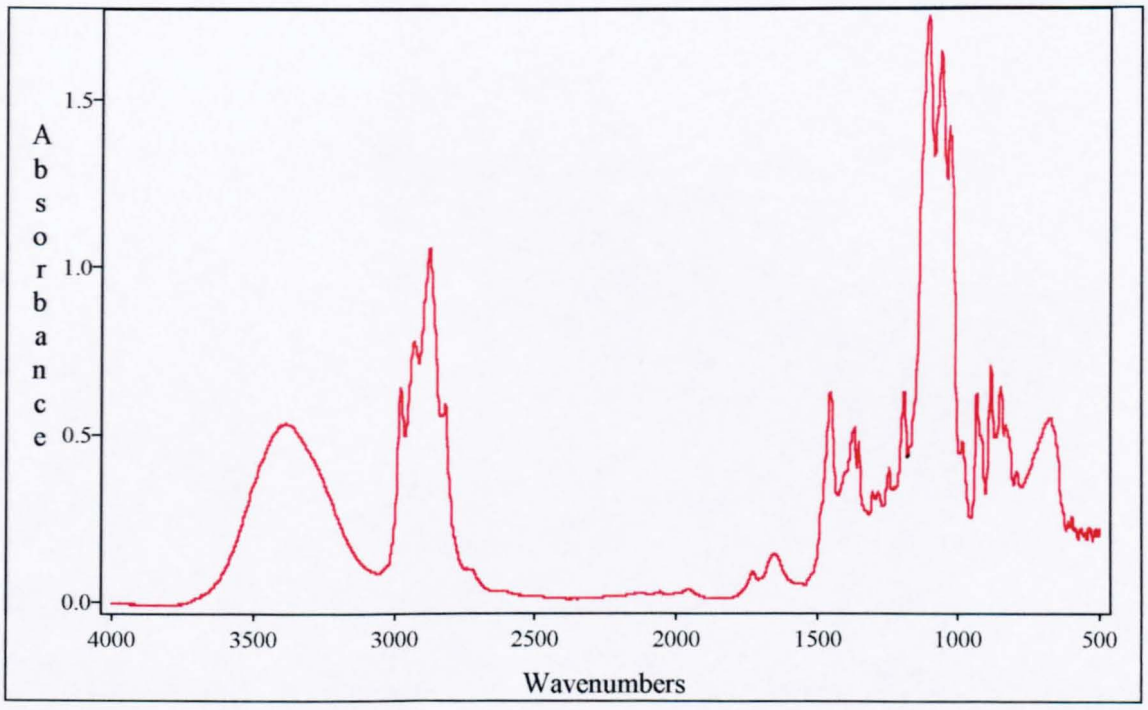

Figure 7.13. The FT-IR ATR spectrum of pure ethylene glycol.

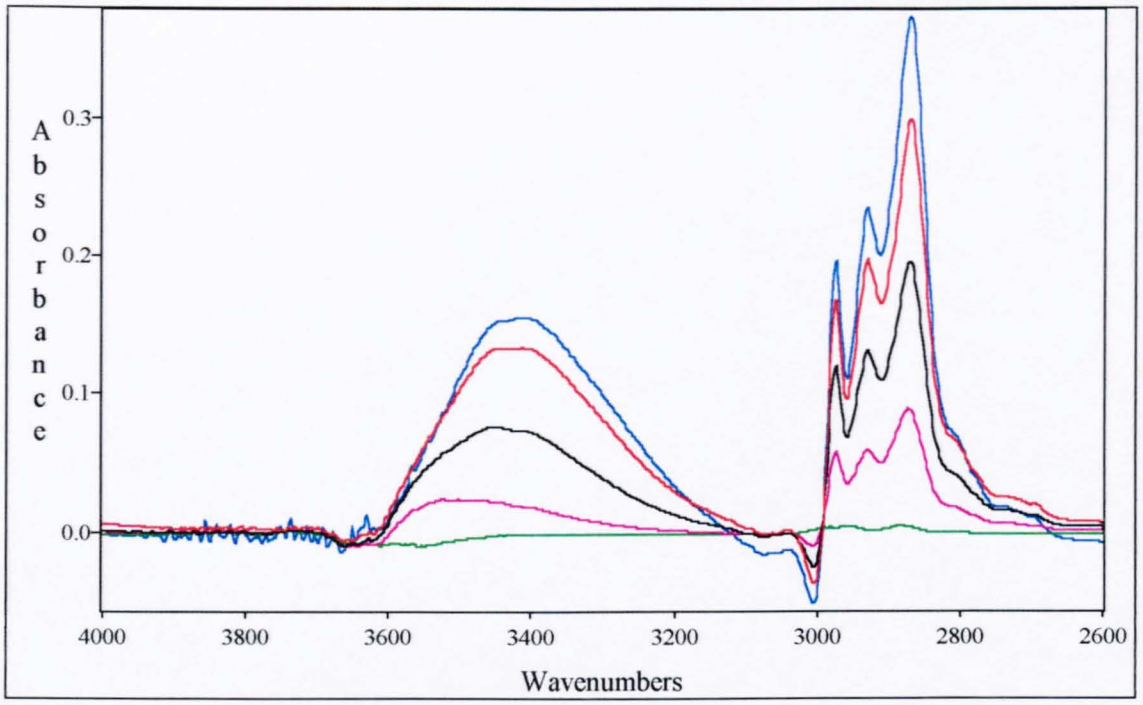

Figure 7.14. The ν(OH) and ν(CH) regions of ethylene glycol diffusing into 4.7 % crystalline PET at 1, 2, 3 and 10 minutes and at equilibrium (4 hours)

Figure 7.14. shows the growth of the ν(OH) and ν(CH) bands, as ethylene glycol diffuses into a 4.7 % crystalline PET film. Initially, one can observe the equilibrium of hydrogen bond strengths shifted to higher frequency, indicating an overall weakening of the HB network. In some ways this behaviour differs to that of methanol diffusing into PET, as there is not the same dramatic evidence for a high frequency ethylene glycol-PET species. As the diffusion progresses, the equilibrium of hydrogen bond strengths shifts back towards that of pure ethylene glycol, but in a manner similar to water in PET, the equilibrium ν(OH) band seems to remain at a higher frequency, never reaching that of pure ethylene glycol.

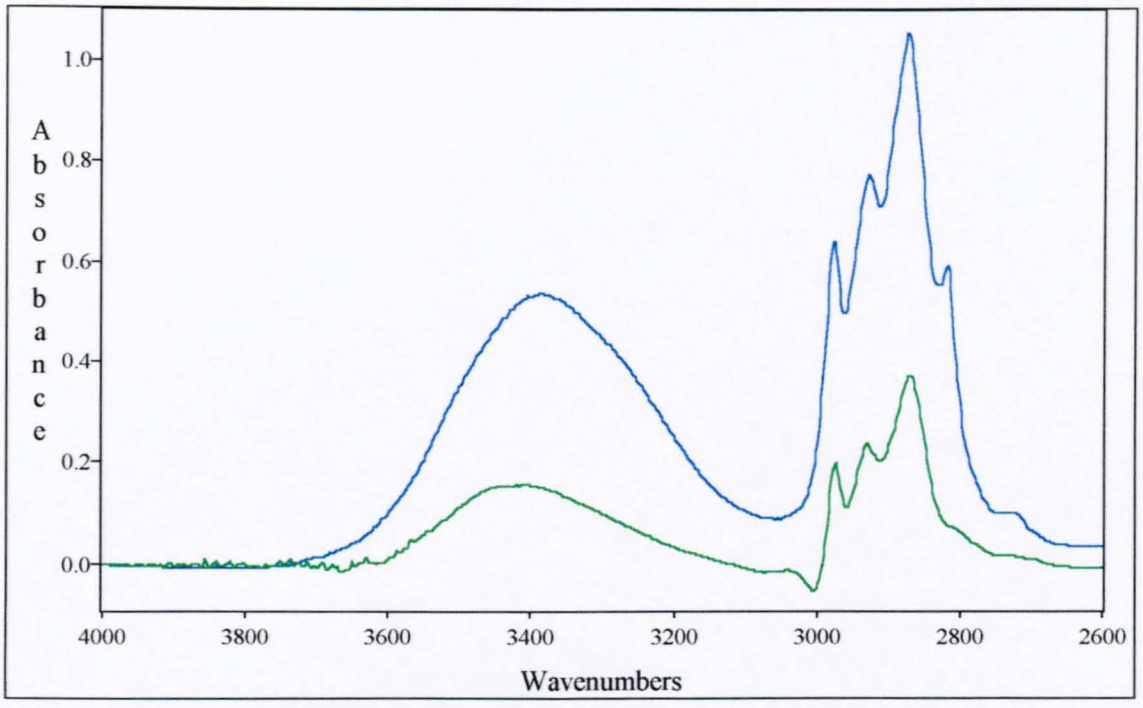

Figure 7.15. ***Comparison of the ν(OH) and ν(CH) regions of pure ethylene glycol and ethylene glycol at equilibrium in 4.7 % crystalline PET.***

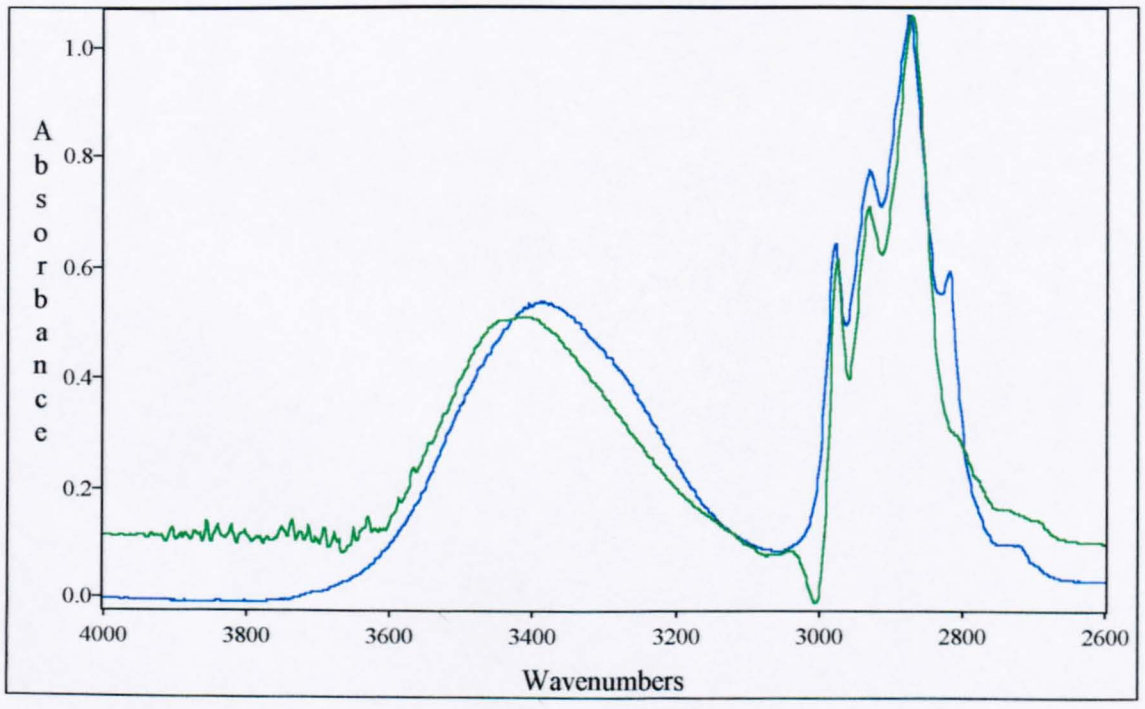

Figure 7.16. ***Comparison of the ν(OH) and ν(CH) regions of pure ethylene glycol and (on an expanded scale) ethylene glycol at equilibrium in 4.7 % crystalline PET.***

Figures 7.15. and 7.16. show a comparison of the shape of the ν(OH) and ν(CH) of pure ethylene glycol with ethylene glycol in 4.7 % crystalline PET at equilibrium. Figure 7.15. shows that at polymer film saturation, the intensity of the ethylene glycol bands are, as expected, lower than those for pure ethylene glycol.

Figure 7.16. highlights the perturbation of the ν(OH) band of ethylene glycol in PET compared to that of pure ethylene glycol. There is a definite overall shift to higher frequency of the ν(OH) band, which is more marked that that observed between pure methanol and methanol in PET (section 7.3.1.), but less marked than that seen for pure water and water in PET.

Perhaps differences between the degree of perturbation for the different systems, tell us that in the methanol-PET system we have two distinct species of methanol, 'bound' and 'bulk'. But in the ethylene glycol and water systems the boundaries between 'bound' and 'bulk' species are less well-defined. This difference in H-B distribution may be due to the fact that each ethylene glycol or water molecule can hydrogen bond to another ethylene glycol or water molecule even after it has hydrogen bonded to a PET carbonyl. It is less likely that a methanol, hydrogen bonded to a PET carbonyl, could undergo more hydrogen bonding with another methanol, due to the steric effects of the polymer, hindering the approach of other methanol molecules. This is schematically illustrated in figure 7.17.

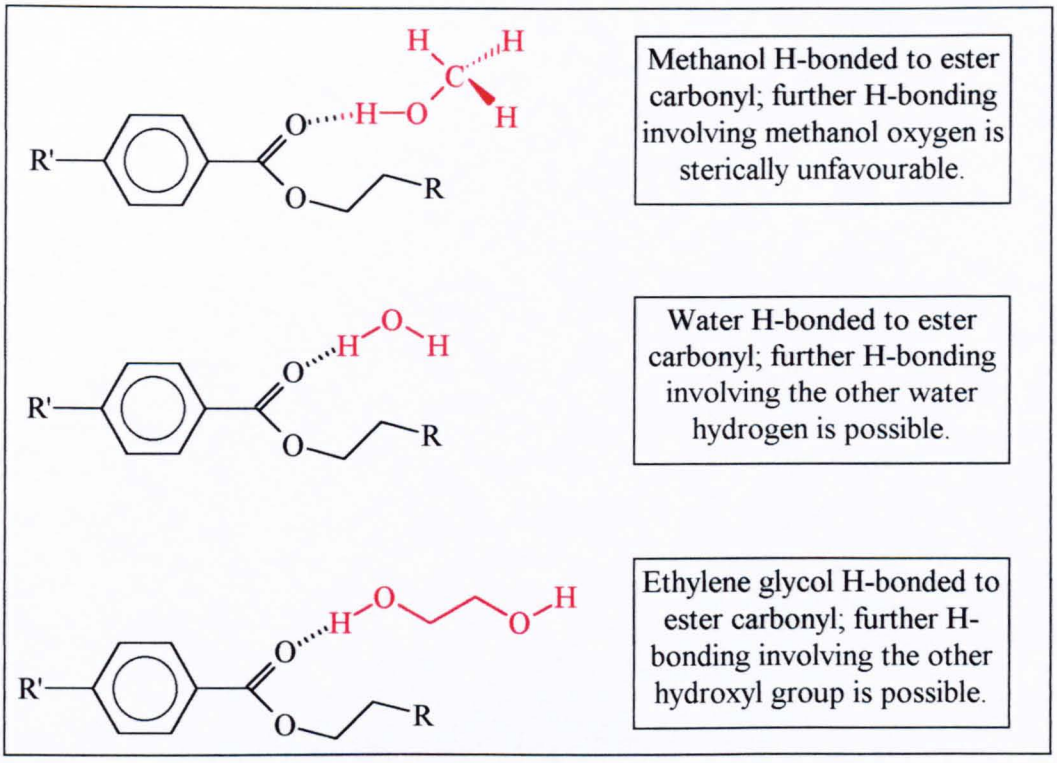

Figure 7.17. Possible interactions involving penetrants and the PET matrix.

Figure 7.18. shows the FSD of the ν(OH) bands for ethylene glycol in PET and pure ethylene glycol. A band at 3540 cm^{-1}, which is not present in the pure ethylene glycol spectrum is indicated. This band may be ethylene glycol hydrogen bonded to the polyester carbonyl. It has a similar frequency (c.f. 3565 cm^{-1}) to the band that we have assigned to methanol hydrogen bonded to the PET carbonyl. The intensity of this band appears to be greater in the more amorphous polymer than in the more crystalline polymer, the implications of this will be discussed later in this section.

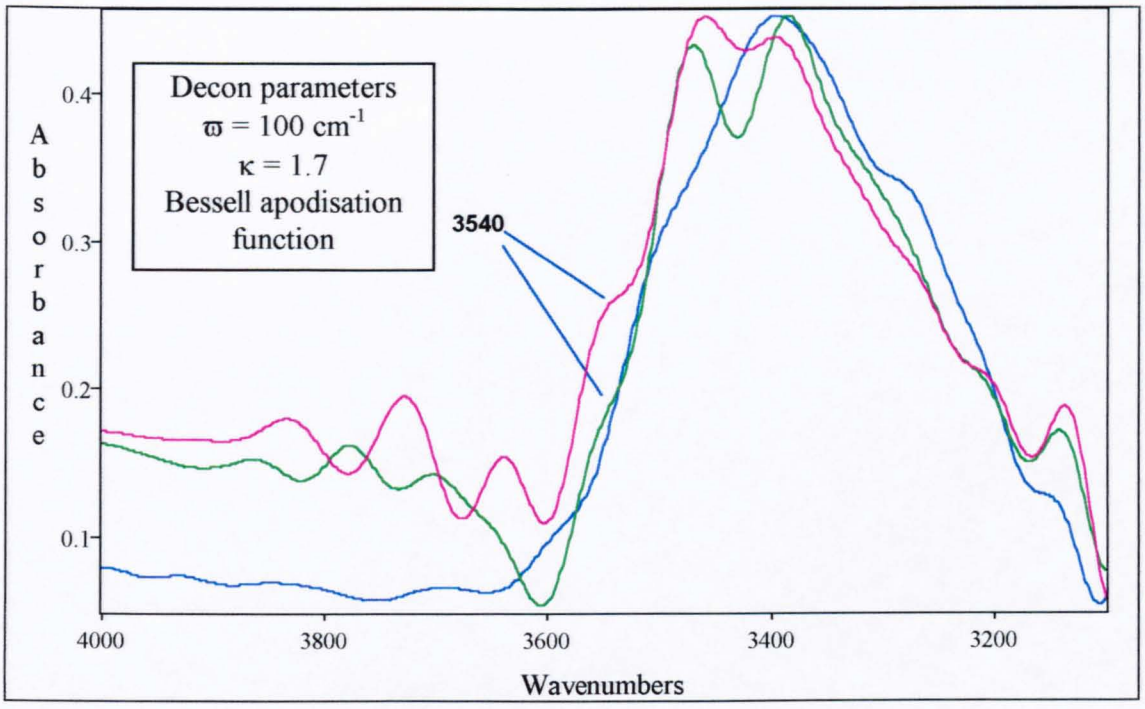

Figure 7.18. ***Comparison of the Fourier self deconvolution of the ν(OH) regions of pure ethylene glycol and (on an expanded scale) ethylene glycol at equilibrium in 4.7 % and 29 % crystalline PET.***

As is quite common with organic penetrants, the polymer undergoes swelling during diffusion. As shown in section 7.3.1. the carbonyl band can be used as a crude indicator of swelling in PET, as it is relatively free of interfering bands. As figure 7.19. shows the result is a negative doublet, which is again a function of swelling, crystallinity changes, interference from the ethylene glycol band at 1725 cm^{-1} and interactions between ethylene glycol and the polymer.

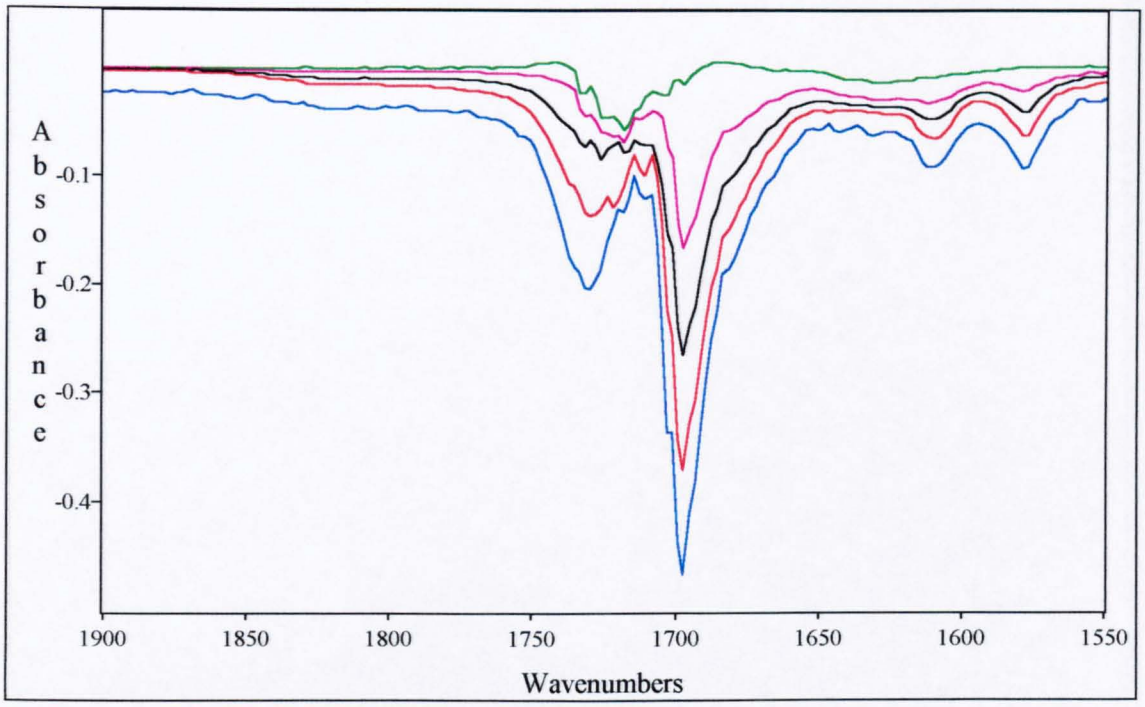

Figure 7.19. The ν(C=O) region of ethylene glycol diffusing into 4.7 % crystalline PET at 1, 2, 3 and 10 minutes and at equilibrium (4 hours).

Figure 7.20. shows the integrated intensity of the carbonyl bands, shown in figure 7.19., as a function of time. From figure 7.20. it is clear that the polymer had swollen to a maximum extent after thirty minutes. This is about the same time as it takes to reach equilibrium ethylene glycol content, as shown in figure 7.21. This confirms the close link between diffusion and swelling. As the polymer swells, it allows more diffusant into the matrix, essentially filling up the free space volume. Once swelling has reached its' maximum, there is not enough room to accommodate more ethylene glycol molecules and equilibrium is reached. Again diffusion is accompanied by crystallisation, this is evident by the changes in optical clarity of the polymer films. Before treatment with ethylene glycol, the polymer film was clear and transparent. After treatment, the film became opaque to visible light, which is a good indicator of crystallinity changes.

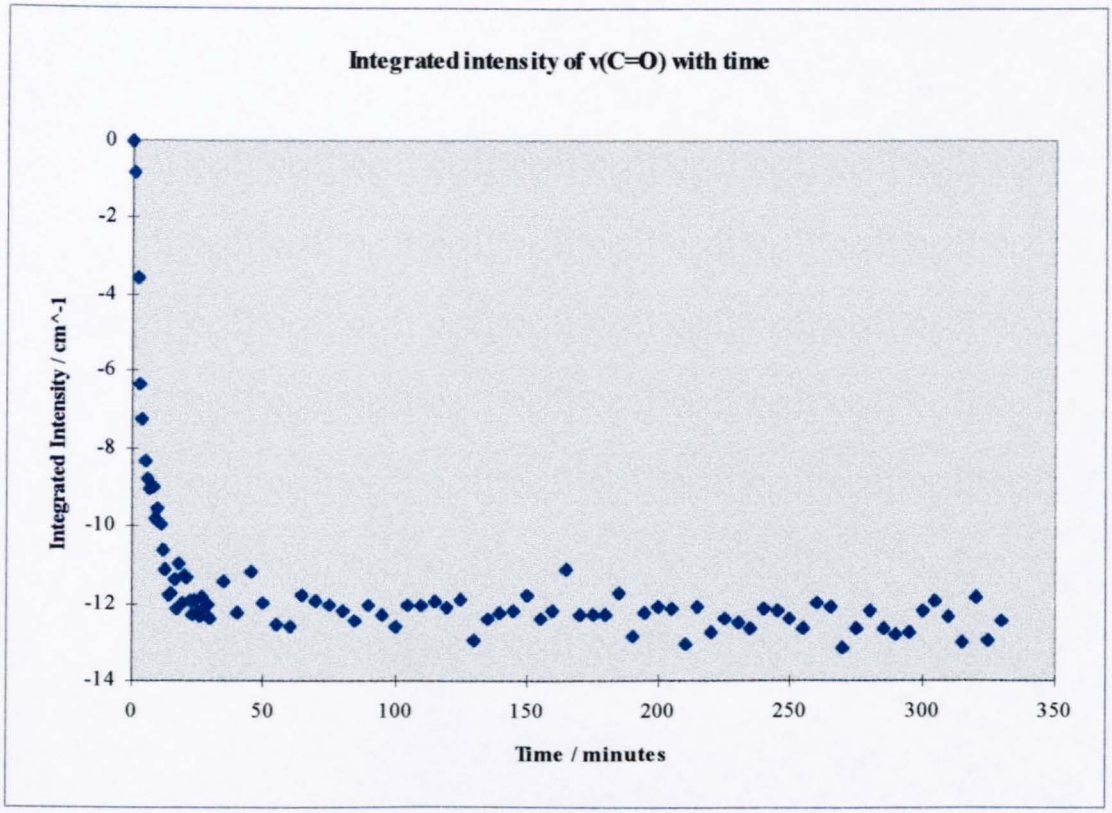

Figure 7.20. The integrated area of the ν(C=O) band of 4.7 % crystalline PET as ethylene glycol diffuses in.

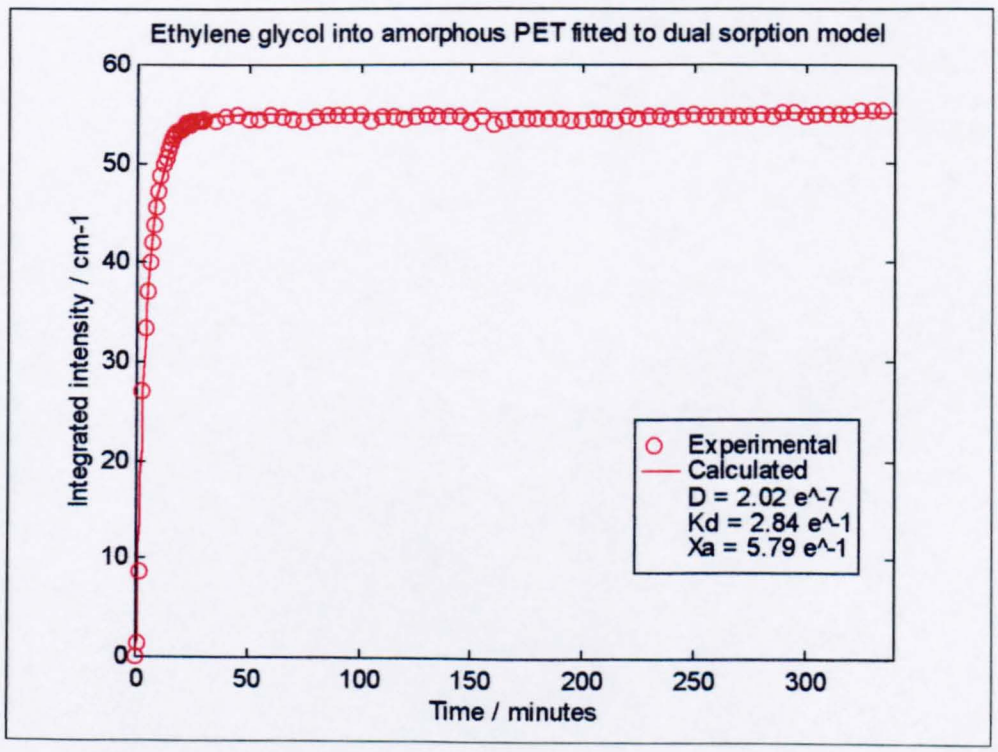

Figure 7.21. The plot of ν(OH) intensity versus time for ethylene glycol diffusing into 4.7 % crystalline PET fitted to a dual sorption model.

Figure 7.22. shows the growth of the ν(OH) and ν(CH) bands of ethylene glycol in 29 % crystalline PET. The ν(OH) band appears to have a negative component at around 3600 cm^{-1} and a feature at 3430 cm^{-1} which coincides with the ester ν(C=O) overtone of PET. It is unlikely that the feature at 3430 cm^{-1} is a direct result of the swelling of the polymer during diffusion, creating a negative band where the ester carbonyl occurs, as the band would have been noted in the amorphous sample. It is most likely to be a function of the microscopic environment of the ethylene glycol sorbed in the polymer.

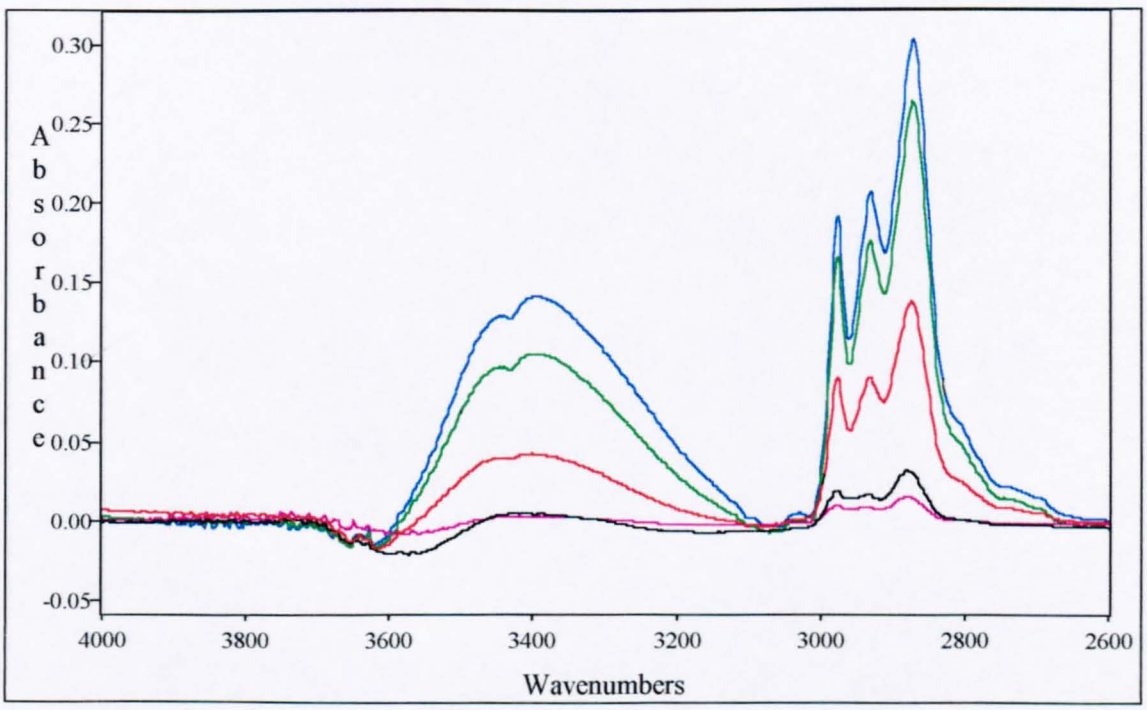

Figure 7.22. The ν(OH) and ν(CH) regions of ethylene glycol diffusing into 29 % crystalline PET at 1, 2, 10 and 120 minutes and at equilibrium (4hours)

Perhaps more light can be cast on the feature at ~ 3600 cm^{-1} by comparing the short time ATR spectra, with the spectrum of the cast film which was obtained using a transmission

technique (figure 7.23.). The negative feature observed in this set of spectra may be phenolic OH from the residual solvent or atmospheric H_2O in the ethylene glycol. The film was treated in the same manner as all the other films prepared in this project, annealed at 60° C, to remove all the solvent, so there should not be any residual solvent. Figure 7.23. shows that there may be a small feature (shoulder) in the 3600 cm^{-1} region. It is unlikely to be a shift of the ester overtone causing distortions at low levels of intensity. As the intensity of the ν(OH) band increases this distortion does become insignificant. The overall shape of the ν(OH) band at low intensity indicates a multi component band undergoing swelling, band shifts and band growth simultaneously.

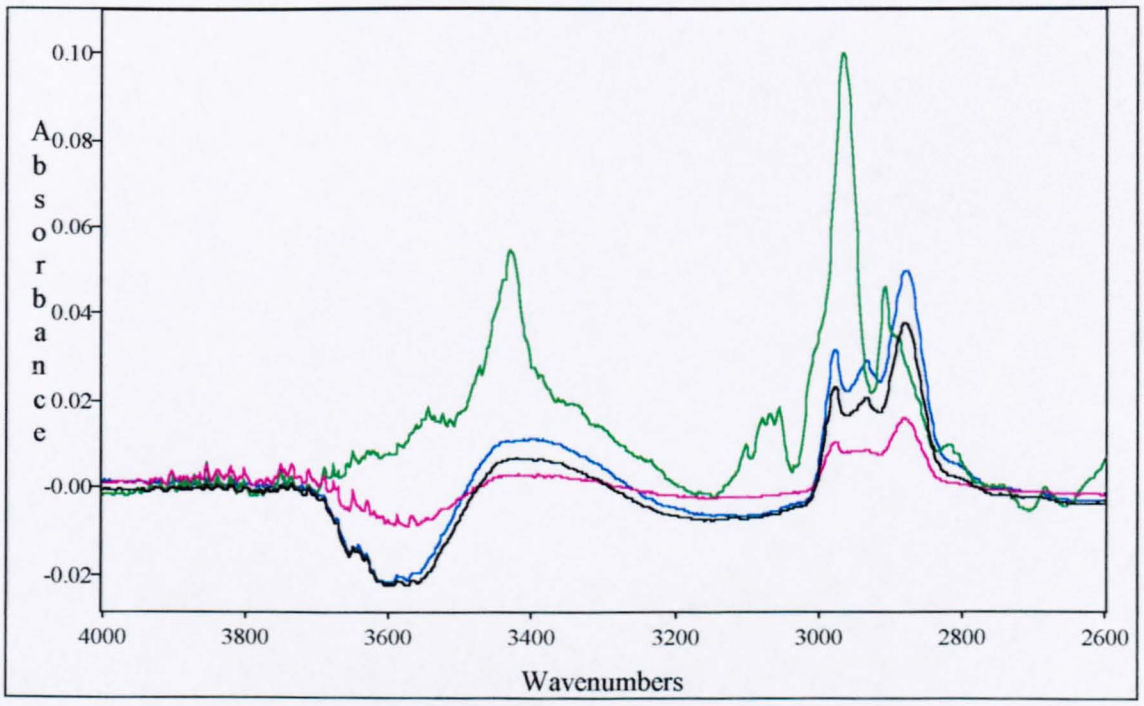

Figure 7.23. Comparison of ethylene glycol in PET after 1, 3 and 5 minutes and the dry PET film.

Unlike in the methanol diffusion experiments, increasing the crystallinity does not seem to impair the swelling of the polymer, to such a great extent during ethylene glycol

diffusion. Figure 7.24. shows the ν(C=O) region for a 29 % PET film during the diffusion of ethylene glycol. The short time spectra show a 'differential' type peak, which is indicative of band shifts. This once again implies interaction between the polymer and the penetrant. It is fair to say that overall there has been a greater degree of swelling in the more amorphous polymer. The rate of swelling is also faster in the amorphous sample, as shown by the comparison of figure 7.20. with figure 7.25.

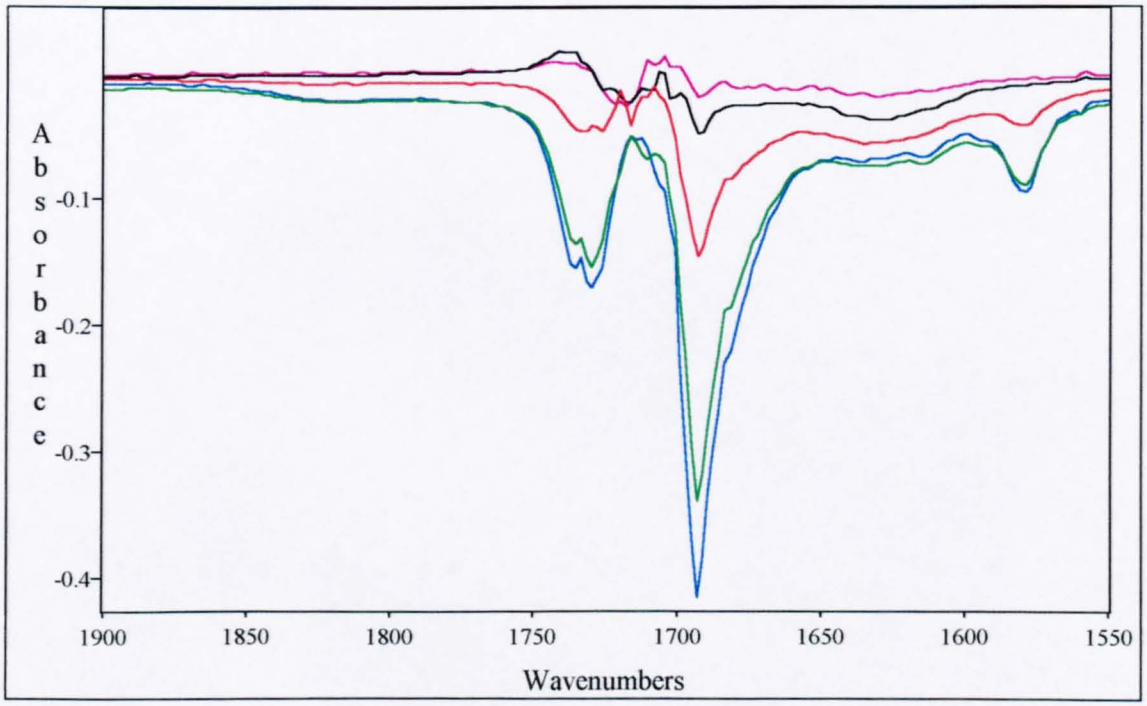

Figure 7.24. The ν(C=O) region of ethylene glycol diffusing into 29 % crystalline PET at 1, 2, 10 and 120 minutes and at equilibrium (4hours)

The fact that swelling is still significant in the more highly crystalline sample may tell us about the permeability of ethylene glycol in the crystalline regions. In the methanol diffusion experiments, the diminished swelling, and lower concentrations of penetrant within the polymer matrix, could be explained by the crystalline regions acting as an impermeable barrier to the diffusing molecules. In the diffusion of ethylene glycol into

PET, the crystalline regions merely slow down the rate of sorption and swelling, suggesting that the ethylene glycol can penetrate the crystalline regions. This is a very important finding, as small amounts of ethylene glycol may well be present in commercially available PET films. Some procedures use soxhlet extraction for the removal of small organic molecules from PET. Therefore the solvent used in the extraction must therefore be able to penetrate the crystalline regions to remove the ethylene glycol which is presumably in both the amorphous and crystalline phases.

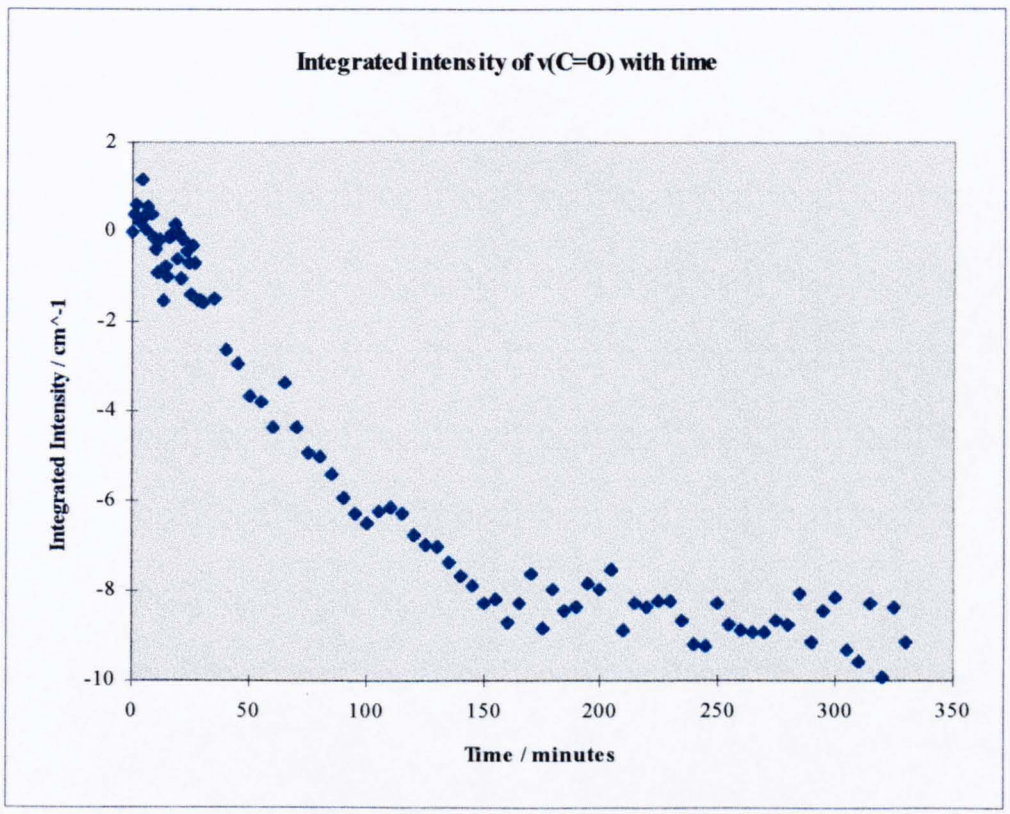

Figure 7.25. The integrated area of the ν(C=O) band of 29 % crystalline PET as ethylene glycol diffuses in.

Figure 7.25. shows the integrated intensity of the ν(C=O) region of ethylene glycol undergoing diffusion into 29 % crystalline PET, ratioed against the dry 29 % crystalline

film. The short time positive values in this plot show that interactions involving the carbonyl band occur before the swelling becomes dominant. The swelling is almost linear with time up to about 150 minutes where a maximum is reached.

The decrease in both the rate of polymer swelling and the level of polymer swelling can be attributed to the increase in the rigidity of the polymer chains with increased crystallinity.

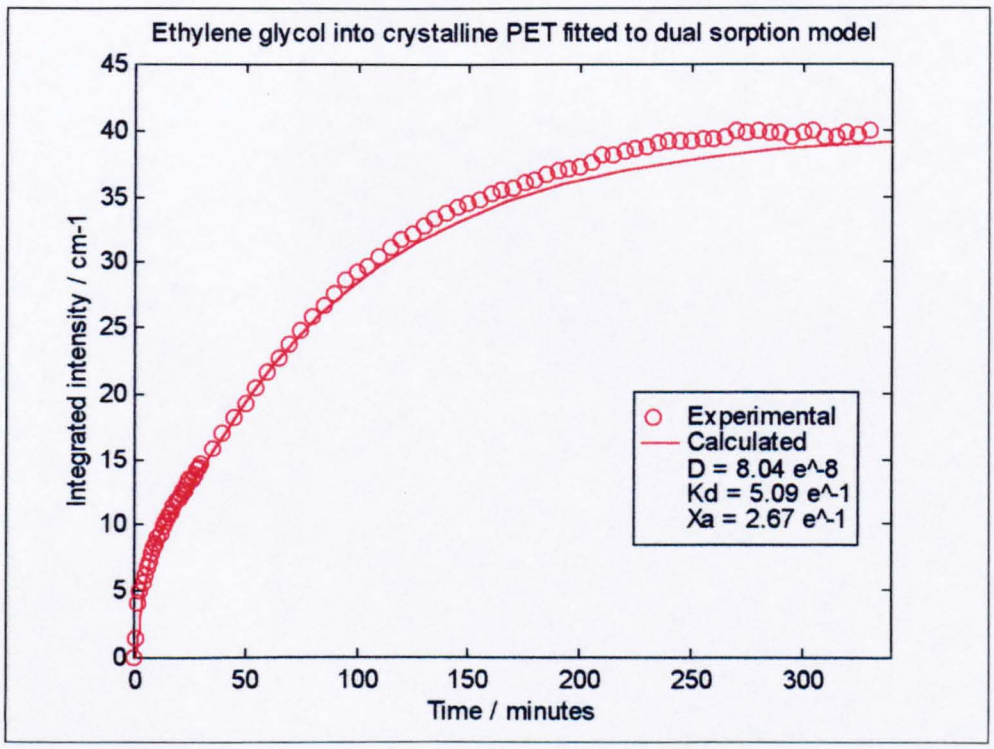

Figure 7.26. The plot of ν(OH) intensity versus time for ethylene glycol diffusing into29 % crystalline PET fitted to a dual sorption model.

Figure 7.26. shows the output from fitting the experimental data to a dual sorption model with two diffusion coefficients. In a similar fashion to that seen in the diffusion of methanol into PET, the more crystalline sample does not fit the model as well as the amorphous sample. Once more at shorter times the model fits the data well, but as the data tends towards equilibrium the fit is not so good. This may be attributed to the

swelling slightly increasing the rate of diffusion at longer times. The output seen during the ATR experiment may thus be higher than predicted by the model. Anomalous diffusion involving swelling has been known to cause an increase in the rate of diffusion with penetrant content up to a maximum of swelling in other polymers [7.6].

Similarly to the diffusion of methanol into PET, a change in crystallinity has dramatically changed the rate of sorption to a greater extent than observed for water. Table 7.3. shows the calculated diffusion coefficients and proportion of strongly 'bound' penetrant for the diffusion of ethylene glycol into two different PET films.

Sample	4.7 % crystalline	29 % crystalline
D_1 / x 10^{-8} cm^2s^{-1}	20.2 (± 0.24)	8.04 (± 0.13)
D_2 / x 10^{-8} cm^2s^{-1}	5.73 (± 0.11)	4.09 (± 0.12)
X_a	0.57 (± 0.03)	0.27 (± 0.03)

Table 7.3. Calculated diffusion coefficients and fraction of 'bound' penetrant for ethylene glycol diffusing into PET.

From table 7.3. it is clear that the increase in crystallinity has more of an effect on the rate at which the diffusant 'binds' onto the polymer, D_1. Indeed it could be argued that there is no significant difference between the values for D_2, which is the progression of the penetrant molecules.

These findings suggest that the rate of sorption of ethylene glycol, into sites within the polymer matrix, is dependent on the level of crystallinity, but that the rate of the subsequent diffusion of the penetrant molecules is independent of the morphology.

The dual sorption model also indicates a difference in the proportions of strongly 'bound' and 'unbound' penetrant between the two PET samples. The more amorphous

film contains a bigger proportion of hydrogen bonded ethylene glycol molecules, than the more crystalline polymer. Figure 7.27. shows the band shapes of ethylene glycol in 4.7 % and 29 % PET at equilibrium.

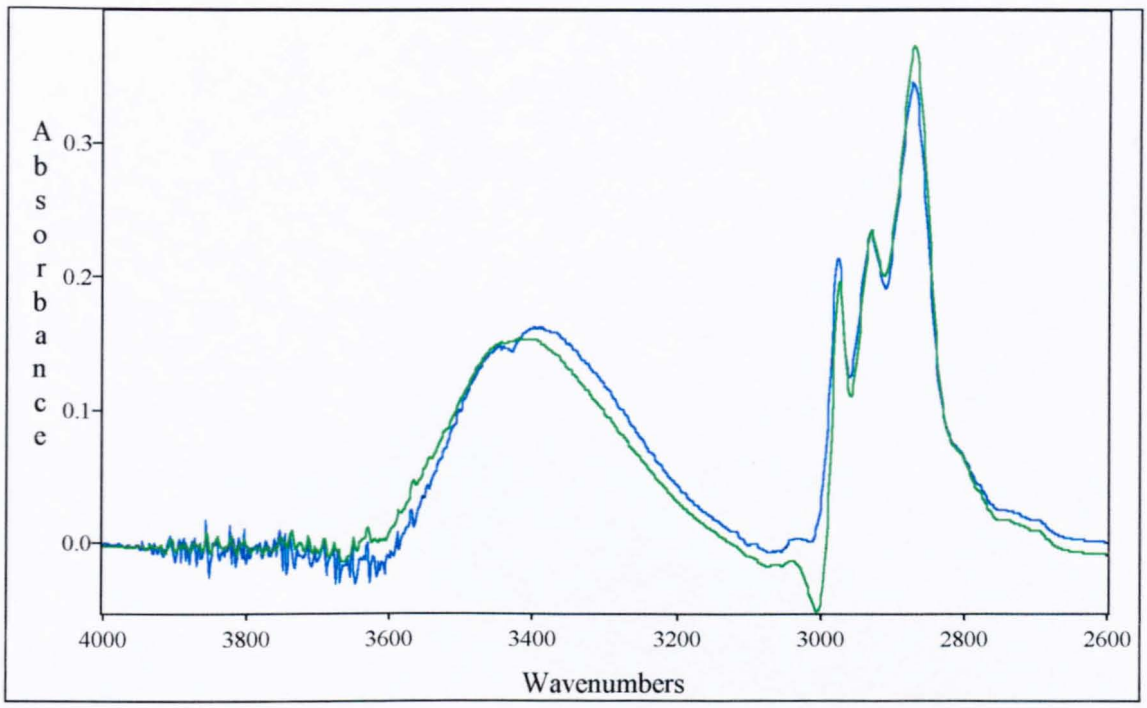

Figure 7.27. Comparison of the equilibrium ν(OH) for ethylene glycol in 4.7 % and 29 % crystalline PET.

Examination of the two equilibrium band shapes (figure 7.27.) shows that the equilibrium band of ethylene glycol in 4.7 % PET, has a larger proportion of high wavenumber component, which would lend support to the argument that the band seen in the FSD at 3540 cm^{-1} is due to ethylene glycol hydrogen bonded to the PET carbonyl.

Another interesting feature of figure 7.27. is the fact that the equilibrium intensities of the two bands are very similar. There are two possible explanations for this, one is that the equilibrium ethylene glycol content of PET is independent of morphology. Another, explanation is that the molar extinction coefficients, ε, of the hydrogen bonded and 'bulk'

ethylene glycol ν(OH) vibrations are quite different, with the ε of the 'bound' ethylene glycol extinction coefficients being smaller. As there is a greater proportion of 'unbound' ethylene glycol in 29 % crystalline PET, this may make the intensity of the ν(OH) band the same magnitude of that seen for an amorphous PET film containing the more ethylene glycol. This finding of a greater proportion of 'bound' penetrant in the more amorphous sample is in direct contrast to the findings for methanol.

Comparison of the relative rates of diffusion and the apparent differences in the state of the sorbed molecules between methanol in PET and ethylene glycol in PET lead to some interesting findings. One would reasonably expect the diffusion rate of methanol into PET to be faster than that of ethylene glycol, because of steric (size) effects. But one finds the opposite to be the case. This is most probably due to the greater degree of swelling found when ethylene glycol diffuses into PET. PET also contains an ethylene glycol unit within its structure and as such there may be some 'special affinity' between them.

One other factor in the differences may be elucidated from the ν(OH) spectra where distinct environments, possibly 'bound' and 'bulk' methanol, are clearly observed. This 'binding' on to the polymer may also slow down the rate of diffusion. Distinct environments are not so apparent in the ν(OH) spectra of ethylene glycol in PET.

7.4. Summary.

The diffusion of the organic molecules, methanol and ethylene glycol, into PET can be followed successfully by FT-IR ATR. In the amorphous PET films, diffusion is accompanied by swelling and crystallisation for both molecules and can be fitted to a dual sorption model. There is spectroscopic evidence for both a 'bound' alcohol - PET moiety and a 'bulk' alcohol species (not strongly interacting with the polymer) within the polymer matrix. For methanol in PET the proportion of the sorbed alcohol which is 'bound' is found to increase with crystallinity, but for ethylene glycol the reverse is true. For methanol diffusion, increasing the crystallinity is shown to have a drastic effect on both the rate of diffusion and degree of swelling. For ethylene glycol diffusion, the degree of crystallinity appears to affect the rate of swelling and the initial rate of sorption of penetrant, the rate of the subsequent diffusion of the penetrant molecules seems to be unaffected by morphology.

7.5 References

7.1. P.S. Hope, D.A.G. Parsons, G. Capaccio and M.J. Kitchiner, *Makromol. Chem. Macromol. Symp.*, **57**, 383, (1992)

7.2. M.M. Nir, A. Ram and J. Miltz, *Polym. Eng. Sci.*, **36**, 6, 862, (1996)

7.3. C.T. Costley, J.R. Dean, I. Newton and J. Carroll, *Anal. Comm.*, **34**, 3, 89, (1997)

7.4. 'Permeability of Plastic Films and Coatings to Gases, Vapours and Liquids', (Ed H.B. Hopfenberg), 73, Plenum Press, New York, (1974)

7.5. 'The Mathematics of Diffusion' 2nd edition, (Ed J. Crank), 254, Clarenden Press, Oxford, (1975)

7.6. N.J.M. Kuipers and A.A.C.M. Beenbackers, *Chem. Eng. Sci.*, **48**, 16, 2957, (1993)

7.7. P.J. Makarewics and G.L. Wilkes, *J. Polym. Sci. Polym. Phys. Ed.*, **16**, 1559, (1978)

7.8. O.Y. Hao and C.C. Chen, *J. Appl. Phys.*, **81**, 10, 6680, (1997)

7.9. N.P. Desai and J.A. Hubbell, *Macromolecules*, **25**, 1, 226, (1992)

7.10. C.J. Durning and W.B. Russel, *Polymer*, **26**, 119, (1985)

7.11. C.J. Durning and W.B. Russel, *Polymer*, **26**, 131, (1985)

7.12. C.-P.A. Lui, and P. Neogi, *J. Memb. Sci.*, **35**, 207, (1988)

7.13. C.J. Durning and L. Rebenfeld, *J. Appl. Polym. Sci.*, **29**, 3197, (1984)

7.14. C.J. Durning, L. Rebenfeld, W.B. Russel and W.B. Weigmann, *J. Polym. Sci. Polym. Phys. Ed.*, **24**, 1321, (1986)

7.15. C.J. Durning, L. Rebenfeld and W.B. Russel, *Polym. Eng. Sci.*, **26**, 1066, (1986)

7.16. C.-P.A. Lui, and P. Neogi, *J. Macromol. Sci. Phys.*, **B31**, 3, 265, (1992)

7.17. A.B. Desai and G.L. Wilkes, *J. Polym. Sci. Symp.*, **46**, 291, (1974)

7.18. P.J. Makarewics and G.L. Wilkes, *J. Appl. Polym. Sci.*, **23**, 1619, (1979)

7.19. M.R. Pereira and J. Yarwood, *J. Chem. Soc., Faraday Trans.*, **92**, 15, 2731, (1996)

7.20. M.R. Pereira and J. Yarwood, *J. Chem. Soc., Faraday Trans.*, **92**, 15, 2737, (1996)

7.21. S. Hajatdoost and J. Yarwood, *J. Chem. Soc., Faraday Trans.*, **93**, 8, 1613, (1997)

7.22. L.Cottam, R.P. Sheldon, D.A. Hemsley and R.P. Palmer, *Polym. Lett.*, **2**, 761, (1964)

7.23. H.N. Beck, *J. Appl. Polym. Sci.*,**19**, 2601, (1975)

7.24. C.A. Barson and Y.M. Dong, *Eur. Polym. J.*, **36**, 6, 862, (1996)

7.25. A.V. Popoola, *J. Appl. Polym. Sci.*, **49**, 2115, (1993)

7.26. A. Sfirakis and C.E. Rogers, *Polym. Eng. Sci.*, **21**, 9, 542, (1981)

7.27. G. Sadler, D. Pierce, A. Lawson, D. Suvannunt and V. Sethil, *Food Additives and Contaminants*, **13**, 8, 979, (1996)

7.28. M. Pereira, Thesis, Durham, (1994)

7.29. G.T. Fieldson and T.A. Barbari, *Aiche J.*, **41**, 4, 795, (1995)

7.30. J.A. Horas and F. Nieto, *J. Polym. Sci. Part B: Polym. Phys.*, **32**, 1889, (1994)

7.31. K.C. Cole, J. Guèvremont, A. Ajji and M.M. Dumoulin, *Appl. Spec.*, **48**, 12, 1513, (1994)

7.32. R. Belali and J.M. Vigoureux, *Appl. Spec.*, **48**, 4, 465, (1994)

Chapter 8

Probing the interface of PET laminates using confocal Raman microscopy

8.1. Studying crystallinity using Raman spectroscopy.

As was demonstrated in chapter 1, the vibrational spectrum of PET is highly sensitive to conformational changes. Whereas chapter 1 dealt with the infrared spectrum of PET, this section will give a brief survey of some of the relevant work that has been carried out determining the structure of PET using Raman spectroscopy. As technological advances have improved the output from a 'typical' Raman spectrometer, so the amount of published work carried out using the instrumentation has grown.

Polarised Raman spectra has readily been used to obtain information on the orientation of PET [8.1]. Non polarised Raman methods can be used to readily give information about the conformation and crystallinity of PET samples. For example, the bands at 1000 and 1096 cm^{-1} have been attributed to the *trans* conformer of the ethylene glycol moiety of PET [8.2]. Adar and Noether have shown that these bands not only increase with increased crystallinity, but also increase in oriented amorphous PET leading to the conclusion that these bands are not true crystalline bands, but are bands associated with the *trans* conformer of the ethylene glycol moiety [8.3]. The same cannot be said for the carbonyl band width at ~ 1730 cm^{-1}, which as Melveger first pointed out, is related solely to the crystallinity of the sample [8.4]. The narrowing of the bandwidth has been attributed to the benzene ring and the carbonyl groups being in the same plane, allowing resonance stabilisation of the π electrons. The simple relationship between Raman

carbonyl bandwidth and crystallinity (from density measurements) has been used quantitatively [8.4].

However, orientation has also been shown to affect the carbonyl bandwidth [8.5]. So care must be taken to ensure that the calibration standards are of the same type as the samples being determined, e.g. biaxially oriented standards, for a biaxially oriented calibration. Because of the tedious nature of obtaining the same type of standards for a particular set of samples, more complex data manipulation techniques, i.e. multivariate analysis, have been applied to this system.

Everall et al have used a partial least squares calibration technique, using the bands at ~1700, 1094, 997 and 860 cm^{-1} on a calibration set containing both oriented and isotropic annealed PET samples [8.6]. The same data analysis was applied to a fibre-coupled Raman microprobe to obtain density (i.e. crystallinity) maps of PET samples [8.7].

In order to qualitatively distinguish between a highly crystalline and an amorphous PET sample, the carbonyl bandwidth is a good guide. In order to quantify the difference in crystallinity between the two, a good calibration set and a robust data analysis technique is necessary. For the probing of the interface of a polymer laminate containing coextruded layers of PET and PET containing an *iso*phthalate comonomer to reduce crystallinity, then the carbonyl bandwidth will give semi quantitative information about the magnitude and nature of that interface. But the method will not be able to quantify the actual crystallinity level at a specified point without a proper set of standards.

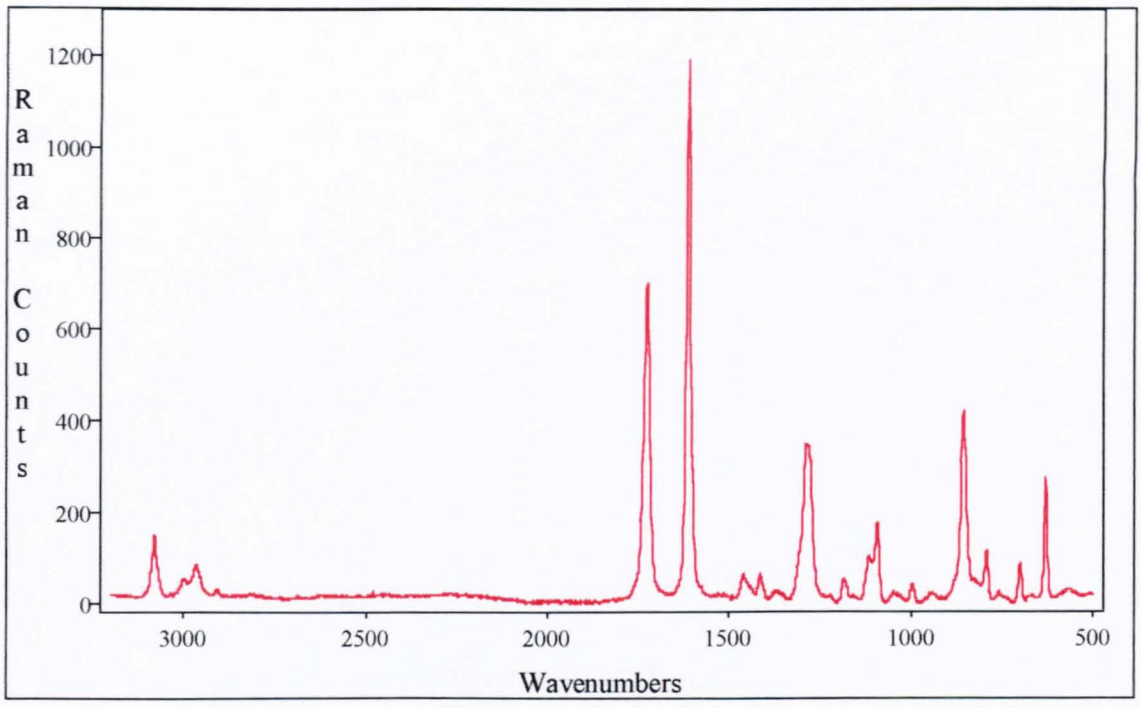

Figure 8.1. The typical Raman spectrum of a 25 % crystalline PET chip.

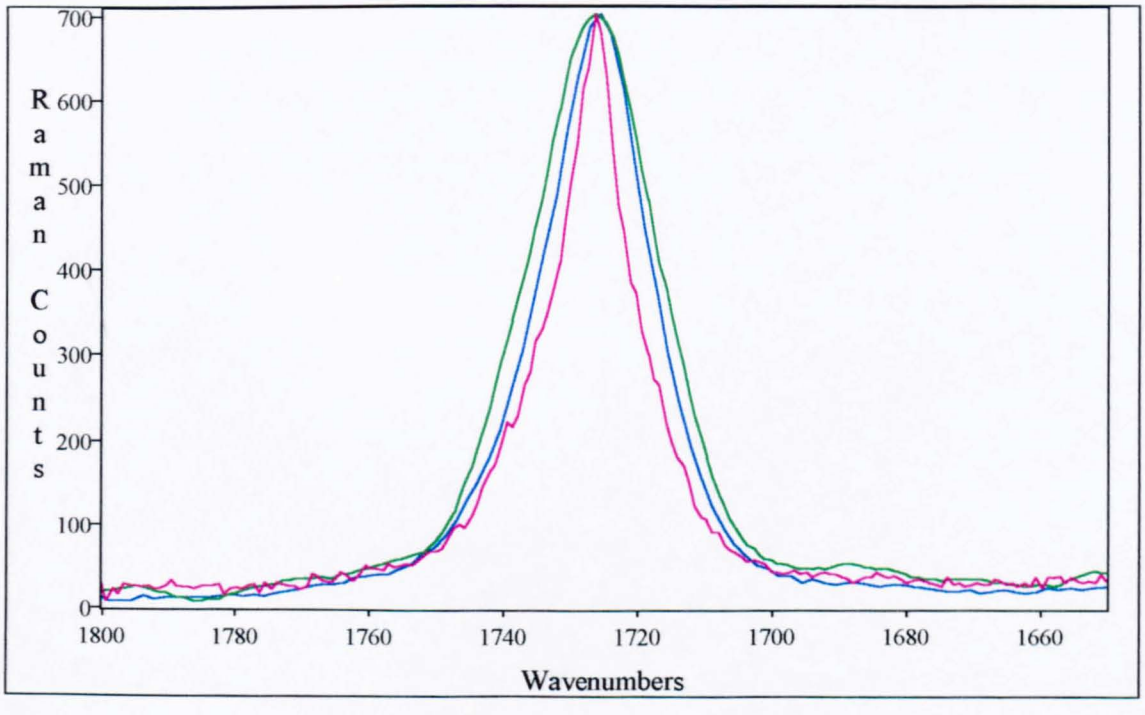

Figure 8.2. The ν(C=O) of 100 % amorphous, 25 % and 50 % crystalline PET.

Figure 8.1. shows a typical spectrum of a ~ 25 % crystalline PET chip. The spectrum has been baseline corrected to remove the background fluorescence.

Figure 8.2. shows the ν(C=O) bandwidth change for PET of various crystallinities. There are two important features of this figure. Firstly as is clearly shown, the increase in crystallinity leads to a decrease in carbonyl bandwidth. This is a true guide of crystallinity and is due to the coplanarity of the carbonyl groups with the benzene ring, allowing resonance stabilisation. The second feature is more subtle, but is equally important. As the band decreases in width, it becomes more symmetrical. The amorphous (green) band is clearly asymmetric. This has implications with regard to the calculation of Raman bandwidths. As a result of the change in symmetry with crystallinity, all the ν(C=O) Raman bandwidths must be calculated manually, as the 'width' obtained from most curve fitting procedures, will be the bandwidth of the symmetric band that fits the real asymmetric band best. This calculated width may or may not be the true bandwidth of the ν(C=O) band.

8.2. Depth profiling of polymer laminates.

Layering two (or more) polymers, is a simple method of changing the physical or chemical properties of a polymer film. Polymers layered in this way are called laminates. Laminates are used for a whole host of applications, such as packaging (foodstuff and non foodstuff), overhead projection slides or protective casings. How polymer laminates

interact with their surroundings (e.g. *vis a vis* biocompatablity **[8.8]** and adhesion **[8.9]**) defines their effective usage.

Consider a simple two layer polymer laminate. The properties of the laminate will be determined by the concentration profiles of the two polymers across the interface. The concentration profiles will be determined by the degree of interaction and interdiffusion between the two polymers.

There are numerous techniques, with many different advantages and disadvantages which have been used to study the interface of a polymer laminate. These include FT-IR ATR **[8.10 - 8.12]**, waveguide Raman spectrometry **[8.13]**, scanning electron microscopy coupled with energy-dispersive spectrometry (SEM / EDS) **[8.14]**, transmission electron microscopy (TEM) **[8.15, 816]** and confocal Raman microscopy **[8.17, 8.18]**.

The FT-IR ATR technique, requires the preparation of numerous polymer laminates of differing thickness and the use of spectral subtraction methods **[8.11]**. The use of waveguide Raman spectroscopy is often hampered by the difficulties in obtaining a suitable waveguide **[8.13]**. SEM / EDS and TEM, provide exception spatial resolution but sample preparation is often time consuming. Confocal Raman microscopy, requires no sample preparation and is non-destructive in nature, but suffers from relatively poor spatial resolution ($> 2\mu m$).

The theory of confocal Raman microscopy is given in chapter 3, but to remind the reader; in confocal microscopy, light scattered from a 'selected' plane within the laminate, is focused to a point and allowed to pass through a pinhole or slit. The light

above and below the plane of illumination are (mostly) blocked out by the pinhole or slit, thereby effectively controling the spatial resolution.

8.3. Experimental.

Commercially available, Melonex 850 films of 20 and 30 μm thickness were kindly donated by ICI films, Wilton. The films were prepared by the coextrusion of 80 % E47 PET and 20 % E99 PET, the latter being PET containing 18 % *iso*phthalate group as comonomer, to reduce the crystallinity. The E99 layer gives the finished film better adhesive properties (towards ink for example) than just pure PET. The films were then biaxially drawn, thermally annealed and cut into the desired shape. The finished films are generally used as over head projector transparencies.

Films were prepared in three different ways. For confocal Raman depth profiling, with the motorised stage, the samples were simply stuck down on a piece of silicon wafer using adhesive tape. Two samples were prepared for each film, one with the E99 side up, the other with the E47 side up. The spectra were obtained by running a macro program, which took a 200 second exposure 'grating spectrum' of the 1300 - 1800 cm^{-1} region at each 1 μm space interval in the z direction. The stage was automatically adjusted so that the next spectrum was taken from the region of the polymer 1 μm, directly below the last. In order to calculate the 'confociality' of the system, a 'reverse depth profile' of the 520 cm^{-1} band of silicon in air was performed. This was where the motorised stage was moved in 1 μm steps away from the microscope objective in between sampling. The silicon band intensity versus distancein the z direction was

plotted and the full width at half height criterion of this response was used to assess the depth resolution of the instrument for that particular experiment. It was important to check the confociality of the system prior to every experiment as it was liable to change over the course of time.

For the sideways-on depth profile, two different methods were used. Firstly a clean edge was cut using a scalpel, and the film was supported in plasticine, so that the clean edge was facing the lens of the microscope. The spectra were then obtained by focusing the microscope at one edge of the film and moving the stage manually in the x direction, in 1 μm steps. The distance moved was measured using the graticule on the microscope eyepiece. The final method of sample preparation involved the embedding of pieces of the polymer laminate in an epoxy resin. Blocks of the resin were then polished to give a flat surface with the polymer accessible. Spectra were obtained in the same manner described above for the scalpel cut polymer laminates. The films studied are shown in table 8.1.

Film type	Film thickness / μm
Melonex 850 E99 side up	20
Melonex 850 E99 side up	30
Melonex 850 E47 side up	20
Melonex 850 E47 side up	30
Melonex 850 embedded in epoxy resin	20
Melonex 850 embedded in epoxy resin	30
Melonex 850 supported by plasticine	20
Melonex 850 supported by plasticine	30

Table 8.1. Films studied for depth profile work.

8.4. Results and discussion.

Before each experiment the confocal response of the instrument was tested, by plotting the intensity obtained at each point, upon moving the microscope objective away from a silicon wafer in 1 μm steps. The full width at half height of this plot was deemed to be the confocal response. The instrument was realigned if the half width of the plot was greater than 1 μm, which corresponds to a depth resolution of 2 μm. A typical intensity verses distance of the silicon wafer from the microscope objective is shown in figure 8.3. Figures 8.4. - 8.8. show plots of the full width at half height of the PET ν(C=O) band verses depth / distance obtained from the various experiments.

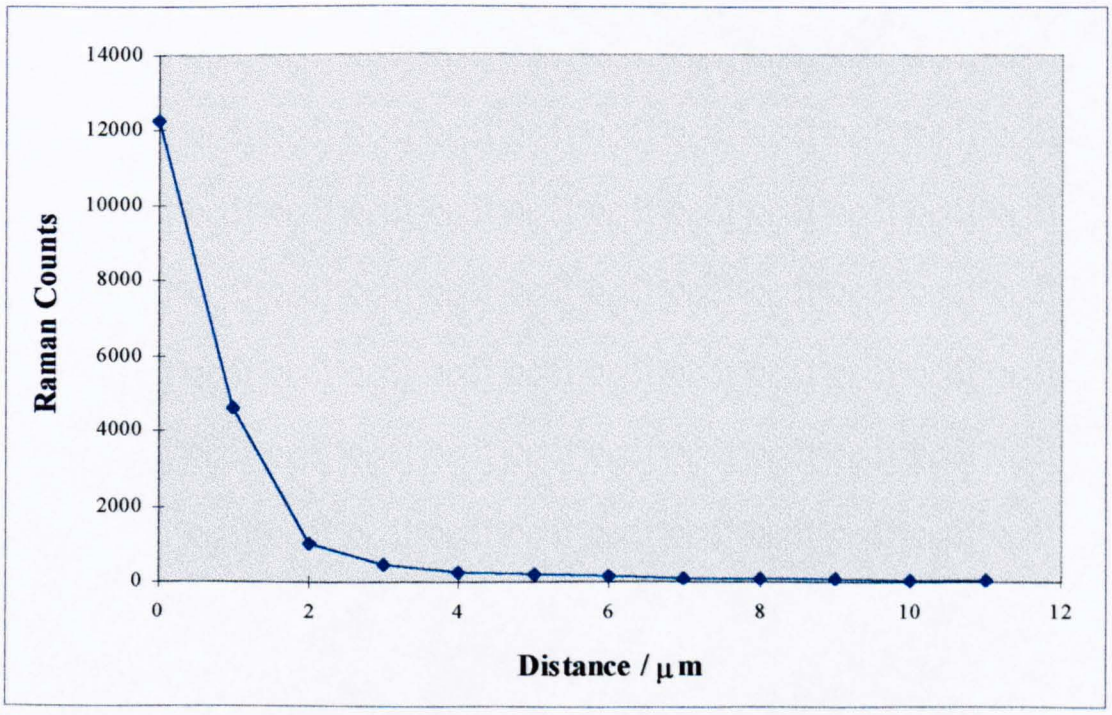

Figure 8.3. ***The confocal response of the Renishaw Raman Microprobe; obtained by a reverse depth profile of a silicon wafer with a 10 second exposure time using the X 100 objective, a 15 μm slit width and a 4 X 576 pixel area of the CCD camera.***

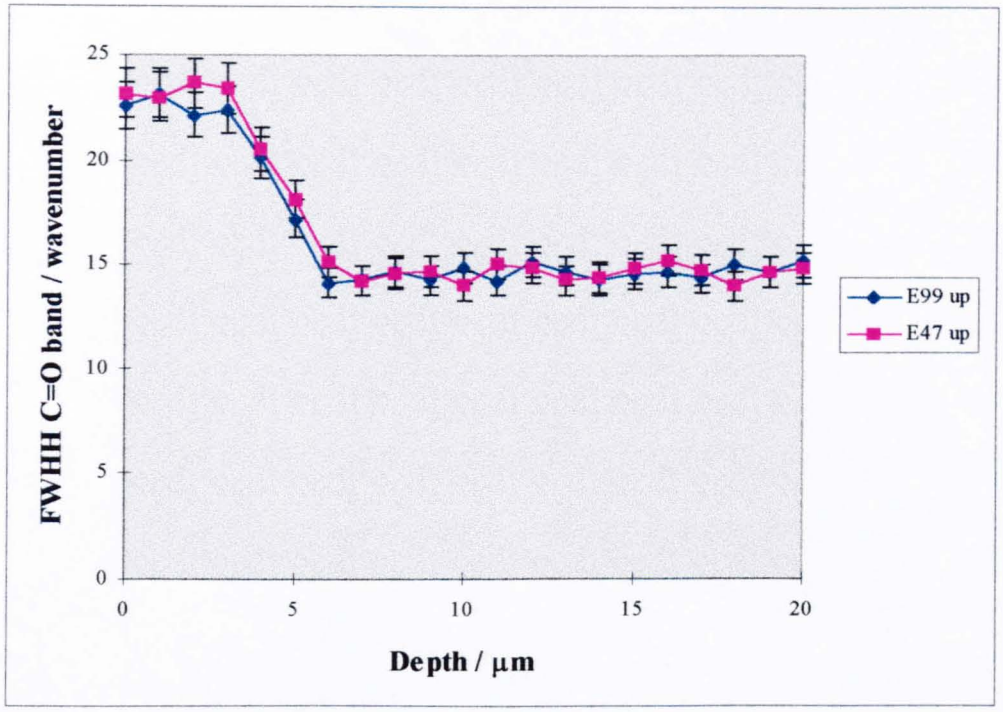

Figure 8.4. Confocal Raman depth profiles of a 20 μm Melonex 850 film.

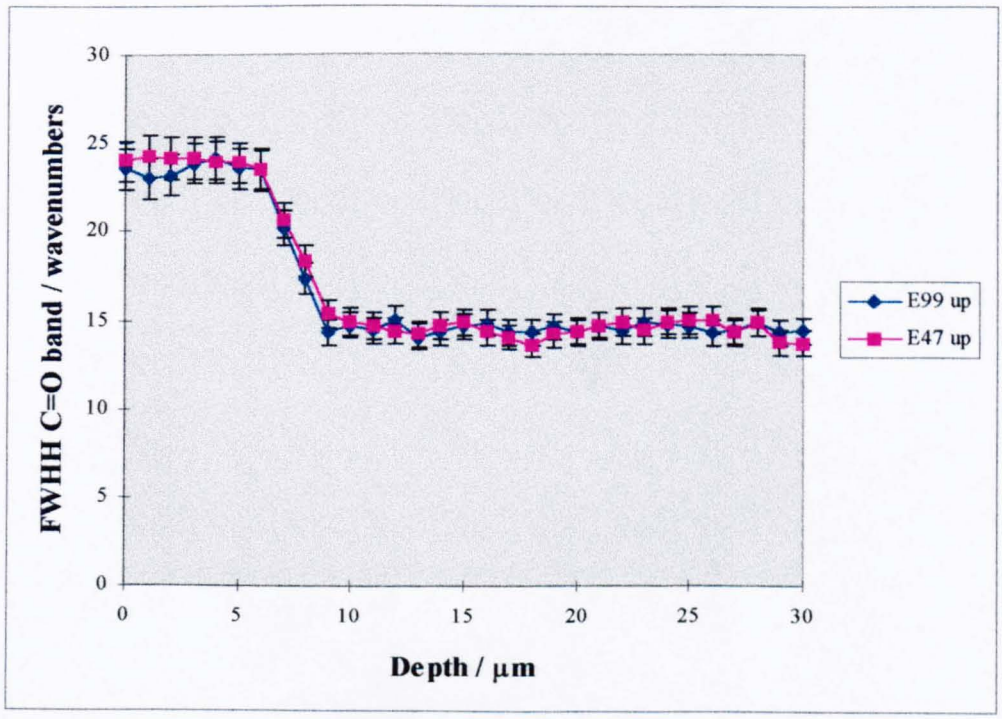

Figure 8.5. Confocal Raman depth profiles of a 30 μm Melonex 850 film.

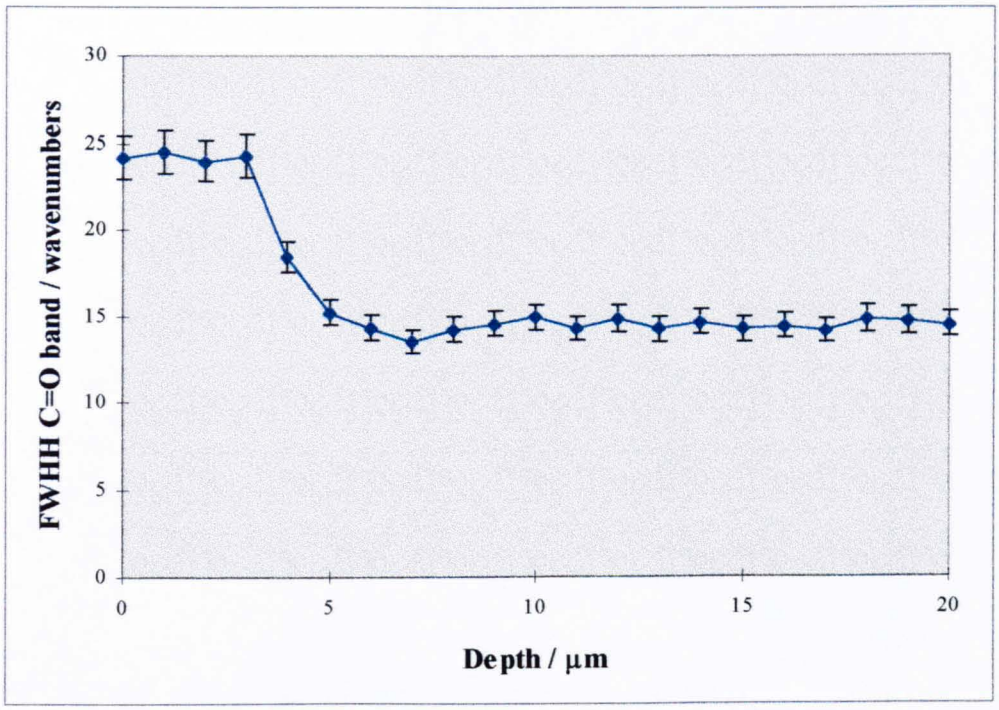

Figure 8.6. Confocal Raman lateral edge profile of a 20 μm Melonex 850 film.

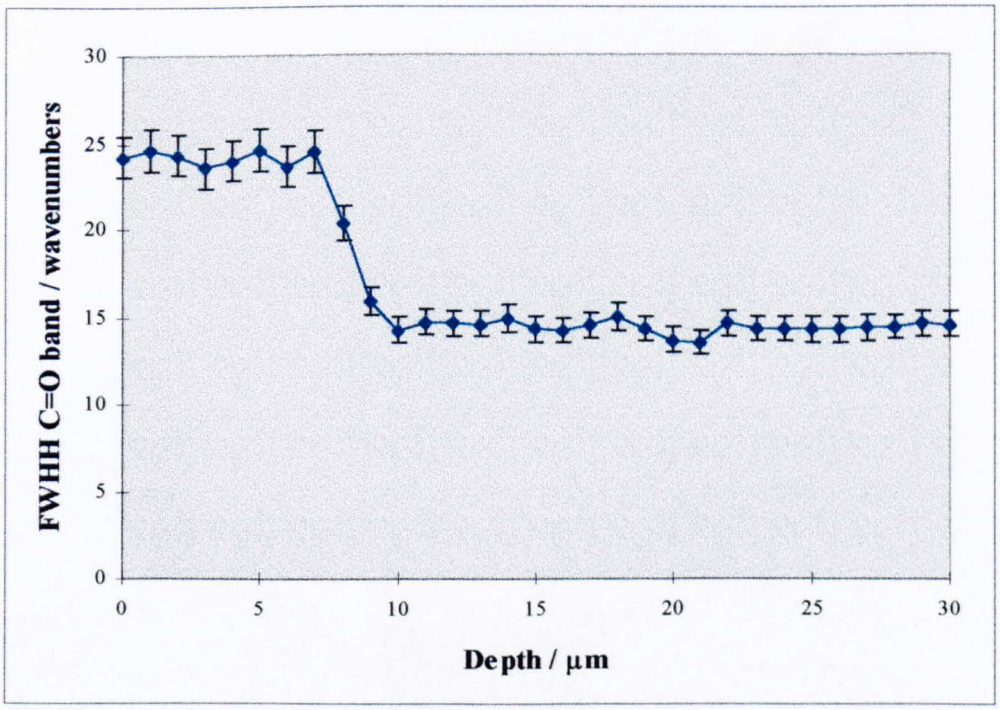

Figure 8.7. Confocal Raman lateral edge profile of a 30 μm Melonex 850 film.

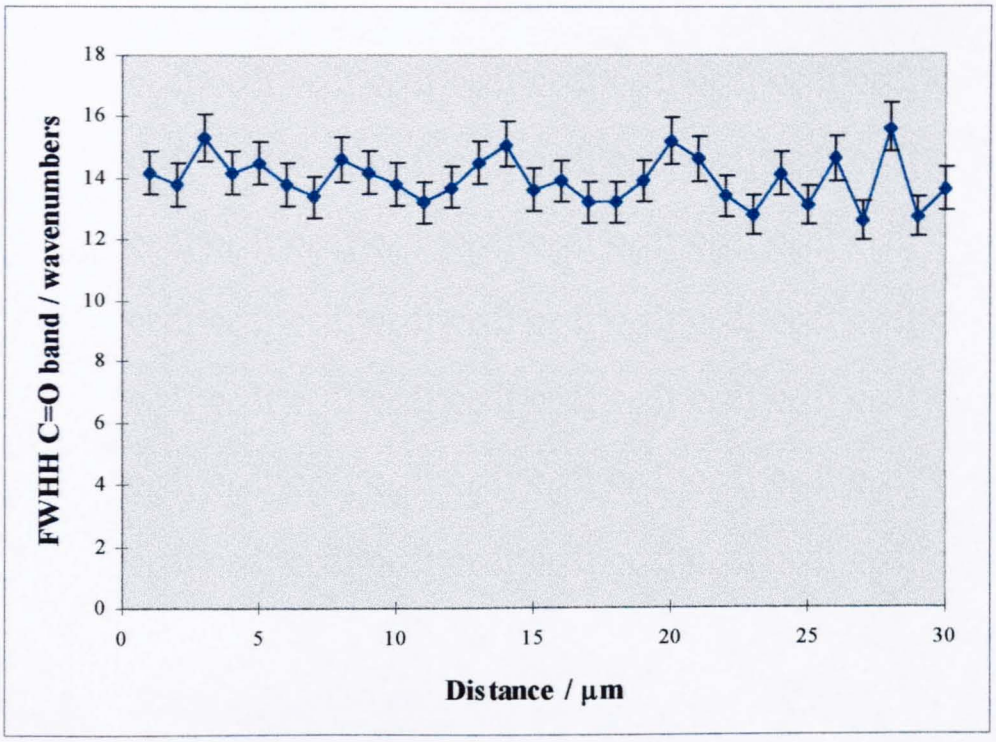

Figure 8.8. ***Confocal Raman lateral edge profile of a 30 μm Melonex 850 film, supported and polished in an epoxy resin.***

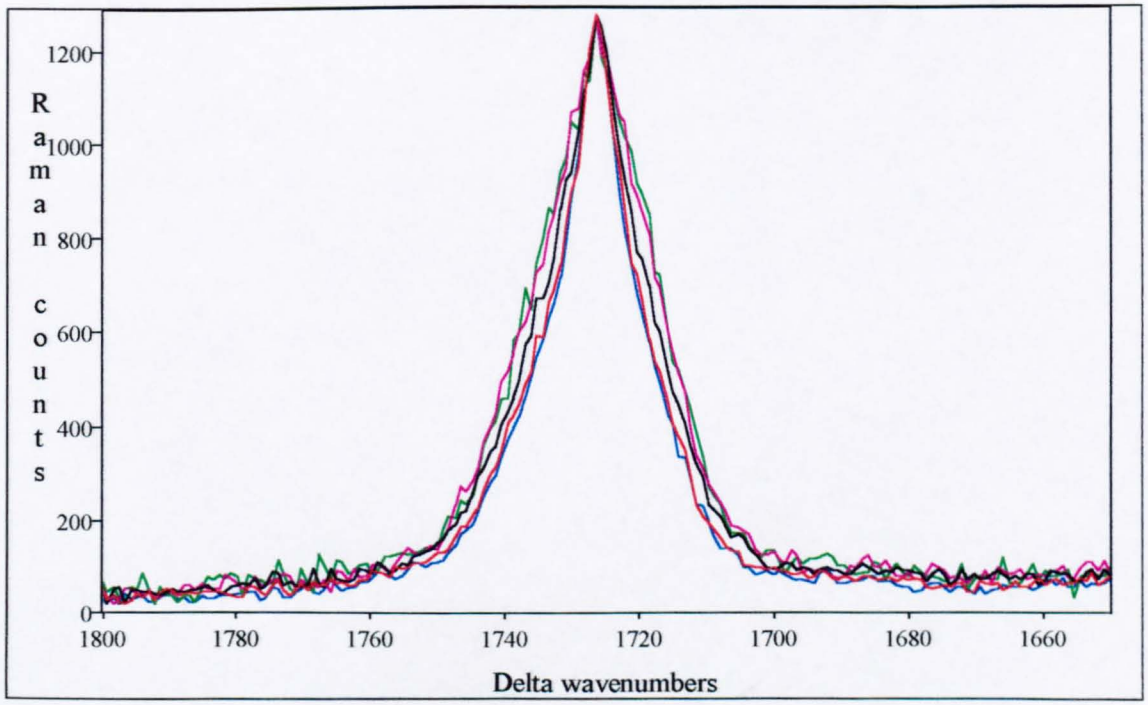

Figure 8.9. ***The changes in width of the carbonyl band at the interface of a 20 μm Melonex 850 laminate, measured using confocal Raman microscopy.***

Figures 8.4. and 8.5. were produced by obtaining the depth profile of a piece of Melonex 850 film from one direction, then reversing the film and obtaining a depth profile from the other direction. This should give some idea of the reproducibility of the technique.

Figures 8.4. - 8.7. show that the laminates consist of three regions. The first region is made up of low crystallinity, PET containing ~ 18 % *iso*phthalate. In a 20 μm film, this region is of the order of 3 - 4 μm thick. This value is about what one would expect since this layer should be ~ 20 % of the total laminate thickness.

Going through the laminate, the next region of the film is the interface. This region, in both 20 and 30 μm thick films is ~ 2 - 3 μm thick and consists of a crystallinity gradient between the essentially amorphous E99 layer (containing 18 % *iso*phthalate) and the 50 % crystalline E47 layer. This crystallinity gradient is either the result of interdiffusion between the two polymers, or a result of *trans*-esterification occurring as the two molten polymers come into contact with each other. *Trans*-esterification is a common phenomenon which occurs between polyesters, at elevated temperatures in solution or in a molten state [**8.19**]. In the case of PET, it involves the making and breaking of essentially labile ethylene glycol linkages, to form homogenous polymer chains from a mixture of two separate polymers.

The final region of the film is approximately 50 % crystalline PET and corresponds to the E47 region of the laminate. This is the largest section of the laminate and as such dominates the physical properties such as film rigidity and optical clarity.

Figure 8.8. shows the results of the lateral scanning of a Melonex 850 film supported in epoxy resin and polished to give a smooth surface. As can be seen by the comparison between this figure and figures 8.4. - 8.7. the polishing has greatly disrupted the structure of the laminate at the surface. The polishing appears to have 'spread' the E47 (pure PET) layer over the E99 (PET with *iso*phthalate comonomer) thus giving the profile the appearance of a pure E47 film. In this instance it would appear that the sample preparation technique used to obtain the polymer films for the lateral, or sideways-on laminate profiles is critical.

Figure 8.9. shows the carbonyl band for the interface region for a 20 μm Melonex 850 film examined using the confocal Raman depth profile technique. The band narrowing across the interface as a result of crystallinity changes is clearly shown. As stated earlier, Adar and Noether **[8.3]** have shown that this is a pure crystallinity band and not just an indication of an increase in *trans* ethylene glycol content (N.B. some *trans* conformers do exist in the amorphous phase).

Figures 8.4. and 8.5. show the results of the confocal Raman depth profiles of the 20 and 30 μm thick Melonex 850 films and figure 8.10. shows a schematic of the laminate depth profiles from the Raman data. It is interesting to note that the size of the interface is apparently independent of the thickness of the two polymer layers. This suggests that the interactions between the two polymer layers are occurring in the molten phase upon co-extrusion (stopping when the polymers solidify) and not during the annealing process. It would not be unreasonable to expect the thicker film to have a broader interface if the interactions (i.e. interdiffusion / *trans*-esterification) were (still) occurring during the annealing process, since it takes more time for thicker objects to cool than thinner ones,

(they have less surface area as a proportion of their overall volume from which the heat can dissipate). But, as the interface is independent of film thickness, it would appear that the interactions occur in the molten state. Both interdiffusion and *trans*-esterification, would be possible in the molten state.

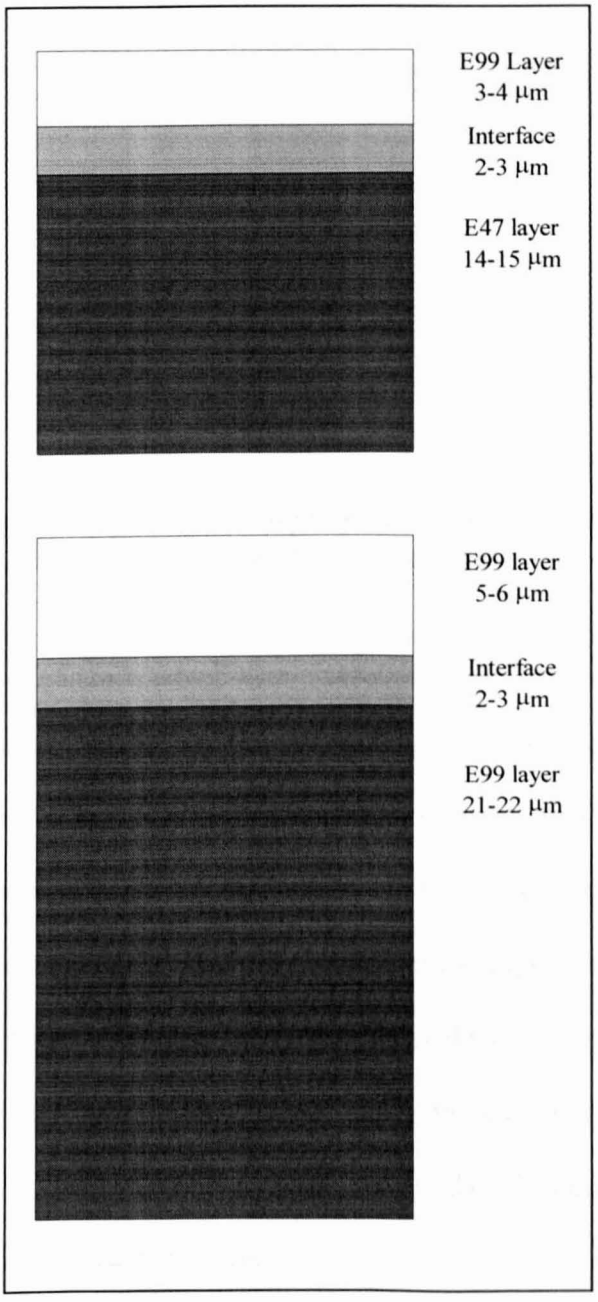

Figure 8.10. A schematic of the laminate depth profiles produced from the Raman data

8.4.1. Deconvolution of the confocal response from the depth profiles.

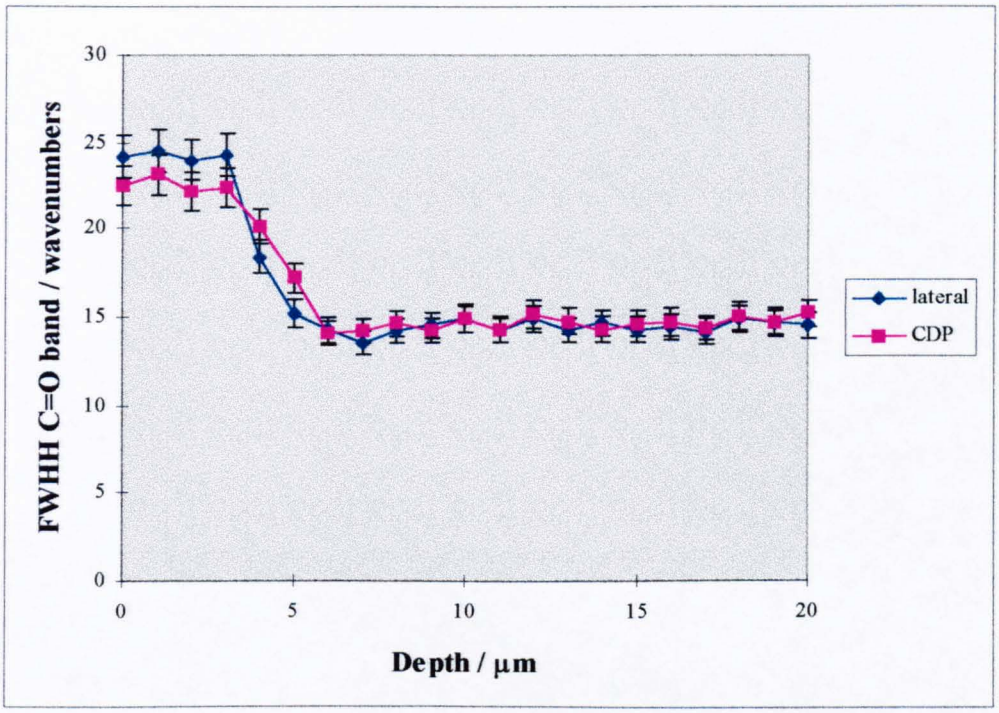

Figure 8.11. Comparison of confocal depth profile (CDP) and the lateral profile along the edge of a 20 μm Melonex 850 film.

Figure 8.11. shows the comparison of the output from a confocal Raman depth profile experiment compared to the sideways-on experiment from different portions of the same film. As is shown the interface is slightly broader in the confocal experiment. This broadening may be a result of the confocal response of the experiment. In the confocal experiment, scattered light above and below the confocal plane, is excluded by the slits. Although the slits exclude most of the unwanted light, there is still a significant amount of light from regions outside the confocal plane that reaches the detector. This will have an effect on the shape of the depth profile.

Figure 8.3. shows the estimated shape of the confocal response. It is necessary to assume that the confocal response in air, which has been measured, is the same as the confocal response in a polymer film, where the refractive indices involved are significantly different. If one makes this assumption then it is possible to remove the effects of the confocal response, by deconvoluting the confocal Raman depth profile output (RDPO), with the confocal response.

The deconvolution can be carried out by obtaining the Fourier transform of the RDPO and dividing it by the Fourier transform of the confocal response. The inverse Fourier transform of this new function will give the deconvoluted depth profile. But because of the fluctuating signal to noise causing significant scatter of the depth profile and confocal response, it was not possible to use the raw data from the experiments. Instead it was necessary to generate models of a similar shape to the output.

In this instance, an exponential function was chosen to closely mirror the confocal response and a Gaussian function was used to model the interface between two straight lines, representing the E99 and E47 layers. The result of the deconvolution is shown in figure 8.12.

The deconvoluted experimental profile in figure 8.12., shows a strange feature corresponding to about 4.5 - 6 μm in depth. This is a result of the Gaussian lineshape chosen for the deconvolution process and as such is spurious. The dotted red line is a continuation of the line representing the highly crystalline region of the polymer and is a more reasonable estimate of the deconvoluted output for the 4.5 - 6 μm depth. The deconvolution could perhaps have been carried out on the real data if the time taken to

acquire the data in the bulk of the polymer laminate was increased, thus improving the S/N. Doubling the time taken to obtain the data would give the same S/N as that observed for spectra taken from the top surface. It may also be argued that due to the low number of points within the data then the deconvolution would still be difficult on the real data.

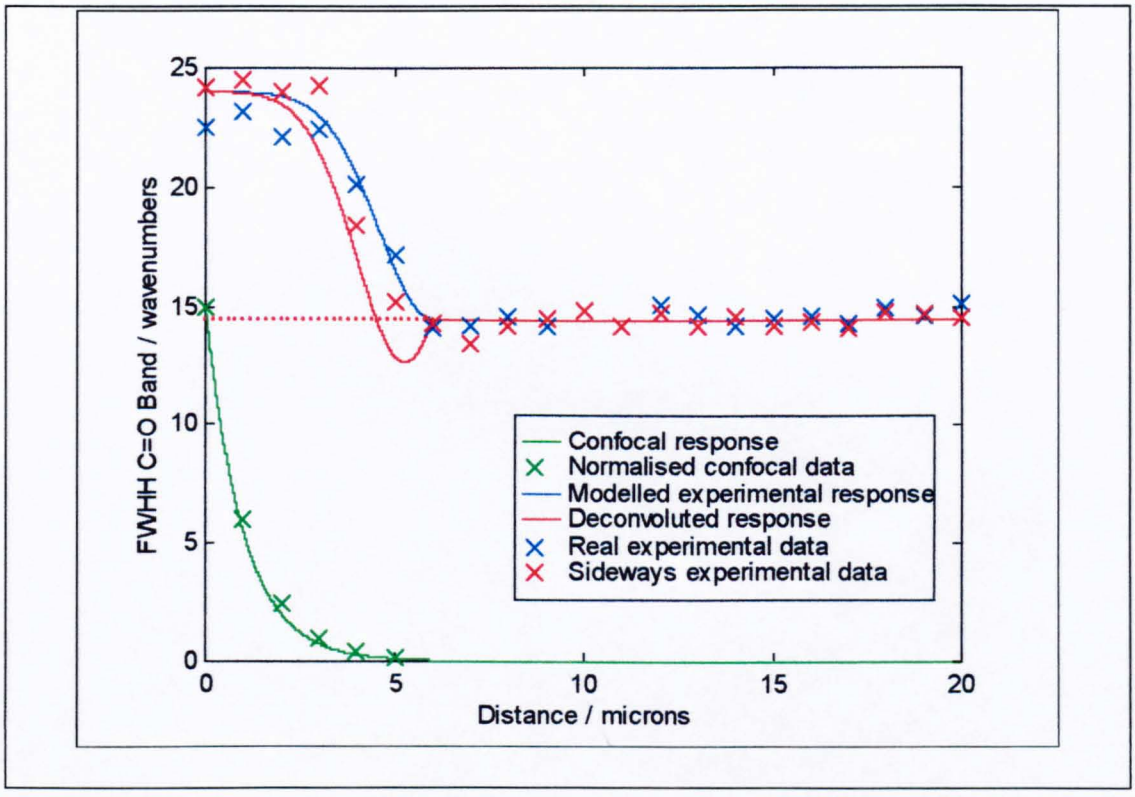

Figure 8.12. The deconvolution of the confocal response from the confocal depth profile experiment.

Figure 8.12. clearly demonstrates that the deconvolution process produces a sharper interface, as expected. The deconvoluted depth profile, has a more similar shape to the profile obtained from the Raman data obtained from the edge of the Melonex 850 film.

Another possible difference between the data obtained using the sideways-on method and the confocal Raman depth profile, may result from the differences in the refractive index as a function of light entering the polymer. When a Raman spectrum is obtained from the surface, the irradiating light, is scattered off the surface and the transmitting medium is just air. When a Raman spectrum is obtained from within the polymer bulk, part of the transmitting medium is the polymer itself which has a refractive index higher than air. This may change the position of focus, hence in this experiment, distort the shape of the probed interface. This is shown in figure 8.13.

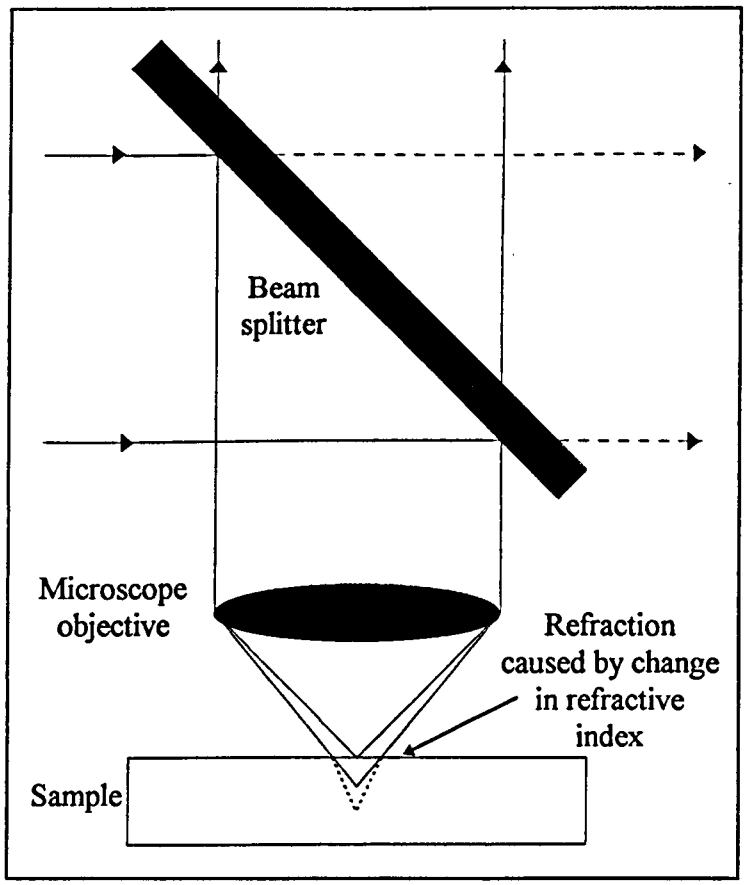

Figure 8.13. The effect on the change of refractive index during the confocal experiment on the focal point.

Closer examination of figure 8.12. shows that the deconvoluted Raman depth profile, has an interface that is still not as sharp as that obtained from the sideways-on experiment. This difference may be a result of refraction as described above, differences between the confocal response in the polymer and in air or a mixture of the two. It should also be considered that the spot size of the Raman experiment, using the 100x objective in the confocal mode, is 1-2 μm in diameter which implies that the sideways on measurement does not give an exact measure of the interface.

8.5. Summary.

The interface of two commercially available PET laminates has been successfully studied using Raman microscopy. Confocal Raman depth profiling was shown to successfully probe the interface between two PET layers, by using the Raman ν(C=O) band width as an indicator of crystallinity. The interface was shown to be ~ 2 - 3 μm thick.

Deconvolution of the confocal Raman depth profile, with the confocal response, resulted in a lineshape that was more similar to that obtained by examination of a cut edge of the same laminate by Raman microscopy.

Embedding the laminates in epoxy resin and polishing one edge flat, was shown to disrupt the profile of the laminates. Confocal Raman microscopy depth profiling, circumvents these problems by enabling the depth profile to be obtained without sample preparation.

8.6. References

8.1. J. Purvis, D.I. Bower and I.M. Ward, *Polymer*, 14, 398, (1973)

8.2. F. Adar and H. Noether, *Polymer*, **26**, 1935, (1985)

8.3. F.J. Boerio, S.K. Bahl, G.E. McGraw, *J. Polym. Sci. Phys. Ed.*, **14**, 1029, (1976)

8.4. A.J. Melveger, *J. Polym. Sci. (A2)*, **10**, 317, (1972)

8.5. J.M. Chalmers, L. Croot, G.J. Eaves, N. Everall, W.F. Gaskin, J. Lumsden and N. Moore, *Spectrosc. Int. J.*, **8**, 13, (1990)

8.6. N. Everall, P. Taylor, J.M. Chalmers, D. Mackerron, R. Ferwerda and J. Van der Maas, *Polymer*, **33**, 15, 3184, (1994)

8.7. N. Everall, K. Davis, H. Owen, M.J. Pelletier and J. Slater, *Appl. Spec.*, **50**, 3, 386, (1996)

8.8. H. Younes and D. Cohn, *J. Biomed. Mater. Res.*, **21**, 1301, (1987)

8.9. G. Gillberg, *J. Adhes.*, **21**, 129, (1987)

8.10. G. Boven, R.H.G. Brinkhuis, E.J. Vorenkamp, G. Challa and J. Schouten, *Polymer*, **33**, 6, 1150, (1992)

8.11. M.R. Pereira and J. Yarwood, *J. Polym. Sci. Part B: Polym Phys.*, **32**, 1881, (1994)

8.12. L.J. Fina, *Appl. Spec. Rev.*, **39**, 3&4, 309, (1994)

8.13. J.K.F. Tait, J. Yarwood, N.M. Dixon, N. Everall, G. Davis and R. MacIntyre, *J. Raman Spectrosc.*, **24**, 511, (1993)

8.14. F.P. Price, P.T. Gilmore, E.L. Thomas and R.L. Laurence, *J. Polym. Sci. Polym. Symp.*, **63**, 33, (1978)

8.15. R.S. Raghava and R.W. Smith, *J. Polym. Sci. Phys.*, **27**, 2525, (1989)

8.16. S. Koizumi, H. Hasegawa and T. Hashimoto, *Macromolecules*, **23**, 2955, (1990)

8.17. S. Hajatdoost and J. Yarwood, *Appl. Spec.*, **50**, 5, 558, (1996)

8.18. S. Hajatdoost, M. Olsthoorn and J. Yarwood, *Appl. Spec.*, In Press.

8.19. E. Anderssen and H.G. Zachmann, *Colloid Polym. Sci.*, **272**, 11, 1352, (1994)

Chapter 9

Summary and further work

9.1. Interactions between liquid water and PET at ambient temperature.

The technique of FT-IR ATR has been successfully applied to the study of the diffusion of water into PET films of the order of ~ 8-10 μm thick. The technique has allowed information on both the kinetics of diffusion and the disruption of the water network to be obtained *in-situ*. Two types of method preparation were employed to obtain a range of crystallinities. The first involved annealing the film above the T_g (~ 73 °C) to induce crystallinity. The second was more elegant and involved incorporating different levels of *iso*phthalate into the polymer film, which reduced the tendency of the polymer chains to form all *trans* conformers.

The rate of diffusion of water into PET was shown to be classically Fickian in nature and decreased with increased crystallinity, regardless of the film preparation history. Calculated diffusion coefficients, D, ranged between 8.57 and 0.52 x 10^{-9} cm^2s^{-1}, for samples of 4 - 25 % crystallinity. The relationship between crystallinity and D value was found to be non-linear and best fitted to an exponential model; $y = 17.636\exp(-0.136x)$, with a correlation coefficient, R^2, of 0.9854.

During the diffusion, dramatic changes in the shape of the ν(OH) band of water were noted. The band was deconvoluted into 4 component bands, which were shown to represent different 'strengths' of hydrogen bonding between the water and itself, and the water and the polymer membrane. At lower concentrations, i.e. short times during the diffusion, the ν(OH) band of water was at a much higher frequency relative to that of

pure water. This has been interpreted in terms of a 'breaking up' of the water hydrogen bonding network by the polymer membrane.

Interaction between the sorbed water and the ester carbonyl group of PET was illustrated by highlighting the changes occurring in the carbonyl region, where bands at 1735 and 1695 cm^{-1} have been interpreted as 'non-interacting' and 'hydrogen bonded' ester carbonyl respectively. There is some evidence of a concentration dependence on the strength of the perturbation of the ester carbonyl. At low water concentration, the perturbation seemed disproportionately high (denoted by the magnitude of the 1735 cm^{-1} band) As the water concentration increased the perturbation decreased, indicating that the clustering of water weakened the hydrogen bonding between sorbed water and the ester carbonyl. As the concentration of the water increased further still, the band at 1735 cm^{-1} was seen to increase in magnitude due to the number of ester carbonyls involved in interactions with the sorbed water.

A systematic deconvolution of the 4 components of the ν(OH) band of sorbed water was carried out as a function of time. At low concentrations (short times) the two high frequency components shift dramatically to higher frequency indicating interactions between the sorbed water and the ester carbonyl. The shift of the low frequency components was less dramatic but was still observed. As the concentration of sorbed water increased then there was a general shift of all the band component frequencies towards those calculated for pure liquid water.

The same deconvolution was carried out on the equilibrium sorbed water ν(OH) bands as a function of crystallinity. The intensities of the ν(OH) bands were shown to be much

higher than expected for the concentration of water. This was interpreted in terms of the perturbation of the water tetrahedral network by the polymer matrix. The perturbation was quantified by the comparison of the molar extinction coefficients, ε, of the component bands of pure water, with those at similar frequencies for sorbed water. The perturbation was found to be greatest for the high frequency components, further supporting the assertions that these bands were associated with the interaction of water with the ester carbonyl.

9.2. The Degradation of PET in water

The study of the interactions of water at elevated temperatures was undertaken using reflection absorption infrared spectroscopy (RAIRS). Films of < 150 nm were immersed in pure water at 52, 62, 70, 80 and 90° C, allowed to dry and the effect on the polymeric structure was examined. At temperatures below 90° C the effects noted, on the time scales studied, were annealing effects, resulting in an increase in *trans* ethylene glycol content. This was thought to be the result of the water acting as a plasticiser.

At 90° C, during several days of immersion, the polymer was found to undergo hydrolysis. During the first few hours, the effects were shown to be annealing affects, with increases in the *trans* ethylene glycol content of the polymer film. This was shown by an increase in the 1370 cm^{-1} CH_2 wagging mode and a shift to lower frequency of the ν(C=O) band. The first indications of hydrolysis were increases in the intensity and frequency shifts of the ν(C-H) band, that has been interpreted as in increase in the number of alcohol end groups (R-CH_2-CH_2-OH). As the hydrolysis became more

obvious, a broad doublet at ~ 3300 cm^{-1} emerged, that has been assigned to an increase in the number of alcohol and carboxyl end groups in a strongly hydrogen bonded environment. Changes in the CH_2 wagging mode band intensities indicated a loss of crystallinity as the degradation progressed. The loss of material from the polymer matrix was monitored by the intensity of the ring mode at 1410 cm^{-1}. The autocatalytic nature of the degradation was highlighted by normalising the ν(OH) intensity with the 1410 cm^{-1} band. A mechanism involving the preferred site of hydrolysis being a terminal ester group was proposed. Comparisons with hot alkaline hydrolysis were made. This occurred much faster and with more random chain scission.

9.3. The diffusion of organic liquids into PET

The diffusion of the organic liquids, methanol and ethylene glycol into PET was followed by FT-IR ATR. The diffusion of both molecules was found to be non-Fickian in nature and was accompanied by swelling and an increase in crystallinity. The diffusion was fitted to a 'dual-sorption' model for both sorbants. Spectroscopic evidence for a high frequency 'bound' alcohol-PET moiety and an 'un-bound' alcohol species within the polymer matrix was shown. The proportion of this 'bound' species was shown to depend on the morphology of the polymer film. For ethylene glycol diffusion, the initial degree of crystallinity was found to affect the initial rate of sorption of the penetrant and the rate of swelling. But, the rate of subsequent diffusion was shown to be independent of morphology. For methanol diffusion, the initial degree of crystallinity was shown to affect the rate of sorption, the degree of swelling and the rate of subsequent diffusion.

9.4. Probing the interface of a PET laminate using confocal Raman microscopy.

The interface between two commercially available PET laminates has been successfully studied using confocal Raman microscopy. The Raman bandwidth of the ν(C=O) band was used as a semi-quantitative guide to crystallinity. Confocal Raman depth profiles indicated that the interface was 2-3 μm thick and independent of film thickness. The confocal Raman depth profile was compared to a profile obtained by cutting a 'clean edge' of a piece of the laminate. The two profiles were shown to be similar although not identical. Deconvolution of the confocal response from the confocal raman depth profile, produced a depth profile that was more similar to that obtained from the 'clean edge'. Embedding and polishing the polymer laminates was shown to disrupt the surface of the laminate, producing an unreliable profile. Confocal Raman microscopy was shown to circumvent this problem by not requiring any sample preparation.

9.5. Further work.

In order to obtain a better understanding of the interactions between water and PET, especially at low water concentration (short times), it may be possible to follow the scheme of experiments outlined below.

a) In order to obtain a better understanding of the interactions occurring at low water concentrations, it may be possible to use thicker PET films (>15 μm). This would make use of the fact that the evanescent field only samples the first couple of μm of sample. This would mean that there would be a low concentration of water in the

evanescent field for longer and allow more scans to be obtained per spectrum improving the signal to noise ratio.

b) Purging the spectrometer with N_2 or dry air, would also allow a better quality of spectrum, free from the effects of water vapour, to be obtained. The implementation of this would need serious consideration if both kinetic and structural information was to be obtained. If the levels of water vapour decrease during the experiment this will also create interference problems.

c) The effect of temperature on both the kinetics of diffusion and the interactions between water and the polymeric membrane could be studied, if a heated ATR cell was employed. The interactions between the water and the polymer may well be different at elevated temperatures, since the distribution of hydrogen bond strengths within the bulk water will be different. At sufficiently high temperatures, it may be possible to examine the interactions between water and PET during *gauche* to *trans* isomerism and possibly relate these interactions to the reduction of the T_g. At even higher temperatures, it may be possible to follow the degradation process *in-situ*, but the sorbed water may make the interpretation of the results even more complicated that it already is due to the overlapping ν(OH) band.

d) It would be useful to obtain the real weight of the water in PET at equilibrium. This could be done by simply weighing the film before the diffusion experiment and after equilibrium water content had been reached. Because the films are quite thin, the levels of water involved will be quite low, therefore this may not be quite so simple as it seems. It may be necessary to use thicker films. Thicker films would present no problems spectroscopically, as the evanescent field limits the sampling thickness.

There is a great deal of scope for further understanding in the 'diffusion of organic liquids' work.

a) The most obvious set of experiments to perform would involve developing a matrix of morphologies. Diffusion coefficients and swelling characteristics for a series of films with different degrees of crystallinity would be of interest.

b) As mentioned above, good quality data at low concentrations may be obtained by purging the instrument with N_2 or dry air.

c) It would be useful to be able to quantify the change in crystallinity from the infrared spectra. This may be possible by generating a calibration plot, using bands that are free from interference of the sorbing molecule. Alternatively, chemometric techniques may be implemented.

d) One other area of interest would involve a rigorous deconvolution of the ν(OH) bands of the sorbed ethylene glycol and methanol. This may involve determining the number of component bands in the pure liquid, as it is unlikely that the same volume of data (that was available for water) is available for the alcohols.

The work on the degradation of thin PET films could also be expanded:

a) Films with a range of initial crystallinities could be prepared in an attempt to find the effect that morphology has on the degradation rate.

b) Different temperature regimes could be employed, for example using an autoclave to obtain degradation data at 120° C. A series of temperatures could then be used to calculate the activation energy of the degradation process and see if the values obtained for the 'surface' differ for those obtained for the 'bulk'.

c) Another useful experiment to carry out would involve carrying out the degradation in D_2O. This may give evidence about the preferred site of hydrolytic attack. This

would also have to be carried out in an inert environment as D_2O would readily become HOD in the presence of water vapour.